NORTHWESTERN UNIVERSITY

Atomic Scale X-ray Studies of the Electrical Double Layer Structure at the Rutile TiO_2 (110) – Aqueous Interface

A DISSERTATION

SUBMITTED TO THE GRADUATE SCHOOL
IN PARTIAL FULFILLMENT OF THE REQUIREMENTS

For the degree

DOCTOR OF PHILOSOPHY

Field of Materials Science and Engineering

By

Zhan Zhang

EVANSTON, ILLINOIS

June 2004

ABSTRACT

Atomic Scale X-ray Studies of the Electrical Double Layer Structure at the Rutile TiO_2 (110) – Aqueous Interface

Zhan Zhang

When a metal oxide surface comes in contact with an aqueous solution, an electrical double layer (EDL) is formed at the interface. The EDL region greatly affects many natural and industrial processes. Efforts for more than a century have been put forward to understand the features of the EDL. However, with little atomic scale structural knowledge, the ability is very limited to test current competing models and further understand or predict EDL properties. In this work, the surface and the adsorbate structure at the rutile TiO_2 (110)-aqueous interface is probed with synchrotron based X-rays.

Combining X-ray standing wave (XSW) imaging, which is direct and model independent, with tradition XSW triangulation, precise atom positions and absolute coverages are achieved. Crystal truncation rod (CTR) measurements yield the interfacial structure.

It has been revealed the rutile (110) surface termination and structure and the specifically adsorbed ion locations while contacting with the bulk water. In the aqueous

solution, both the bridging (BO) and the terminal oxygen (TO) rows are present and the surface undergoes minimal relaxations. An additional layer of water molecules with well-defined vertical and lateral positions are formed on top of surface oxygen groups. No more water structure is found farther away from the interface. The metal ions, including mono-, di-, and tri-valent ions, are all found to be 'inner sphere' adsorbates at the rutile (110)-aqueous interface. The adsorption location is primarily determined by the ion sizes. The larger ions, like Rb^{+}, Sr^{2+}, and Y^{3+}, take the tetradentate positions, which are of equal distances to the two TO and BO atoms. Small ions, like Zn^{2+}, are at the extended bulk Ti positions.

With monovalent ions as the only background electrolytes at concentrations < 1 mol/kg, we found that, the adsorbed divalent ions are independent of the type of the background electrolyte and the solution ionic strength; both Zn^{2+} and Sr^{2+} ions adsorbed in the condensed layer saturate around 0.4 monolayer; negligible amount of divalent ions are in the diffuse layer; no evidence of surface ternary complexation is observed; and the Gouy-Chapman-Stern model is more appropriate for describing divalent ion distribution in the EDL.

Approved

_____

Professor Michael J. Bedzyk
Department of Materials Science and Engineering
Northwestern University
Evanston, IL

ACKNOWLEDGEMENTS

I am grateful to my advisors Professor Michael Bedzyk, Dr. Paul Fenter, and Professor Neil Sturchio for their guidance and encouragement during this work.

I thank Drs. Likwan Cheng, Tien-Lin Lee and Zhong Zhong for their instruction and help on the experimental techniques. I thank Drs. Dave Wesolowski, Michael Machesky, Lawrence Anovitz, Milan Předota, Jim Kubicki, Andrei Bandura, Sergei Lvov, Peter Cummings, Ariel Chialvo, Moira Ridley, Pascale Bénézeth, and Donald Palmer for consultations and collaborations. I thank Professors David Seidman and Kenneth Shull for serving on my examination committee. I thank former and current group members: Drs. Osami Sakata, Alexander Kazimirov, Don Walko, Changyong Park, David Marasco, William Rodrigues, Brad Tinkham, John Okasinski, Changyong Kim, Kai Zhang and graduate students Duane Goodner, Anthony Escuadro, Joseph Libera, and Yongseong Choi for their help and company. I thank the scientists and staffs at the Advanced Photon Source and Environmental Research Division, Argonne National Laboratory and at the National Synchrotron Light Source, Brookhaven National Laboratory.

I thank the Graduate School for the awards of the University Fellowship; Argonne National Laboratory for a Laboratory Graduate appointment; and the U.S. Department of Energy for funding the research project.

Finally I thank my family and friends, especially my beloved wife, for the supports they offered selflessly.

TABLE OF CONTENTS

LIST OF TABLES

LIST OF FIGURES

Chapter 1 Introduction

1.1 Electrical double layer

1.1.1 General concept

When mobile ions are present in a system that includes an interface, the distribution of the ions will be disturbed by that interface. The ions with different charges will follow different distribution profiles at the vicinity of the interface. Suppose we can separate the system at the interface, each of the separated parts would carry an equal but opposite charge. These two charged portions of the interfacial region are called the Electrical Double Layer (EDL).[1]

Here we are primarily interested in the EDL at the solid-liquid interface, specifically, at the oxide-aqueous solution interface. Due to the truncation of the oxide lattice, a charge is often found at the surface, which derives from either permanent charges (for instance, from isomorphic replacement of lattice ions) or induced charges (for instance, by protonation/deprotonation reactions of surface oxygen atoms). Ions in the solution are expected to form a concentrated layer adjacent to the interface. This concentrated ion layer, although strictly speaking only half of the EDL, is of greater importance in most circumstances. Therefore in the oxide-aqueous system, the EDL is normally refers to the solution ion layer alone, as adopted in this work.

The adsorption, desorption and redistribution of the ions in the EDL influence

numerous of chemical reactions occurring at the oxide-aqueous solution interface, including both the natural and industrial processes, such as the nanoparticle assembly, heterogeneous catalysis, bacterial attachment and nutrient uptake, colloid and contaminant transport, metal corrosion and fuel cell efficiency.[2,3] Therefore direct knowledge of EDL properties and how they are affected by the changes in solution conditions is necessary to understand, predict, and thus control the processes at the interface.

1.1.2 Gouy-Chapman model of electrical double layer

When the original EDL concept was introduced and developed by Helmholtz, Gouy, Chapman and Stern, the EDL was described primarily from the perspective of the electrostatic potential.[4,5,6,7] Since the charges are distributed on both sides of the interface, it is natural to model it as a capacitor with the oxide surface as one flat plate and the ions in solution as the other plate. This is generally referred to as the Helmholtz model, and is appropriate for ions that form a specifically bound layer at an interface. However, ions in solution often do not form a flat plate in many situations because they may also be distributed continuously from the interface into the solution. Therefore, to describe the variation of potential, ψ, with respect to distance from a charged interface, the Poisson equation is need:

$$\nabla^2\psi(x,y,z)=\left(\frac{\partial^2\psi(x,y,z)}{\partial x^2}\right)+\left(\frac{\partial^2\psi(x,y,z)}{\partial y^2}\right)+\left(\frac{\partial^2\psi(x,y,z)}{\partial z^2}\right)=-\frac{\rho^*(x,y,z)}{\varepsilon} \quad (1.1)$$

Here $\varepsilon = \varepsilon_r\varepsilon_0$ is the permittivity of the solution with ε_0 the vacuum permittivity and ε_r the

dielectric constant of the solution, and $\rho^*(x, y, z)$ is the charge distribution. Following the traditional definition, ψ is positive at a positively charged interface and vise versa. At infinity it is 0. In the case that the surface is a flat plane, the equation is reduced to a one-dimensional form (in z direction):

$$\frac{\partial^2 \psi(z)}{\partial z^2} = -\frac{\rho^*(z)}{\varepsilon} \tag{1.2}$$

z is the distance from the interface. The charge distribution, $\rho^*(z)$, is associated with the ion distributions, $n(z)$, which follow the Boltzmann equation:

$$n_i(z) = n_i^{\infty} \exp\left[-\frac{Z_i e_0 \psi(z)}{k_B T}\right] \tag{1.3}$$

Here $n_i(z)$ is the concentration of the ith ion at the interface region; n_i^{∞} is the concentration of the ith ion far from the interface; Z_i is the valence number of the ith ion, it has both magnitude and sign—the same sign as the charge of the ion; e_0 is the elementary charge; k_B is the Boltzmann constant; and T is the absolute temperature, in Kelvin (K). The equation shows that the probability to find an ion at a distance z from the interface is related to the work needed, $Z_i e_0 \psi(z)$, to bring the ion from infinity to the position z where the potential is $\psi(z)$.

Thus the charge density will be the sum of all the ion charges:

$$\rho^*(z) = \sum_i Z_i e_0 n_i(z) = \sum_i Z_i e_0 n_i^{\infty} \exp\left[-\frac{Z_i e_0 \psi(z)}{k_B T}\right] \tag{1.4}$$

Combining the Equation (1.2) and (1.4), a description of the diffuse double layer

is obtain, which is the so-called Poisson-Boltzmann equation:

$$\frac{\partial^2\psi(z)}{\partial z^2} = -\frac{e_0}{\varepsilon}\sum_i Z_i n_i^{\infty} \exp\left[-\frac{Z_i e_0 \psi(z)}{k_B T}\right] \tag{1.5}$$

This equation has no explicit general solution. It can only be solved in certain limited cases.

For a symmetrical $|Z_+| = |Z_-| = Z$ type electrolyte in solution, the solution of Equation (1.5) can be written as:

$$\Gamma(z) = \Gamma_0 \exp\left(-\frac{z}{\kappa^{-1}}\right) \tag{1.6}$$

$$\text{where, } \Gamma(z) = \frac{\exp(Ze_0\psi(z)/2k_BT) - 1}{\exp(Ze_0\psi(z)/2k_BT) + 1} \tag{1.7}$$

Here $\kappa^{-1} = \sqrt{\frac{\varepsilon k_B T}{2Se_0^2}} = \Lambda$ is the characteristic length, or Debye length, of the diffuse double layer, where $S = \frac{1}{2}\sum_i Z_i^2 n_i^{\infty}$ is the ionic strength of the solution, (in the case of symmetrical $|Z_+| = |Z_-| = Z$ type electrolyte, e.g., NaCl, the ionic strength is $S = Z^2(n^{\infty})^2$,) Γ_0 is the value of $\Gamma(z)$ *at* $z = 0$, where $\psi(z = 0) = \psi_0$ is the potential at the oxide surface; Z, again, is the absolute value of the valence number of the electrolyte whose bulk solution concentration is n^{∞}.

If the surface potential is low, i.e., $Z_i e\psi(z) << k_B T = 25.7\, meV$, the exponential terms in Equation (1.5) can be expanded and thus the Equation (1.5) takes the form:

$$\frac{\partial^2 \psi(z)}{\partial z^2} = \left(\frac{1}{\Lambda}\right)^2 \psi(z) \tag{1.8}$$

Obviously the solution to Equation (1.8) is:

$$\psi(z) = \psi_0 \exp\left(-\frac{z}{\Lambda}\right) \tag{1.9}$$

The same solution can also be achieved from the Equation (1.6) based on the same low potential assumption. Equation (1.9) is called linearized Poisson-Boltzmann equation and the low potential assumption model is also called Debye-Hückel approximation.[1.]

With the Debye-Hückel approximation, the Equation (1.3), which describes the ion distribution, can be written as:

$$n_i(z) = n_i^{\infty}\left[1 - \frac{Z_i e_0 \psi(z)}{k_B T}\right] = n_i^{\infty} - n_i^{\infty}\frac{Z_i e_0 \psi_0}{k_B T}\exp\left(-\frac{z}{\Lambda}\right) \tag{1.10}$$

Note that in this expression both Z_i and ψ_0 have both a magnitude and a sign. For instance, ψ_0 is negative for a negatively charged oxide surface. In this case the second item in Equation (1.10) is positive, so that cations accumulate at the interface and the concentration of the cations exponentially decays as distance from the interface increases. Similarly, anions are repelled by the interface. The potential and the ion distribution at the interface are shown schematically in Figure 1.1 (A) and (B).

In considering the charge balance near the interface, if the charge density on the oxide surface is σ^0, the total net charge on the solution side should be $-\sigma^0$, i.e.:

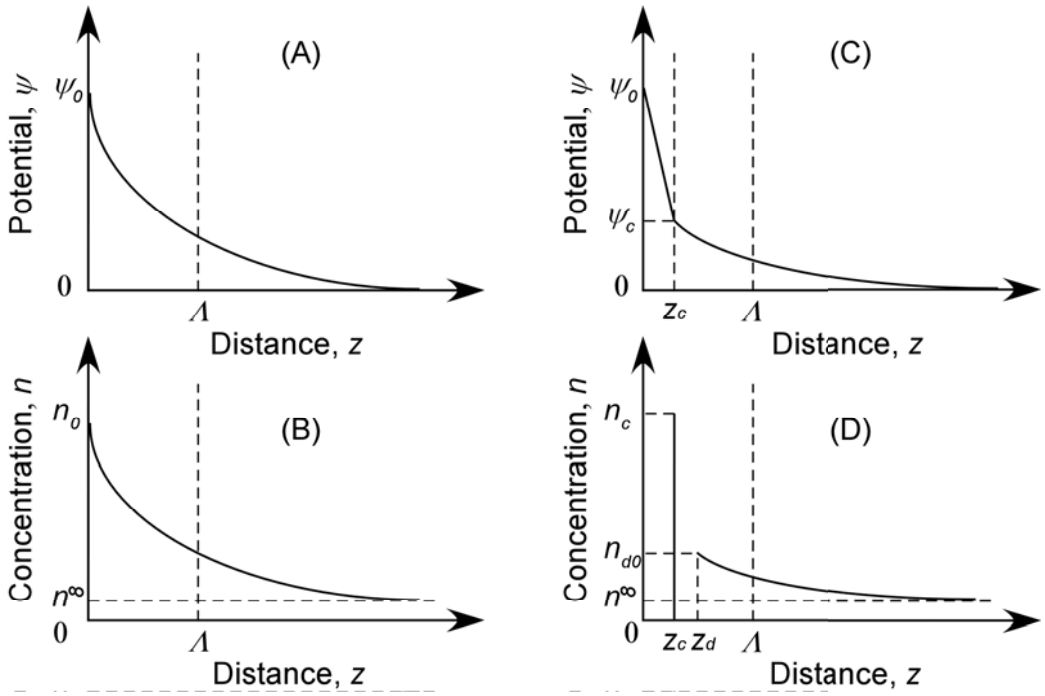

Figure 1.1. The potential and ion distribution as a function of distance at the oxide-aqueous interface at low potential. (A) and (B) represent the interfacial distribution without a Stern layer. (C) and (D) with a Stern layer. z is the distance from the interface. Ψ and n are the potential and the ion concentration adjacent to the interface, respectively. n^{∞} is the ion concentration in the bulk solution far away from the interface. Λ is the Debye length of the diffuse double layer.

$$\sigma^0 = -\int_0^\infty \rho^*(z)dz \tag{1.11}$$

For the charge density $\rho^*(z)$, we use the linearized version of Equation (1.4) that is expanded at low potential:

$$\rho^*(z) = \sum_i Z_i e_0 n_i^\infty \left[1 - \frac{Z_i e_0 \psi(z)}{k_B T}\right] = -\sum_i \frac{Z_i^2 e_0^2 n_i^\infty \psi(z)}{k_B T} = -\left(\frac{1}{\Lambda}\right)^2 \varepsilon\psi_0 \exp\left(-\frac{z}{\Lambda}\right) \tag{1.12}$$

Note that $\sum_i Z_i e_0 n_i^\infty = 0$ because of electro-neutrality of the solution. Combining equations (1.11) and (1.12):

$$\sigma^0 = \varepsilon\left(\frac{\psi_0}{\Lambda}\right) \tag{1.13}$$

This is the analog to the parallel plate capacitor relation. Equation (1.13) shows that a diffuse double layer at low potentials behaves like a parallel plate capacitor in which the separation between the plates is given by Λ. This is the reason that Λ is also called the double layer thickness. However, this simple relation has not be directly tested experimentally since hardly any of the parameters appearing in Equation (1.13) has been directly measured, except for the a few measurements of Debye length, Λ, with X-ray standing wave method.[8,9]

1.1.3 Stern layer of EDL

The Gouy-Chapman model dictates that the ion distribution follows the Boltzmann equation considering only electrostatic potential. However, at the interface, the chemical energy of the ion adsorption process is another significant contribution.

Ions from solution may be directly bound to the oxide surface to form a distinct layer with well-defined positions primarily determined by the underlying oxide surface structure. This layer of ions is the so-called Stern layer or condensed layer, as shown at $z = z_c$ position in Figure 1.1 (D).

The stern layer resembles the parallel plate capacitor model. Therefore we have:

$$\frac{(\psi_0 - \psi_c)}{z_c} = \frac{\sigma_c}{\varepsilon_c} \tag{1.14}$$

Here ψ_c, σ_c, and z_c are the potential, charge density and position of the condensed layer and ε_c is the permittivity within the condensed layer. The surface occupation factor, i.e., the fraction of the surface sites which is occupied, θ ($0 \le \theta \le 1$), for the adsorbed condensed layer ions can be written as:

$$\theta = \frac{\sigma_c}{\sigma^0} = \frac{Kn^\infty}{1 + Kn^\infty} \tag{1.15}$$

The constant K is proportional to a Boltzmann factor:

$$K \approx \exp\left[\frac{(Ze_0\psi_c + \phi)}{k_B T}\right] \tag{1.16}$$

The term $Ze_0\psi_c$ accounts for the electrostatic energy associated with the ion in the condensed layer and the term ϕ accounts for the specific chemical energy associated with the adsorption process. Combining Equations (1.14) and (1.15):

$$\frac{(\psi_0 - \psi_c)}{z_c} = \frac{\sigma^0}{\varepsilon_c} \cdot \theta = \frac{\sigma^0}{\varepsilon_c} \cdot \frac{Kn^\infty}{1 + Kn^\infty} \tag{1.17}$$

This indicates that the potential drop in the condensed layer increases with the

surface occupation. The potential drop approaches a constant value when the surface adsorption is saturated ($\theta = 1$). Depending upon the surface charge density and the nature of adsorption process, this condensed layer may or may not completely neutralize the substrate surface charge, i.e., ψ_c may be greater, equal to, or less than 0.

Further from the interface, outside of the condensed layer, the EDL can still be described with the Gouy-Chapman model. Only the starting point is the condensed layer position, z_c, instead of at the interface and the potential is ψ_c instead of ψ_0, as shown in Figure 1.1 (C). If the potential drop in the condensed layer is sufficiently large, the value of ψ_c may be sufficiently small, i.e., $\psi_c << k_B T$ (even if $\psi_0 << k_B T$ is not valid), so that the assumptions associated with the derivation of the linearized Poisson-Boltzmann equation are satisfied, and the diffuse layer can be simply described with an exponential function for both the potential and the ion distribution.

This model though long accepted, has not been generally validated because many of the model parameters are not directly available from experimental data. For instance, to date, the potential ψ_0 and ψ_c at the oxide-aqueous interface can not be directly measured, the permittivity ε_c within the condensed layer is assumed to have a value somewhere between 6 - 78 ε_0,[2.] and precise measurements of the position of the condensed layer, z_c, and the diffuse layer thickness, Λ, are very limited.

1.1.4 Surface complexation model

If condensed layer ions are present at the interface, the oxide surface should not be considered a charged hard wall. Instead, chemical reactions between the adsorbed

ions and the surface sites need to be taken into account. Evidence for such reactions derive from powder titration data, in which a mineral powder with large surface area in contact with solution is titrated upon changed in pH to determine the net amount of adsorbed ions and protons, through measurements of the surplus/deficit in the solution phase.

In the analysis of powder titration data, a three-layer model with one proton adsorption site (referred to as "1-pK_a" models) is normally adopted, as shown in Figure 1.2.[10] In a three-layer model, the specifically adsorbed cations reside in the first layer (labeled as M1); the specifically adsorbed anions and the background indifferent cations reside in the second layer (labeled as A and M2, respectively); and the third layer is the diffuse double layer. The capacitances for the first and the second layer are C_1 and C_2, respectively; and the general relation $1/C_n = h_n/\varepsilon_n$ stands for both cases with h_n and ε_n represent the thickness and the permittivity of the n^{th} layer (n = 1 or 2), respectively. $MeOH^{-x}$ and $MeOH_2^{1-x}$ are the unprotonated and protonated surface sites, and $MeOH^{-x} - M1^{+}$ and $MeOH_2^{1-x} - A^{-}$ are the cation and anion complexes bound to surface sites. Here the charges assigned to the sites (-x and 1-x) are based on the Pauling bond theory and therefore might not be integer numbers.[11,12,13] The Protonation constant, K_H, for the reaction:

$$MeOH^{-x} + H^{+} = MeOH_2^{1-x} \tag{1.18}$$

is given by:

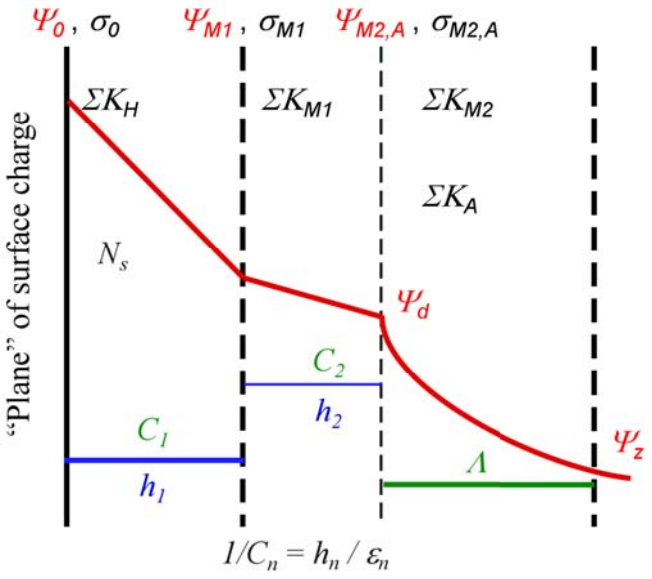

Figure 1.2. Stern based three-layer model for ion adsorption. Ψ_x is the potential in the electrical double layer; σ_x and K_x are the charges and bonding constants of the ions at the interface, respectively; (x = 0/H, M1, M2, and A stands for proton, adsorbed cation at inner sphere, background cation, and anion, respectively.) h_n and C_n are the thickness and the capacitance of the adsorbed ion layer; N_s is the surface adsorption site density and Λ is the diffuse double layer Debye length.

$$K_H = \frac{\left[MeOH_2^{1-x}\right]}{\left[MeOH^{-x}\right]\left\{H^+\right\}_b \exp\left(-Z_H e_0 \psi_0 / k_B T\right)} \tag{1.19}$$

The cation binding constant, K_{M1}, for the reaction:

$$MeOH^{-x} + M1^+ = MeOH^{-x} - M1^+ \tag{1.20}$$

is given by:

$$K_{M1} = \frac{\left[MeOH^{-x} - M1^+\right]}{\left[MeOH^{-x}\right]\left[M1^+\right]_b \gamma_\pm \exp\left(-Z_{M1} e_0 \psi_{M1} / k_B T\right)} \tag{1.21}$$

The anion binding constant, K_A, for the reaction:

$$MeOH^{-x} + A^- = MeOH^{-x} - A^- \tag{1.22}$$

is given by:

$$K_A = \frac{\left[MeOH^{-x} - A^-\right]}{\left[MeOH^{-x}\right]\left[A^-\right]_b \gamma_\pm \exp\left(-Z_A e_0 \psi_A / k_B T\right)} \tag{1.23}$$

Here [$MeOH^{-x}$], [$MeOH^{-x}$—$M1^+$], and [$MeOH^{-x}$—A^-] indicate the site concentrations (e.g., in mol/m^2) of surface sites $MeOH^{-x}$, $MeOH^{-x}$—$M1^+$, *and* $MeOH^{-x}$—A^-, respectively; [$M1^+$]$_b$ and [A^-]$_b$ indicate the ion concentration in the bulk solution; $\{H^+\}_b$ is proton activity in the bulk solution; $\gamma_\pm$ accounts for the activity of the ions in the solution at given temperature and ionic strength; Z_H, Z_{M1}, and Z_A are the charges for H^+, $M1^+$ and A^-, respectively, and they are usually the nominal charge of the ion (e.g., +1 for H^+); ψ_0, ψ_{M1}, and ψ_A are the potentials at the surface plane, the specifically adsorbed cation and anion plane, respectively, where the relationship between the potential and the binding constants is established. The potentials can be replaced with the charge density and

capacitors to emphasize the relation to the adsorption structure (here, assuming a negatively charged oxide surface):

$$\psi_0 = \frac{\sigma_0}{C_1} + \frac{\sigma_0 + \sigma_{M1}}{C_2} + \psi_d \qquad (1.24)^{14}$$

$$\psi_{M1} = \psi_0 - \frac{\sigma_0}{C_1} = \frac{\sigma_0 + \sigma_{M1}}{C_2} + \psi_d \qquad (1.25)^{15}$$

$$\psi_A = \psi_d = \frac{2k_BT}{e_0}\sinh^{-1}\left(-\frac{\sigma_d}{\sqrt{8\varepsilon k_BTn^{\infty}}}\right) \qquad (1.26)^{16}$$

Here ε is the permittivity of the bulk solution. σ_0, σ_{M1}, σ_A, and σ_d are charge density of the surface charge, the counter-cation charge, the counter-anion charge, and the diffuse layer charge, respectively (with signs). σ_0 is the sum of the surface structural charge, σ_{sc}, and the adsorbed or desorbed proton charge, σ_H. And all these charges except σ_d can be directly obtained from the charged surface site densities, e.g., [$MeOH^x$]. The condition of electro-neutrality requires that:

$$\sigma_0 + \sigma_{M1} + \sigma_{M2} + \sigma_A + \sigma_d = 0 \qquad (1.27)$$

Titration data, which primarily measures the adsorption and desorption of protons from the interface at the different solution conditions, can be fitted using the three layer model described above with K_H, $K_{M1} = K_A$, C_1 and C_2 as fitting parameters. Once C_1 and C_2 are determined, the heights of the counter-cations and counter-anions above surface charge plane can be estimated with:

$$C_1 = \varepsilon_1 / h_1 \quad \& \quad C_2 = \varepsilon_2 / h_2 \qquad (1.28)$$

Here ε_n (n = 1, 2) are unknown, so that h_n values can only be estimated with the bulk

water permittivity. If h_n values can be independently measured, the actual interfacial permittivity, ε_n, can be derived.

To provide a sense for the complexity of the adsorption process at the interface, different approaches have been taken to modify the model, including the use of the multi-site complexation model (MUSIC) to have the different surface sites accounted for;[17,18] the 2-pK_a model accounting for the multi-step of adsorption of protons;[19,20] and the four layer model, which separates the position of the counter-anion and background indifferent cation explicitly.[21]

These different approaches all emphasize different aspects of the EDL, which can yield very useful information about the macroscopic properties of EDL, such as the temperature dependent proton or ion adsorption constant, the potential change and the capacitance of the condensed layer.[14,18, 22,23] However, there is little or no atomic scale structure information being used in or generated from these models. Because the detailed atomic scale structure information at the interface is so limited, it has not been possible to directly test the different models for their ability to uniquely describe the EDL phenomena. Therefore the atomic scale structure at the oxide-aqueous solution interface is desired.

1.2 Atomic scale structure at oxide-aqueous interface

1.2.1 Importance of oxide surfaces

Oxide surfaces have received increasing attention in recent years because of their wide usage and their broad range of mechanical, electrical, and chemical properties. They can be insulators, semiconductors, conductors, or even superconductors. They can be used as supporting catalytic media or the catalyst themselves. They can be used as hard coatings or simply as paints. The ever-increasing usage of oxides is only limited by the knowledge of their properties.

Oxide crystals normally contain a high density of defects, including the non-stoichiometry composition and impurity atoms/ions. At the surface of such crystals, the atomic scale structures may be quite different from the ideal termination of the bulk lattice structure. Substantial efforts have been expended towards understanding oxide surfaces, both in vacuum and in ambient conditions.[24,25,26,27] These surfaces are simpler in vacuum, and more experimental approaches can be applied to understand their structures in vacuum, such as low-energy electron diffraction (LEED) and X-ray photon-electron spectroscopy (XPS).[26.] However, chemical reactions at oxide surfaces usually occur at ambient condition or elevated pressure rather than in vacuum. The surface structures and/or properties could be significantly different under those conditions. Therefore it is uncertain whether knowledge of the structure of oxide surfaces in vacuum is relevant to understanding chemical reactions at oxide interfaces. This is referred as the 'pressure gap' problem, which has led to increasing number of studies of oxides surfaces

at ambient condition, in contact with either gas phase or aqueous solution.[2.]

1.2.2 Atomic scale picture of EDL

When an oxide is immersed in an aqueous solution, the structure of the interfacial region, including the terminated surface, the adsorbate, and the solution layers, may be quite complicated, as shown schematically in Figure 1.3.[2.]

Here a negatively charged oxide surface is assumed. The surface charge, including the adsorbed protons (H^+), is located at the so-called 0-plane, normally taken as the average position of the charged surface oxygen group. The specifically adsorbed cations are in the condensed layer at the inner Helmholtz plane (IHP) or β-plane. Solvated ions, including both cations and anions, are distributed starting from the outer Helmholtz plane (OHP) or d-plane. Sometimes a second inner Helmholtz plane (IHP-2) is introduced at the position of the specifically adsorbed anions, i.e., the outer sphere ion position. The dielectric constants of water for the primary and secondary water layers are generally estimated rather than measured.[2.]

Emphasized in this figure are the various adsorption positions that might be found for the cations and anions. The dipole of the water molecules are shown as oriented at the interface rather than randomly distributed due to both surface charges and the cations and anions charges nearby.

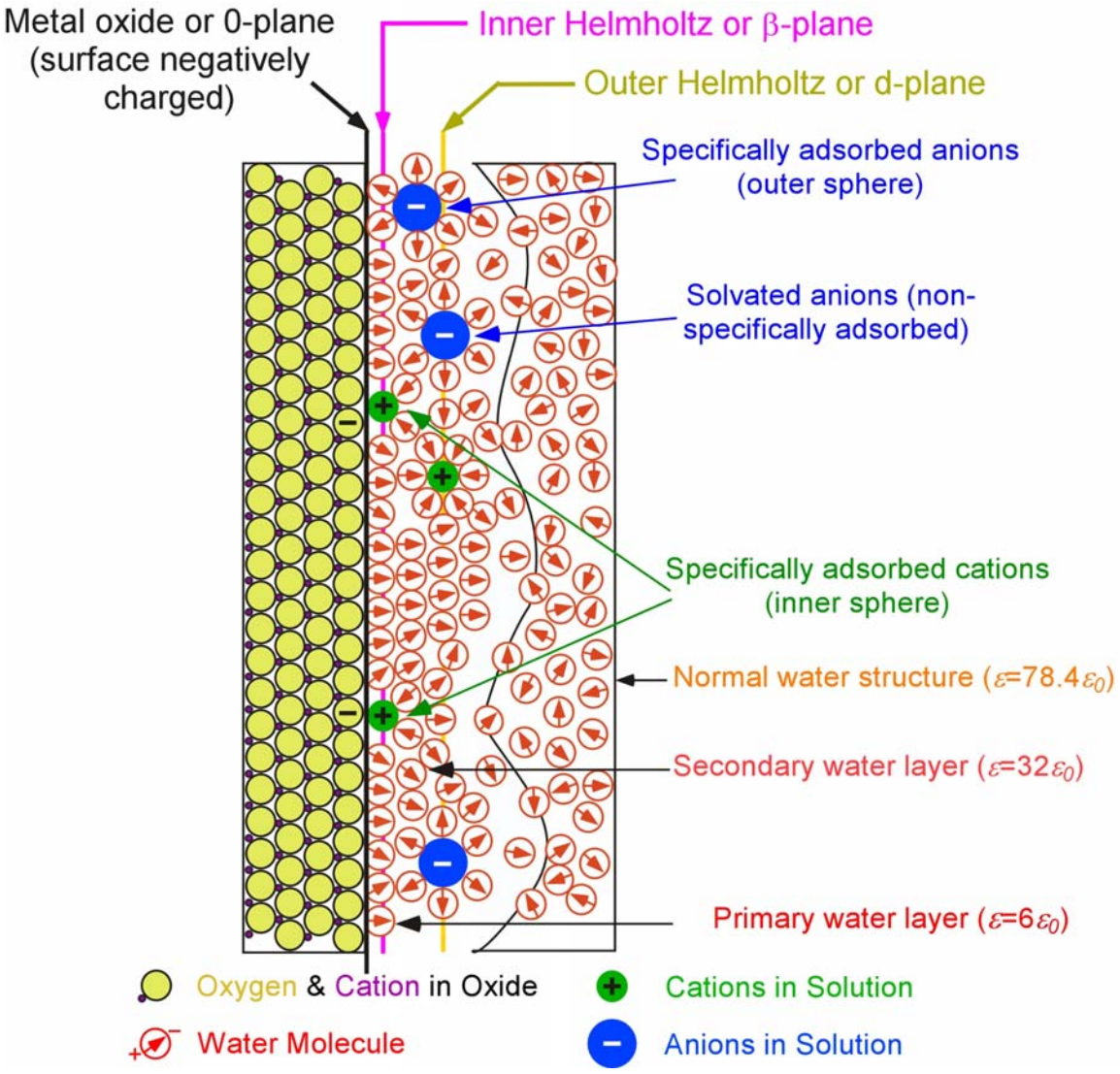

Figure 1.3. Schematic picture of electrical double layer structure at the oxide-aqueous solution interface. Adapted from reference 2.

The details described in this picture could significantly affect the chemical process at the interface. However, little is known about the structure. The knowledge of the interfacial structures will not only answer questions concerning the microscopic processes at the interface, but will also help put constraints on the interpretation of macroscopic EDL properties.

Considering the versatility of oxides and their surface structures, I chose to focus on the systematic behavior of a single oxide surface. Rutile (TiO_2) is the oxide to which this work primarily is devoted.

1.3 Rutile (TiO_2)

1.3.1 Why rutile

Rutile (TiO_2) is widely used as paint, coating material, photo-catalyst and in heterogeneous catalysis.[26.] It is also one of the most heavily studied oxides, as recently reviewed in references 24 and 26. Rutile has simple structure and it is very stable over a broad range of pressure, temperature and pH. Finally, high quality rutile powders and single crystals are available commercially. These factors make rutile an ideal system.

1.3.2 Rutile crystal structure

Rutile is the tetragonal structure ($P4_2/mnm$ space group), with $a = b = 4.594$ Å, and $c = 2.959$ Å at $T = 298$ K.[28] The primary tetragonal unit cell is shown in Figure 1.4 (A).[26.] Each titanium atom is surrounded by six oxygen atoms in a slightly distorted

octahedral configuration. The bonds between Ti and the O atoms at the vertex of the octahedral are slightly longer (~ 1.98 Å) than the other four (~ 1.93 Å). Also shown in Figure 1.4 (B) is the Wulff construction of the equilibrium shape of a macroscopic TiO_2 crystal at 0 K.[29] (110) surface of rutile crystal is the most stable surface according to the calculation.

1.3.3 Rutile (110) surface structure

Rutile (110) surface, as shown in Figure 1.5, has three possible terminating planes theoretically, indicated with the dashed lines in Figure 1.5 (B). Termination #1 has both a surface oxygen bonded to two Ti atoms (named bridging oxygen or BO) and an oxygen singly bonded to the surface (named terminal oxygen or TO) present on the surface, as shown in the figure. Termination #2 is terminated with only BO atoms present on the surface. Termination #3 is terminated with neither BO or TO, but only a bare Ti-O plane, as shown shaded in green in Figure 1.5, which we define as the surface Ti-O plane. Based on the crystal symmetry and the charge balance, termination #2 should be favored in vacuum. For instance, a simplified consideration is that when a rutile crystal is cleaved at this position, the two newly created surfaces would be identical and charge neutral. In fact that is the stable rutile (110) surface observed in vacuum.[30,31] The surface relaxation was both calculated [29,32,33,34] and measured [35,36] for this termination, which shows significant relaxations occurring along the surface normal direction.

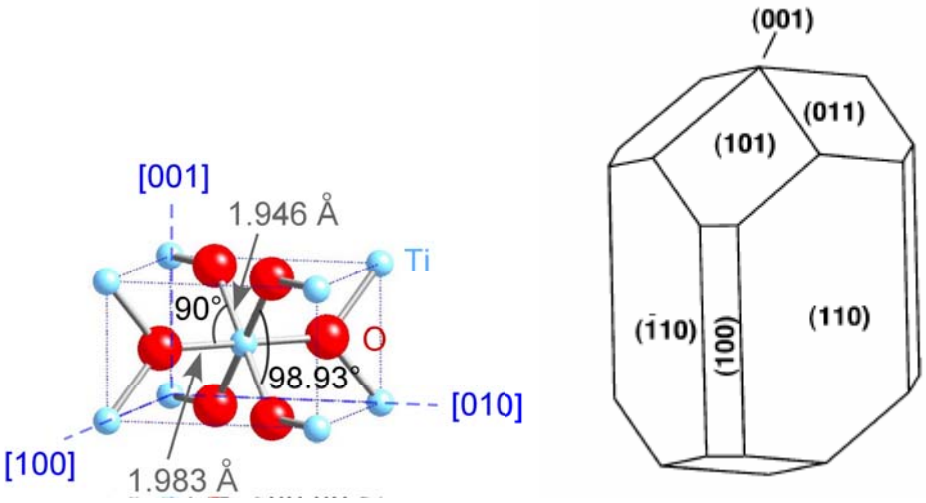

(A) (B)

Figure 1.4. (A) Unit cell of rutile TiO_2 (adapted from reference 26); and (B) Calculated Wulff construction of the equilibrium shape of a macroscopic TiO_2 crystal (taken from reference 29).

There are two kinds of Ti atom positions on such a surface. One is fully six-coordinated Ti, which is bonded to two BO atoms. The other is five-fold coordinated Ti atom where one longer Ti-O bond is broken. The two Ti positions are denoted as BTi (for titanium atom bonded to BO) and TTi (for titanium atom bonded to TO), respectively. For convenience of working with rutile (110) surface, a non-primitive tetragonal unit cell is defined, as sketched out in blue in Figure 1.5, with $a = c = 6.495$ Å and $b = 2.959$ Å, the unit vector $\boldsymbol{a}$, $\boldsymbol{b}$, and $\boldsymbol{c}$ along bulk crystal [-110], [001], and [110] direction, respectively. The transformation matrix from the primitive tetragonal unit cell to the non-primitive tetragonal unit cell is: $\begin{pmatrix} -1 & 1 & 0 \\ 0 & 0 & 1 \\ 1 & 1 & 0 \end{pmatrix}$. From here on, the subscript 'S' is used for the notations based on the non-primitive tetragonal unit cell, or the surface notations. The non-primitive tetragonal unit cell is twice the volume of a primitive tetragonal unit cell, i.e., there are four Ti atoms and eight oxygen atoms in such a unit cell. On the surface, however, there are 1, 2 and 3 oxygen atoms missing from one non-primitive tetragonal unit cell for termination #1, #2, and #3, respectively.

Although the termination #2 with BO atoms is a stable surface in vacuum, a fraction of the BO atoms can be relatively easily removed from the surface to create the surface oxygen vacancies. However, a rutile (110) surface with BOs completely removed (termination #3 configuration) is not energetically favorable because of too high a density of dandling bonds. Many studies have been devoted to understand the vacuum terminated surface and the adsorption of organic or inorganic molecules [see 26 and the

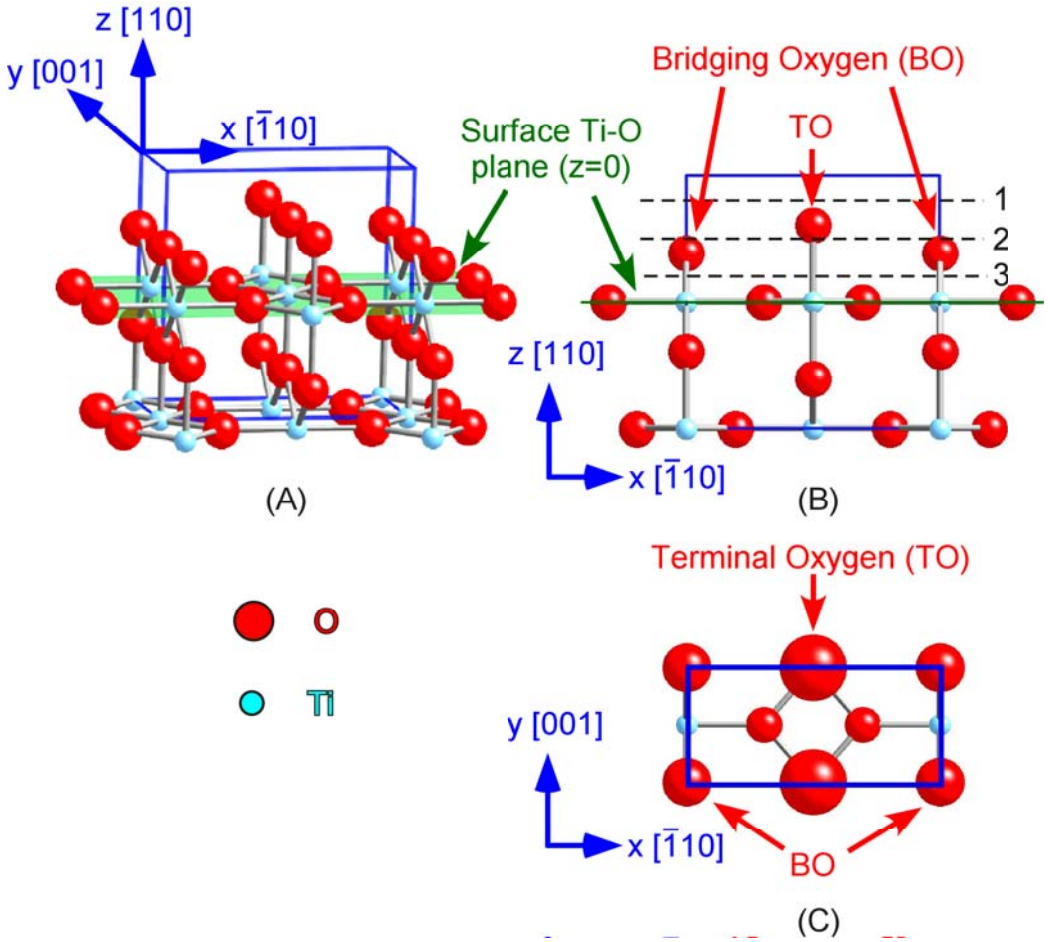

Figure 1.5. Rutile TiO_2 (110) surface structure shown as ball-and-stick model in (A) perspective view, (B) side view and (C) top view. The non-primitive tetragonal unit cell is shown (in blue); oxygen atoms are in red and Ti atoms in cyan.

reference there in]. Water, as one of the most important adsorbate at rutile surface, has been found to adsorb to the rutile (110) surface when introduced from the gas phase. Despite the disagreement over details of the adsorption process and status of adsorbed water, the bottom line is that water molecules adsorb onto rutile (110) surface, primarily on top of TTi, i.e., at TO site.[26,37,38,39]

For the EDL studies, the surface is instead immersed in bulk aqueous solutions, where abundant water molecules can be adsorbed onto the surface. Consequently, it might be expected that the TTi site on the (110) surface would be fully covered with either water molecule (H_2O) or hydroxyl group (OH^-).[40] So it is natural to consider the rutile surface in aqueous solution in the context of having both BO and TO present (termination #1), as shown in Figure 1.5. The unit shown in Figure 1.5 (C) is also defined as rutile (110) surface unit cell, which has an area of $6.495 \times 2.959 = 19.22$ Å^2.

1.3.4 Microscopic structure at rutile (110)-aqueous interface

In a schematic of the rutile (110)-aqueous interface, in Figure 1.6, the rutile surface is shown as an ideally truncated bulk crystal. The water molecules (or the hydroxyl groups) first complete the coordination shell of the TTi atoms. There are two kinds of surface protonation processes which could take place at TO and/or BO site:

$$Ti\text{-}OH^{x-1} + H^+ = TiOH_2^{\,x} \tag{1.29}$$

$$Ti_2O^{-x} + H^+ = Ti_2OH^{1-x}; \qquad Ti_2OH^{1-x} + H^+ = TiOH_2^{\,2-x} \tag{1.30}$$

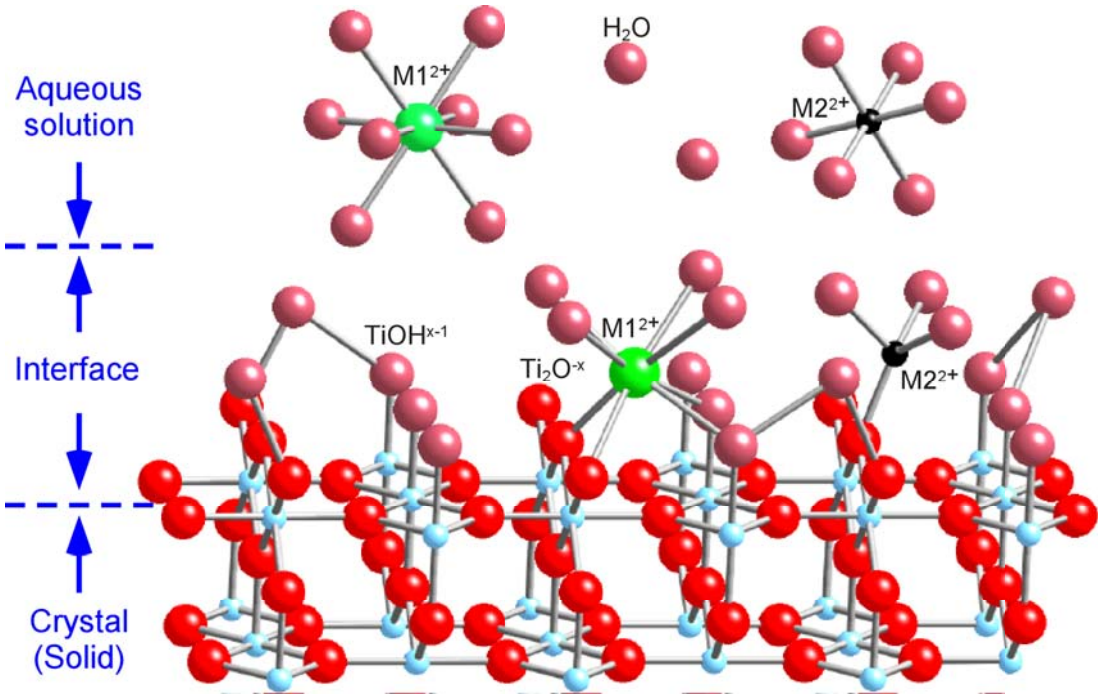

Figure 1.6. The proposed microscopic structure at the rutile TiO_2 (110)-aqueous interface.

Above the water molecules which are directly bound to TTi atoms, there could be one or more layers of water bound to the surface oxygen (for simplicity, the TO and BO site oxygen groups are generally referred to as surface oxygen. Chemically, they could be O atoms, OH^- groups, or H_2O molecules). Only cations are shown since the surface is assumed to be negatively charged (pH > 5.8 for TiO_2). The adsorbed ion could be bound to the surface oxygen by losing some of the water molecules in its hydration shell, e.g., the ion $M1^{2+}$ in the figure loses four of its eight coordinated water and instead binds to four surface oxygen sites. There might also be a change in the number of the coordinated oxygen atoms when the ion adsorbed onto the surface from the solution as illustrated for the $M2^{2+}$ ion. These microscopic structures are actually parts of the EDL and closely associated with macroscopically measured properties. Knowledge of the detailed adsorption structure of ions at the rutile (110)-aqueous interface will help to understand EDL properties, which is the focus of this work.

1.4 Current knowledge about the rutile (110)-aqueous interface

In the aqueous solution, some of the methods used in vacuum studies are not applicable, such as those methods that use electron-based techniques because of the short mean free path of electrons in aqueous solutions. Furthermore, any method that used charge transfer will be difficult to use because of charge build up on the insulated oxide surfaces.

1.4.1 Point of zero charge at the rutile-aqueous interface

The sources of the interfacial charges include (a) the structural charge σ_{sc} of the oxide (such as from the structure substitution or preferential ion dissolution); (b) the adsorbed or desorbed proton charge σ_H; (c) the adsorbed ion charges $\Delta q = q^+ - q^-$. The total charge across the interface should be neutral, i.e.[41]

$$\sigma_{sc} + \sigma_H + \Delta q = 0 \tag{1.31}$$

Here the first two terms can be considered as the intrinsic charge of the oxide surface σ_0 (as shown in Figure 1.2) contacting with aqueous solution.

$$\sigma_0 = \sigma_{sc} + \sigma_H \tag{1.32}$$

And the adsorbed ion charge can be divided into Stern layer charges σ_{Stern} ($\sigma_{Stern} = \sigma_A + \sigma_M$) and diffuse layer charges σ_d.

$$\Delta q = \sigma_{Stern} + \sigma_d \tag{1.33}$$

Considering the microstructure of the oxide-aqueous interface, the specifically adsorbed ions (Stern layer ions) cannot be separated from the oxide itself easily. Therefore the oxide surface charge σ_{surf} is usually defined as

$$\sigma_{surf} = \sigma_0 + \sigma_{Stern} \tag{1.34}$$

Depending on where the boundary between oxide and solution is drawn, there are different definitions of the point of zero charge. Point of zero net proton charge (pHznpc) is the pH value at which the net surface proton charge is equal to zero, i.e., $\sigma_H = 0$. Point of zero net charge (pHznc) is the pH value at which the intrinsic surface charge is equal

to zero, i.e., $\sigma_0 = 0$. Point of zero charge (pHzc) is the pH value at which the surface charge is equal to zero, i.e., $\sigma_{surf} = 0$. Based on these definitions, we know that there are no adsorbed ions on the surface at pHznc; and that there is no diffuse layer ion but only the Stern layer ion at pHzc. And none of these points of zero charge is strictly the property of the oxide since they are affected by aqueous solution conditions.

Powder titration measurement measures proton release upon the adsorption of the ions at the oxide-aqueous solution interface. The ion uptake vs. pH or ionic strength can be measured directly. Also the pHznpc can be derived from the measurements at different ionic strength by assuming that all protons released into the solution derive from the interface.[18,22] Result on the powder rutile TiO_2 (60% (110) surface and 20% each of (101) and (100) surface) shows that the pHznpc = 5.4 at 25 °C. This value decreases as the temperature increase. At 250 °C, pHznpc = 4.3. For the ion adsorption measurements, the desired pH for cations should be normally higher than pHznc to achieve the negatively charged surface.

Titration measurements measure the macroscopic properties of the EDL. With the surface complexation model, as described earlier, a link between the atomic scale structure and the macroscopic properties can be established. For instance, knowing the site densities, the detailed solution condition, (including, the ionic strength, the specific ion concentrations, temperature and pH) and the proton release, the EDL condensed layer capacitances and the adsorption constant of proton and ions on rutile surface can be derived.[10,42] With an estimated water dielectric constant in the Stern layer region of ε_r =

27, the adsorbed Na^+ ion height from the rutile surface was derived as 3.62 Å and 0.88 Å for 25 and 250 °C, respectively. That is, as the temperature increased, the Na^+ ions are found to move closer to the surface.[10.] These predictions can be directly compared to the measured ion positions to check the validity of the SCM models.

The second harmonic generation (SHG) measurement of the pHznpc on TiO_2 (110) single crystal surface yielded a value of 4.9.[43] This value is reasonably close to that from the titration measurements on rutile powder, which confirms the validity of the pHznpc value on the rutile TiO_2 surface, as well as a proving that the (110) surface is dominant in the powder work and contributes to the measured properties. So the results from this work, which is derived from single crystal rutile TiO_2 (110) surfaces, can be directly related to the titration works on rutile powders.

1.4.2 Adsorbed water and other molecules at rutile-vapor interface

When a rutile surface in vacuum is exposed to a vapor, molecules will adsorb onto the surface. In earlier days (1960s' and 1970s'), the Temperature Programmed Desorption (TPD) measurements in vacuum were carried out on the powder oxide surface. By monitoring the changes of the Infrared (IR) absorption spectrum during the adsorption or desorption of the molecules to the oxide surface, the surface structure, the adsorption sites and paths were proposed.

Infrared (IR) absorption spectra measurements have been used for a few decades and are well developed [see reference 44 for review of recent applications in geochemistry science]. Generally, an IR absorption spectrum shows the absorption of the

photons by vibrations that induce dynamic dipole moments. Dynamic dipoles are oscillations in the density of electrons or electron charge due to atomic motion. If the incident IR field is parallel to the charge oscillation and the photon frequency is similar to the oscillation of the dynamic dipoles, the photon can be absorbed. Therefore an IR absorption spectrum directly contains information about the oscillation frequencies of the dynamic dipoles and thus reveals the bond strength in a sample. Since the bond strength within a molecule is altered upon adsorption to a surface, the determination of the bond strength can be invaluable to understand the surface reaction path.

For example, Jones and Hockey et al.[45,46,47] and Parfitt and coworkers [48, 49 ,50, 51, 52, 53, 54] tried to identify the species and the structure of the adsorbate, such as H_2O, HCl, and NH_3, on the rutile (TiO_2) surface. Commercially available TiO_2 powders were used. The powders were made from $TiCl_4$, so the Cl impurity from the bulk powder particles was blamed for some 'mystery' components in the spectrum. The powder were rutile crystals, with a dominant face being the (110) surface (60% of exposed area), but with another two surfaces of (101) and (100), roughly 20% each.

The experiments were carried out in the vacuum environment (~ 10^{-3} Torr). The adsorbate was added to the system as gas phase precursor. Oxidized and reduced surfaces were studied from room temperature up to 973 K in TPD experiments. The surface is observed to be acidic and two different Ti surface adsorption sites (i.e., TO and BO sites) with different activities are observed. Both chemisorbed (as OH^- groups) and physisorbed (as H_2O molecules) water could be presented on the rutile surface. And HCl and NH_3 could also be directly bonded to the surface Ti atom when surface is

hydroxylated. Because there are multiple surface Ti sites in the powder measurement, there could be multiple interpretations for the same data.

The IR measurements, though yielding useful information about the adsorption process, did not directly probe the structure of adsorbate at the surface. The assignment of a signature absorption frequency to an irrelevant bond could be misleading upon understanding the adsorption process.

Decades later, with the newly available techniques such as scanning tunneling microscopy (STM) and molecular beam scattering, the adsorption of water was further investigated on single crystal rutile surfaces. Most of the studies show that the water adsorbed onto the rutile (110) surface associatively (i.e., as H_2O), while it is only dissociatively adsorbed (i.e., as OH^-) at defect sites.[55,56,57]

Many simulations/calculations of water adsorption on rutile (110) surfaces were also performed. Contrary to experimental results, most studies indicate that water dissociatively adsorbs even on the defect-free surface.[26,37,38,58] Calculations of multilayer water adsorbed on rutile surface were also reported in a few cases. A layered adsorbed water structure with hydrogen bonding chain structure was proposed.[59, 60] Meanwhile, molecular dynamic simulations using a large number of water molecules showed no further layering of water a few Angstrom away from the surface.[40.]

1.4.3 Metal ion adsorption at rutile (110)-aqueous interface

There are many studies of metal adsorption on the rutile surface in vacuum.[26.] However, the studies of metal ion adsorption at rutile-aqueous interface are much less.

This is partly because there are very few available methods for probing the structure of the oxide-aqueous interface. X-ray-based methods have proven to be powerful tools to probe oxide-aqueous interfaces.

X-ray absorption fine structure (XAFS) monitors the modulated X-ray fluorescence signals of a specific element due to backscattering of photoelectrons from its neighbor elements as a function of the incident X-ray photon energy. The modulation contains information about distance and number of the neighbor atoms/ions, i.e., the coordination information of the center atom. The Near Edge XAFS (NEXAFS) or the X-ray Absorption Near Edge Structure (XANES) data contains information about the electronic structure of the central atom, therefore is able to indicate the adsorbed species, e.g., Se(IV) vs. Se(VI).[61]

For the ions adsorbed at the oxide surface, Extended XAFS (EXAFS) has been widely applied to determine the adsorption mechanism. For instance, Hayes et al. studied the selenite (SeO_3^{2-}) and selenate (SeO_4^{2-}) ions adsorbed onto powder goethite (α-FeOOH) surface.[61.] Selenite was found directly bonded to the surface Fe atoms as inner sphere complex. Selenate, on the other hand, was adsorbed onto the surface with its hydration shell intact as outer sphere complex. Different ions, such as Pb^{2+}, Zn^{2+}, Co^{2+}, adsorbed onto various oxide powder surfaces, such as α-Al_2O_3, α-Fe_2O_3, TiO_2, are also investigated with EXAFS method.[62,63,64,65,66,67] Measurements were also performed to determine the structure of ions adsorbed to single crystal oxide surface, including Zn^{2+} and Pb^{2+} on α-Al_2O_3 and Co^{2+} on TiO_2 (rutile). Combining with the knowledge of the single crystal surface structure, EXAFS data can lead to a detail adsorption structure at

the oxide-aqueous interface. For instance, the Co^{2+} was found to take the extended bulk Ti atom position on the TiO_2 (rutile) (110) surface and was six-fold coordinated by neighboring oxygen atoms. Zn^{2+} was found to be inner sphere complex at Al_2O_3 (0001) and (10-12) and was four-fold coordinated as compared to the six-fold coordination of Zn^{2+} ion in the aqueous solution. Pb^{2+} was found to be outer sphere complex at the α-alumina (0001) surface, while it is inner sphere on the (10-12) surface of the same crystal.

EXAFS measurements can also suggest the precipitation, i.e., the multi-nuclei adsorption complex, at the solution concentration below the soluble limit of the ion through observing the signal from the second nearest neighbor atoms.[63.]

X-ray surface scattering has been used to study the surface structure for many years.[68] The Crystal Truncation Rod (CTR) measurement of oxide surface in vacuum and at ambient conditions illustrates its ability to reveal the atomic scale structure. For instance, Charlton et al. measured the rutile TiO_2 (110) surface in vacuum and showed the surface relaxations of the atoms in a few top atomic layers.[35.] Eng et al. measured the hydrated α-Al_2O_3 (0001) surface structure and proposed the fully oxygen terminated surface with a full layer of adsorbed water on top of that.[69] Chu et al measured the surface adsorbed water structure change on the RuO_2 (110) surface under the applied potentials.[70] Other measurements with CTR method also shows it can be applied to solve the structure of complex surface or the surface in the aqueous solution with adsorbed ions.[71,72,73,74,75]

Neutron scattering is sensitive to the distribution of protons (deuterium) , which is a great advantage over X-rays methods, where the proton is practically invisible. The

recent measurement of the counterion distribution in the clay interlayer by Williams et al. obtained a result contradictory to the traditional Poisson-Boltzmann distribution of EDL ions.[76] This might be an artifact of having a large cation (~ 15 Å long $C_3H_7NH_3^+$) in a confined space (43.6 Å interlayer spacing). Though this measurement did not present much information about EDL ion distribution, with a better-designed system it could lead to important information about the protons adsorption/desorption at the interface and their distribution in the EDL.

1.4.4 Metal ion distribution near the rutile (110)-aqueous interface

When ion adsorption is mentioned, it usually refers to the Stern layer ion adsorption site and geometry. However, the EDL structure does not refer solely to the Stern layer ions. The total ion distribution profile is needed.

X-ray Standing Wave (XSW) method (more details in Chapter 2), monitors the characteristic fluorescence of the selected element inside of the standing wave field.[77,78,79,80] Unlike the EXAFS method, which focuses on the local structure around a central atom, the XSW actually probes the ion distribution, i.e., the EDL profile.

Bedzyk et al. probed the Zn^{2+} distribution in the diffuse double layer next to the phospholipids membrane, which is supported by the Silicon-Tungsten layered-synthetic-microstructure (LSM).[8.] This was the first time that a diffuse double layer ion distribution was directly measured. And the Zn^{2+} distribution, which affected by the charge of the membrane and the solution pH, can actually be interpreted as an exponential function similar to the Equation (1.10). Similar results were also achieved by Wang et al.[9.]

Fenter et al. combined the XSW and EXAFS method to study the Sr^{2+} and Rb^{+} ions at rutile TiO_2 (110)-aqueous interface.[81] The results proved the ions form a Stern layer at the interface. And tetradentate adsorption geometry of the Sr^{2+} ions on rutile (110) surface was derived.

As the accumulation of the knowledge of the atomic scale ion adsorption structures, it's finally possible to establish the link between the microscopic structure and distribution and the macroscopic EDL properties.

1.4.5 Other EDL related measurements at the interface

Other measurements are used to probe different aspects of EDL, such as the ζ-potential measurement;[82] the EDL force measurement with pulsed-force-mode atomic force microscopy (AFM);[83] and measurements of the shear plane.[84] All these various studies contribute to the better understanding of the EDL phenomenon from different aspects. However, the fundamental problem remains the basic structure of EDL, including the oxide surface structure, the interfacial water arrangement and the distribution of the adsorbed counterions.

1.4.6 Purpose of this study

Structure determines properties. And knowledge of the EDL structure will greatly enhance our ability to understand, predict and thus design different EDL properties. Given the complexity and variety of the EDL structure and the relatively lack of knowledge of oxide-aqueous interface structure, we have to begin with the structure in a

better-defined region—Stern layer ions. The adsorbed ion positions and the coverage in Stern layer will be used separately as the input or constraint for the surface complexation model and thus offer more than structural information. By comparing the different adsorption structures for the different ions, general trends can be summarized for the ion adsorption at rutile (110)-aqueous interface. Furthermore, the diffuse layer ion distribution can be probed and the complete EDL ion distribution can be revealed.

With the increasing calculating power of computer, more and more calculation and simulation works has been carried out. Density functional theory (DFT) calculation can give the minimum energy state of a cluster of atoms.[85] And the molecular dynamic (MD) simulation can give a picture of the stable interfacial adsorption structure.[40,86]

The simulation method is relatively cheap and easy. It can also simulate those situations where a real experiment is impractical, once the simulation is proven to be valid. However, to gain the confidence of a model and make it more realistic, the fair amount of experimental results are still needed. This last point determined the particular studies that we performed so that they could be closely associated with the theoretical calculation and simulations.[87]

Chapter 2 Experimental methods

2.1 Advantages of synchrotron based X-rays

X-rays interact weakly with matter. As a specific example, the absorption coefficient of liquid water as a function of linear frequencies is shown in Figure 2.1.[88] Other than a narrow window at visible frequencies, electro-magnetic waves can not penetrate through macroscopically thick water until its energy reaches the X-ray region. For instance, the linear attenuation length of X-rays in water at photon energies of 10 and 20 keV are 2 and 12 mm, respectively. This allows the X-rays to reach the liquid-solid interface with minimal attenuation while passing through a macroscopic (> 2 μm thick) water layer. The weak interaction of X-rays with water, as well as with the bulk crystal underneath, also implies that X-ray based structural techniques are non-destructive methods.

The wavelength of hard X-rays is ~ 1 Å, which is the same scale as the atom size. The resolution of the X-ray measurements can easily be achieved at < 1 Å level. Therefore X-ray based methods are good candidates for probing the atomic scale structures.

When X-ray photons are absorbed by atoms, the atoms could be excited to a higher energy levels causing X-ray absorption. The secondary processes associated with the de-excitation of atoms (i.e., back to the ground state), such as the emission of fluorescence photons and Auger electrons are elementally specific, which can be

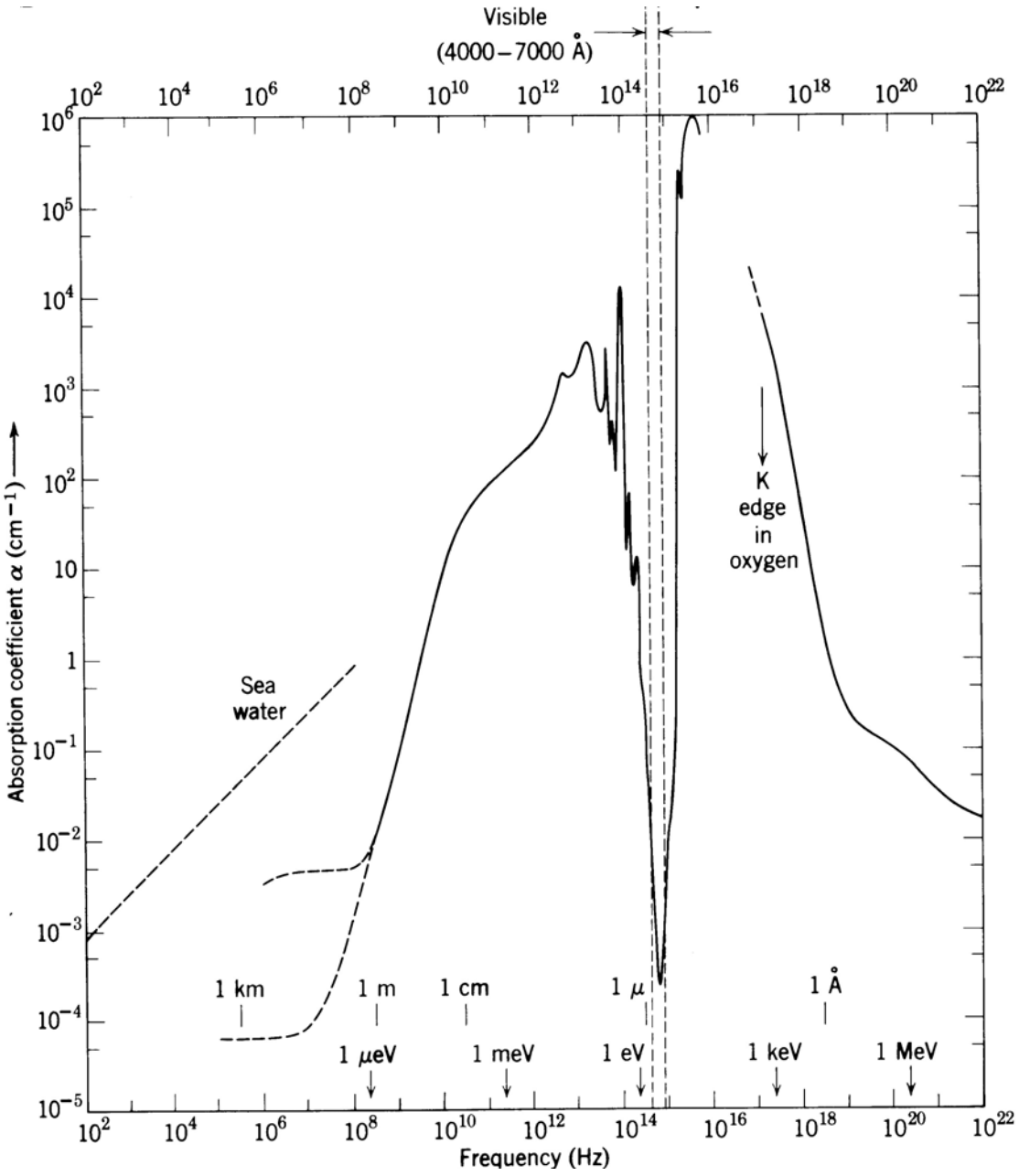

Figure 2.1. The adsorption coefficient for liquid water as a function of linear frequency. Taken from reference 88.

monitored to achieve the elemental specific atomic scale structure.

An X-ray carries no charge, so it does not bring or take away electrons from the sample directly, though electrons can be removed from atoms either directly through photo-electron emission or indirectly through secondary processes. Little or no net charge accumulation on the sample means that a conducting substrate is not required, which is quite important for studying oxides since they are mostly insulators.

The theory of X-ray interactions with matter has been well developed. Consequently, data from X-ray measurements can be quantitatively associated with the atomic structure of the sample. For example, kinematical scattering theory can often be applied for the surface X-ray scattering measurements (excluding the Bragg peaks, where the dynamical diffraction theory should be applied) because of the weak interaction with matters.[89,90,91] The atomic structure information can be retrieved with the direct relation between structure and measured data.[92,93,94,95]

The third generation synchrotron sources (e.g., Advanced Photon Source (APS), located in Argonne National Laboratory, IL) offer the high-brilliance broad-band X-ray sources, which can be highly collimated, polarized and continuously tunable in energy. As shown in Figure 2.2, the brilliance of an undulator X-ray beam can be 6 to 8 orders of magnitude higher than a rotating anode X-ray tube can offer.[96] The higher flux and better defined X-ray source make it possible to probe much weaker signal thus achieve the higher resolution in the surface structure study as well as to study the dynamical processes in real-time.

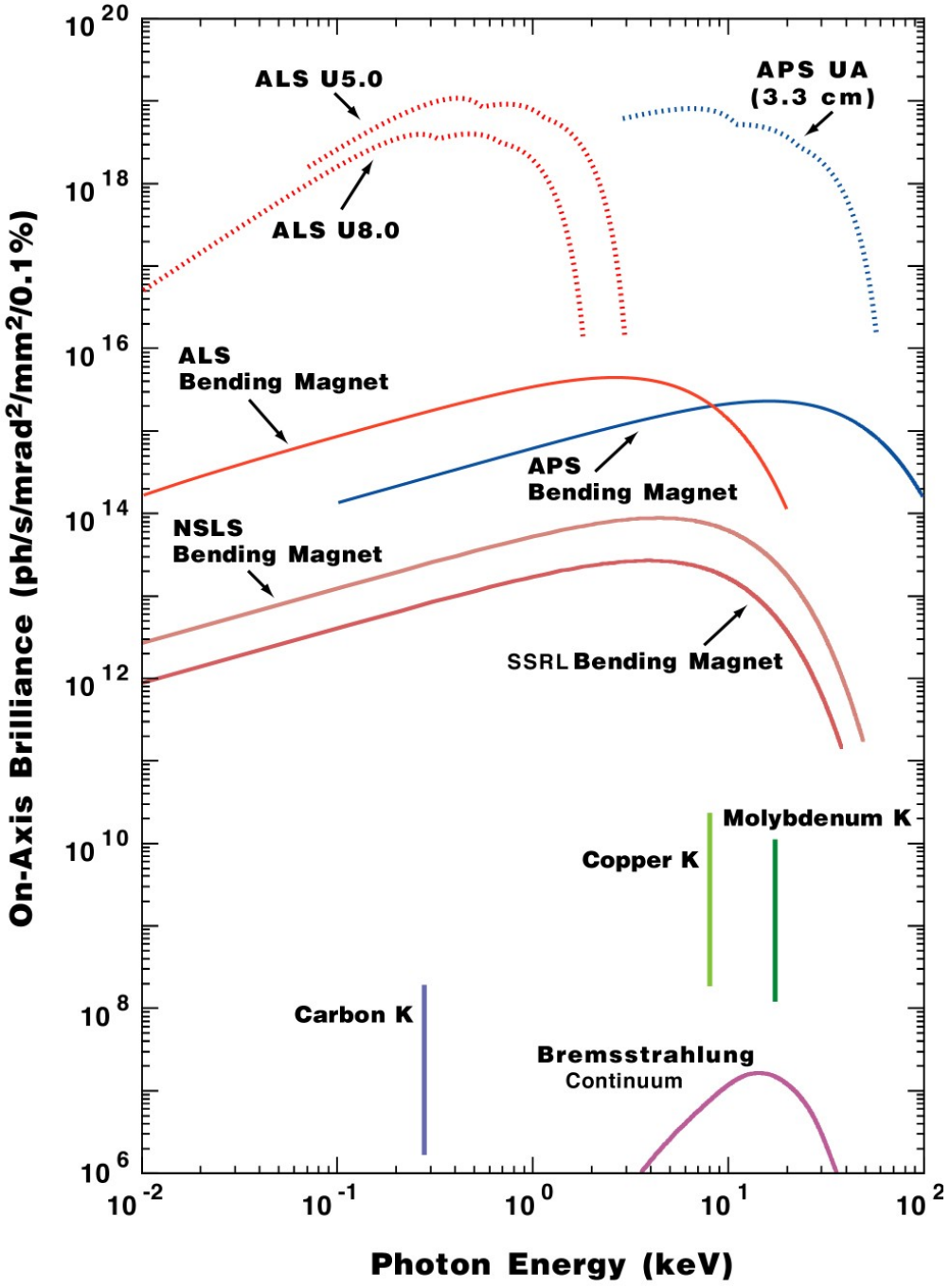

Figure 2.2. Characteristics of the different X-ray sources. Taken from APS gallery.

X-ray beam cross sections, depending on the source and optics used, are normally macroscopic sizes, which are practically larger than a few micrometers across even after being focused and/or cut down with slits. While this means, on the one hand, that no information about a single atom can be obtained, on the other hand the data are statistically averaged over a large quantity of atoms and are less sensitive to the local structure disturbance (such as defects) and thus yield the overall structure.

2.2 X-ray standing waves method

2.2.1 Basic concepts about X-ray standing waves

X-ray standing wave (XSW) is generated when two X-ray waves with the same wavelength coherently interference with each other, as shown in the Figure 2.3. [77,78,79,80] The XSW period, *D*, is given as

$$D = \frac{\lambda}{2\sin(2\theta/2)} = \frac{2\pi}{q} \qquad (2.1)$$

where λ is the wavelength of X-ray; $q = |\boldsymbol{Q}|$, is the amplitude of the standing wave vector $\boldsymbol{Q} = \boldsymbol{K_f} - \boldsymbol{K_0}$,; $\boldsymbol{K_0}$ and $\boldsymbol{K_f}$ are the wave vectors of the two waves, respectively, with the amplitudes $|\boldsymbol{K_0}| = |\boldsymbol{K_f}| = 2\pi/\lambda$; and 2θ is the angle between them.

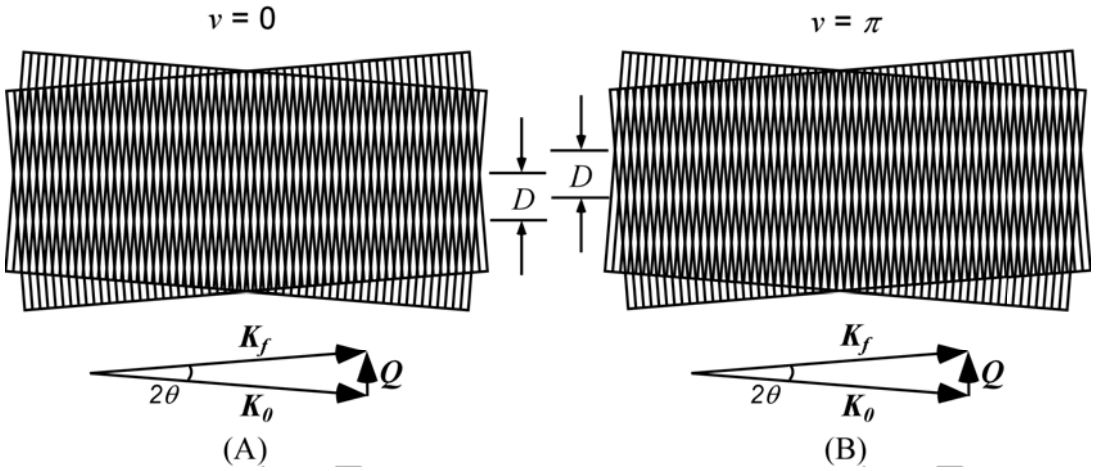

Figure 2.3. Standing wave, whose period is D, is formed by the superposition of two traveling plane waves with wavelength λ at angle 2θ. The phases between the two plane waves, v, are (A) 0 and (B) π, respectively.

When the angle 2θ changes, the XSW period will change accordingly. Given the fact that $\lambda \sim 1$ Å, it is typical to obtain an XSW period ranging from a few Angstroms (at larger values of 2θ, e.g., corresponding to Bragg diffraction) up to a few hundred Angstroms (at small values of 2θ, e.g., corresponding to total external reflection). If the relative phase between the two waves, v, changes, the XSW field will shift in space. As shown in Figure 2.3 (A) and (B), upon shifting one wave with respect to another by $\lambda/2$, i.e., the relative phase between them changes from $v = 0$ to $v = \pi$, while keeping the XSW period the same, the XSW antinode positions (marked with solid line) move by half the XSW d-spacing, i.e., the XSW field shifts by $D/2$. These features of the XSW field can be taken advantage of as an atomic scale probe by monitoring the photoelectric effect, such as photoelectron emission, X-ray fluorescence, and/or Auger electron emission.

The simplest and most widely used method to generate an XSW field is by reflection, where the XSW is generated by the superposition of the incident and the reflected X-ray plane waves. There are a few different ways to achieve this, including the strong Bragg reflection from a single crystal, total external reflection (TER) from a mirror surface, the strong Bragg reflection of a periodic layered synthetic microstructure, and kinematical Bragg diffraction from a single-crystal thin film.

The XSW method has been used in the past two decades to investigate a wide range of bulk impurity, surface, interface and thin film structures.[79,80] Here the focus is limited to the few aspects that are most important to probe the rutile-aqueous interface. More detail and thorough information about XSW can be found in reference 79 & 80.

2.2.2 Single crystal Bragg reflection based XSW method

The single crystal Bragg reflection based X-ray standing wave method has already proven to be a powerful tool to probe adsorbate positions at the solid-water interface.[81,97] As shown in the Figure 2.4 (A), when an X-ray plane wave is Bragg diffracted from the ideal single crystal lattice, an X-ray standing wave is generated both below and above the crystal surface as a result of the coherent superposition of the incident and the reflected X-ray beams. The reflectivity and the fluorescence signal are measured simultaneously while rocking the sample through the H^{th} (= *hkl*) Bragg reflection. According to the X-ray dynamical diffraction theory, as the angle of incidence is varied through the Bragg angle θ_b, the phase shift between the reflected beam ($\boldsymbol{E_H}$) and the incident beam ($\boldsymbol{E_0}$) changes continuously from π to 0. Thus the nodes and antinodes of the XSW field move from the diffraction plane inward by $d_H/2$, where $d_H = D$ is both the period of the XSW field and the d-spacing of the H^{th} Bragg diffraction planes. When the incident X-ray energy is higher than the absorption edge of the element of interest (here the EDL ions), a modulation of the fluorescence signal at its specific emission energy will be observed as the Bragg peak is excited (e.g., as a function of incident angle). Shown in Figure 2.4 (B) are the XSW measurements at the rutile (110)-aqueous solution interface for the solutions of 10^{-4} mol/kg Sr^{2+} at pH = 10.7 and 10^{-3} mol/kg Rb^{+} at pH = 11, respectively. The points are the measured TiO_2 (110) reflectivity and element specific fluorescence signals. The lines represent the best fit to the data for each dataset. θ - θ_b indicates the angular range over which the measurements are done and θ_b is the

Bragg angle calculated from Bragg law, i.e., the kinematical diffraction theory. The normalized fluorescence yield *Y(θ)* (which is measured next to the sample surface at a small take-off angle) varies with respect to the incident angle θ as:

$$Y(\theta) = 1 + R(\theta) + 2\sqrt{R(\theta)} f_H \cos[v(\theta) - 2\pi P_H] \tag{2.2}$$

Here, $R(\theta) = \left| \frac{E_H(\theta)}{E_0} \right|^2$ is the reflectivity, $v(\theta)$ is the phase between the reflected and the incident X-ray plane wave, i.e., $\frac{E_H(\theta)}{E_0} = \left| \frac{E_H(\theta)}{E_0} \right| \exp[i \cdot v(\theta)]$. Both *R(θ)* and *v(θ)* can be directly calculated with the known bulk crystal structure using X-ray dynamical diffraction theory. P_H and f_H, which are the so-called coherent position and coherent fraction for the measured element, respectively, are directly obtained from the experimental XSW data using Equation (2.2). These two parameters represent the phase and the amplitude of the H^{th} Fourier component of the spatial distribution of the fluorescing species at the reflection $H = hkl$, which is located at $\boldsymbol{H} = 2\pi(h\boldsymbol{a}^* + k\boldsymbol{b}^* + l\boldsymbol{c}^*)$ in the reciprocal space, where ***a****, ***b****, and ***c**** are the reciprocal space unit vectors:

$$f_H \exp[i 2\pi P_H] = \boldsymbol{G}(\boldsymbol{H}) = \mathscr{F}_{\boldsymbol{H}}(\rho(\boldsymbol{r})) = \int_{UC} \rho(\boldsymbol{r}) \exp[i\boldsymbol{H} \bullet \boldsymbol{r}] d\boldsymbol{r} \tag{2.3}$$

Here ***r*** is the vector indicating the atom position; $\rho(\boldsymbol{r})$ represents the normalized distribution profile of the fluorescent species ($\int_{UC} \rho(\boldsymbol{r}) d\boldsymbol{r} = 1$); ***G(H)*** = $\mathscr{F}_{\boldsymbol{H}}(\rho(\boldsymbol{r}))$ is the

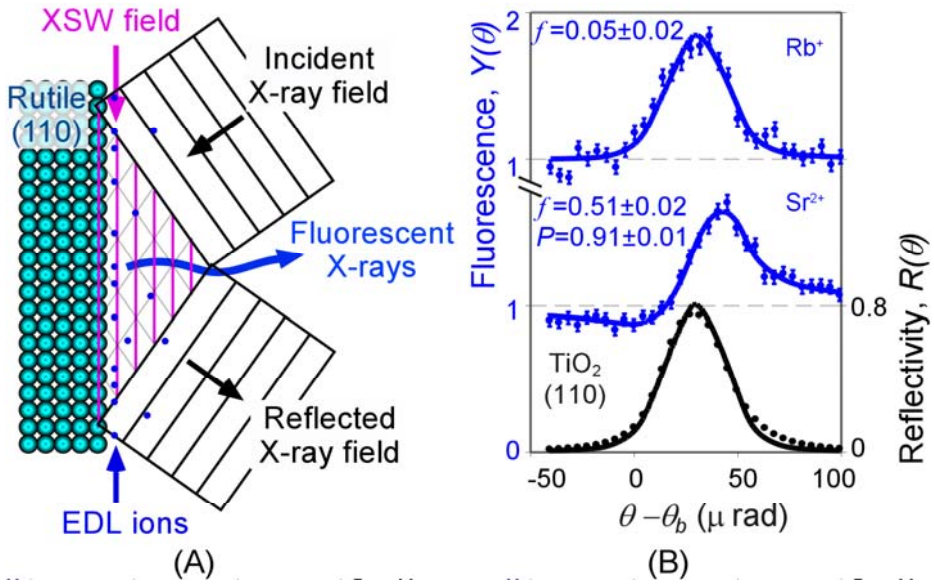

Figure 2.4. (A) Schematic of the generation of the Bragg XSW. (B) Typical XSW data of the Sr^{2+} and Rb^{+} fluorescence signals ($Y(\theta)$, top 2 curves, in blue) and the X-ray reflectivity signal ($R(\theta)$, bottom curve, in black), when rocking the X-ray incidence angle θ through TiO_2 (110) Bragg peak. θ_b is the nominal TiO_2 (110) Bragg peak position. Points are the experimental data and lines are the best fit to the data. P and f are the coherent position and fraction from the best fits.

inverse Fourier transform of $\rho(\mathbf{r})$ at $\mathbf{H}$.

Both P_H and f_H are unitless quantities ranging between 0 and 1. When the fluorescing atom has a unique projected location within the substrate crystallographic unit cell, $P_H = \delta_H/d_H$, where δ_H is the height of the atom along the diffraction plane normal direction with respect to the unit cell origin. $P_H = 0$ or 1 indicates that ad-ions are located at the origin. The coherent fraction, f_H, is a measure of the distribution of the atoms around the position defined by P_H. In the case of all atoms on a unique ion site, $f_H = 1$; and for a random distribution, $f_H = 0$. More generally, f_H can be described as the product of three factors, $f_H = a_H * C * D_H$, where a_H is the geometry factor that accounts for the coherent sum of contributions from atoms at different positions (e.g., ions with multiple adsorption heights), $a_H = \dfrac{\left|\sum_i \Theta_i \exp(i\mathbf{H} \bullet \mathbf{r_i})\right|}{\sum_i \Theta_i}$, where Θ_i is the coverage, i.e., atom number density, at position r_i; (e.g., in the EDL, Θ_i indicates the coverages of the ion at different adsorption sites, and $\Sigma\,\Theta_i = \Theta_c$ is the total Stern layer coverage of same ion.) C is the ordered fraction, thus $(1-C)$ accounts for the contribution from the randomly distributed atoms (e.g., precipitates, diffuse layer, and/or bulk solution ions). For the EDL system, $C = \Theta_c/\Theta_{tot} = \Theta_c/(\Theta_c + \Theta_d + \Theta_{bulk} + \Theta_{precip})$, where Θ_{tot} is the coverage (as the equivalent 2-D density) of all the same ion in the system, and Θ_x refers to the coverage of the ion in the different parts of the EDL or the solution, i.e., Θ_d, the diffuse layer coverage, Θ_{bulk}, the bulk solution ion coverage, and Θ_{precip} the coverage from the

possible precipitates; D_H is the Debye-Waller factor that accounts for thermal vibrations of the fluorescing atoms (and/or any contribution to the elemental distribution having a Gaussian distribution form).[79] For a Gaussian distribution with a root mean squared (rms) width σ, (e.g., due to thermal vibrations), $D_H = \exp[-q^2 \sigma_H^2 / 2] = \exp[-2\pi^2 (\sigma_H / d_H)^2]$ is a fixed number for a given fluorescing species at one crystal reflection and at a constant temperature. It is usually close to 1. When an atom has only one position in the unit cell, $a_H = 1$. Therefore, $f_H \approx C$, simply reveals the ordered fraction information. In the case that there are multiple atom positions, the coherent position P_H from a single XSW measurement reflects the coherently averaged position and cannot by itself uniquely reveal individual atom position. The experimentally measured coherent fraction includes not only the ordered fraction, but also the geometrical factor. Generally speaking, more than one XSW measurement is needed to determine the multi-site atom distribution. This will be discussed further in detail later.

2.2.3 Traditional method to analyze the Bragg XSW data

As illustrated in Figure 2.5, a trial and error method is traditionally adopted to obtain the adsorbate structure from one or more coherent positions, P_H, and coherent fractions, f_H, derived from the Bragg based XSW measurements. Briefly, a guessed structure model based on *a prior* knowledge is built. The coherent positions and coherent fractions can be calculated for the measured H^{th} reflections according to Equation (2.3). The structure then could be adjusted by matching the measured and the calculated P_H and f_H values, e.g., by a non-linear χ^2 fitting.

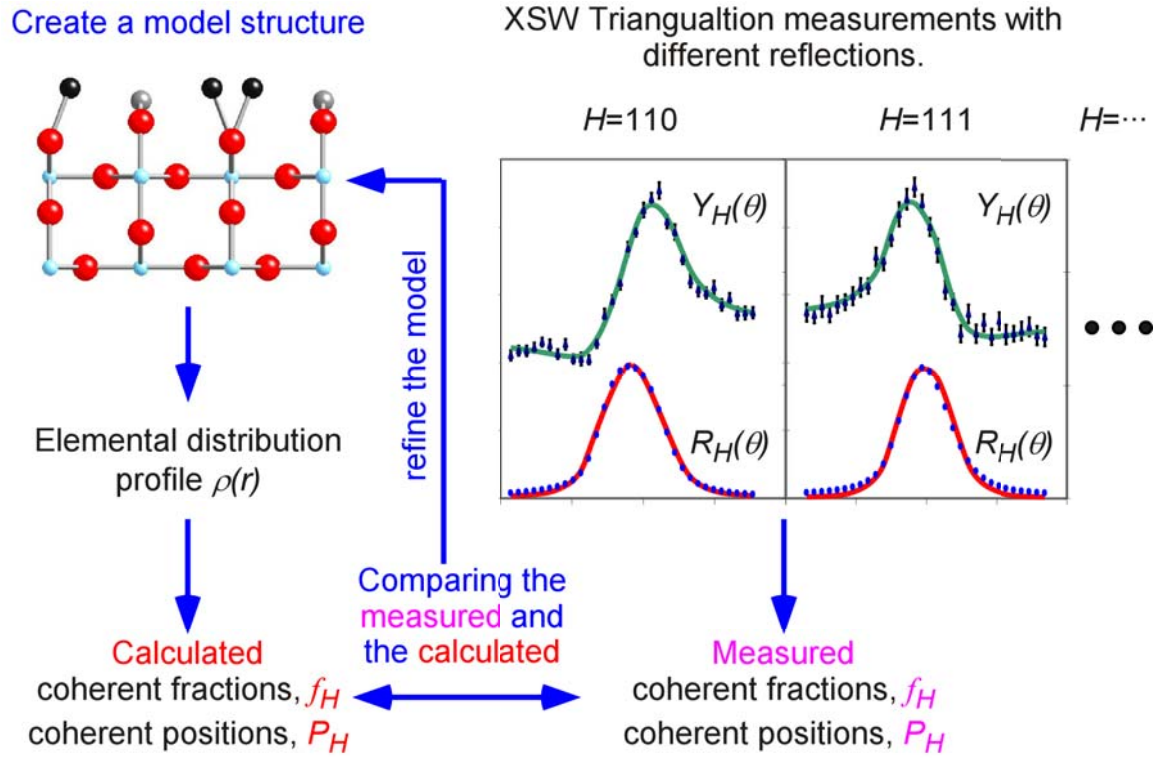

Figure 2.5. Flowchart of traditional way to analyze the Bragg XSW data. Rutile is used as the example structure.

For a simple structure, e.g., where an atom occupies only a single position in the unit cell, the structure can be easily derived from the coherent positions directly and the method works well. The atomic position could be determined with a precision of a few hundredths of Angstrom. However, for a more complicated structure, such as one single element occupies different sites with different occupation factors, the measured coherent positions do not simply indicate the actually atom locations, but instead an averaged location. In such cases, the starting model may become important, and an optimized structure from the analysis is not guaranteed to be the correct one if the starting guessed structure is inappropriate (i.e., missing an essential feature of the structure). This difficulty in the traditional XSW data analysis calls for a direct method to construct the structure from the measured coherent fractions and coherent positions without guess. In this context, the XSW imaging method has many advantages.

2.2.4 The XSW imaging method

Because the phase information is not lost in the XSW approach, the complete density profile (projected into the substrate crystallographic unit cell) can be obtained by the inverse statement of Equation (2.3) through a discrete Fourier summation with all the H^{th} Fourier components.[98,99,100]

$$\rho(\mathbf{r}) = \sum_H \mathscr{F}_H \cdot \exp(-i\mathbf{H} \bullet \mathbf{r}) = \sum_H f_H \exp\left[i2\pi\left(P_H - \frac{\mathbf{H}}{2\pi} \bullet \mathbf{r} \right)\right] \tag{2.4}$$

For H = 0, the 0th Fourier component, $\mathscr{F}_0 = 1$ because $\rho(\mathbf{r})$ is a normalized function. Furthermore, based on the Friedel's law, the components at H and $-H$ are

simply related by complex conjugation because $P_H = -P_{-H}$. Therefore the Equation (2.4) can be rewritten as:

$$\rho(\mathbf{r}) = 1 + 2 \sum_{\substack{H \neq 0 \\ H \neq -H}} f_H \cos\left[2\pi \left(P_H - \frac{\mathbf{H}}{2\pi} \bullet \mathbf{r} \right) \right] \tag{2.5}$$

Practically, it is impossible to measure all of the (infinite) reflections $\boldsymbol{H}$. So the density profile $\rho(\mathbf{r})$ has to be approximated by summation over a finite number of terms. By doing this, it is explicitly assumed that the terms not summed over have zero amplitude (f_H). This might be true for some of the components but not for all. Thus a question is raised concerning whether the approximation with a finite number of terms is proper or not. Additional questions must also be addressed. If the missing terms follow pattern dictated by symmetry, can the imaging method give a false profile? To find the answer to these questions, two model systems are investigated.

First a 1-dimensional system is used for its simplicity. Then a face center cubic (FCC) system is used to demonstrate the effect of symmetry in a 3-dimensional system. In both cases, the atom positions are assumed. The coherent fractions and coherent positions are calculated for a series of reflections. Finally the element density profile is generated from the coherent fractions and positions using Equation (2.5). The validity and robustness of the imaging process can be judged by comparison of the initially assumed atom position and the imaged profile.

For the Bragg reflection based XSW measurement, the measured coherent positions are all referenced to the origin of the unit cell and since only allowed reflections are used, the resulting image is a projection into the bulk primitive unit cell. For these

examples, the unit length 1 refers to the unit cell dimension. For the 1-D structure, the atom of interest is located at a height of *z0* from the unit cell origin. For the FCC structure, the atom of interest is located at a position of (*x0, y0, z0*). Therefore, the element density profile, $\rho(z)$ or $\rho(x, y, z)$, is obtained by summation of all the components available. For convenience of comparison in the plot, the element density is rescaled so that its maximum is always 1.

For the 1-dimension case, first let *z0* = 1/3, i.e., the actual atom distribution profile is $P(z) = \delta(z - z0) = \delta(z - 1/3)$. The imaged atom normalized density profile is obtained with the 1-D version of Equation (2.5):

$$\rho(z, M) = 1 + 2\sum_{m=1}^{M} \cos[2\pi m(z - z0)] \tag{2.6}$$

Shown in Figure 2.6 (A) are the constructed profiles, $\rho(z, M)$, following Equation (2.6) with $M = 1$ (black line with square marker), $M = 2$ (black line with cross marker), $M = 3$ (red line with circle marker) and $M = 10$ (blue line with dot). First of all, in all profiles, only one peak appears at the correct position, even with a single Bragg reflection. There are always oscillations in the "background" in the profile due to the sharp termination of the Fourier synthesis. It is also worth noting that the peak heights are all significantly higher than the background oscillation levels. The peak widths on the profile are different, though—the higher order the reflections are included, the narrower the peak. Both features derive from finite number of terms used for the Fourier summation. Theoretically if infinite number of Fourier terms were used for reconstructing the profile, the profile would be a delta function over a flat background line at 0 since a unique atom

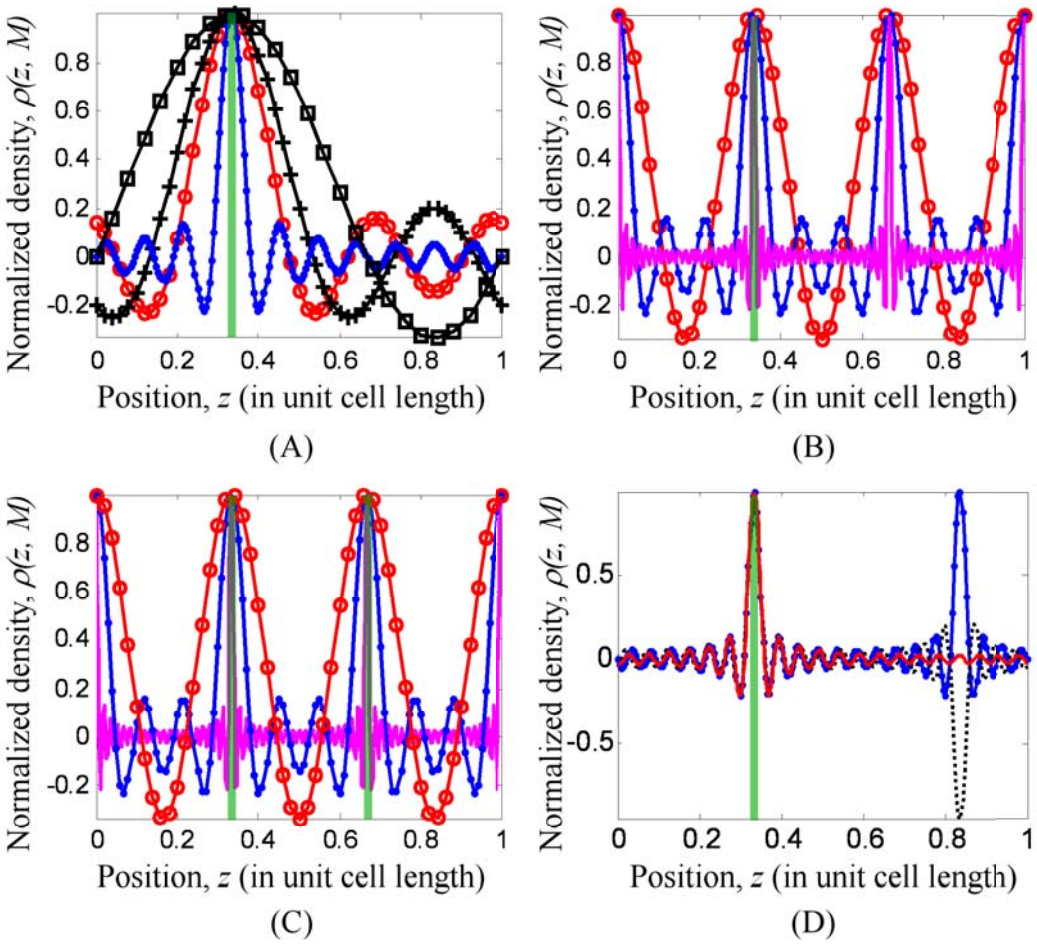

Figure 2.6. XSW imaging of element density profile, $\rho(z, M)$, for atom of interest in a 1-dimensional structure. For convenience of comparison, $\rho(z, M)$ is rescaled so that the maximum of element density is 1. The actual atom distribution, $P(z)$, is shown as vertical green bars. (A), $P(z) = \delta(z\text{-}1/3)$, calculated element density profiles based on Equation (2.6) with: $M = 1$ (black line with square marker –□–); $M = 2$ (black line with plus marker, –+–); $M = 3$ (red line with circle marker, –o–); and $M = 10$ (blue line with dot, –•–). (B), $P(z) = \delta(z\text{-}1/3)$, and (C) $P(z) = [\delta(z\text{-}1/3) + \delta(z\text{-}2/3)]/2$; based on Equation (2.7) with $M = 1$, (red with circle marker, –o–); $M = 3$, (blue with dot, –•–); $M = 20$ (pink line, ——). (D) $P(z) = \delta(z\text{-}1/3)$; calculation based on Equation (2.8), with $M = 20$ (blue with dots, –•–); based on Equation (2.8a), $M = 20$ (black dot line, ••••••); and the summation of the two (red line, ——).

location was assumed. Where a finite number of terms are used, the inclusion of higher order the reflections results in better precision in the position of atom due to the shorter period of the XSW. Also the more reflections are included, the less significant the background oscillations are relative to the peak height. This is because the Fourier components all peak at the actually atom position, while the background oscillations have different periods, therefore the amplitude of the summation in the background region is not enhanced as much as that on the peak.

Next assume the same 1-D host structure but only every 3rd order reflections (i.e., 3, 6, 9, etc) are measured. The atom again has a position of *z0* = 1/3, i.e., $P(z) = \delta(z - 1/3)$. In this case, the Equation (2.6) can be rewritten as:

$$\rho(z, M) = 1 + 2 \sum_{(m/3)=1}^{M} \cos[2\pi m(z - z0)] \tag{2.7}$$

(Here $M = 2$ means $m = 3$ & 6.) The constructed profiles are shown in Figure 2.6 (B) for $M = 1$ (red line with circle marker), $M = 3$ (blue line with dot) and $M = 20$ (pink line). Again, as higher order reflections are included, the profile becomes finer, i.e., with a narrower peak and relatively less significant background. However, this time additional peaks show up at $z = 0$ and 2/3 except for the actual position at *z0* = 1/3 above the surface plane. This degeneracy comes from the symmetry of a subset of reflections included in the XSW imaging process. Using of only 3rd order reflections dictates that the largest XSW period is 1/3 the size of the original unit cell. Therefore a structure with a larger length scale (here, the full original unit cell length) cannot be uniquely probed. The false peaks that show up at (*z0* + 1/3) and (*z0* + 2/3) cannot be removed simply by adding the

higher order of reflections in the same subset. With only this subset of reflections, the XSW imaging technique cannot distinguish which one (or more) of the three positions are real. As shown in Figure 2.6 (C), where the only difference from those in (B) is adding another assumed atom position at *z0* = 2/3, i.e., $P(z)=\frac{1}{2}[\delta(z-1/3)+\delta(z-2/3)]$, the constructed element distribution profiles are exactly the same as those in (B).

Now if we return to the case where there is only one atom position *z0* = 1/3, i.e., $P(z)=\delta(z-1/3)$, and assume only all the even order reflections are measured. The element density profiles have been constructed with the following equation:

$$\rho(z,M)=1+2\sum_{(m/2)=1}^{M}\cos[2\pi m(z-z0)] \tag{2.8}$$

(Here *M* = 3 means *m* = 2 4, & 6.) For *M* = 10 (blue line with dot marker), an additional peak shows up at *z* = *z0* + ½, as shown in Figure 2.6 (D). This is because only the even order reflections are included. The summation of the excluded odd order reflections are:

$$\rho^*(z,M)=\overline{\rho(z,M)}=2\sum_{[(m+1)/2]=1}^{M}\cos[2\pi m(z-z0)] \tag{2.8a}$$

(here *M* = 3 means *m* = 1 3, & 5.) With *M* = 10, the calculated $\rho^*(z, M)$ is plotted in Figure 2.6 (D) (black dotted line), which has a negative density peak at *z* = *z0* + ½ with almost the same amplitude as that from the calculation with even order reflections. Adding the two calculated profiles together, the additional peak at *z* = *z0* + ½ is eliminated. And the result density profile agrees well with the actual atom distribution (red solid line). It is actually the same as the calculation with Equation (2.6) at *M* = 20.

Note that at $z = z0$, the density peaks have the similar width, i.e., the same resolution, for the subset of even and odd order of reflections and the full set of reflections. This is because the resolution of the XSW imaging is limited only by the highest order of reflection included. The different subsets, however, yield different density profiles with additional peak(s); while using the full set of reflections, a nice and clean profile is achieved.

Briefly summarizing the above simulations, the correct atom position is always present in the density profile. The more reflections used, the finer the derived profile. However, the simulated profiles could also reveal "false" atom locations depending on the chosen reflections. If a subset of reflections selected overwhelmingly presents one or more symmetry components, the same symmetries will show up in the constructed element density profile. Therefore, in practice, selecting a complete set of reflections is more important than measuring more reflections from a single subset containing the same symmetry components. Even with a few or only one reflection, the elemental distribution is clearly shown on the image. The resolution of the image, which can be characterized as the full width at half maximum (FWHM) of the density peak, is roughly $d_{Hmax}/2$, where $d_{Hmax} = 2\pi/H_{max}$, is the d-spacing of the highest order reflection $H_{\boldsymbol{max}}$. For example, to achieve ~ 0.5 Å resolution on a unit cell length of 3 Å, it would be enough to just measure up to the 3rd order reflection, where $d_{H=3} = 1$ Å.

For the FCC structure, it is assumed that the atoms are located at the face center and corner positions, i.e., (0, 0, 0), (0, ½, ½), (½, 0, ½), and (½, ½, 0). Again the effect of the choice of the reflections is explored. Unlike in the 1-D case, there are equivalent

reflections based on the symmetry of the crystal. For instance, in the bulk FCC lattice, (111), (-111), (1-11) and (11-1) are the equivalent reflections, which can be noted as {111} family. The Fourier components of an atom distribution for any reflection in the family should be exactly the same if the bulk symmetry is followed. This means that the coherent fractions and coherent positions are identical for all the equivalent reflections. If one is measured, all are known.

The constructed 3-D element density profiles generated by Equation (2.5) are more difficult to visualize. Shown in Figure 2.7 are the three surfaces of the unit cell cube. Since all the atoms are actually on the outside surface of the cube, all of the critical structural information is included in this view. Also shown in Figure 2.8 are the slices along one of the (111) directions at one of the highest density positions, which reveals more information about the distribution profile inside the unit cell. In both figures, the element densities are rescaled so that their maximums are all 1.

When only {111} reflections are included, as shown in Figure 2.7 (A) and Figure 2.8 (A), the constructed map already reveals the atom positions clearly. Adding {022} reflections to the XSW imaging, the resolution gets better and the map is still clear and clean as shown in Figure 2.7 (B) and Figure 2.8 (B). However, if {333} instead of {022} reflections are included, many false peaks appear, in Figure 2.7 (C) and Figure 2.8 (C), though the resolution is improved because of the larger $|\boldsymbol{H}|$ at {333} reflection than at {022}. It is easy to see that the false peaks follow the same three-fold symmetry as found for the real atom distribution has, only with 3 times higher density. This is directly connected to the fact that both {111} and {333} follows the same symmetry and the

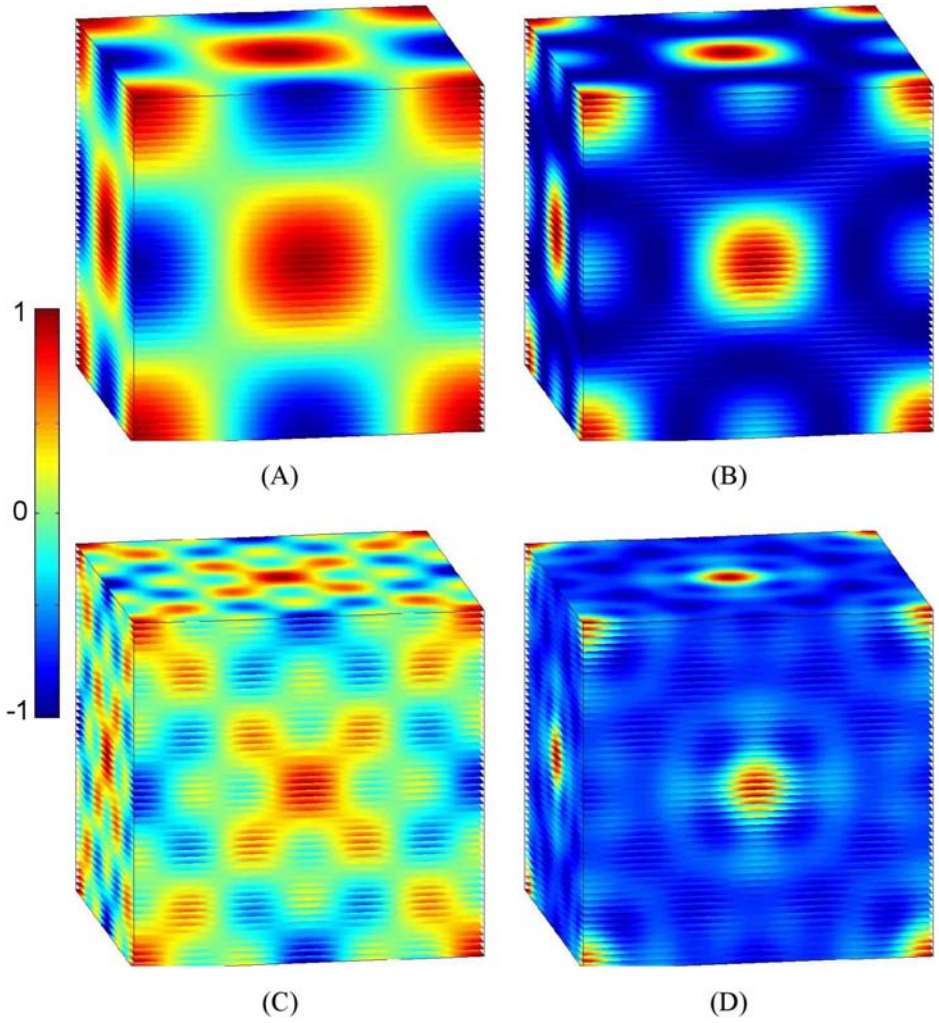

Figure 2.7. Based on Equation (2.5), XSW imaging of element density for a face center cubic (FCC) structure. Only three of the six surfaces can be seen on the constructed density maps. The atom positions as the inputs are at the corners and the face centers, i.e., (0,0,0), (0, ½, ½), (½, 0, ½), and (½, ½, 0). (A), with only {111} reflections, i.e., (111), (11-1), (-111) and (1-11). (B), with only {111} and {022} reflections. (C), with only {111} and {333} reflections. (D), with {111}, {200}, {220}, {113}, {400}, {204}, {333} and {115} reflections. The density scale is shown in the picture with a color bar.

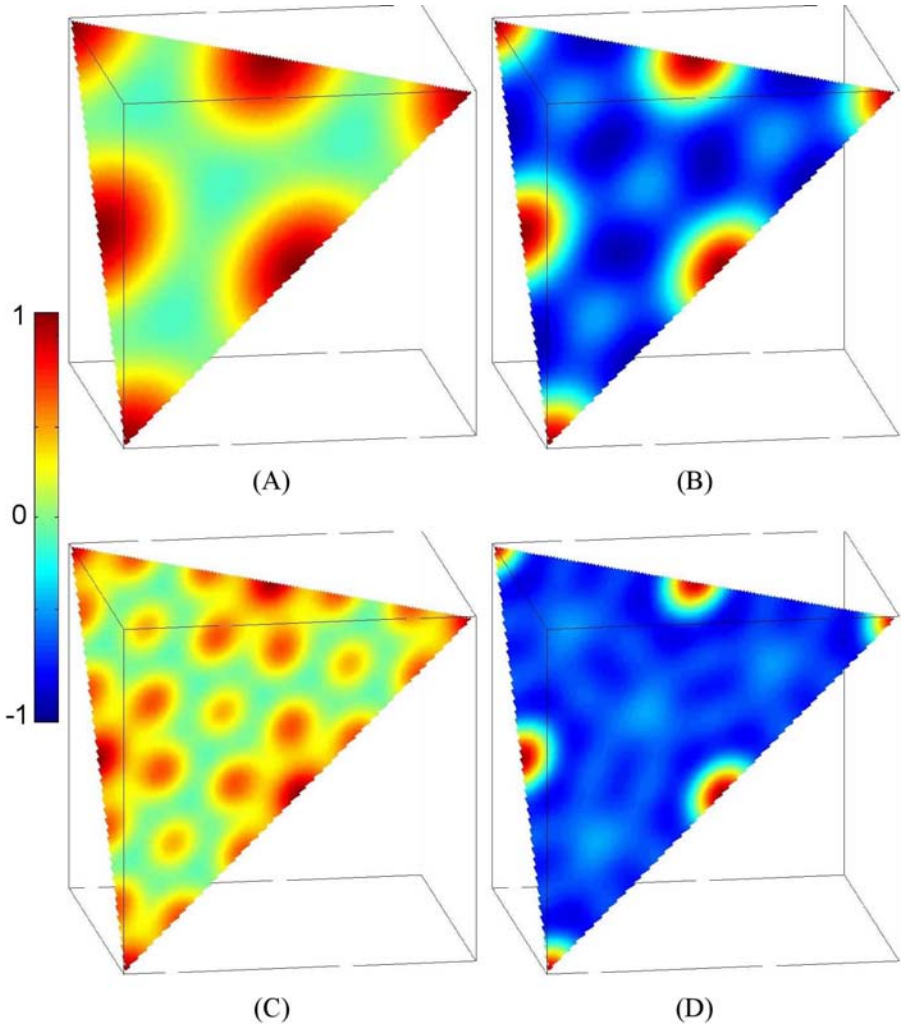

Figure 2.8. Slices of XSW images along (111) plane with the same configurations as shown in Figure 2.7. The density scale is shown in the picture with a color bar.

period of {333} is only 1/3 of that of {111}. So the false peaks show up as a result of not having the enough counter components to balance them out. As expected, when more reflections (namely, {200}, {220}, {113}, {400}, {204}, and {115}) are included, as shown in Figure 2.7 (D) and Figure 2.8 (D), the real atom densities stand out clearly from the oscillating background.

As in the 1-D case, it is again true in the 3-D case that the number of reflections (Fourier components) is not as important as obtaining a complete set in order to get the correct density profile. Using reflections that carry different symmetry components will give a cleaner background (no false peaks). This is because all of the reflections yield a peak density at the same real atom positions, while the false peaks from the symmetry are at different places. When summed up, the averaging effect of different symmetry components reduces the background signals while the real peaks are enhanced.

The resolution of the density map in the $\boldsymbol{H}$ direction can be expressed as $d_{Hmax}/2 = \pi/H_{max}$. $H_{\boldsymbol{max}}$ is the equivalent (projected) maximum *hkl* along the specific direction, $\boldsymbol{H}$. For instance, if only {111} reflections are used, the resolution along the {100} direction is $d_{100}/2$.

When measuring the adsorbates at surfaces or interfaces, the above discussion will still be valid because the measured reflections are still derived from the bulk crystal lattice. However, the full bulk symmetry may not be preserved for the surface adsorbate because the element distribution symmetry is limited to 2-dimensions. That is, the symmetry operations along the surface (or interface) normal direction are eliminated, even if the surface inplane symmetry is still followed. Therefore the new symmetry

needs to be taken into account instead of the bulk symmetry when the analysis is carried out. For instance, on the (111) surface of an FCC crystal, for an adsorbate following the same (111) surface symmetry, the (-111), (1-11) and (11-1) reflections are still symmetry equivalent ones. The surface-normal direction Bragg reflection, (111), however, is not in the same symmetry family as the other three any more. Thus to utilize all the {111} family information, at least two, instead of one, independent measurements, i.e., (111) and one of the other three, need to be measured. For an adsorbate at the interface, the crystal surface symmetry may not always be followed, e.g., in the case of adsorption primarily occurring at the step edges. Therefore, to make sure the crystal surface symmetry applies to the adsorbate, at least one set of the surface equivalent reflections should be checked.

From the above simulations with both 1-D and 3-D systems, it is clear that the XSW imaging method are quite stable. In practice it does not need a large number of reflections to achieve the density profile of a species with a fairly good resolution. The symmetries of the surface adsorbates can be checked against the bulk crystal symmetries. If the bulk symmetry is found to be conserved, only one measurement is needed for each symmetry equivalent reflection family, and all the symmetry equivalent ones can be assumed to have the same values. It is possible that the XSW imaging process may yield a distribution profile containing the false information if the available information is from a subset of reflections containing the same symmetry elements. This can be eliminated by carefully choosing the reflections to measure and avoiding using only the reflections from a same symmetry group. If this is not practical, a full awareness of this potential

false information must be maintained.

To obtain a 3-D image with reasonable resolution on all directions, it is essential to have reflections along different directions measured. For a crystal surface with high symmetry, one or two measurements might be enough for this purpose, e.g., on the (111) surface of the FCC structure, one measurement out of {-111} family (assuming the crystal surface symmetry preserved) can yield the information along different directions. But for a surface without enough symmetry element, more explicit measurements along varies directions might be necessary.

Once an element density profile is obtained with the direct XSW imaging method, further refinement can be done by the traditional XSW triangulation analysis, using the atom positions derived from the imaging method as the initial model structure. The combination of the XSW imaging and the traditional XSW triangulation thus gives a model independent structural probing method with the sub-Angstrom level resolution and a few hundredths of an Angstrom precision.

The XSW imaging and the traditional XSW triangulation method together provide a complete process for interpreting the measured XSW data to gain direct structural knowledge. The resolution of the derived structure is limited by the reflection with the largest reciprocal space vector, $\boldsymbol{H}_{max}$, ever measured, as described above. There is also another limitation when working with the Bragg reflection XSW. The reflection with the smallest reciprocal space vector available, $\boldsymbol{H}_{min}$, is determined by the crystal structure. Therefore the maximum real space dimension over which the XSW method can yield a unique structure is defined as $d_{max} = 2\pi/\boldsymbol{H}_{min}$, i.e., the d-spacing of the reflection with the

lowest index. Consequently the elemental distribution over distances larger than the unit cell size (i.e., site-to-site variations) can not be uniquely determined by Bragg XSW measurements.

2.2.5 Layer synthetic microstructure XSW method

The period of an XSW field generated by a single crystal Bragg reflection is normally only a few Angstroms in length, which is optimal to probe the structures with the same or smaller length scale, (e.g., the positions of the impurities in the single crystal lattice or of the condensed EDL ions). But this approach cannot probe structures of length scales larger than the unit cell (e.g., the diffuse EDL ion distributions, where the Debye length could be hundreds of Angstroms). Therefore it is also necessary to generate XSW fields with a large period. Two long-period XSW techniques were developed by Bedzyk and coworkers.[8,101,102]

A layer synthetic microstructure (LSM) can be fabricated to have a 1-dimentional periodic structure. It usually consists of 10 to 200 bi-layers of alternating high and low electron density materials, such as W/Mo and Si. When the periodic quality of the LSM is good, the measured Bragg reflectivity is comparable to dynamical diffraction theory. The XSW is generated in a manner that is similar to that in Bragg XSW. This approach can be used to probe the adsorbate structure on top the LSM surface. The thickness of a bi-layer could be between 20 Å and 200 Å, therefore the XSW generated by the first order Bragg reflection from such LSM structure can be as large as 200 Å. Higher order Bragg reflections will generate XSWs with smaller periods, i.e., the integer fraction of

the bi-layer d-spacing. When multiple Bragg peaks from LSM structure can be measured, the smallest d-spacing can be smaller than 10 Å, which is comparable to that obtained for the Bragg XSW measurement, allowing for direct comparisons to be made of the two sets of results.

The data analysis is different from that of Bragg XSW case. The reflectivity of LSM can be calculated with Parratt's recursion formulation.[103] The E-field intensity, $I(\theta, z)$, can also be calculated this way at a given depth and angular position. And the fluorescence yield can be calculated for any given element distribution, $\rho(z)$, with:

$$Y(\theta) = \int_0^\infty I(\theta, z)\rho(z)dz \tag{2.9}$$

By comparing the calculated and the measured fluorescence yield, the element distribution profile could be obtained in the range of period of the bi-layer.

2.2.6 Total external reflection XSW method

Another way to generate a large period XSW is use the total external reflection (TER) from a mirror. When the incident angle changes from 0 to the critical angle, θ_c, continuously, the period of the generated XSW field, D, changes from ∞ to $D_c = \lambda/2\sin\theta_c \approx \lambda/2\theta_c$ following Equation (2.1). Substituting θ_c in the equation, the critical period D_c can be written as:

$$D_c = \frac{1}{2}\sqrt{\frac{\pi}{N_e r_e}} \tag{2.10}$$

Here N_e is the effective electron density of the mirror and r_e is the classic electron radius.

D_c is a material property dependent on the electron density, e.g., for TiO_2 D_c = 151 Å.

The complex E-field at the TER region can be derived with dynamical diffraction theory at 0^{th} order of Bragg peak, with the ratio as:

$$\frac{E_H}{E_0} = \frac{x - \sqrt{x^2 - 1 - iy}}{x + \sqrt{x^2 - 1 - iy}} = \left|\frac{E_H}{E_0}\right| \exp(iv) \tag{2.11}$$

Here E_H is the complex amplitude of the reflected plane wave; $x = \theta/\theta_c$ is the normalized angle parameter, and $y = \beta/\delta << 1$ is the absorption factor, with the index fraction of the materials $n = 1 - \delta - i\beta$. For the case of no absorption, $\beta = y = 0$,

$$R(\theta) = \left|\frac{E_H}{E_0}\right|^2 = \begin{cases} 1 & 0 \le x \le 1 \\ \left(x - \sqrt{x^2 - 1}\right)^4 & x > 1 \end{cases} \tag{2.12}$$

and the phase is:

$$v(\theta) = \begin{cases} \cos^{-1}\left(2x^2 - 1\right) & 0 \le x \le 1 \\ 0 & x > 1 \end{cases} \tag{2.13}$$

Between $\theta = 0$ and $\theta = \theta_c$, the reflectivity is 1 and the phase shift at the mirror surface changes continuously from π to 0. So a XSW node is at the surface at $\theta = 0$, and the first antinode is at infinity. As θ increases, the first antinode moves in toward the surface till $\theta = \theta_c$ when the antinode reaches the surface. At the same time, the higher orders of XSW antinodes are following in as the period D decreases.

The normalized E-field intensity is:

$$I(\theta, z) = 1 + R(\theta) + 2\sqrt{R(\theta)}\cos(v(\theta) - Qz) \tag{2.14}$$

where z is the coordinate along the surface normal direction, and $Q = 2\pi/D$ is also a

function of angle θ.

Equation (2.9) can be used to calculate the fluorescence yield for an arbitrary atom distribution on top of the mirror surface. For both TER and LSM XSW, the data analysis has relied on assuming a reasonable atom distribution model and having it optimized through fitting or simulations.

With TER-XSW, we measure the Fourier transformation of an atom distribution over a continuous range Q. TER-XSW is ideally suited to measure surface and interface structures of length scales in the range of tens to a few thousand Angstroms.

Unlike the Bragg reflections at the relatively high angle, both TER and LSM XSW measurements are carried out at low angles, where the reflection and refraction and absorption of the additional layer, such as the bulk aqueous solution layer, have to be included. This can be accomplished by making use of Parratt's recursion formulation to calculate the transmitted and reflected fields at any interface. Including the refraction and absorption effect of the E-field through the media, the E-field can be calculated at any given point between interfaces.

With the long-period XSW, the diffuse EDL ions distribution can be probed. Combining with the Bragg XSW which probes the condensed layer ion position, the whole EDL structure can be revealed by this powerful tool.

2.3 Crystal truncation rod method

Although very powerful, XSW has some limitations. For the Bragg XSW, it is required to have near perfect crystal. Some of the oxides and minerals are acceptable in this perspective, such as calcite and muscovite. But it might be difficult to find a sufficiently perfect crystal for many oxides. The secondary signal from the atoms inside the E-field is monitored in XSW measurement, such as the X-ray fluorescence signal in all our measurements. Therefore the experiment has to be carefully designed so that the signal from the atoms of interest can be measured. When such condition can not be satisfied, the analysis of the XSW data could be difficult. It is not unusual for an oxide to have impurities. Even an impurity fraction of 1% in the bulk crystal could correspond to large surface quantities since X-rays probe the micrometer deep region through which X-rays penetrate. For the in-situ measurements at the oxide-aqueous interface, at least a few micrometers of aqueous solution is present, which may also contain a significant amount of the same element adsorbed at the interface. Therefore, for practical considerations, it is essential for XSW measurements to have a 'clean' crystal that has a minimal amount of that element in the system. For instance, this leads to the general requirement that the elemental concentration of the aqueous solution should be lower than 10^{-3} mol/kg. While some ions will adsorb under such conditions, others do not. Also additional information is required to eliminate the module-d problem of XSW. So other structure probing methods are needed for the oxide-aqueous interface. Crystal truncation rod method (CTR) is one such method.

2.3.1 The crystal truncation rod method

The CTR measurement, an analog to the bulk crystallography applied to the surface, focuses on the diffraction signals from the surface/interface instead of the bulk crystals. With its quantitative capability and the sub-Angstrom resolution, it has been successfully applied to the oxides surface in both vacuum and ambient condition.[35,69,70,71] Since X-rays interact weakly with H_2O, the measurement can be carried out in-situ with the bulk fluid present on top of the oxide surface. And since the electron densities of adsorbed water molecules or any other ions or groups are comparable to that of top surface layer of the oxide, CTR data is very sensitive to the interfacial structure variation and capable of revealing the interfacial structure.

Unlike the heavy-element specific XSW measurement, CTR measurement is sensitive to the total electron density distribution at the interface. The structures of surface oxygen atoms and the interfacial water molecules, which are practically invisible in the in-situ XSW measurements, can be revealed by analyzing the CTR data. Also the limitation concerning the solution concentration and/or thickness in XSW measurements is eliminated since the randomly distributed atoms in the bulk solution are invisible to the CTR method.

The X-rays reflectivity can be generalized as $R \propto |F|^2$, where F is the structure factor, which in turn is the Fourier transform of the electron density distribution of the system. For an infinite 3D periodic structure, i.e., a single crystal, the Fourier transformation yields the discrete points, i.e., Bragg peaks, in the reciprocal space. If the real space structure, however, is not infinite along one of the dimensions, but has a

surface, i.e., a truncated crystal, the Fourier transformation will be a series of rods perpendicular to the surface in additional to the Bragg peaks in the reciprocal space. Those are the so-called surface truncation rods, or crystal truncation rods. In analogy to the Bragg crystallography, in which the Bragg peak positions and intensities are determined by the bulk crystal structure and chemical composition, the intensity modulation of the truncation rods are directly related to the surface structure and species. Because the CTR intensities between Bragg peaks are orders of magnitudes weaker than those on the Bragg peaks, the method was not widely used until synchrotron X-ray sources became available. For instance, at Advanced Photon Source (APS), the absolute reflectivity as low as 10^{-11} can be measured with a reasonable statistics. (The comparative number is 10^{-8} for a rotating anode.) The surface structure can be measured faster and with higher precision at such facilities.

As an example, for the solid-aqueous interface, the reflectivity, R, comes from three parts (Figure 2.9),[104]

$$R \propto \left|F\right|^2 = \left|F_{bulkcrystal} + F_{\text{int}erface} + F_{water}\right|^2 \tag{2.15}$$

Here $F_{bulkcrystal}$ is from the semi-infinite bulk crystal; F_{water} is from the macroscopic thick water; and $F_{interface}$ is from the interfacial region, including the top a few layers of the crystal, which could be relaxed and/or reconstructed, any specifically adsorbed species at the crystal surface, and the first a few layers of the water near the interface.

Briefly, the structure factor can be written as $F(\boldsymbol{Q}) = \sum_n f_n \exp(-i\boldsymbol{Q}\cdot\boldsymbol{r_n})$, where f_n is the atomic form factor of atom n; $\boldsymbol{r_n}$ is the position vector of the same atom; $\boldsymbol{Q}$ is the

momentum transfer; the summation is over all the atoms in the X-rays path. For a periodic semi-infinite structure, such as the bulk crystal part we have here, $F_{bulkcrystal}$, the structure factor: $F(\boldsymbol{Q}) = F_{CTR}(\boldsymbol{Q}) \cdot F_{UC}(\boldsymbol{Q}) = F_{CTR}(\boldsymbol{Q}) \cdot \sum_{UC} f_n \exp(-i\boldsymbol{Q} \cdot \boldsymbol{r_n})$, where $F_{UC}(\boldsymbol{Q})$ is the unit cell structure factor, which sums over all the atoms in a unit cell; $F_{CTR}(\boldsymbol{Q}) = \frac{1}{1-\exp(-i\boldsymbol{Q} \cdot \boldsymbol{R})}$ accounts for the semi-infinite stacking of the surface layer to complete the substrate lattice. Here $\boldsymbol{R}$ is the translation vector relating the relative separation, both vertical and lateral, between neighboring crystal layers (a 2-D repetition of the unit cell in the surface plane) from which a semi-infinite bulk crystal is generated. For instance, in our study of rutile (110) surface, the non-primitive tetragonal unit cell is used for convenience, and $\boldsymbol{R} = \boldsymbol{a} + \boldsymbol{b} = 2d_{(110)} \cdot \boldsymbol{r}_{[110]} = d_{(001)S} \cdot \boldsymbol{r}_{[001]S}$, here $\boldsymbol{r}_{[110]}$ and $\boldsymbol{r}_{[001]S}$ are the same unit vector along the $[110]$ or $[001]_S$ direction. If the primitive tetragonal unit cell is used, $\boldsymbol{R} = \boldsymbol{a} = d_{(100)} \cdot \boldsymbol{r}_{[100]} = d_{(-101)S} \cdot \boldsymbol{r}_{[-101]S}$, here $\boldsymbol{r}_{[100]}$ and $\boldsymbol{r}_{[-101]S}$ are the same unit vector along the $[100]$ or $[-101]_S$ direction.

Usually the structures of both the bulk crystal and bulk water parts, i.e., $F_{bulkcrystal}$ and F_{water}, are known before hand. With the measured reflectivity, R ($\propto |F|^2$), the structure of the interfacial region can be determined.

The typical way to solve an unknown structure with CTR measurement is by model fitting. First a guessed model structure based on the best knowledge about the system is generated. And the reflectivity is calculated from the model structure. The calculated and the measured reflectivity values are then matched by adjusting the

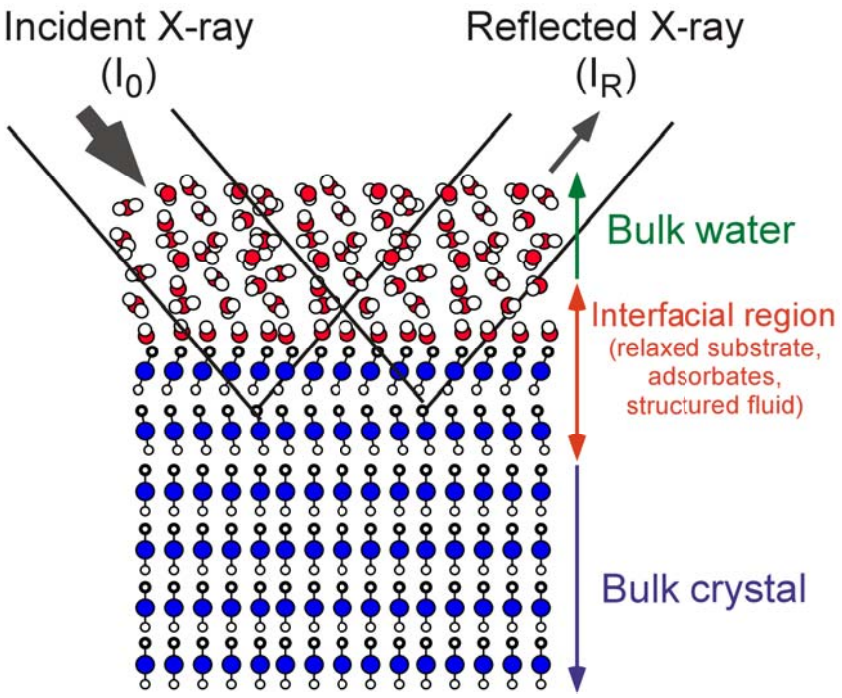

Figure 2.9. The oxide-aqueous interface structure seen by CTR measurement.

parameters for the model structure (e.g., with non-linear χ^2 fitting). The final optimized model structure is the possible structure sought. Because the fitting procedure most likely finds only a local minimum, the proper starting structure is critical for CTR data analysis. Also the final structure should be physically and chemically plausible, e.g., the atom packing density and bond length should both be meaningful. In this sense, the model dependent CTR analysis is not 'simple' or 'direct'.

2.3.2 Technical details about CTR measurement

As shown in the Figure 2.10, the diffraction geometry can be denoted with the momentum transfer $\boldsymbol{Q}$, which is defined as $\boldsymbol{Q} = \boldsymbol{K_f} - \boldsymbol{K_0}$, with $\boldsymbol{K_0}$ and $\boldsymbol{K_f}$ are the incident and diffracted X-ray wave vectors, respectively. The angle between them is the scattering angle 2θ. And $|\boldsymbol{K_0}| = |\boldsymbol{K_f}| = 2\pi/\lambda$, where λ is the wavelength of the X-rays. The components of $\boldsymbol{Q}$ along the reciprocal lattice vector $\boldsymbol{a^*}$, $\boldsymbol{b^*}$, and $\boldsymbol{c^*}$ are $\boldsymbol{Q_X}$, $\boldsymbol{Q_Y}$, and $\boldsymbol{Q_Z}$, respectively. Here we have the surface normal direction is along $\boldsymbol{c^*}$ direction. So, in an orthogonal system,

$$|\boldsymbol{Q}| = \frac{4\pi \sin(2\theta/2)}{\lambda};\ \boldsymbol{Q} = \boldsymbol{Q_Z} + \boldsymbol{Q_{//}};\ \boldsymbol{Q_{//}} = \boldsymbol{Q_X} + \boldsymbol{Q_Y} \tag{2.16}$$

$$\boldsymbol{Q_X} = H\boldsymbol{a^*};\ \boldsymbol{Q_Y} = K\boldsymbol{b^*};\ \boldsymbol{Q_Z} = L\boldsymbol{c^*} \tag{2.17}$$

H, K, and L are the indices for the reflection. On the Bragg peaks, all three indices are integers normally noted as (hkl), where $\boldsymbol{Q} = \boldsymbol{H} = h\boldsymbol{a^*} + k\boldsymbol{b^*} + l\boldsymbol{c^*}$.

CTR measurements usually probe a set of rods. For each rod, which has a fixed in plane momentum transfer component, $\boldsymbol{Q_{//}}$, i.e., fixed H and K values, the reflectivity is

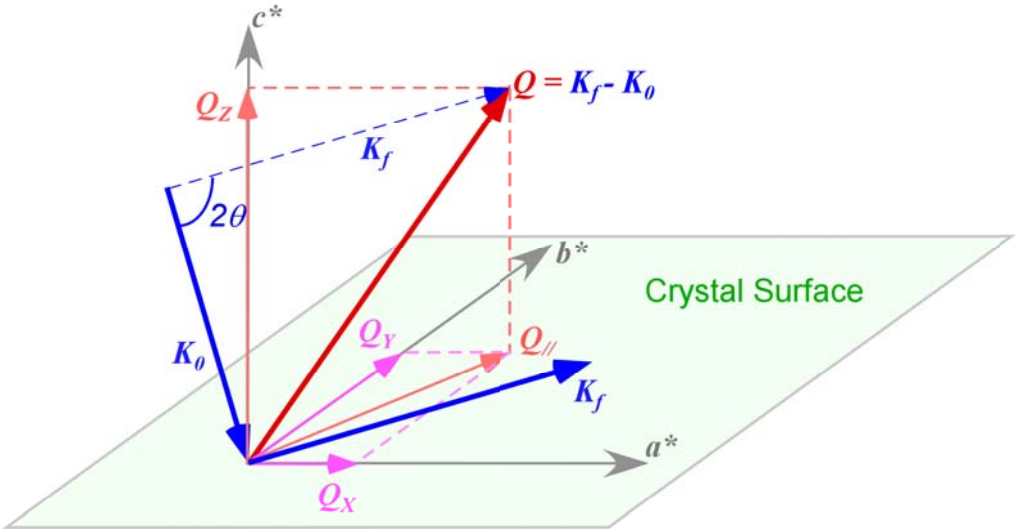

Figure 2.10. The momentum transfer $\boldsymbol{Q}$, is related to the incident and reflected X-ray beam wave vector $\boldsymbol{K_f}$ and $\boldsymbol{K_0}$ as $\boldsymbol{Q} = \boldsymbol{K_f} - \boldsymbol{K_0}$. The component of $\boldsymbol{Q}$ along $\boldsymbol{c^*}$ direction is $\boldsymbol{Q_Z}$ and those in the surface plane are $\boldsymbol{Q_X}$ and $\boldsymbol{Q_Y}$, along $\boldsymbol{a^*}$ and $\boldsymbol{b^*}$ direction, respectively.

measured at different $\boldsymbol{Q_Z}$ or L value by rotating the crystal (e.g., in the diffraction plane) with respect to the incident X-ray beam while measuring the reflected signal. The obtained reflectivity curve over the angular space (θ) is the so-called rocking curve at the given L or $\boldsymbol{Q_Z}$. A rocking curve might look like a Gaussian shape curve on top of a background signal. The reflectivity at $\boldsymbol{Q_Z}$ can be retrieved as the integral area under the background subtracted curve, which can be obtained by fitting the curve and the background to proper forms, e.g., a Gaussian function with a linear background. (When the rocking curve is resolution limited, the curve would be more like rectangular shape, where the Gaussian fitting actually introduces large error. In such cases, the simple numerical integral method can be used to calculate the background removed integral and the errorbar.)

To directly connect the amplitude of structure factor $|F|$ to the reflectivity, R, some corrections are needed, including (1), the surface active area, A, which accounts for the variation with $\boldsymbol{Q}$ of the actual area from which the reflected beam reaches the detector. Normalizing the active surface area with the incident beam size, $A0$, a unitless quantity will be obtained. (2), ΔQ_Z correction, which accounts for the varying length of the surface rod as seen by the detector slit along the $\boldsymbol{Q_Z}$ direction at different $\boldsymbol{Q}$. (3), Attenuation factor, T_{cell}, which accounts for the attenuation of the incident and reflected X-ray beam through the cap material on top of the sample (i.e., the aqueous layer and the cell window) as a function of angle. Since these measurements were all obtained with a symmetrical scattering geometry, the incident and reflected beam paths are always the same. (4), Lorentz factor, $1/\sin(2\theta)$, which accounts for how the intensities were

integrated. Considering all these, the measured intensity normalized to the beam monitor should be:[104.]

$$\frac{I_{\text{int}}}{M} = \left(\frac{e^2}{mc^2}\right)^2 \left(\frac{T_{cell}}{\alpha_{mon}}\right)\left[\frac{A}{A_0}\right]\left[\frac{B\lambda^3 P}{a_{uc}^2}\right]\left[\frac{1}{\sin(2\theta)}\right]|F|^2\left(\frac{\Delta Q_Z}{2\pi}\right) \tag{2.18}$$

A pre-factor, *Y*, which is a constant, is defined as:

$$Y = \left(\frac{e^2}{mc^2}\right)^2 \left[\frac{\lambda^3 P}{a_{uc}^2}\right]\left(\frac{1}{2\pi}\right); \tag{2.19}$$

here *P* is the polarization factor, for the polarized synchrotron beam and diffraction plane is perpendicular to the polarization direction, it is 1; a_{uc} is area of the non-primitive tetragonal unit cell on the (110) surface, which is also defined as the surface unit cell; λ is the wavelength of the X-ray; and e^2/mc^2 is the classical electron radius. Therefore, the measured reflectivity R_M will be:

$$R_M = Y \bullet \left(\frac{T_{cell}}{\alpha_{mon}}\right) \bullet B \bullet \left(\frac{A}{A_0}\right)\left[\frac{1}{\sin(2\theta)}\right](\Delta Q_Z)|F|^2 \tag{2.20}$$

here *B* is the roughness factor, (details later); α_{mon} is the conversion factor of ion chamber count to photon flux; *F* is the structure factor of the system.

During the calculation/fitting, except for T_{cell}, *B*, and $|F|^2$, all the parameters are constant at a given **Q**. To simplify the calculation, normalized reflectivity R_N is used in the fitting:

$$R_N = \frac{R_M}{Y \bullet (A/A_0)\left[\frac{1}{\sin(2\theta)}\right](\Delta Q_Z)} = X \bullet T_{cell} \bullet B \bullet |F|^2 \tag{2.21}$$

Here, X is an overall scale factor, which is used to compensate for any mis-scaling during the normalization/calculation, including α_{mon}.

The roughness factor B is calculated assuming the roughness taking the form of partial layering with the occupancy of nth layer as β^n, where β ($0 \le \beta \le 1$), the fractional occupancy factor, is one of the fitting parameters:[68].

$$B = \frac{(1-\beta)^2}{\left[1+\beta^2 - 2\beta\cos(\boldsymbol{Q}\bullet\boldsymbol{c})\right]} = \frac{(1-\beta)^2}{\left[1+\beta^2 - 2\beta\cos(Q_\perp c)\right]} \tag{2.22}$$

Here $\boldsymbol{Q}$ is the momentum transfer vector, and $\boldsymbol{c}$ is the non-primitive tetragonal unit cell vector.

To calculate the absolute reflectivity, the following equation can be used:[104].

$$R = \left(\frac{e^2}{mc^2}\right)^2 T_{cell}\left[\frac{(A/A_0)\lambda^3 P}{a_{uc}^2}\right]\left[\frac{1}{\sin(2\theta)}\right]|F|^2\left(\frac{\Delta Q_z}{\pi\cdot\Delta(2\theta)}\right) \tag{2.23}$$

This is actually the normalized reflected signal divided by the normalized direct through signal. Both are integrated signals and normalized to the monitor signal (I_0).

For the specular case (along the surface normal direction), R is geometry independent. But for the off-specular cases, R depends on the geometry of the measurement because A and ΔQ_Z are geometry dependent.

The resolution of the CTR measurements can be estimated as ~ π/Q_{max} along direction of $\boldsymbol{Q}$, where Q_{max} is the maximum $\boldsymbol{Q}$ value measured along that specific direction. Further details can be found in reference 104.

CTR data can reveal nearly all aspects of the structure. But since it is mostly not a model independent method, it requires a substantial amount of fitting, and guesses,

especially for understanding the complex oxide-aqueous interfaces. Therefore so far there are only limited applications in this field.

2.4 Extended X-ray absorption fine structure method

Both XSW and CTR method make use of the long range order of the crystalline materials. So both methods require a macroscopic single crystal. The extended X-ray absorption fine structure (EXAFS) method, on the other hand, focuses on the local structure around a central atom. Therefore its requirement for materials quality is less demanding.

EXAFS, like XSW, rely on secondary X-ray processes. When the incident X-ray energy is higher than the absorption edge of the specific atom, the absorption of X-ray photon will occur and a photoelectron is excited. Treated quantum mechanically, the wavelength of the photoelectron, λ_e is

$$\lambda_e = \frac{h}{p} \tag{2.24}$$

Here h is Planck's constant and p is the momentum of the photoelectron. In the EXAFS region, p can be determined by the free electron relation:

$$\frac{p^2}{2m} = h\nu - E_0 \tag{2.25}$$

Here $h\nu$ is the incident X-ray photon energy and E_0 is the binding energy of the electron. The photoelectron can be represented as an outgoing spherical wave from the central atom. The surrounding atoms will scatter the outgoing wave. The superposition of the scattered and the outgoing wave at the center of the absorbing atom, either in phase or out

of phase, modifies the overall cross-section for the absorption of X-rays. As the X-ray energy changes, so does the photoelectron wavelength (i.e., due to its kinetic energy). Thus the relative phase of the scattered wave and the outgoing wave at the center of the absorbing atom varies, which results in the modulation of the photo effect cross-section and therefore the intensity of the fluorescence emitted from the absorbing atom. An EXAFS equation describing such intensity oscillation, $\chi(k)$:[105]

$$\chi(k) = \sum_j \frac{N_j F_j(k)}{kR_j^2} \exp\left(-2k^2\sigma_j^2\right) \exp\left(\frac{-2R_j}{\lambda}\right) \sin\left[2kR_j + \delta_j(k)\right] \qquad (2.26)$$

Here $k = \sqrt{2m(E - E_0)/\hbar^2}$ is the wave number, $F_j(k)$ and $\delta_j(k)$ are scattering properties of the neighboring atom; λ is the photo electron mean free path; R_j is the distance to the neighboring atom; N_i is coordination number of the neighboring atom; σ_j is mean-square disorder of neighbor distance.

Therefore the EXAFS spectrum contains the information about the surroundings of the center photo-emitting atom. The derivation and the details of the Equation (2.26) can be found in reference 105.

The general knowledge about the surroundings of the center atoms is needed before hand when analyzing the EXAFS data, such as the type of the atoms and it is possible structure. When such information is available, by comparing/fitting the measured spectrum with the calculated spectrum from a known structure, the local structure information, such as the coordination shell position and the coordination number of the surrounding atoms can be obtained.

EXAFS method, similar to XSW method, is vulnerable to interference from background fluorescence signals. When a relatively large amount of the same element is found in the system but not bound to the surface of interest as a simple adsorbate, the fluorescence of such atoms results in a substantial background, and the measured spectrum may not reflect the structure of the specifically bound atoms. Therefore care must be given to control the source of the fluorescence signal when working with ion adsorption on the single crystal surface.

When combining complimentarily the in-situ XSW, CTR and EXAFS methods, we have the capability of fully probing the atomic scale structure of the EDL at the oxide-aqueous interface.

Chapter 3 Divalent ion adsorption at rutile-aqueous interface: Ionic strength independence & absolute coverage

3.1 Questions raised/addressed about electrical double layer

The EDL structure near a planar interface can be considered as a one-dimensional structure as described in Chapter 1. For such a structure, the position of the condensed layer, i.e., the specifically adsorbed ion height from the surface plane, is an important parameter. In surface complexation models (SCMs, see section 1.1.4), it is usually assumed that the bonds between the adsorbate and surface oxygens are bulk-like. The height of the adsorbate is derived from the bond length and geometry of the bulk crystal. With this assumption, the SCMs can explain the EDL features. However, lack of solid structure information about the adsorbate at the interface makes it hard to judge the different models and extend our understanding further.

Also normally assumed in SCMs is the independence of the ion height on the solution ionic strength. The dependence of the ion height on the solution pH and/or temperature is predicted by some models.[10.] It would be nice to have this kind of information directly achieved from the structure measurements to directly test these models.

Another important aspect of the EDL is the amount of the ions in the condensed and diffuse layer, respectively. This quantity helps to constrain the distribution of the electrostatic potential as well as the ion adsorption strength at an interface. The predicted

condensed and diffuse layer ion coverages at rutile (110)-aqueous interface from the MUSIC model are listed in Table 3.1.[106] (Details about MUSIC model can be found in references 17 & 18. The details of application of MUSIC model at rutile (110)-aqueous interface can be found in references 22 & 23) Corresponding experimental data, if available, can place additional checks on the validity of the model.

Table 3.1. The Stern layer coverages from XSW and CTR measurements and the predicted results based on the MUSIC model at rutile (110)–aqueous interface. All solution concentrations and the ionic strength, *S*, are in the unit of mol/kg.

	XSW measurements		SCM predictions		
	Coverage Θ (ML)	Solution Condition	Coverage Θ (ML)	Solution Condition	Coverage ratio Diff/Stern
Zn^{2+}	~ 0.4	pH = 8 & 10; $[Zn^{2+}] = 10^{-5}$ or 10^{-6}	0.47	pH = 8; $[Zn^{2+}] = 10^{-5}$; $S = 0.03$	0.02
Sr^{2+}	~ 0.4	pH = 10.7; $[Sr^{2+}] = 10^{-4}$	0.32	pH = 10.7; $[Sr^{2+}] = 10^{-4}$; $S = 0.001$	0.04
Y^{3+}	≥ 0.1	pH = 6.11; $[Y^{3+}] = 10^{-5}$	0.15	pH = 6.1; $[Y^{3+}] = 10^{-5}$, $S = 5 \times 10^{-4}$	0.01
Rb^{+}	~ 0.25-0.50 (from CTR)	pH = 12; $[Rb^{+}] = 1$	0.20	pH = 12; $[Rb^{+}] = 1$	1.31
			0.17	pH = 11; $[Rb^{+}] = 1$	1.30

The XSW method offers a powerful way to directly probe to resolve nearly all of the assumptions and questions described above. For instance, recent measurements with a combination of in-situ and ex-situ XSW and EXAFS probe the Sr^{2+} and Rb^{+} ion heights from the surface Ti-O plane at the rutile (110)-aqueous interface,[81] and the heights of Sr^{2+} and Rb^{+} were reported as 2.75 and 3.35 Å, respectively. The direct availability of this information helps to refine the SCM to gain the new ground on exploring the EDL phenomena.[107] However, we have recently found that those limited measurements do not reflect the intrinsic structure of these ions at the rutile (110)-water interface. Instead the

results were characterized by relatively poor order (presumably due to a large contribution from ions adsorbed at defect sites), which has since been determined to be due to the roughness of the crystal surfaces used in those measurements. Since then we have improved our sample surface preparation process and achieved atomically flat rutile (110) surfaces. [87,100]

Here, we present the use of Bragg reflection XSW to probe the variation of divalent ions (Sr^{2+} and Zn^{2+}) distributions at treated single crystal rutile α-TiO_2 (110) aqueous interfaces, and the influence of background electrolytes and solution ionic strength on the divalent ion distributions in EDL. Additional measurements of absolute ion coverages (both total and Stern-layer) reveal insight into the distribution of ions between the Stern layer and other adsorption channels. Gouy-Chapman (GC) and Gouy-Chapman-Stern (GCS) models of the EDL are discussed for their capabilities to describe the adsorption of divalent ions at rutile (110) aqueous interface. Partitioning of ions between the condensed and diffuse layers and other sources is discussed.

3.2 Experimental details

3.2.1 Beamline setup

The XSW measurements were preformed primarily at beamline X15A at the National Synchrotron Light Source (NSLS), Brookhaven National Laboratory and at beamline 12-ID-D (BESSRC-CAT) at the Advanced Photon Source (APS), Argonne

National Laboratory. Measurements at the X15A, schematically shown in Figure 3.1, used two Ge(111) crystals (the first one with 6° miscut and the second one with no miscut) as a double-bounce monochromator to select the photon energy at 17.0 keV for both Zn^{2+} and Sr^{2+}. Beam size was controlled by slits with typical beam cross section of 0.1×0.4 mm^2. Measurements at the 12-ID-D, schematically shown in Figure 3.2, used a symmetrical Si (111) high heat load monochromator to select the X-ray energy of 11.5 keV for Zn^{2+} measurements and 17.5 keV for Sr^{2+} measurements. A Si(Li) or LEGe fluorescence detector was used to collect characteristic X-ray fluorescence signals from the crystal surface at a take-off angle ~ 5°.

Care was taken to choose a beam spot where the rocking curve width and reflectivity was a close match to the theory predicted rocking curve for a perfect crystal. Experiments were performed on spots where the measured absolute reflectivity was > 70%, and the rocking curve width was less than 1.5ω, where ω is the expected Darwin width of the rocking curve based on the dynamical diffraction theory including dispersion due to the specific monochromator that was used.

Shown in the Figure 3.3 is one example of comparison of the calculated and the measured TiO_2 (110) rocking curve at beamline X15A. At E = 17 keV, the b-factor from the α = 6° miscut Ge (111) crystal is $b = -\dfrac{\sin(\theta_b - \alpha)}{\sin(\theta_b + \alpha)} = 0.03$. The intrinsic TiO_2 (110) rocking curve (green dashed line) and the rocking curve convoluted with b = 0.03 Ge (111) monochromator (black solid line) are only slightly different. The measured rocking curve with large beam size (1 mm horizontally and 0.4 mm vertically, red triangles) is

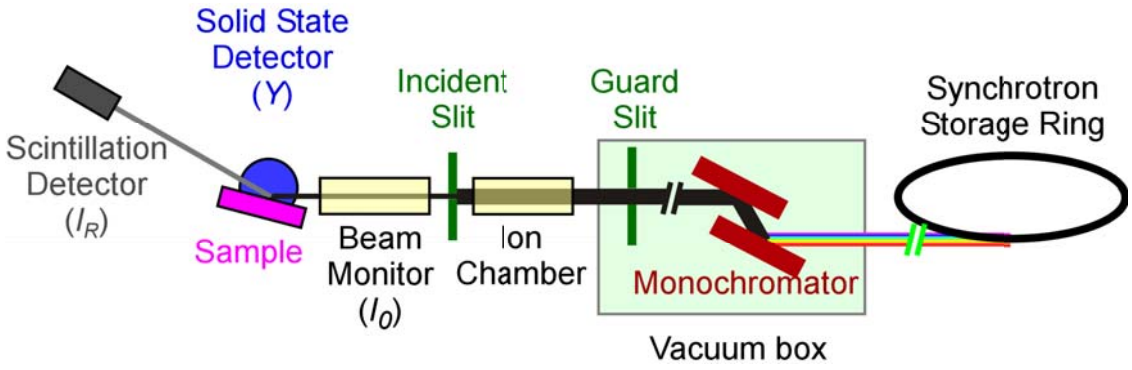

Figure 3.1. Experimental setup at bending magnet beamline X15A, NSLS, BNL.

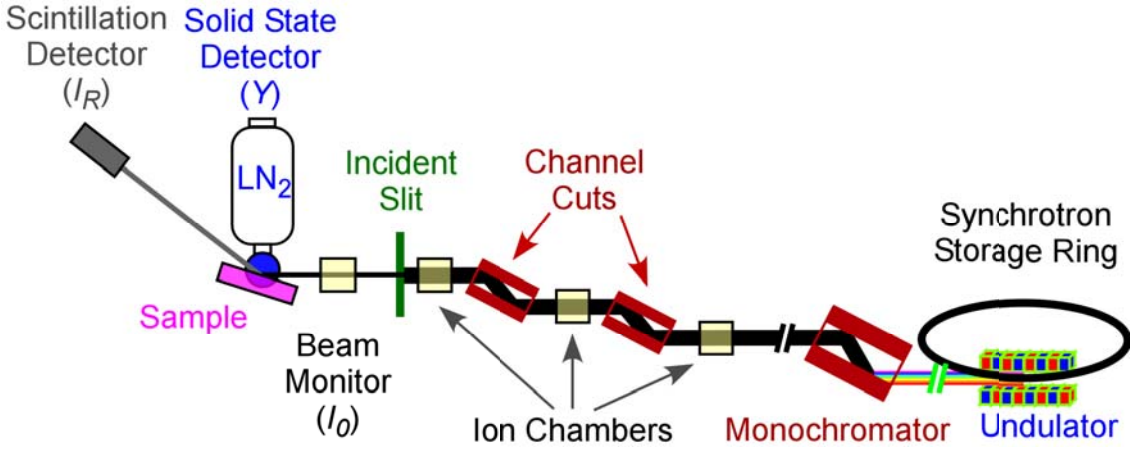

Figure 3.2. Experimental setup at undulator beamline 12ID-D, BESSRC-CAT, APS, ANL.

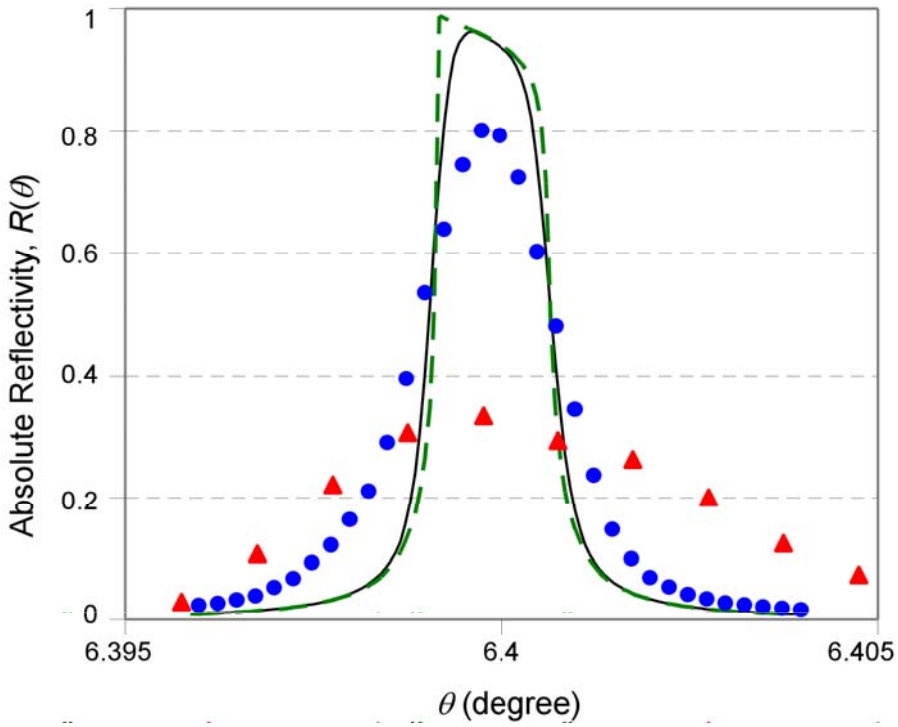

Figure 3.3. Comparison of the measured and the calculated TiO_2 (110) rocking curves at E = 17 keV. The calculated TiO_2 (110) intrinsic rocking curve (green dashed line) and the convoluted rocking curve with a 6° miscut Ge (111) monochromator (b = 0.03, black solid line). The measured rocking curve with a (horizontal × vertical) beam size of 1 × 0.3 mm^2 (red triangles) and 0.4 × 0.1 mm^2 (blue dots).

significantly wider than the calculations. The one measured with the smaller beam size (0.4 mm × 0.1 mm, blue dots), however, are close enough to the calculation to work with.

3.2.2 Sample handling

The measurements were performed in-situ in a thin-film cell as show in Figure 3.4. Solution can be injected into the cell through the tube with a syringe. Equilibration of the sample surface was obtained when the solution was injected into the cell, and the sample was exposed to a ~ 1 mm thick aqueous solution layer, held between the Kapton film and the sample surface. To ensure full equilibration of the surface at proper solution conditions, 10 to 15 minutes was allowed after each injection, and the solution exchange was repeated at least three times for each solution.

At the experimental concentrations of the measured adsorbate that were used (10^{-5} or 10^{-4} mol/kg), a single solution injection contains a substantial excess of ions with respect to the nominal available surface site density, expressed in units of monolayer (ML). (We define 1 ML as 1 ion per TiO_2 (110) surface unit cell. With a surface unit cell area of 6.50 Å × 2.96 Å = 19.24 $Å^2$, 1 ML = 5.3×10^{14} ions/cm^2 = 8.8 μmol/m^2.) Assuming that there are two adsorption sites per surface unit cell, the maximum available site density corresponds to 2 ML. However, the theoretical site density of 1 ML is in excess of the expected adsorption density given previous measurements of proton charge at the rutile-water interface [~ -0.5 C/m^2 = 5.2 μmol/m^2 = 0.6 ML].[108] Before each XSW measurement, the solution between the Kapton film and the sample surface was minimized with a small negative pressure and sealed to maintain a minimal solution

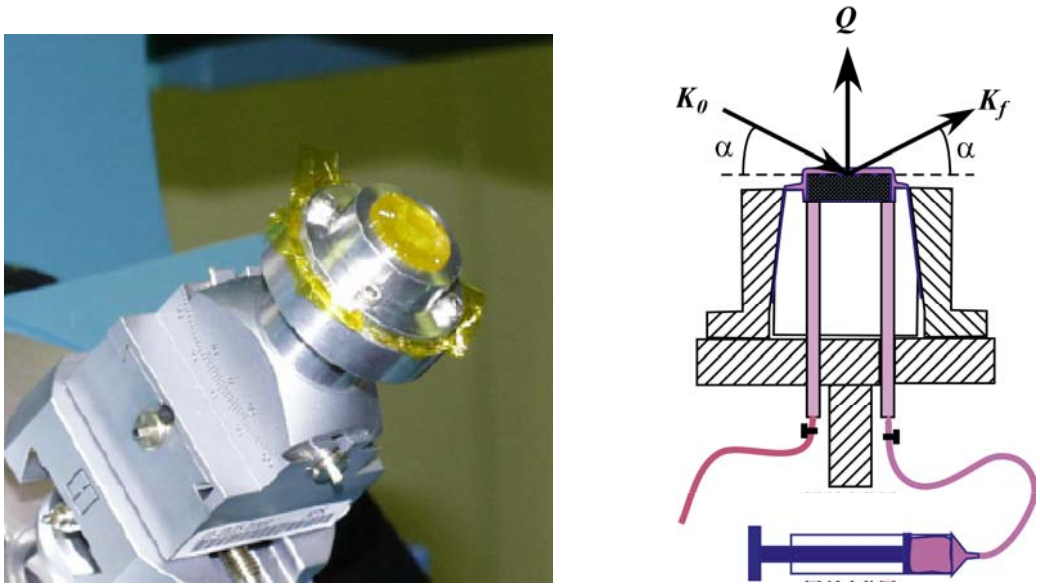

(A) (B)

Figure 3.4. (A), photo of the sample cell on the diffractometer; and (B) the schematic of the sample cell: the sample is held in place with a thin Kapton film. The solution can be injected or removed through the tube. A thin layer of solution is sealed on top of the sample surface during the measurements.

thickness of ~ 2 μm during the XSW measurements. The cell was held in a controlled atmosphere of pure N_2 gas to minimize any diffusion of atmospheric gases (e.g., CO_2) through the Kapton film. Adsorption was found to be fast with respect to the exposure time.

Polished rutile (110) single crystals (10 mm × 10 mm × 1 mm) were obtained from Princeton Scientific with a typical miscut of 0.1° to 0.2° with respect to the (110) crystallographic plane. The crystal surface was treated with the following procedure: (1), ultrasonic cleaning in, successively, deionized (DI) water, 1% HNO_3, high purity methanol, DI water, 10% H_2O_2 and again, DI water; (2), annealing of the vacuum-dried crystals at 1000-1100 °C for one hour in an air furnace; (3), hydrothermal reaction in DI water in a Teflon cup housed within a pressure vessel at 220 °C for 12 hours; and (4), a final ultrasonic treatment in DI water. The treated samples were then stored in deionized water in sealed Teflon cells until the X-ray measurements were performed.

Sample preparation is very important for the ion adsorption measurements. AFM images of rutile samples as received from the manufacturer, shown in Figure 3.5 (A), and after annealing and hydrothermal processing, shown in Figure 3.5 (B), reveal that the original surface is very rough while large (> 0.1 μm across) atomically flat terraces are observed separated by steps with single unit cell height (3.25 Å) after the treatments. CTR measurements of the treated surface (see Chapter 5) show no evidence of the (1 × 2) or other surface reconstructions as observed for oxygen depleted surfaces prepared by sputtering and annealing in high vacuum.[31,109,110] Representative XSW results for Sr^{2+}

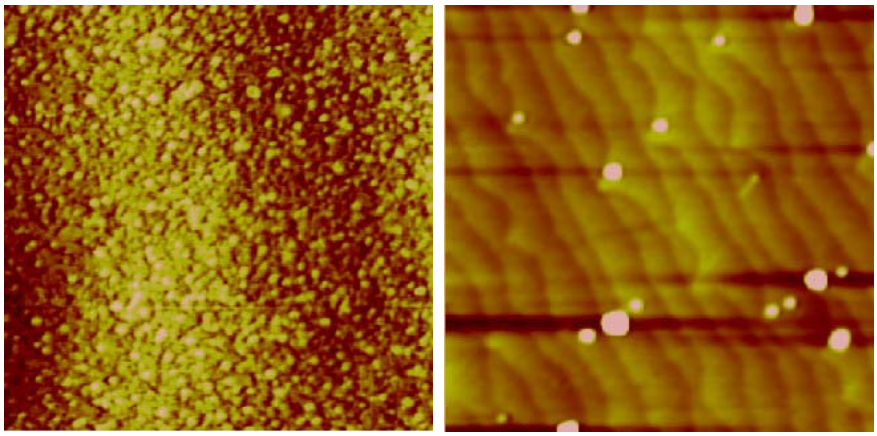

(A) (B)

Figure 3.5. AFM images of the rutile (TiO_2) (110) surface (A) As-received and (B) after 1000 °C annealing in air. Both images are 2 μm × 2 μm in area. The treated surface shows the atomic scale flat terraces separated by steps with single unit-cell height.

and Rb^+ adsorption at rutile (110) surface on these treated samples, as shown in Figure 2.4 (B), are quantitatively different from previously reported results.[81] These data show that the Sr^{2+} ion has a relatively large coherent fraction (0.51) while Rb^+ ion has a coherent fraction that is consistent with zero. These values differ from previously reported values measured on untreated samples that showed a substantially lower coherent fraction for Sr^{2+} (< 0.3) and a marginally non-zero coherent fraction for Rb^+ (< 0.25). Given the large differences in surface topography, the differences in the earlier results can be associated with adsorption of the ions at surface defect sites associated with the more highly roughened untreated rutile surfaces. Given the high reproducibility of the results described below (with duplicate measurements on the same sample as well as measurements on separately-prepared samples) and the ideal nature of the surface topography observed in the AFM image, we believe that the present results reflect the intrinsic ion adsorption behavior at the rutile-aqueous interface.

The detailed solution conditions, the ionic strengths, and the calculated Debye lengths of each solution are listed in Table 3.2 and Table 3.3 for Zn^{2+} and Sr^{2+} measurements, respectively. The Debye length was calculated with the relation $\Lambda = \sqrt{\frac{\varepsilon k_B T}{2Se_0^2}}$, where $S = \frac{1}{2}\sum_i z_i^2 n_i^\infty$ is the ionic strength; z_i and n_i^∞ are the charge and bulk concentration of the i^{th} ion species, respectively; e_0 is the elementary charge; ε is the permittivity of the solution, where the bulk water permittivity $\varepsilon(H_2O)$ = 78.54 × 8.85 × 10^{-12} C^2/J/m is used; k_B = 1.38 × 10^{-23} J/K is the Boltzmann constant, and T is the absolute temperature, for which room temperature 298 K is used. For the ionic strength

Table 3.2. The solution conditions for Zn^{2+} measurements (all concentrations in the unit of mol/kg), the ionic strength S (mol/kg, by assuming the density of solution 1 kg/L, it is equivalent to mol/L), and the calculated Debye length, Λ, (Å) of the EDL diffuse layer. Also listed in the table are the measured coherent positions, P; and coherent fractions, f; and the total-coverage, Θ_{tot} (in the unit of Mono-Layers [ML]) with the statistical uncertainties from each single measurement.

Label	$[Zn^{2+}]$	$[Na^{+}]$	$[Cl^{-}]$	$[Tr^{-}]$	pH	S	Λ (Å)	P	f	Θ_{tot} (ML)
Zn-1	10^{-5}	0	0	2×10^{-5}	8	3×10^{-5}	554	0.91(1)	0.63(3)	0.35
Zn-2	10^{-5}	0.01	0.01	2×10^{-5}	8	0.01003	30	0.90(1)	0.61(2)	0.6
Zn-3	10^{-5}	0.1	0.1	2×10^{-5}	8	0.1	9.6	0.91(1)	0.72(3)	0.2
Zn-4	10^{-5}	0.1	0	0.1	8	0.1	9.6	0.91(1)	0.72(2)	0.4
Zn-5	10^{-5}	1	1	2×10^{-5}	8	1	3.0	0.93(1)	0.60(2)	0.45
Zn-6	10^{-5}	10^{-4}	10^{-4} Br^{-}	2×10^{-5}	8	1.3×10^{-4}	266	0.93(1)	0.72(4)	0.5
Zn-7	10^{-5}	5×10^{-4}	5×10^{-4} Br^{-}	2×10^{-5}	8	5.3×10^{-4}	132	0.92(1)	0.70(2)	0.5
Zn-8	10^{-4}	5×10^{-4}	5×10^{-4} Br^{-}	2×10^{-4}	4.3	8×10^{-4}	107	-	-	0.2
Zn-9	10^{-5}	0.1 Rb^{+}	0.1	2×10^{-5}	7.9	0.1	9.6	0.92(1)	0.68(1)	0.6
Zn-10	10^{-5}	0.1 Rb^{+}	0.1	2×10^{-5}	7.9	0.1	9.6	0.94(1)	0.65(1)	0.6
Zn-11	10^{-6}	0.1 Rb^{+}	0.1	2×10^{-6}	10	0.1	9.6	0.91(1)	0.73(1)	0.6
Zn-12	10^{-6}	0	0	2×10^{-6}	10	1.02×10^{-4}	302	0.90(1)	0.56(1)	0.5
Zn-13	10^{-6}	0	0	2×10^{-6}	10	1.02×10^{-4}	302	0.89(1)	0.65(2)	0.5
Zn-14	10^{-5}	0	0	2×10^{-5}	7.9	3.08×10^{-5}	549	0.92(1)	0.57(2)	0.55
Zn-15	10^{-5}	0	0	2×10^{-5}	7.9	3.08×10^{-5}	549	0.91(1)	0.37(2)	0.3
Zn-16	10^{-5}	0	0	2×10^{-5}	8	3.1×10^{-5}	547	0.97(1)	0.52(2)	0.5
Zn-17	10^{-5}	0	0	2×10^{-5}	8	3.1×10^{-5}	547	0.99(1)	0.39(1)	1.4
Zn-18	10^{-5}	0	0	2×10^{-5}	8	3.1×10^{-5}	547	0.96(1)	0.46(1)	0.5
Zn-19	10^{-5}	0	0	2×10^{-5}	8	3.1×10^{-5}	547	0.97(1)	0.38(1)	1.1
Zn-20	10^{-5}	0.1	0.1	2×10^{-5}	8	0.1	9.6	0.90(1)	0.64(3)	0.20
Zn-21	10^{-5}	0	0	2×10^{-5}	8	3.1×10^{-5}	547	0.88(1)	0.70(3)	0.30
Zn-22	10^{-5}	0	0	2×10^{-5}	8	3.1×10^{-5}	547	0.84(2)	0.45(5)	0.10

Table 3.3. The solution conditions for Sr^{2+} measurements (all concentrations in the unit of mol/kg), the ionic strength S (mol/kg, by assuming the density of solution 1 kg/L, it is equivalent to mol/L), and the calculated Debye length, Λ, (Å) of the EDL diffuse layer. Also listed in the table are the measured coherent positions, P; and coherent fractions, f; and the total-coverage, Θ_{tot} (ML) with the statistical uncertainties from each single measurement.

Label	$[Sr^{2+}]$	$[Na^{+}]$	$[Cl^{-}]$	$[OH^{-}]$	pH	S	Λ (Å)	P	f	Θ_{tot} (ML)
Sr-1	10^{-4}	5×10^{-4}	2×10^{-4}	5×10^{-4}	10.7	8×10^{-4}	107	0.91(1)	0.51(2)	0.6
Sr-2	10^{-4}	5×10^{-4}	2×10^{-4}	5×10^{-4}	10.7	8×10^{-4}	107	0.91(1)	0.62(2)	0.5
Sr-3	10^{-4}	0.01	0.01	5×10^{-4}	10.7	0.01045	30	0.92(1)	0.59(2)	0.6
Sr-4	10^{-4}	0.1	0.1	5×10^{-4}	10.7	0.10045	9.6	0.91(1)	0.65(2)	0.4
Sr-5	10^{-4}	1	1	5×10^{-4}	10.7	1.00045	3.0	0.93(1)	0.74(2)	0.3
Sr-6	10^{-4}	1	1	5×10^{-4}	10.7	1.00045	3.0	0.91(1)	0.74(2)	0.3
Sr-7	10^{-4}	8×10^{-4}	5×10^{-4} Br^{-}	5×10^{-4}	10.7	1.1×10^{-3}	92	0.93(1)	0.66(2)	0.5
Sr-8	10^{-4}	3×10^{-4}	5×10^{-4} Br^{-}	5×10^{-4}	10.7	1.1×10^{-3}	92	0.91(1)	0.37(1)	1.0
Sr-9	10^{-4}	3×10^{-4}	5×10^{-4} Br^{-}	5×10^{-4}	10.7	1.1×10^{-3}	92	0.95(1)	0.31(2)	1.2
Sr-10	10^{-4}	0.0092	0.0092 Br^{-}	5×10^{-4}	10.7	0.0099	30.6	0.91(1)	0.57(1)	0.7
Sr-11	10^{-4}	0.0092	0.0092 Br^{-}	5×10^{-4}	10.7	0.0099	30.6	0.91(1)	0.60(1)	0.7
Sr-12	10^{-4}	0	2×10^{-4}	5×10^{-4}	10.7	8×10^{-4}	108	0.92(1)	0.54(4)	0.3
Sr-13	10^{-4}	0	2×10^{-4}	5×10^{-4}	10.7	8×10^{-4}	108	0.90(2)	0.54(5)	0.4
Sr-14	10^{-4}	0	2×10^{-4}	5×10^{-4}	10.7	8×10^{-4}	108	0.91(1)	0.51(2)	0.6
Sr-15	10^{-4}	0	2×10^{-4}	5×10^{-4}	10.7	8×10^{-4}	108	0.93(1)	0.29(2)	1.1
Sr-16	10^{-4}	0	2×10^{-4}	5×10^{-4}	10.7	8×10^{-4}	108	0.93(1)	0.56(1)	0.7
Sr-17	10^{-4}	0	2×10^{-4}	5×10^{-4}	10.7	8×10^{-4}	108	0.93(1)	0.53(1)	0.8
Sr-18	10^{-4}	0	2×10^{-4}	5×10^{-4}	10.7	8×10^{-4}	108	0.95(1)	0.55(1)	0.8

dependence measurements, the pH and the divalent ion concentration were held constant for all solutions: $[Sr^{2+}] = 10^{-4}$ mol/kg at pH = 10.7 and $[Zn^{2+}] = 10^{-5}$ mol/kg at pH = 8.0. pH was adjusted with NaOH for the Sr^{2+} solutions. For the Zn^{2+} solutions it was controlled by the addition of HTr (Tr^- refers to trifluoromethanesulfonate—$CHF_3O_3S^-$, a synthetic, non-complexing, monovalent anion) and buffered by the addition of Tris(hydroxymethyl)aminomethane (Tris—$NH_2C(CH_2OH)_3$).

Ionic strength was controlled in both cases by the addition of NaCl. Four different concentrations were measured for each ion at [NaCl] = 0, 0.01, 0.1, and 1 mol/kg. Additional measurements were performed to check the sensitivity of the condensed layer ion height to the divalent ion concentration, pH (by using solutions with $[Zn^{2+}] = 10^{-6}$ mol/kg at pH = 10 and $[Zn^{2+}] = 10^{-4}$ mol/kg at pH = 4.3), and background electrolytes (with solutions containing $[NaBr] = 5\times10^{-4}$ mol/kg for both Sr^{2+} and Zn^{2+} measurements; [NaTr] = 0.1 mol/kg and [RbCl] = 0.1 mol/kg for Zn^{2+} measurements). For most of the solutions, we repeated the measurement at least once to test stability and reproducibility of the adsorbed divalent ion heights.

The measurements of cation height as a function of ionic strength were arranged so that the background electrolyte was varied from low to high concentrations whenever the solution change is performed. After the measurements for a specific EDL ion were finished, the sample surface was cleaned by the same injection process with dilute HCl (pH = 3) and deionized water several times each. A fluorescence spectrum was taken at the end of the cleaning process to ensure that there were no divalent ions, either on the surface or in the solution, before the next solution was injected. When subsequent

solutions differed only in background electrolyte concentration, the new solution was introduced simply by flushing it a few times through the cell.

3.2.3 Data taking

The stability of the sample cell and surface composition are monitored by X-ray fluorescence during the course of the measurements. Ti K_α fluorescence from substrate rutile crystal (at 4.5 keV) is strongly attenuated by the solution and Kapton film at the experimental take-off angle of ~ 6°. Consequently the Ti signal is sensitive to the aqueous layer thickness, which in turn affects the fluorescence signal of the metal ions through linear attenuation. Constancy of the Ti signal during each experiment implies that the aqueous layer thickness is stable. The K_α fluorescence of EDL ions (e.g., Sr^{2+}), on the other hand, is sensitive to the total amount of ions in the sample cell (including adsorbed and bulk solution ions, with the latter contribution expected to be proportional to the solution thickness). This provides information about EDL stability, the degree to which ion coverages have equilibrated, and any X-ray beam induced perturbation.

The absolute total coverage of Zn^{2+} was calibrated with a Ga-implanted silicon wafer with a density of 1.2×10^{15} Ga atoms/cm^2 (with additional corrections for different elements such as atomic cross section, fluorescence yield ratio, attenuation through the water layer and detector efficiencies at the specific energies). The Sr^{2+} coverage was calibrated with a Sr implanted silicon wafer with a density of 1×10^{15} Sr atoms/cm^2. Given our experimental cell geometry with an expected ~ 2 μm thick solution layer, the

amount of ions in the bulk solution would be no more than $1.2 \times 10^{13}/cm^2$, i.e., ~ 0.02 ML, which is much smaller than the expected or measured ion coverage in the EDL, normally > 0.2 ML and typically ~ 0.5 ML for the divalent ions (see Table 3.2 and Table 3.3). This suggests that the signal from the bulk solution ions is negligible. Thus the XSW measurements reflect the intrinsic distributions of the EDL ions as opposed to bulk solution ions. The bulk solution thickness is also substantially greater than the Debye length, Λ, in our experiments, which should be less than a few hundred Angstroms. Thus these XSW measurements reflect the EDL distribution at a free surface-solution interface without any complications associated with overlapping diffuse layers.

3.3 Results and discussions

3.3.1 Cation adsorption

For the specifically adsorbed ions Sr^{2+} and Zn^{2+}, the effect of background electrolyte concentration on the adsorbed cation heights was explored first. XSW data in Figure 3.6 show, for the measurements of Zn-1 through Zn-5, measured TiO_2 (110) reflectivity, $R(\theta)$, and Zn^{2+} fluorescence signals, $Y_{Zn}(\theta)$, as a function of the incident angle, $\theta - \theta_b$, where θ_b is the Bragg angle, with the best fit to the data using Equation (2.2). Similar data for Sr^{2+}, i.e., measurements Sr-1 through Sr-5, are plotted in Figure 3.7.

The variation of the nominal ion height, δ_{110} ($= P_{110} * d_{110}$), vs. the solution ionic

strength, *S*, for measurements Zn-1 through Zn-5 and Sr-1 through Sr-5 are summarized in Figure 3.8 (A) and (B), respectively. The ion heights do not change significantly as function of ionic strength over the whole data range. Though there is no apparent trend of δ_{110} vs. *S*, the data are fitted to a functional form, $\delta_{110} = k * ln(S) + \delta_{110}^{0}$. These data are summarized by $k = 0.006 \pm 0.004$ and $\delta_{110}^{0} = 3.00 \pm 0.02$ Å for Sr^{2+}; $k = 0.005 \pm 0.006$ and $\delta_{110}^{0} = 2.98 \pm 0.03$ Å for Zn^{2+}. If we initially assume that there is a single ion adsorption site for each of these ions and that the diffuse layer distribution has no effect on the derived heights (these assumptions will be discussed in more detail later in this chapter), these data can be simply interpreted, and imply that the height of adsorbed Zn^{2+} or Sr^{2+} changes by only $\sim 0.03 \pm 0.06$ Å and $\sim 0.06 \pm 0.06$ Å, respectively, while the background electrolyte concentration in the solution changed by more than 3 orders of magnitude. Given that the statistical uncertainty of an individual measurement is about ± 0.03 Å, (and the systematic error may well be as large as 0.1 Å) this implies that there are no significant changes in the coherent positions of Zn^{2+} and Sr^{2+} ions in our measurements.

Summarizing all the available ion heights data from different and repeated Zn^{2+} and Sr^{2+} measurements, as shown in Figure 3.8 (C) and (D), again, there is no observable trend of δ_{110} vs. *S* other than the fluctuations maybe due to the systematic errors. For Sr^{2+}, all the δ_{110} value falls into the region $\delta_{110} = 3.02 \pm 0.10$ Å, i.e., $P_{110} = 0.93 \pm 0.03$; and for Zn^{2+}, most of the data points also fall into $\delta_{110} = 3.02 \pm 0.10$ Å, i.e., $P_{110} = 0.93 \pm 0.03$.

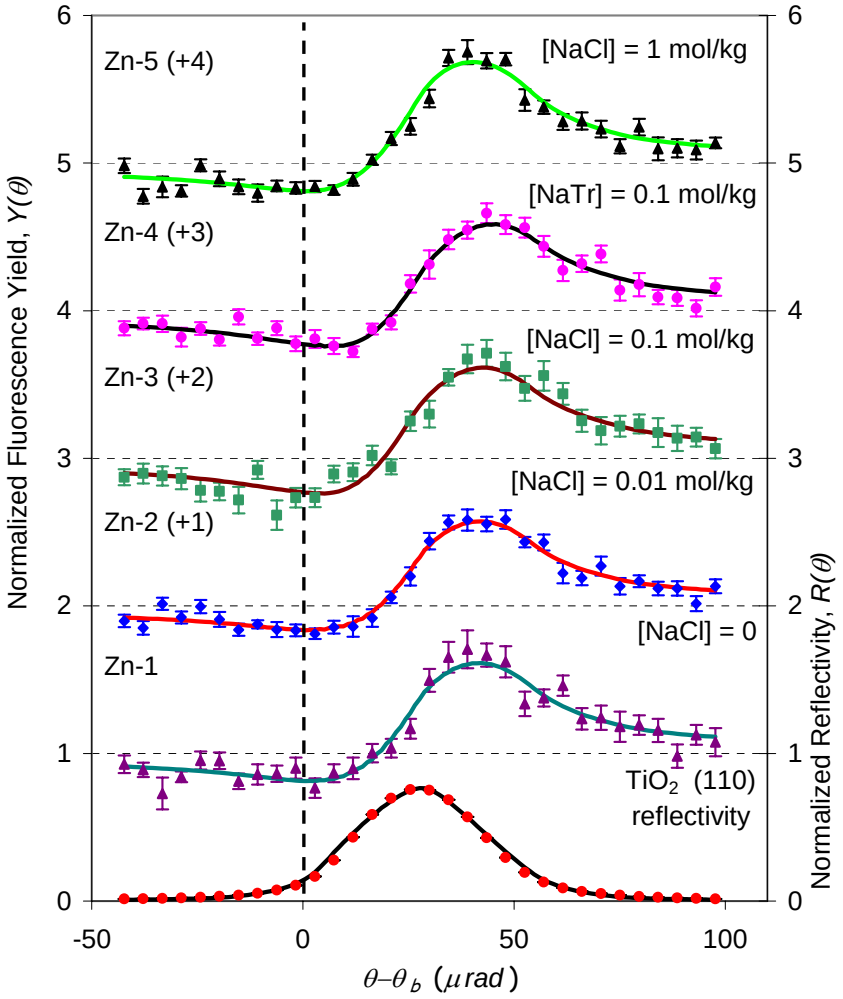

Figure 3.6. XSW measurements of Zn^{2+} ion heights at TiO_2 (110)–aqueous interface at different solution ionic strength *S*. At the bottom is the normalized TiO_2 (110) reflectivity curve. The normalized fluorescence curves are shifted up by integer units, for Zn-2 through Zn-5. The solutions were all controlled at $[Zn^{2+}] = 10^{-5}$ mol/kg and pH = 8 by the addition of HTr and Tris. The electrolyte medium is NaCl in all but one case (Zn-4), where 0.1 mol/kg NaTr instead of 0.1 mol/kg NaCl is used. See Table 3.2 for more details.

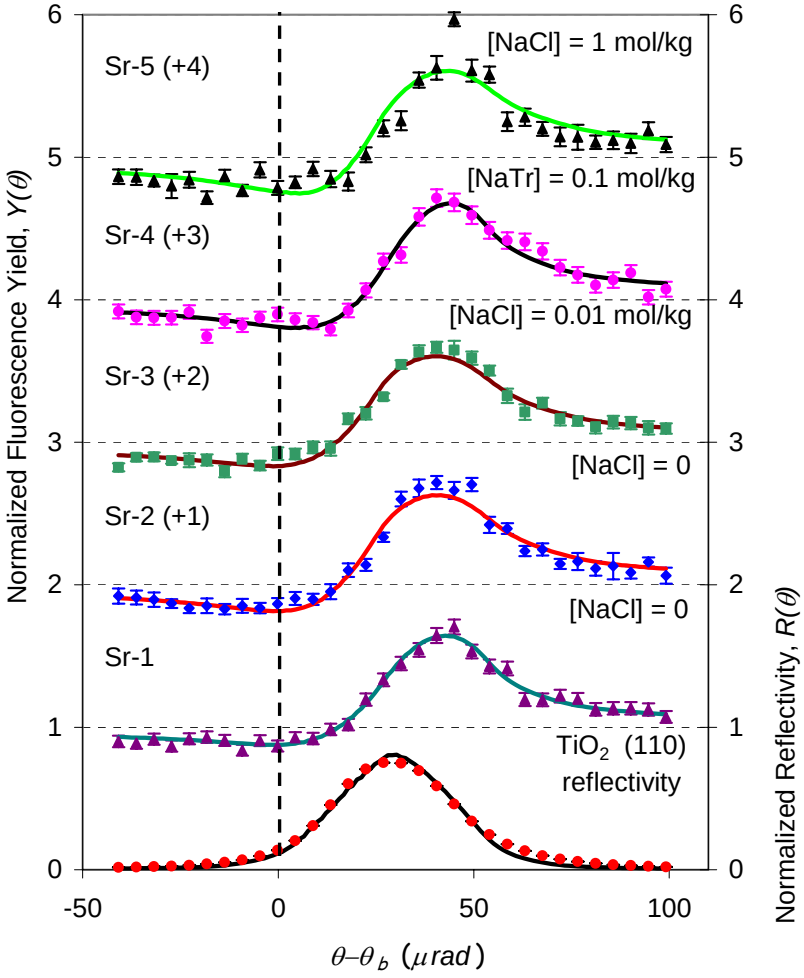

Figure 3.7. XSW measurements of Sr^{2+} ion heights at TiO_2 (110) –aqueous interface at different solution ionic strength *S*. At the bottom is the normalized TiO_2 (110) reflectivity curve. The normalized fluorescence curves are shifted up by integer units for Sr-2 through Sr-5. The solutions were all controlled at $[Sr^{2+}] = 10^{-4}$ mol/kg and pH = 10.7, adjusted by adding NaOH. The electrolyte medium is NaCl in all but one case (Sr-4), where 0.1 mol/kg NaTr instead of 0.1 mol/kg NaCl is used. See Table 3.3 for the detail information about the solutions and results.

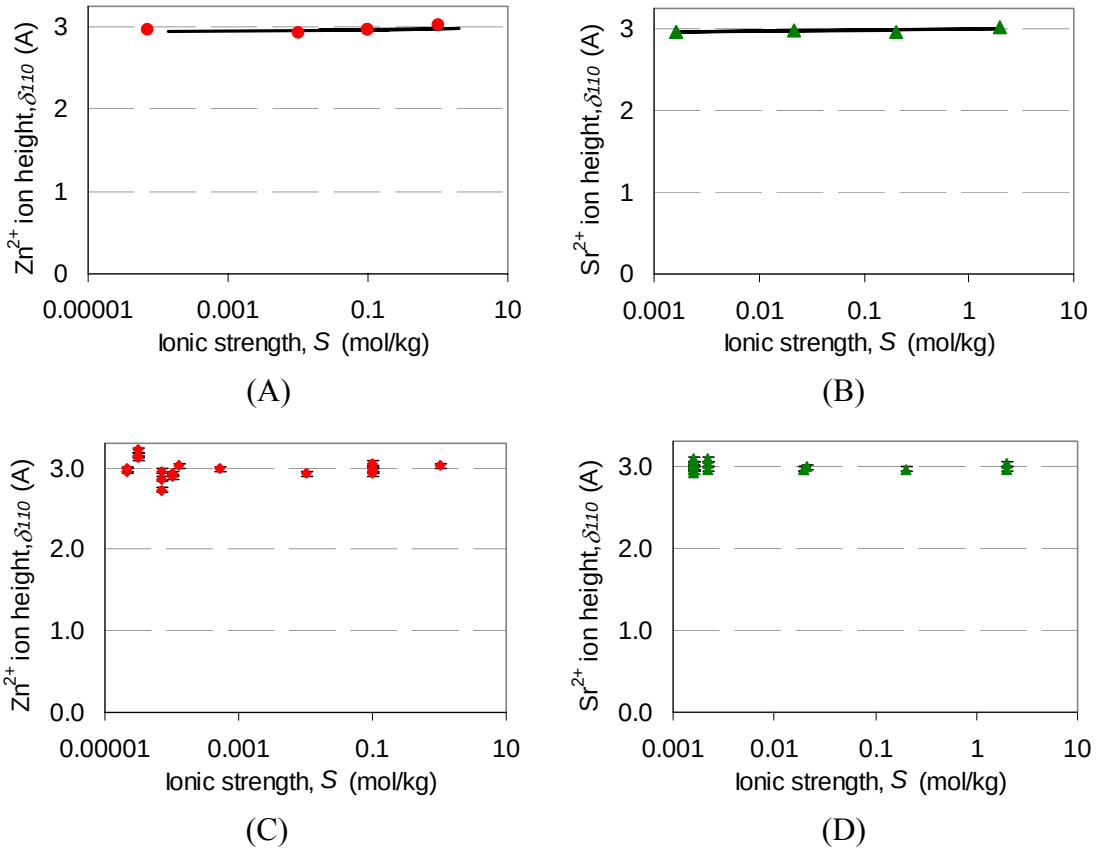

Figure 3.8. The coherently adsorbed ion heights, δ_{110}, vs. the solution ionic strength, S, for (A) Zn^{2+} ion, measurements Zn-1 to Zn-5; and (B) Sr^{2+} ion, Sr-1 to Sr-5. The lines are the fits to the experimentally derived data points with the functional form: $\delta_{110} = k \ln(S) + \delta_{110}^{0}$. For Sr^{2+}: $k = 0.006 \pm 0.004$, and $\delta_{110}^{0} = 3.00 \pm 0.02$ Å. And for Zn^{2+}: $k = 0.005 \pm 0.006$, and $\delta_{110}^{0} = 2.98 \pm 0.03$ Å. All the measurements included, the ion heights for (C) Zn^{2+} and (D) Sr^{2+} are both around 3.0 Å.

Since the EDL ions balance the surface charge leading to electrical neutrality, the surface charge density, the total number of the adsorbed counterions, and the ion distribution should be constant for a given solution condition. It has been suggested that ion adsorbs as the outer-sphere complex at the interface in some cases based on the powder titration data.[107.] If this is true, background electrolyte ions should directly compete with the specifically adsorbed ions (in the condensed layer). Therefore it would be expect to have changes in the ion distribution as a function of ionic strength and/or other solution variables. Such kind of changes would be clearly revealed by the measured coherent fraction, f, which is determined by the spatial distribution of the specifically adsorbed ion, and the EDL ion coverage, which would be controlled by the surface charge and the ratio of the charge of background electrolyte in the diffuse layer to that of the specifically adsorbed condensed layer ions. The prediction from the MUSIC model can be checked against the measurements under the similar conditions. The coherent fractions, f, and the total coverages, Θ_{tot}, of the specifically adsorbed divalent ions are summarized in Figure 3.9. First of all no significant trends vs. ionic strength are found; in stead, the data vary strongly from one measurement to another.

Because the XSW measurement sees all of the ions in the system, the total coverage may not be directly related to the structure of the EDL. Therefore it is improper to compare the measured total ion coverage with the prediction from the MUSIC model. To focus on the EDL ions, or more specifically, the condensed layer ions, a few concepts need to be introduced. The Stern (condensed layer) coverage, Θ_{Stern}, i.e., the density of specific adsorbed ions, can be derived from the product of the ordered fraction parameter,

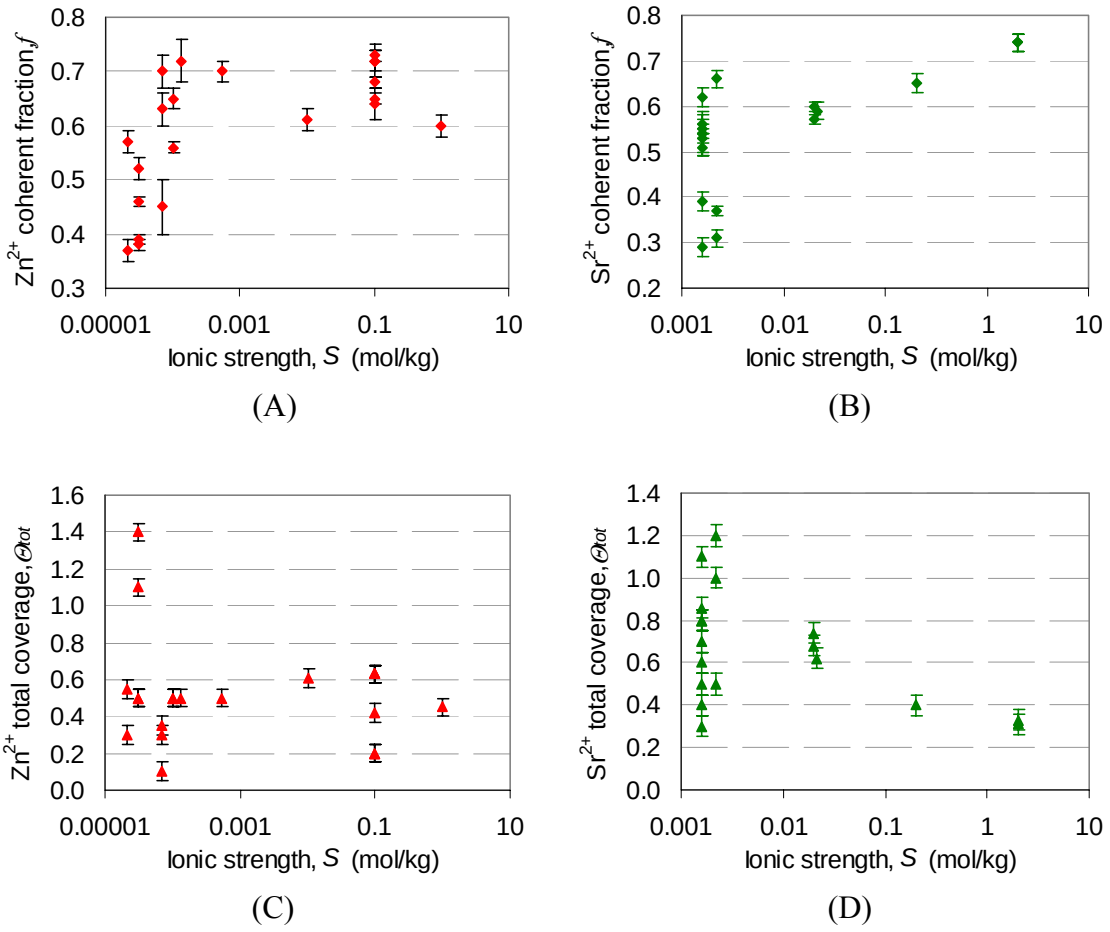

Figure 3.9. Measured coherent fractions, f, and total ion coverages, Θ_{tot}, as function of ionic strength, S, for Zn^{2+} in (A) and (C), and Sr^{2+} in (B) and (D) measurements.

C, and the total coverage, Θ_{tot}, as $\Theta_{Stern} = C * \Theta_{tot}$. Because C is not a directly measurable parameter, coherent coverage, defined as $\Theta_{coh} = f_H * \Theta_{tot}$, is used as an approximation of Θ_{Stern}. This implicitly assumes that $a_H \sim 1$, i.e., there is a single specific adsorption height.

In the case of multiple adsorption sites, i.e., $a_H < 1$, there will be a systematic difference between Θ_{coh} and Θ_{Stern}, such that Θ_{coh} will always be equal to or smaller than Θ_{Stern}. (E.g., in the extreme case where $a_H = 0$, we find that $\Theta_{coh} = 0$ while Θ_{Stern} can be non-zero.) The incoherent coverage, $\Theta_{incoh} = \Theta_{tot} - \Theta_{coh}$, corresponds to all ions not in the Stern layer, including those in the diffuse layer, bulk solution, and precipitates etc. And for XSW method, there is no way to obtain the coverage information for a single 'incoherent' source separately (say, diffuse layer) if all the sources co-exist. So the ion coverage in the diffuse layer is not a directly measurable parameter. However, there is linkage between the diffuse layer coverage and the coherent fraction and therefore limits can be set for the diffuse layer coverage. This will be discussed later in the context of the EDL model.

To probe whether the specifically adsorbed ion height depends upon the Stern-layer coverage, the measured coherent positions, P_{110}, are plotted as a function of coherent coverages, Θ_{coh}, as shown in Figure 3.10 (A) & (B). The coherent positions of Zn^{2+} seem to increase slightly with the coherent coverage. However, the data points shown as yellow squares are those where the pH may be smaller than the nominal value (due to pH = 3 HCl acid flushing through the cell just prior to the measurements). The

data points shown as red triangles are found to have a substantially higher than expected total coverage (> 1.4 ML) and consequently may not be directly comparable to the other data. With these points excluded, the coherent positions are found to be scattered randomly around the value of $P_{110} = 0.93$ for both Sr^{2+} and Zn^{2+} and show no significant trend as a function of coherent coverage.

When compared with the predicted Stern-layer coverage, the measured coverages do not covert to a single number at all. To find out whether there is any general trend about the Stern-layer coverage and whether the distribution of ions between the Stern and diffuse layers depends upon the total coverage, plots of Θ_{coh} vs. Θ_{tot} for both Sr^{2+} and Zn^{2+} are shown for all of our XSW measurements using the rutile (110) Bragg reflection in Figure 3.10 (C) and (D). These plots immediately reveal that both sets of data can be divided into two regions. At low values of Θ_{tot}, Θ_{coh} increases linearly with increasing Θ_{tot}. Above a threshold value, i.e., $\Theta_{tot} \sim 0.6$ ML, Θ_{coh} apparently saturates at Θ^{0}_{coh}. In both cases, we find that $\Theta^{0}_{coh} \sim 0.4$ ML. Since this is a lower limit on the coverage considering that a_{110} may be less than 1, we conclude that the maximum surface adsorption site density for Sr^{2+} and Zn^{2+} is ≥ 0.4 ML ($= 2.2 \times 10^{14}$ /cm^2) at TiO_2 (110)-aqueous interface, in good agreement with the prediction from the MUSIC model as shown in Table 3.1.

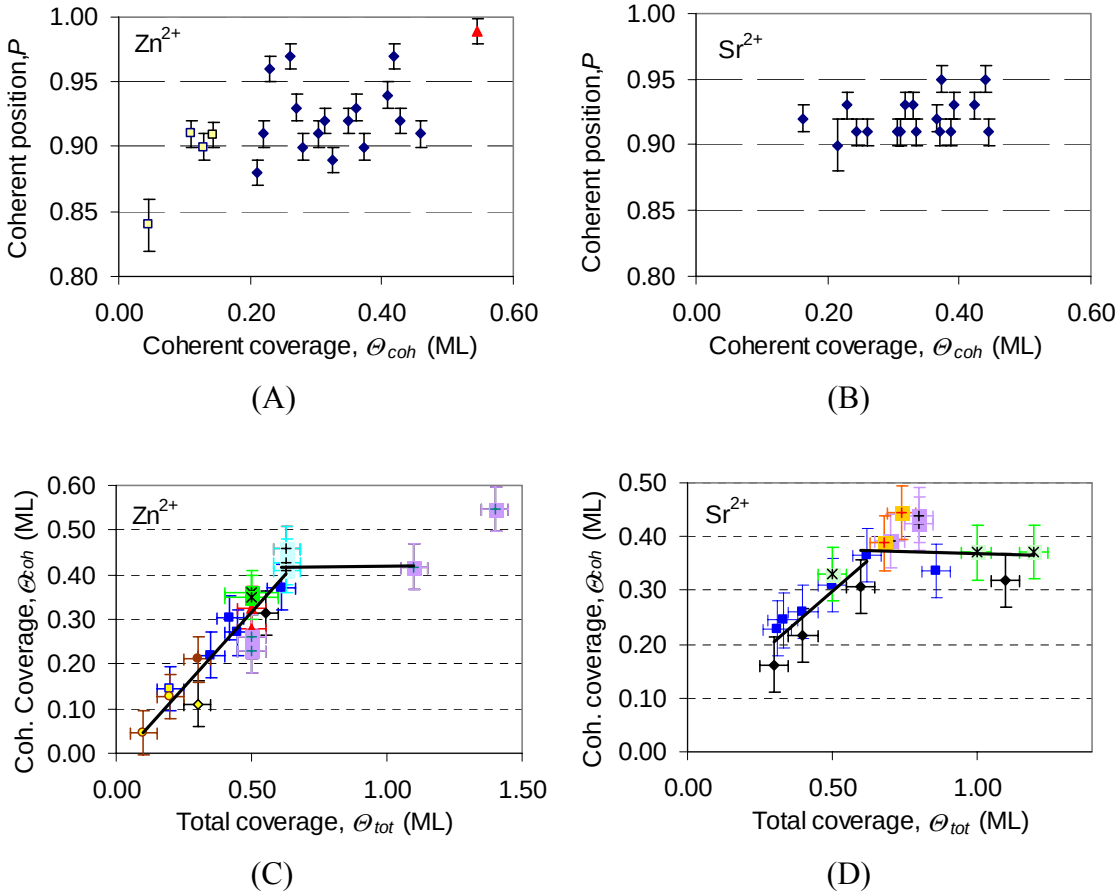

Figure 3.10. Coherent position, P, vs. coherent coverage, Θ_{coh}, for (A) Zn^{2+} and (B) Sr^{2+}; and coherent coverage, Θ_{coh}, vs. total coverage, Θ_{tot}, for (C) Zn^{2+} and (D) Sr^{2+}. For the total coverage and coherent coverage, the uncertainties were assigned to 0.05 ML. It is the typical number, valid in most cases. In (A), the yellow square points are the measurements following the acid flushing through the sample cell thus might be at lower pH. In (C) and (D), different markers indicate the different experiment sets measured, e.g., the blue squares are from the ionic strength dependence measurements and the pink squares with cross inside are from the triangulation measurements (see Chapter 4).

3.3.2 Anion adsorption

A more subtle issue concerns the role of anions in controlling and/or influencing cation adsorption.[111] Anions might form ternary sorption complexes with the multi-valent cations at the interface, e.g., adsorption of $ZnCl^+$ or $ZnCl_2^0$ instead of Zn^{2+} at the rutile water interface. We explored this effect in two ways. First, we searched for changes in the cation height for various background anions (Cl^-, Br^-, and Tr^-) and/or indifferent cations (i.e., Na^+ and Rb^+). There was no observed effect on the height of the specifically adsorbed divalent cations (Table 3.2 and Table 3.3), as was the case with NaCl as a background electrolyte, confirming the similarity of behavior of both Sr^{2+} and Zn^{2+} in the presence of Cl^- and Br^- as anions. Second, we directly probed specific anion adsorption using Br^- as the anion.

We observed during these measurements that the Br^- fluorescence signal, which initially was very low, increased substantially with time. The total coverage of Sr^{2+} and Br^- ions vs. time (at pH = 10.7, $[SrBr_2] = 10^{-4}$ mol/kg, and $[NaBr] = 3\times10^{-4}$ mol/kg), and the bulk Ti signal as a monitor of solution thickness, is shown in Figure 3.11 (A). All three sets of signals were fit to linear trends to monitor the systematic variations. The slightly non-zero slopes are positive and negative for Ti and Sr^{2+}, respectively, which can be explained by a slight (< 10%) reduction in solution thickness during the course of these measurements as estimated from the Ti signal, (the Ti_K_α fluorescence increased by ~ 7% at ~ 5° take-off angle,), and associated increase in the Sr signal. Both coherent positions and coherent fractions of Sr^{2+} are unchanged over these measurements, as

shown in Figure 3.11 (B), indicating that the EDL cation distribution is stable. The slope for Br^- coverage, however, is relatively large, such that the derived Br^- coverage eventually exceeds that of the adsorbed Sr^{2+}. Extrapolating this time variation to zero (when the sample was first exposed to the X-ray beam), we find that the intrinsic Br^- coverage is ~ 0.04 ML, which is approximately the expected value from Br^- ions in the bulk solution. In a short period randomly checking a few different points on the sample surface, we find similar Br signal level, which suggests the change is not localized to the region on which X-ray is shining. Flushing the cell with fresh solution returns the Br signal to its original low level and grows with time following the same trend. The cause of this increasing Br^- signal is not understood at this time, but appears to be due to an X-ray induced perturbation (e.g., due to charge build up on the Kapton window).

Once the Br^- fluorescence signal was strong enough, XSW analysis was carried out. It showed no significant Br^- ordering at the interface, as indicated by the measured coherent fractions for Br that are, within error, equal to zero, as shown in Figure 3.11 (C).

Together, the observations of negligible Br^- coherent fractions and an intrinsic Br^- coverage that is consistent with a bulk Br^- concentration, suggest that under our experiment condition there is no significant Br^- co-adsorption with Sr^{2+} at the rutile (110) interface. The time dependence of the Br^- signal was unlike all the other ions that we studied with XSW (Sr^{2+}, Zn^{2+}, and Y^{3+}--shown later) where the fluorescence signal was typically stable over long periods of time. In some cases (e.g., Zn^{2+}), increases in the ion coverage were observe after extended X-ray beam exposure which we associate with X-ray beam induced precipitation.

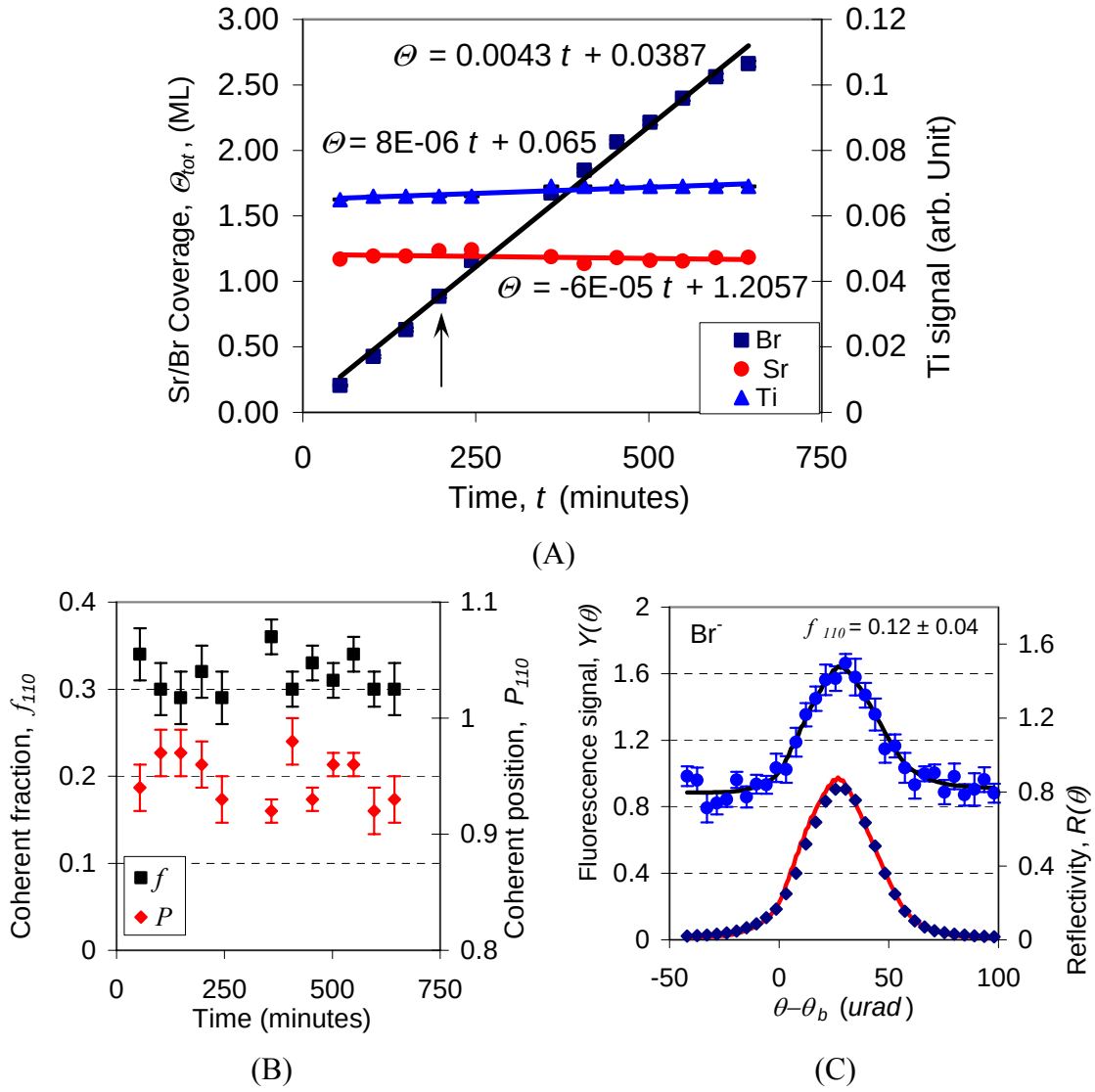

Figure 3.11. (A), The total fluorescence signals of Sr^{2+}, Br^{-}, and Ti in the system as a function of time; (B), The measured coherent positions and coherent fractions of Sr^{2+} as function of time; and (C), The measured Br^{-} fluorescence signal at the TiO_2 (110) Bragg peak at the time marked with the arrow in (A).

3.3.3 Quantitative comparison to EDL model

The observations described above provide a first-order description of changes in ion distributions with solution conditions, but in interpreting these data we have assumed that the measured coherent positions simply reflect the condensed layer ion position. In principle, contributions to the measured values of f_H and P_H from the condensed and diffuse layers and other sources must all be considered with a full EDL model to test these assumptions. We can compare the existing models of the EDL to the experimental data described above. The Bragg XSW coherent position and coherent fraction values can be calculated by Fourier transformation of the model ion distribution profiles $\rho(z)$ with Equation (2.3), and compared to the experimental data to determine the essential elements and the uniqueness of the ion distribution profile.

Here we compare two general EDL models (described previously in section 1.1.2), the Gouy-Chapman (GC) model, as shown in Figure 3.12 (A), and the Gouy-Chapman-Stern (GCS) model, as shown in Figure 3.12 (B). Both models have diffuse ion distributions, with an exponential variation of ion density far from the interface. Near the interface the GCS model has a separate discrete condensed layer while the GC model is assumed to have a saturated ion density with a finite width.

The normalized ion distribution function of GC model is:

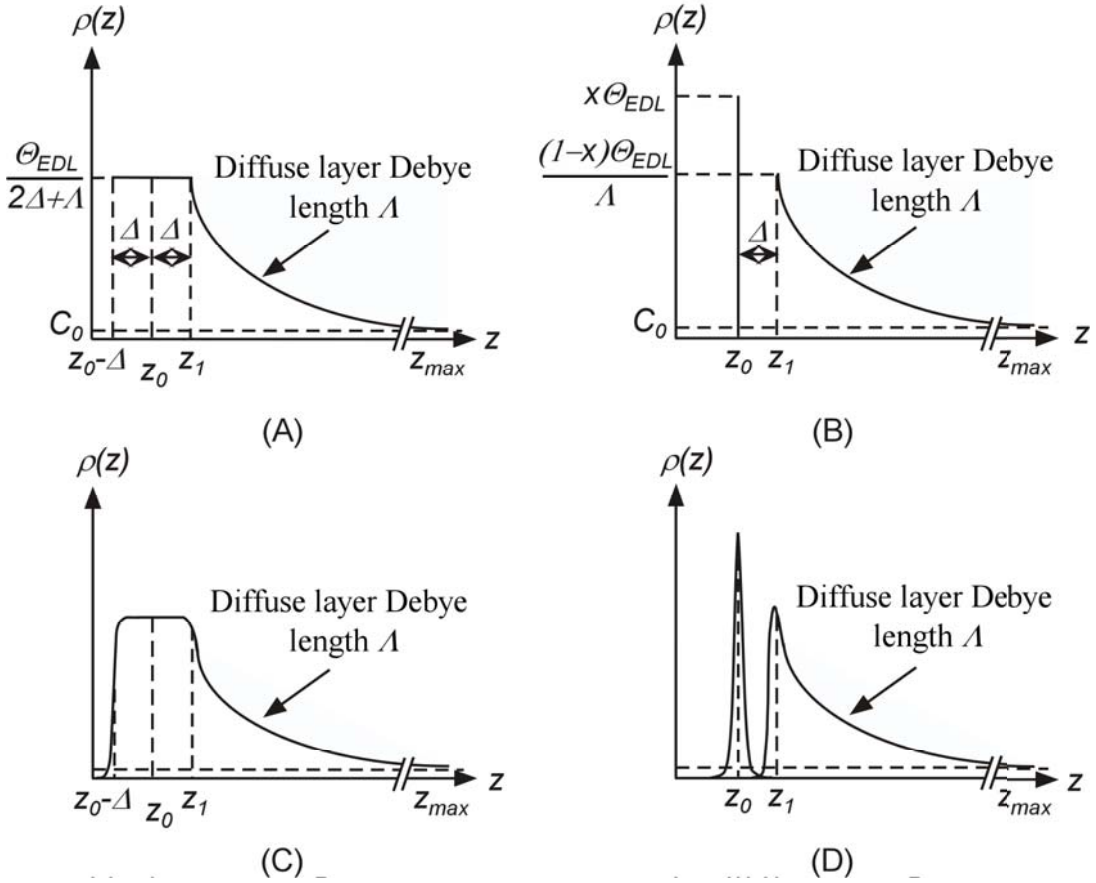

Figure 3.12. Schematic of the EDL ion distribution profile. (A). GC model; (B). GCS model; (C). Gaussian smeared GC model. (D). Gaussian smeared GCS model.

$$\rho_{GC}(z)=\begin{cases}\dfrac{\Theta_{EDL}}{2\Delta+\Lambda} & z_0-\Delta\le z\le z_1\\ \dfrac{\Theta_{EDL}}{2\Delta+\Lambda}\cdot\exp\left[-\dfrac{z-z_1}{\Lambda}\right]+C_0 & z_1<z\le z_{\max}\\ 0 & others\end{cases} \tag{3.1}$$

And the normalized ion distribution function of GCS model is:

$$\rho_{GCS}(z)=\begin{cases}x\Theta_{EDL}\cdot\delta(z-z_0) & 0\le z<z_1\\ \dfrac{(1-x)\Theta_{EDL}}{\Lambda}\cdot\exp\left[-\dfrac{z-z_1}{\Lambda}\right]+C_0 & z_1\le z\le z_{\max}\\ 0 & others\end{cases} \tag{3.2}$$

Where $\Theta_{tot}=\int_0^{\infty}\rho(z)dz=\Theta_{EDL}+C_0\cdot(z_{\max}-z_1)$, is the total amount of the ions in the system; the normalized distribution function is $\rho(z)/\Theta_{tot}$; therefore, the fraction of the ions in the EDL is $c_{EDL}=\Theta_{EDL}/\Theta_{tot}=1-C_0\cdot(z_{\max}-z_1)/\Theta_{tot}\approx 1-c_0\cdot z_{\max}$, which is related to the total surface charge; $c_0 = C_0/\Theta_{tot}$; C_0 is the ion concentration in the bulk solution; x ($0\le x\le 1$) is the partition number of the EDL ions in the condensed layer, i.e., the occupation fractions of the ions in the condensed and diffuse layer are $x\cdot c_{EDL}$ and $(1-x)\cdot c_{EDL}$, respectively; $z_1=z_0+\Delta$, is the starting position of the diffuse layer from the interface, i.e., the so-called d-plane height; z_0 is the center position of the condensed layer, i.e., the so-called β-plane height; Δ is the distance from the d-plane to the β-plane, (for the case of reference 9, $\Delta = 0$); z_{max} is the total thickness of the solution, and Λ is the

Debye length of the diffuse layer. And here $\exp\left[-\frac{z_{\max}-z_1}{\Lambda}\right]=0$ is used, since $z_{\max} >> z_1$ and $z_{\max} >> \Lambda$.

To account for the expected uncertainty of the EDL ion positions, two Gaussian functions with different widths were used to convolute with the functions describing the condensed and diffuse part of EDL, respectively. More realistic distribution profile for GC and GCS can be achieved this way as shown in Figure 3.12 (C) and (D), respectively.

Following Equation (2.3), The Fourier transformations of the ion distributions are:

$$G_{GC}(q)=\frac{c_{EDL}\exp[iqz_0]}{(2\Delta+\Lambda)}\left(\frac{2\sin(q\Delta)}{q}\exp[-\frac{q^2\sigma_C^2}{2}]+\frac{\Lambda\exp[iq\Delta]}{(1-iq\Lambda)}\exp[-\frac{q^2\sigma_D^2}{2}]\right)+G_{bulk}(q) \tag{3.3}$$

$$G_{GCS}(q)=c_{EDL}\exp[iqz_0]\cdot\left(x\cdot\exp[-\frac{q^2\sigma_C^2}{2}]+\frac{(1-x)\exp[iq\Delta]}{(1-iq\Lambda)}\exp[-\frac{q^2\sigma_D^2}{2}]\right)+G_{bulk}(q) \tag{3.4}$$

$$G_{bulk}(q)=\frac{c_0(\exp[iqz_1]-\exp[iqz_{\max}])}{iq}, \tag{3.5}$$

Usually $G_{bulk}(q)$, which represents the contribution of the ions from the bulk solution, has an amplitude orders of magnitude smaller than the other terms.

σ_C and σ_D are the Gaussian function width for condensed and diffuse layer, respectively. Replacing $G(q)$ in Equation (2.3) with Equations (3.3) or (3.4), it can be calculated the coherent fraction, f_H, and the coherent position, P_H, from any arbitrary ion distribution at a given q. For instance, for the GCS model, when $x = 1$, and $c_0 = 0$, which means that all the ions are in the condensed double layer, it is:

$G_{GCS}(q) = \exp[iqz_0]\exp[-\frac{q^2\sigma_c^2}{2}]$. Thus $f_H = |G_{GCS}(q)| = \exp[-\frac{q^2\sigma_c^2}{2}] = D_H$; and

$P_H = q \cdot \frac{z_0}{2\pi} = \frac{2\pi}{d_H} \cdot \frac{P_H d_H}{2\pi}$, where $z_0 = P_H d_H$. It is clear that P_H is a unitless number indicating the height of the condensed layer ions in term of d_H. We thus directly obtained from P_H the condensed layer height: $z_0 = P_H \cdot d_H$, referenced to the projected bulk lattice planes. The Gaussian term, accounting for factors such as the thermal vibration, does not affect the coherent position. And when $x = c_0 = \Delta = 0$, both models give the same diffuse layer only model.

There are potentially other sources of ions in the system not included in the models, such as the precipitation and adsorptions onto the plastic window of the sample cell. These other sources of ions, normally randomly or homogeneously distributed over a broad range, say, from z_{start} to z_{end}, would have contributions similar to what bulk solution ions do. Therefore, strictly speaking, we can generalize the $G_{bulk}(q)$ term to include all the sources of ions other than those in the EDL with a summation, $G_{others}(q) = \sum \frac{c_i(\exp[-iqz_{i\_start}] - \exp[-iqz_{i\_end}])}{iq}$, where c_i, z_{i_start}, and z_{i_end} are the fractional occupation, the start and the end positions of the distribution range for the i^{th} source, respectively. Specifically, for the bulk solution part discussed above, $c_i = c_0$, $z_{i\_start} = z_1$, and $z_{i\_end} = z_{max}$. Given the similarity of contribution from these sources, it is safe to consider them all as bulk solution ions, with the equivalent bulk concentration as

$c_0^e = \frac{\sum c_i \left(z_{i\_end} - z_{i\_start} \right)}{\left(z_{\max} - z_1 \right)}$ (and hereafter, c_0 in the text refers to c_0^e). Considering the periodic character of the exponential term, i.e., $\exp[i(qz \pm 2\pi)] = \exp[iqz]$, and the fact that normally $z_{i\_end} >> z_{i\_start}$, it can also be approximated that $\exp[iqz_{i\_start}] = \exp[iqz_{i\_end}]$, i.e., $G_{others}(q) = 0$. This demonstrates that the randomly distributed sources do not have any contribution to the phase of the Fourier transformation, i.e., the coherent position, P_H. They do, however, reduce the amplitude of the Fourier transformation, i.e., the coherent fraction, f_H, by reducing c_{EDL} as c_0 increases for a given EDL system.

The coherent fraction f_H and coherent position P_H are calculated as the function of the fraction of EDL ions in the condensed layer, x, and the diffuse layer Debye length, Λ, for both models. It is assumed in the calculation that the amount of ions in the EDL is 10 times as large as that in the bulk solution, i.e., $c_0 \cdot (z_{\max} - z_1) = c_{EDL} / 10$, ($c_{EDL}$ = 0.91,) which is the upper limit of the amount of ions from the bulk solution under our experimental conditions assuming no other sources of ions present. Typical values of z_{max} = 2 μm, z_0 = 3.0 Å, and Δ = 2.0 Å are used. Based on the total ion concentration, the Debye length of the diffuse layer Λ is estimated between 3 and 600 Å and a few representative values, 4, 24, 70, and 104 Å, are picked for the simulations. The Gaussian distribution widths are set as 0.1 and 1 Å for ions in condensed and diffuse layer, respectively, which are based on the typical number of vibration amplitude of the ions in the bulk rutile crystal (< 0.1 Å) [112] and for water molecules near an interface (~ 1 Å).[40,73]

The calculated coherent fraction as a function of the condensed layer ion partition number for both GC and GCS models at different Debye lengths are plotted in Figure 3.13 (A) and (B). For all the simulations, z_{max} = 2 μm, z_0 = 3 Å, and Δ = 2 Å except for GCS5, where Δ = 2.5 Å; c_{EDL} = 0.91 except for GCS4, where c_{EDL} = 0.5; Λ = 4 Å for GCS1 and GC1, Λ = 24 Å for GCS2, Λ = 137 Å for GCS3, Λ = 104 Å for GCS4 and GCS5, and Λ = 70 Å for GC2. The GC model, which predicts almost zero coherent fractions all the time, does not describe the divalent ion distribution at TiO_2 (110) aqueous interface properly since we observed much higher coherent fractions in all the measurements. For instance, for the Sr^{2+} solution with [NaCl] = 0.01 mol/kg, the measured coherent fraction f_H = 0.59. But according to the calculation with GC model, for the expected condition of Λ = 30 Å, the coherent fraction would be ~ 0 for any value of condensed layer occupation.

On the other hand, the GCS model provides a reasonable explanation for the measured coherent fraction data. This proves that under our experimental conditions, the divalent ions form a condensed layer with a well defined position at rutile (110)-aqueous interface. Consequently we focus on GCS model hereafter. The calculated coherent fractions for different values of Λ are indistinguishable. They are falling exactly on the same line when all the other parameters are the same. Thus it is clear that the coherent fraction is independent of the diffuse double layer Debye length Λ (as expected since the period of the Bragg X-ray standing wave field is substantially smaller than the Debye length). Instead it is determined primarily by the partitioning of ions in the condensed

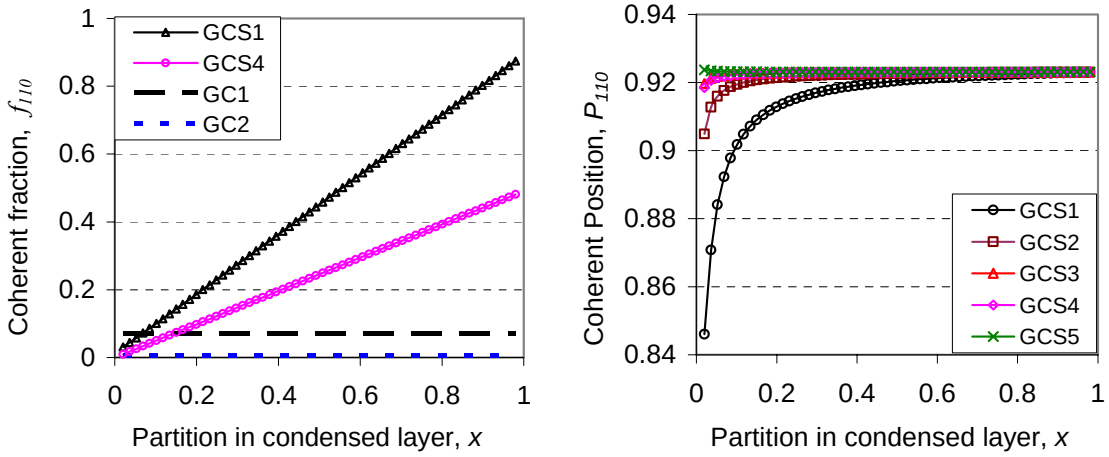

(A) (B)

Figure 3.13. Simulated (A) coherent fraction, f_{110}, and (B) coherent position, P_{110}, as function of the partitioning of the ions in the condensed layer, x, with GC (1 - 2, dashed lines) and GCS (1 - 5, lines + markers) models, respectively. For all the simulations, z_{max} = 2 μm, z_0 = 3 Å, and Δ = 2 Å except for GCS5, where Δ = 2.5 Å; c_{EDL} = 0.91 except for GCS4, where c_{EDL} = 0.5; Λ = 4 Å for GCS1 and GC1, Λ = 24 Å for GCS2, Λ = 137 Å for GCS3, Λ = 104 Å for GCS4, GCS5 and Λ = 70 Å for GC2.

layer, x. Similarly, the coherent fraction is found largely independent of the other two parameters that describe the diffuse layer: the distance between the d-plane and the β-plane, Δ, and the ion concentration in solution, C_0. In our experiments, the coherent fractions are typically in the range of 0.5 to 0.75. Thus we can estimate that the fraction of the EDL ions in the condensed layer must be higher than 0.5. Under these circumstances, it is predicted that the calculated coherent position is independent of x, Δ, C_0 and Λ, and is solely determined by the height of the condensed layer ions, z_0. Also the effect of the diffuse layer ion on the coherent position (< 0.01 Å) is well below our sensitivity (0.02 Å). Only in the case that the coherent fraction is very low and the Debye length is very short will the coherent positions deviate from the typical value determined by z_0. According to our measured solution conditions, this scenario is not relevant for the present measurements of divalent ions Zn^{2+} or Sr^{2+} adsorbed at the rutile (110)-aqueous interface. This directly implies that the divalent condensed layer ions are specifically bound to the rutile surface with a location that is precisely defined, presumably through metal-oxygen coordination with the rutile surface oxygen sites. For a weakly bound adsorbate such as Rb^+, the diffuse ions are dominant (e.g., $x < 0.1$) under similar conditions (e.g., [Rb] < 10^{-3} mol/kg). In such case, the coherent fraction will be ~ 0 for most cases, as observed in our measurements, shown in Figure 2.4 (B). The MUSIC model gives the same predictions for the specifically adsorbed ion, i.e., the divalent ions predominantly reside in the condensed layer, while mono-valent ion is primarily in the diffuse layer.

According to the calculations above, the coherent fraction is close to the fraction

of all ions that are found in the condensed layer, $x \cdot c_{EDL}$. The contributions from the ions in diffuse layer $(1 - x) \cdot c_{EDL}$ and other sources $c_0 \cdot (z_{\max} - z_1)$, (again including the bulk solution ions and any other sources,) are indistinguishable based on the coherent position and coherent fraction from a single measurement. Both have no effect on the coherent positions and only add to the incoherent fraction of the total ions. To understand the source of the incoherent ions, we must look at the variation of the coherent fraction with solution parameters. If the incoherent ions are primarily in the diffuse layer, due to the competition from the background electrolyte, the total amount of ions should decrease when the background electrolyte concentration increases significantly. For instance, in the solution where $[Zn^{2+}] = 10^{-5}$ mol/kg and $[Na^{+}] = 1$ mol/kg, Zn^{2+} ions should be out competed in the diffuse layer since the Na^{+} ions are overwhelmingly abundant in the solution, while the amount of Zn^{2+} ions would not change in the condensed layer. Therefore, as predicted in Figure 3.13 (A), as ionic strength increases, which is equivalent to increasing the partition of Zn^{2+} in the condensed layer, the coherent fraction would go higher. This is not the case, however, for the measured coherent fractions, as in Figure 3.9 (A) and (B), no systematic trend versus the solution ionic strength is observed. This indicates that the incoherent ions are not primarily from the diffuse layer but some other sources, (e.g., precipitates). This observation also implies that the divalent condensed layer ions compensate most or all of the surface charges. Because of lack of the quantitative data about the diffuse layer coverage, no detailed comparison can be directly made. But this suggests that the predictions from the MUSIC model, which gives minimal diffuse layer divalent ion coverages, are consistent with experimental data.

The discussion above assumed that the condensed layer ions have a single height, which is not always the case. For instance, in the XSW triangulation of Sr^{2+} and Zn^{2+} at rutile (110) aqueous interface (see Chapter 4 for details), we found a single Sr^{2+} height, but two substantially different Zn^{2+} heights, with the predominant species at a height of 3.16 ± 0.14 Å above the surface Ti-O plane (with > 75% of Stern layer Zn^{2+}) and the other minor species at a height of 2.70 ± 0.25 Å (with < 25% of Stern layer Zn^{2+}).[100] In this case, the measured coherent position is not only affected by the heights of each of the multiple positions, but also the partitioning of the ions between those positions.

Since it is already known that the diffuse layer has little contribution to the measured coherent position at our experiment condition, it will be ignored when investigating the case where the condensed layer ions have multiple heights. For simplicity, it is assumed that the distributions of ions are a series of δ-functions at different heights convoluted with a normalized Gaussian distribution. The inverse Fourier transformation of that would be:

$$\begin{aligned} \boldsymbol{G}_m(q) &= \mathscr{F}(\rho(z)) = \int_{-\infty}^{+\infty} \left\{ \sum_i c_i \cdot \delta(z - z_i) \otimes \frac{1}{\sigma_i \sqrt{2\pi}} \exp\left[-\frac{z^2}{2\sigma_i^2} \right] \right\} \exp[iqz] dz \\ &= \sum_i c_i \exp[iqz_i] \exp\left[-\frac{q^2 \sigma_i^2}{2} \right] \end{aligned} \tag{3.6}$$

Here c_i and σ_i are the partitioning and the Gaussian distribution width of the ions at the height z_i, respectively. Assuming that all the condensed layer ions have the same Gaussian distribution width, $\sigma_i = \sigma_c$, the inverse Fourier transformation of the ion distribution with two heights is given as:

$$\boldsymbol{G}_m(q) = (c_1 \exp[iqz_1] + c_2 \exp[iqz_2]) \exp\left[-\frac{q^2\sigma_c^2}{2}\right] \tag{3.7}$$

instead of the form

$$\boldsymbol{G}_s(q) = (c_1 + c_2) \exp[iqz_0] \exp\left[-\frac{q^2\sigma_c^2}{2}\right] \tag{3.8}$$

which is appropriate for a single ion height distribution. For Zn^{2+} adsorbed at the rutile (110) aqueous interface, the two ion heights were observed at z_1 = 3.1 Å, and z_2 = 2.7 Å. The coherent fractions and positions calculated with both models are shown in Figure 3.14 (A) and (B), respectively. Here the parameters used: $c_1+c_2 = 1 - n$, n represents the fractional occupation of the incoherent ions in the system, where $n = 0$ means that all ions are in the condensed layer and $n = 0.5$ means that half of the ions are in the condensed layer; σ_c = 0.1 Å, and for the one height model z_0 = 3.0 Å.

The calculated coherent fractions from the two-height model are always lower than those from the one-height one, but the difference is less than 10%. This means that the actual Stern coverage in the two-height case is higher by ~ 10% than the number derived from the measured coherent fractions assuming the single ion height model. And again clearly shown in Figure 3.14, changes in the degree of partitioning of ions between the condensed layer and other sources only affects the coherent fractions, but not the coherent positions.

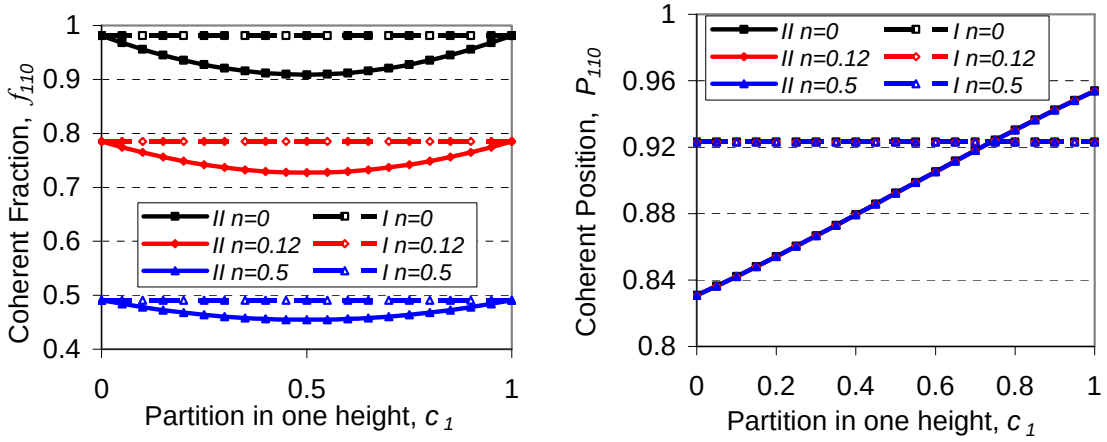

(A) (B)

Figure 3.14. Simulated (A) coherent fractions, f_{110}, and (B) coherent positions, P_{110}, as function of the fractional occupation of the ions at the height z_1 = 3.1 Å, c_1, with one-height (*I*, dashed lines and open markers) and two-height (*II*, solid lines and filled markers) model. Parameters used in the simulations (see text for the meanings): z_{max} = 2 μm, z_0 = 3.0 Å, Δ = 2.8 Å. σ_c = 0.1 Å, and the partition of the incoherent ions n = 0, n = 0.12 and n = 0.5. Note in (B), for n = 0, 0.12 and 0.5, the exactly same calculated coherent positions are achieved for each model.

Diffuse layer and bulk solution ions included, the earlier discussions about the GC and GCS model remain valid when Zn^{2+} ions have two heights, only with more parameters to be taken into consideration when calculating the coherent fraction and position. Knowing the fact that the Sr^{2+} ions are found at a single height at the interface that is fixed over a wide range of solution conditions, it is reasonable to assume that both of the Zn^{2+} heights would also be fixed. Therefore the only parameter that is likely to vary with solution conditions is the ion partitioning between the two heights. That leads us to two possible scenarios as Stern coverage changes: the ratio is fixed and the coherent position is constant (this is similar to the one height case as the weighted average ion position is constant). Or the ratio is sensitive to the condensed layer coverage and the coherent position might vary with the Stern coverage, e.g., due to preferential adsorption to one site at low/high coverage, as the calculations shows in the Figure 3.14 (B). In Figure 3.10 (A), accepting all the data points, it seems that there is a slightly trend in which the coherent positions follows the predicted height from the two-height model. However, it is not clear whether there is a partitioning change when the coherent coverage changes. Combined with the fact that the measured coherent positions that deviated from the averaged value 0.93 ± 0.03 are all from the measurements where the solution conditions are not well controlled, the trend here is not significant enough to neither prove nor disprove either of the possibility. For instance, the residue from the pH ~ 3 acid solution might saturate the buffer in the solution so that the actual pH is lower than its nominal value. These changes in the measured heights on those a few points could be due to the different adsorption sites or heights which are occurred at the

different solution condition. Since we don't have the systematic measurements at pH lower than 8, we can not rule out this possibility. More well-controlled measurements are needed to clarify this issue. (The latest measurements at pH = 6 yield lower total and coherent coverage of Zn^{2+} but no significant difference in adsorption sites.)

The interpretation of the coverage data depends in part upon the nature of the incoherent coverage. When the total coverage, Θ_{tot}, is below the saturation point, the amount of Stern-layer ions increases as more ions is available from the solution. In this region, the rutile surface may be exposed to an insufficient number of adsorbates so that there are still available surface adsorption sites. In the high total coverage region, however, saturated coherent coverage suggests that all the available surface sites have been taken. If additional ions incorporate into the condensed layer, we would observe either a higher coherent coverage or a different coherent position due to any change in the adsorption sites. Neither of the above has been observed. And we already know that there are little if any divalent ions either in the diffuse double layer or in the bulk solution. This leads us to believe that the incoherent ion coverage is not intrinsic to the EDL. The extrinsic sources of incoherent ion coverage include: surface and/or solution precipitates, and/or adsorption on the Kapton window, and/or adsorption to the surface defect sites (such as step edges). Therefore the saturation coherent coverage represents surface associated ions and should be directly related to the total surface charge. For Zn^{2+} and Sr^{2+}we find within error the same coverage of ~ 0.4 ML. Given the geometrical factor for Zn^{2+}, the actual Zn^{2+} Stern coverage could be 10% higher than the derived coherent coverage, i.e., ~ 0.45 ML. The data also implies that the rutile (110) surface charge is

fully compensated by the divalent ions at these solution conditions.

The prediction of the Stern layer ion coverage for Zn^{2+} and Sr^{2+} ions with the MUSIC model is shown together with the measured values as function of the ionic strength, *S*, in Figure 3.15. It is only meaningful to compare the predicted Stern coverage with the saturated coherent coverage. Therefore those points with the saturated coherent coverages are marked with circles and should be the ones to focus on. Though there is no clear trend of the measured data, it is notable that they are of similar value to the predictions in absolute units.

The saturated coherent coverage can only be achieved over a series of measurements. And there are not enough measurements to judge whether the derived coherent coverage reaches the saturated region at any different values of the ionic strength. But the values obtained should, at minimum, be useful as a lower limit of the Stern layer ion coverage.

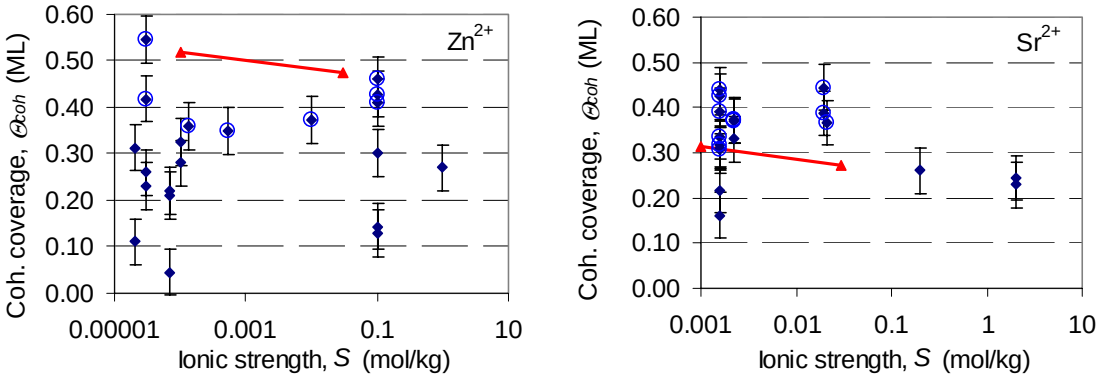

(A) (B)

Figure 3.15. Coherent coverage, Θ_{coh}, vs. ionic strength, S, for (A) Zn^{2+} and (B) Sr^{2+} from the XSW measurements (♦ with the errorbars). Predictions of the MUSIC model are shown as the line with the markers (—▲—). The circle (O) indicates the data points actually fall onto the saturated plateau region in Figure 3.10 (C) and (D).

3.4 Conclusions

Our results provide direct measurement of condensed layer position, and show for the first time that condensed layer position of divalent ions at rutile (110)-aqueous interface is essentially independent of solution conditions even with large changes in ionic strength (spanning 3 orders of magnitude). We find that the presence of other monovalent ions (Cl^-, Br^-, Tr^-, or Rb^+) has little effect on the condensed layer divalent cation positions. We also find negligible amount of divalent ions in the diffuse layer at the rutile (110)-aqueous interface, which suggests the surface charges are mostly compensated by the condensed layer ions. There may be other sources of ions in the system than from the EDL and bulk solution, such as ions adsorbed onto the plastic, and surface and/or solution precipitates. These ions, however, have little effect on the coherent positions, only affecting the measured coherent fractions. The present results provide direct proof that the GCS model is suitable for describing the divalent ions at TiO_2 (110) aqueous interface according to our Bragg XSW measurements.

As we can see from these data and the simulations, the significant amount of incoherently adsorbed ion (presumably some form of precipitation) does not have a measurable effect on the positions we derived from the XSW measurements. This is one great advantage of XSW over EXAFS method, for which the dominant signal from the sources other than the EDL could lead to a result that is not specific to the surface adsorbate. Also most of our measurements are actually done in the region close to, but

lower than, the surface saturation coverage, which is optimal for XSW measurements.

The predictions of the Stern layer ion coverages from the MUSIC model agree well with out measured results in absolute units, which provide independent support for the model. Previously, the model could only be checked with the macroscopic properties. Now a direct link between macroscopic models and the microscopic structures has been established, and a new way to explore EDL phenomena by combining these approaches is open.

There are a few questions remain to be answered. (1) For Zn^{2+} adsorbed onto the rutile (110) surface, is there any preferential adsorption between the two Stern layer heights over the pH range? Out current data are not definitive enough to answer the question. (2) What is the form associated with the incoherently adsorbed species (precipitation, complexes or free ions)? Where do they reside (in solution or on the crystal surface)? And how do they form? Our observations suggest that they appear when flushing the sample with excess solution. Once the excess solution removed from the cell, the system is stable, i.e., no change in the coverage or the distribution of the ions. The only exception of this is the triangulation measurements for Zn^{2+}. We started with the total coverage of ~ 0.5 ML and ended with ~ 1.4 ML over a period about 12 hours. During this time, however, the measured coherent positions did not change.

Chapter 4 Probing condensed layer ion locations with XSW

4.1 Purpose of the work

Direct knowledge of the condensed layer ion heights above the oxide surface and their coverages removes a key uncertainty in understanding EDL phenomena. When those parameters are fixed, the electrostatic potential near the oxide-aqueous interface can be more precisely predicted. Under such circumstances, the other contribution to the interfacial energy that is central to understanding EDL phenomena, the chemical potential, can be understood. In term of the structure, the most important aspect is the ion adsorption geometry. The precise adsorption site of the adsorbate can reveal the exact chemical adsorption process at the interface, thus giving the correct chemical potential information.

Previous efforts to reveal ion adsorption sites at the mineral-water interface have been performed mainly with the EXAFS method in the past decade. Initial measurements studied oxide powders in contact with electrolyte solutions,[61,66] and recently has been extended to measurements of the single crystal-aqueous interface,[63,64,65] where the surface atomic scale structure is better defined. EXAFS is a powerful tool for probing the local structure, such as the coordination number and the bond length of neighboring atoms to a center atom. But sources other than from the directly adsorbed atoms exist or can even dominate.[64.] It is difficult for EXAFS measurements to distinguish whether the signal directly corresponds to a surface adsorbed species or to a process other than adsorption

(i.e., precipitation). Also the data analysis for EXAFS is not simple and direct, and consequently great care must be given to potentially complex structures that may be present during surface adsorption. Therefore a direct, model independent structure probing method would be of great help. This is not only true for probing the EDL structure at oxide-aqueous interface, but could also be useful for any foreign species at the surface, interface and even as impurities in bulk lattice in the sense of structure probing.

To date the ability to *directly* observe cation adsorption sites at the oxide-liquid interface is strongly limited. The development of holographic techniques in recent years has garnered broad interest with their ability to provide model-independent images of atomic structures.[113,114,115] Yet existing holographic techniques have characteristics that make them inappropriate for imaging atomic distributions at the solid-liquid interface: electron holographies cannot probe the solid-liquid interfaces and X-ray holographies do not have yet the sensitivity to probe interfacial structures. Even the more widely used scanning probe microscopies are limited for systems having non-conducting substrates and lack elemental specificity.[116]

XSW method, as described in Chapter 2, measures both the amplitudes and the phases of the Fourier components at given momentum transfers. Recently, the direct construction of the element site density profile based on a full set of XSW measurements has been shown to work very well.[98.] Here we apply this "X-ray standing wave imaging" approach to directly determine the EDL condensed layer ion locations at the rutile (110)-aqueous interface.

4.2 Experimental details

The experiments were carried out at 12IDD, BESSRC-CAT, APS, ANL. The beamline optics is setup the same way as that shown in Figure 3.2. The high heat load Si (111) monochromator is tuned at 80% of the peak intensity (i.e., 20% detuned). One set of Si channel cut is used as post-monochromator to collimate and match the incident beam dispersion to the selected Bragg reflections. Si (111) channel cut is used for (110) rutile reflection. And for all the other Bragg reflections measured for the rutile crystal, including (101), (200), (111), and (211), Si (220) channel cut is used. The energy of incident beam is chosen to be 17.96, 17.5 and 10.92 keV for Y^{3+}, Sr^{2+} and Zn^{2+}, respectively to optimize fluorescent signals. The experimental details are listed in Table 4.1. X-ray fluorescence spectra were collected with a germanium solid-state detector, and corrected for dead-time (see Appendix A for details).

Solution conditions for the XSW triangulation measurements are: 10.49×10^{-6} mol/kg $ZnTr_2$ at pH = 8.0 [with 156.2×10^{-6} mol/kg HTr, and buffered by the addition of Tris], 104.4×10^{-6} mol/kg $SrCl_2$ at pH = 10.7 (with 530×10^{-6} mol/kg NaOH), and 11.2×10^{-6} mol/kg $Y(NO_3)_3$ at pH = 6.11 (88×10^{-6} mol/kg HTr with pH adjusted by addition of Tris).

The same sample preparation and measurement procedures are followed for the rutile crystal with atomic scale flat (110) surface, as stated in Chapter 3. The coverage of Y^{3+} ions is calibrated with the Sr implanted Si standard. And for each of the off-normal

reflection measurement, it is necessary to search around for a spot satisfying the criteria mentioned in last chapter, i.e., the rocking curve width (FWHM) and the peak reflectivity (R) are close to the calculations (Darwin width ω, and absolute reflectivity R_0) based on the dynamical diffraction theory including the dispersion from the optics—typically FWHM < 1.5ω and $R > 0.7 * R_0$ are desired. The fluorescence detector is always fixed along the polarization direction to minimize the elastic and Compton scattering signals.

4.3 Results and discussions

4.3.1 Measured X-ray fluorescence spectrum

Plotted in the Figure 4.1 is a typical X-ray fluorescence spectrum measured with a Solid State Detector (SSD). This one was actually collected on a clean TiO_2 sample sealed in DIW before any ion adsorption counting for ~ 300 seconds. Starting from the lowest energy, i.e., the left side of the figure, in order the peaks are: Al, coming from the Al-foil put in front of the detector Be window to cut down the Ti signal from rutile crystal; pulser, the electronic pulse simulate the real X-ray pulse generated by a random pulse generator, for the purpose of dead time correction (see Appendix A for details); Ar, from Ar in air; Ti_K_α and Ti_K_β, coming from the bulk rutile crystal; Fe_K_α, Fe_K_β and Ni_K_α, coming from the surrounding metal parts, such as the screws on the sample holder; Cu_K_α (and Cu_K_β), coming from the Cu supporting mesh inside the detector; Zn_K_α (and Zn_K_β), coming from the environment, presumably as impurity in the Cu

mesh; Thermal Diffuse Scattering (TDS) and Compton peak, from the elastic and inelastic scattered incident beam. The count rate for Zn_K_α here is only a few counts per second. After exposure to the solution, the sub-monolayer coverage of Zn^{2+} ions adsorbed at the TiO_2 (110) surface produce a yield > 100 counts per second for the exact same setup.

4.3.2 Measured coherent fractions and positions from XSW

The measured reflectivity, $R(\theta)$, and the Sr^{2+} fluorescence yield, $Y(\theta)$, (shown as the points,) together with the best fits to the data (shown as the lines), for rutile Bragg reflections (110), (101), (200), (111), and (211), are plotted as function of rocking angle, $\theta - \theta_b$, in Figure 4.2 (A)-(E), respectively. Similar results are shown for Y^{3+} in Figure 4.3 (A)-(D), where (101) reflection is absent, and for Zn^{2+} in Figure 4.4 (A)-(E). The measured coherent fractions and coherent positions are summarized in Table 4.1.

Also listed in Table 4.1 are the measured coherent positions and coherent fractions for Ti atoms in the bulk crystal during the Zn^{2+} measurements. Note that for the Ti signal, a very strong extinction effect shows up at each Bragg peak. Therefore although the statistic error is really small for the measured coherent fractions and coherent positions, they are greatly affected, especially for the coherent fractions, by the exiting angle of the fluorescence photon reaching the detector, which can be fine tuned during the data analysis. As the result, the actual systematic error for Ti signal could be much larger. However, to the first order, the measured Ti coherent positions and

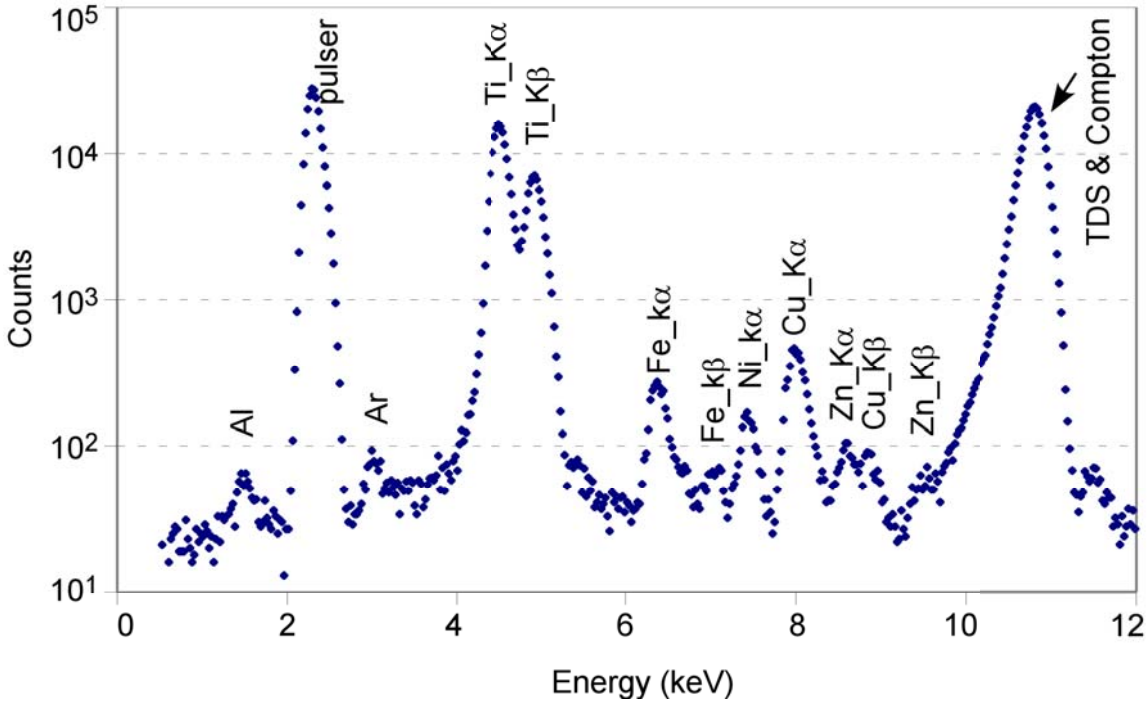

Figure 4.1. Measured X-ray fluorescence spectrum with calibrated energy and all the peaks properly assigned.

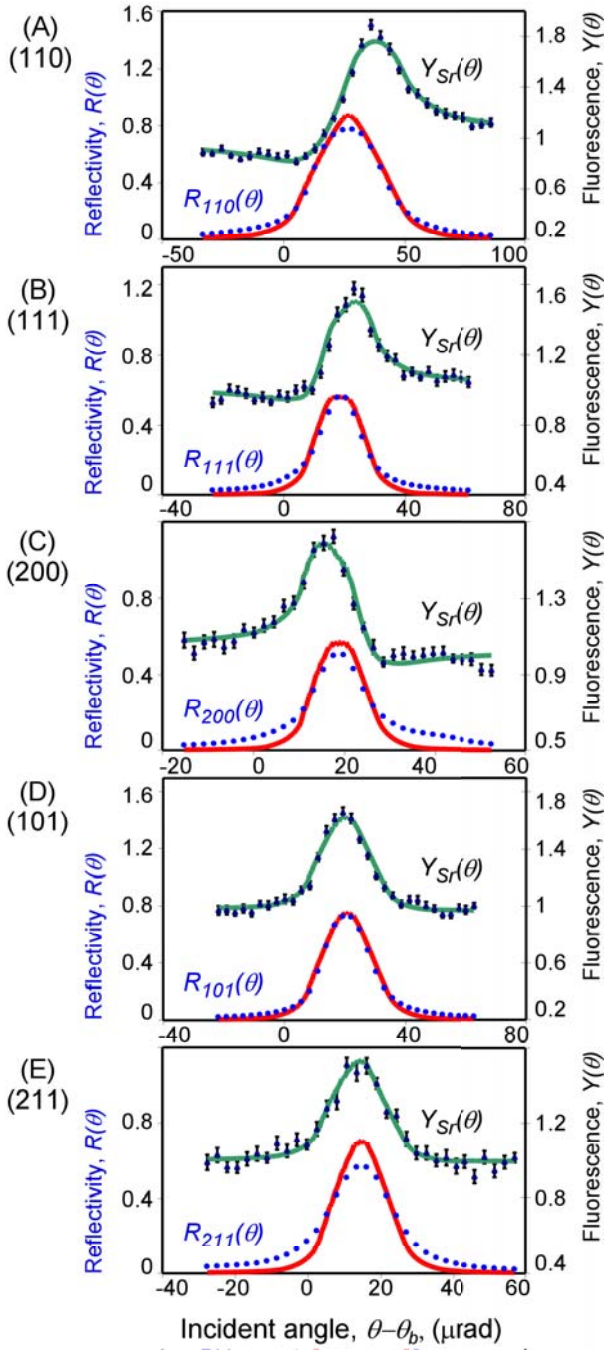

Figure 4.2. Measurements of Sr^{2+} at rutile (110)-aqueous interface for the rutile bulk reflections of (A) (110); (B) (111); (C) (200); (D) (101); and (E) (211). Both the normalized reflectivity, *R(θ)*, (bottom ones) and the normalized fluorescence yield, *Y(θ)*, (top ones) are shown with the best fits (lines) to the data (points).

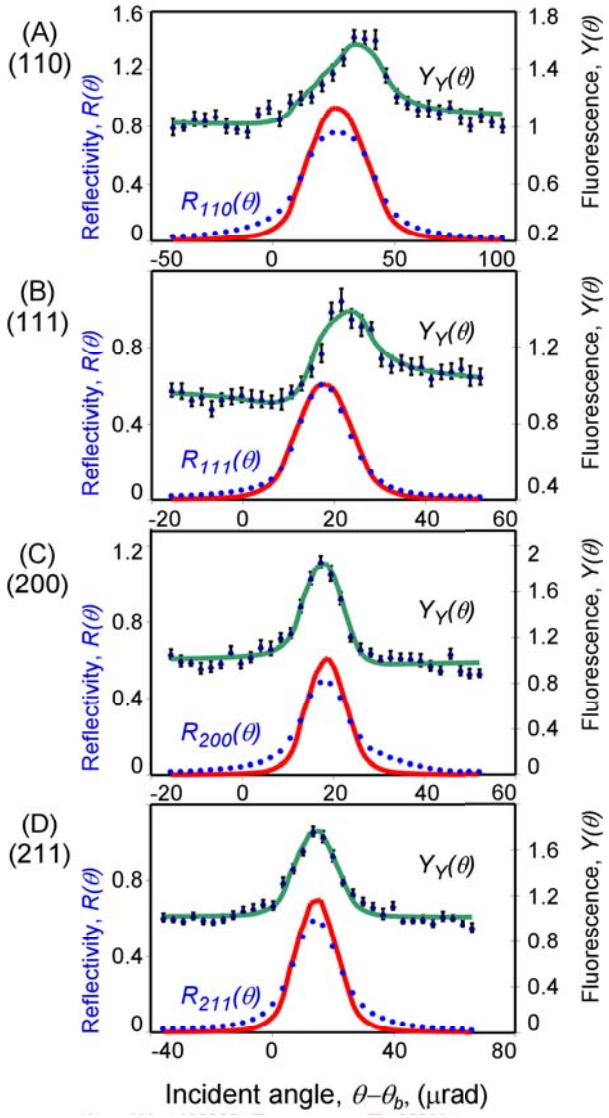

Figure 4.3. Measurements of Y^{3+} at rutile (110)-aqueous interface for the rutile bulk reflections of (A) (110), (B) (111), (C) (200), and (D) (211). Both the normalized reflectivity, $R(\theta)$, (bottom ones) and the normalized fluorescence yield, $Y(\theta)$, (top ones) are shown with the best fits (lines) to the data (points).

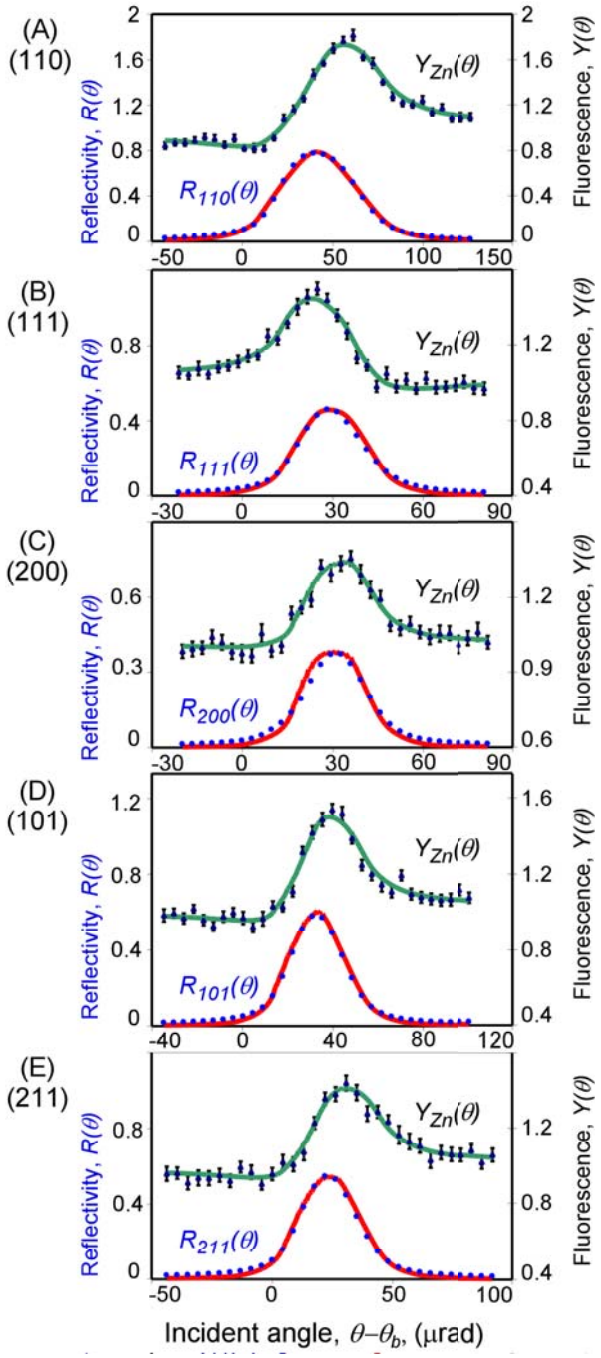

Figure 4.4. Measurements of Zn^{2+} at rutile (110)-aqueous interface for the rutile bulk reflections of (A) (110), (B) (111), (C) (200), (D) (101), and (E) (211). Both the normalized reflectivity, $R(\theta)$, (bottom ones) and the normalized fluorescence yield, $Y(\theta)$, (top ones) are shown with the best fits (lines) to the data (points).

Table 4.1. XSW measurements setup information and the derived coherent positions and coherent fractions for the EDL condensed layer ions, Zn^{2+}, Sr^{2+} and Y^{3+} , as well as the Ti atom in the bulk crystal.

High-heat-load monochromator		Si (111) (2 bounce) 20% detuned											
Post mono 1 & detuned		Not in Use											
Rutile reflection		**(110)**		**(111)**		**(200)**		**(101)**		**(211)**			
		P	*f*	*P*	*f*	*P*	*f*	*P*	*f*	*P*	*f*	Θ_{tot} (ML)	*E* (keV)
Post mono 2 & detuned		Si (111) 50%		Si (220) 30%		Si (220) 30%		Si (220) 30%		Si (220) 30%			
Zn^{2+}	Value	0.95	0.45	0.60	0.31	0.89	0.16	0.91	0.32	0.89	0.38	0.5-1.1	10.92
	uncertainty	0.02	0.03	0.03	0.02	0.04	0.04	0.02	0.02	0.02	0.03		
Ti	Value	0.99	0.95	0.76	0.17	0.99	0.82	0.90	0.99	0.99	0.88	-	
	uncertainty	0.01	0.01	0.01	0.02	0.01	0.01	0.01	0.01	0.01	0.01		
Post mono 2 & detuned		Si (111) 30%		Si (220) 30%		Si (220) 30%		Si (220) 30%		Si (220) 30%			
Sr^{2+}	Value	0.93	0.53	0.93	0.39	0.53	0.36	0.45	0.09	0.66	0.11	0.8	17.5
	uncertainty	0.02	0.02	0.03	0.03	0.04	0.06	0.08	0.03	0.05	0.05		
Post mono 2 & detuned		Si (111) 50%		Si (220) 50%		Si (220) 50%		-		Si (220) 50%			
Y^{3+}	Value	0.83	0.36	0.86	0.50	0.35	0.36	-	-	0.34	0.07	0.3	17.96
	uncertainty	0.02	0.03	0.02	0.03	0.03	0.08	-	-	0.09	0.05		

coherent fractions are all close to their ideal value based on the rutile structure. It is worth noting that the two Ti atoms in the unit cell are exactly out of phase for the (111) reflection, so that the effective amplitude of that Fourier component (i.e., the coherent fraction) should be 0 for the Ti fluorescence. The measured number 0.17 is small enough to be regarded as 0 when considering the error associated with the non-ideal rutile rocking curve. And whenever the amplitude of a Fourier component is 0, the phase (i.e., the coherent position) is meaningless and does not contain any structural information.

4.3.3 XSW imaging of the cations at rutile-aqueous interface

To easily understand the data and show the adsorbed ion location relative to the rutile (110) surface, the redefined rutile non-primitive tetragonal unit cell, as described in the section 1.3.3, is adopted from this point on. The rutile (110) surface structure is shown again in Figure 4.5 together with the redefined non-primitive tetragonal unit cell. The shaded plane indicates the actual termination position for the (110) surface in the aqueous solution. An additional layer of Ti above the surface plane is shown to illustrate the extended lattice Ti atom position.

With the non-primitive tetragonal unit cell, new notations for all the lattice planes and directions are defined. The notations based on the non-primitive tetragonal unit cell are denoted with a subscript ‘S’.

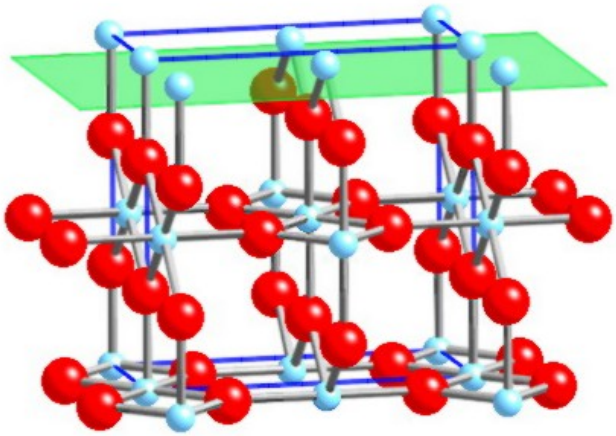

Figure 4.5. The rutile non-primitive tetragonal unit cell (in blue lines) with an imaginary layer of Ti on top. Below the shaded plane is the termination structure of the rutile (110) surface in the aqueous solution.

The transformation matrix from the primitive tetragonal unit cell to the non-primitive tetragonal unit cell is (as given in section 1.3.3): $\begin{pmatrix} -1 & 1 & 0 \\ 0 & 0 & 1 \\ 1 & 1 & 0 \end{pmatrix}$. Some of relations between the primitive notation and the surface notation are listed in Table 4.2 for reference. Also listed are the surface symmetry equivalent reflections for those we measured. Because of the truncation of lattice along surface normal direction, some of the bulk lattice symmetries do not exist at the surface. For instance, for measurement of an impurity in the bulk lattice, (110) and (-110) are equivalent reflections because the position of impurity registers to both planes identically. But for an adsorbate at the (110) surface, (110) is the surface normal direction and (-110) is the inplane direction. An adsorbate at one height along the surface normal direction does not have to be at a bulk symmetry equivalent lateral position. Therefore the two reflections are inequivalent with respect to the surface adsorbate geometry.

The XSW imaging method actually projects the atom distribution into the crystal primitive unit cell, which is the smallest symmetry unit of the crystal. The non-primitive tetragonal unit cell defined here for rutile (110) surface is twice as large as a primitive unit cell. Therefore to simplify the generated picture and reduce the amount of calculation, only top half of the non-primitive tetragonal unit cell was used for the imaging, as shown in the Figure 4.6 (A), where the non-primitive tetragonal unit cell is cut at the surface Ti-O plane, in green. The extended bulk Ti atoms are again shown for later comparison with the constructed Ti image. The half non-primitive tetragonal unit

cell has two mirror symmetry planes.

With the general method described in Chapter 2, using the measured coherent fractions and coherent positions, the images of Ti atom, Sr^{2+}, Zn^{2+}, and Y^{3+} are obtained, shown in Figure 4.6 (B)-(F) as the stacking of slices along the surface normal direction.

The Ti atom location is imaged to check the validity of the method. As we can see by comparison Figure 4.6 (A) and (B), the imaged Ti atom positions agree with the actual bulk atom positions very well. In the images, the boxes indicate the boundary of the half non-primitive tetragonal unit cell.

Table 4.2. The relations between the surface notation (subscript S, *Italic*) and the primitive tetragonal notation for the rutile crystal reflections; and the symmetry equivalent reflections for those actually measured with XSW (underlined). Forbidden reflections are marked as ~~strikethrough~~.

	Primary relations						XSW measured			
Bulk notations	**-110**	**110**	~~**001**~~	~~**100**~~	~~**010**~~		111	200	101	211
Surface notations	***200*$_S$**	***002*$_S$**	~~***010*$_S$**~~	~~***-101*$_S$**~~	~~***101*$_S$**~~		*012*$_S$	*-202*$_S$	*-111*$_S$	*-113*$_S$
	Other relations									
Bulk	002	112	222	011	121	130	-112	022	132	
Surface	*020*$_S$	*022*$_S$	*024*$_S$	*111*$_S$	*113*$_S$	*204*$_S$	*220*$_S$	*222*$_S$	*224*$_S$	
Bulk	120	230	221	-111	~~021~~	131	241	~~012~~	122	232
Surface	*103*$_S$	*105*$_S$	*014*$_S$	*210*$_S$	~~*212*$_S$~~	*214*$_S$	*216*$_S$	~~*121*$_S$~~	*123*$_S$	*125*$_S$
Surface notation and their surface symmetry equivalents	***0 0 2*$_S$**		***0 1 2*$_S$**		***-2 0 2*$_S$**		***-1 1 1*$_S$**		***-1 1 3*$_S$**	
			0 -1 2$_S$		*2 0 2*$_S$		*-1 -1 1*$_S$		*-1 -1 3*$_S$	
							1 -1 1$_S$		*1 -1 3*$_S$	
							1 1 1$_S$		*1 1 3*$_S$	

For the Sr^{2+} and Y^{3+} ions, as shown in Figure 4.6 (C) and (D), it is clear that both ions take the tetradentate position, which is roughly equal in distance from two terminal oxygen (TO) and two bridging oxygen (BO) sites. The heights of the two ions from the surface Ti-O plane are different, though, as can be seen in (D) in which the topmost plane in the image corresponds to the plane of highest Y^{3+} density, and not to the unit cell boundary. This can be interpreted to first order as the result of the different bare ion radii of Y^{3+} (R = 0.90 Å, VIII-coordinated) and Sr^{2+} (R = 1.13 Å VIII-coordinated).[117]

The imaged Zn^{2+} ion position, however, is completely different from the other two. Its primary position is very close to one of the extended bulk Ti atom position—on top of the BO atom, as shown in (E) on the top corners of the box. Other than that, there is a secondary Zn^{2+} position near the other extended bulk Ti atom position—bridging the two neighboring TO atoms, as shown in (F) at the center of the slice some distance below the top of the box.

To better illustrate the lateral positions of the adsorbed ions, top views of the slices passing through the highest atom density planes are shown in Figure 4.7 (B)-(E) for Ti atom, Sr^{2+}, Y^{3+}, and Zn^{2+}, respectively, with the heights of the slice from the surface Ti-O plane labeled next the slices. And the top view of the rutile (110) surface terminated with both TO and BO atoms is shown in (A) as a reference. The oxygen atoms in this view are shown with different size to emphasize their different heights. The higher the atoms above the surface plane, the larger they appear.

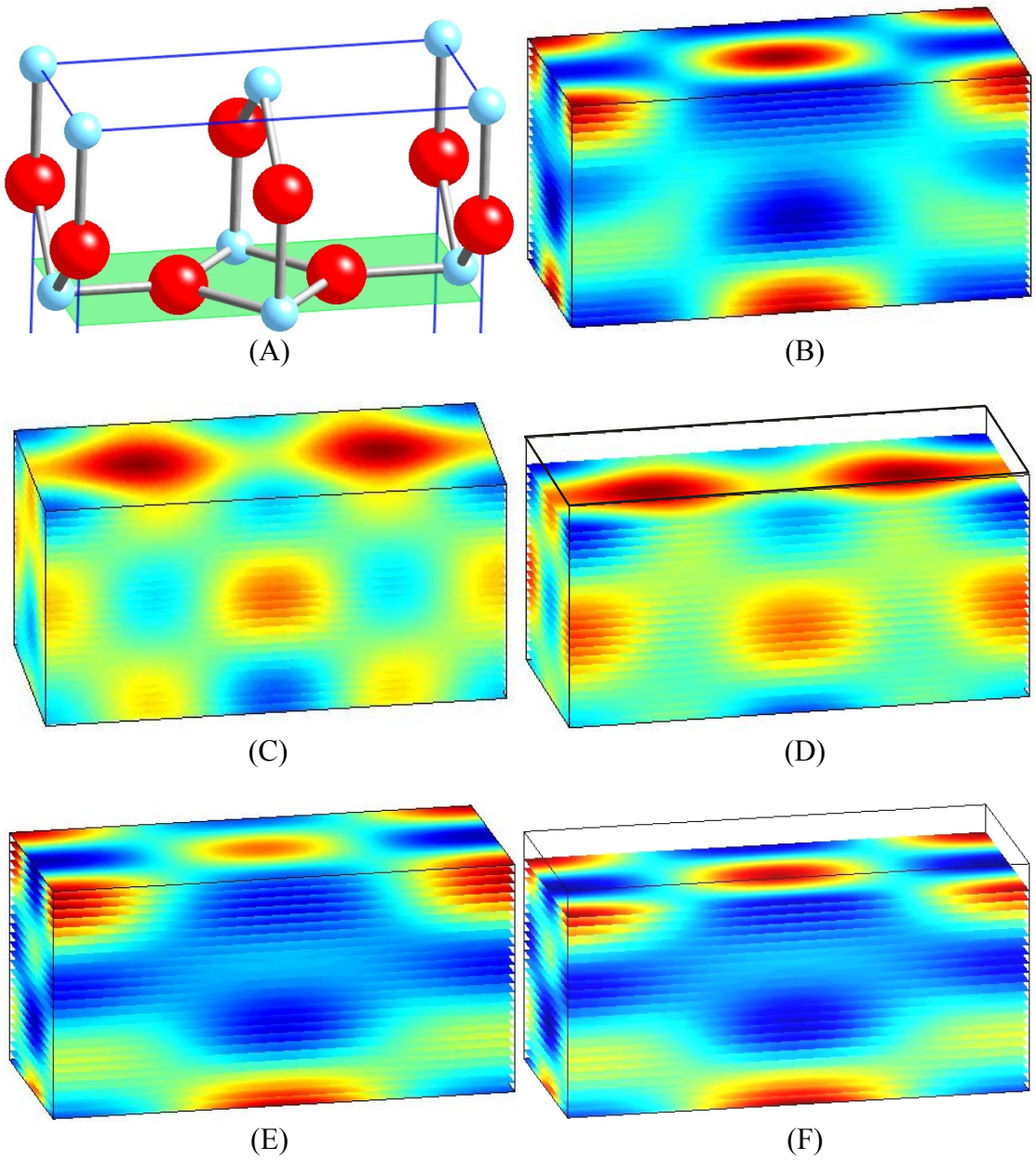

Figure 4.6. (A) Ball and Stick model of half the rutile non-primitive tetragonal unit cell; and XSW image of (B) Ti atom in the lattice, (C) Sr^{2+}, (D) Y^{3+}, (E) & (F) Zn^{2+}, inside of top half of the non-primitive tetragonal unit cell. The boxes indicate the boundary of the top half non-primitive tetragonal unit cell. The negative density comes from the termination error of the truncation of the Fourier series.

Contour-slice maps show side views of the images in Figure 4.7 (G)-(J) for Ti atom, Sr^{2+}, Y^{3+}, and Zn^{2+}, respectively, together with the side view of the top half non-primitive tetragonal unit cell in (F). Only three contour lines at 0.9, 0.7, and 0.5 of the maximum density are shown in the images with the color red, green and blue, respectively. The densities at the very bottom of each box are due to the crystal symmetry along the surface normal direction, i.e., a slide axis along (-110) direction. For the Sr^{2+} and Y^{3+} case, there are weak peaks in the density in the middle of the boxes, as noted with pink arrows.

To explore the source of these weak densities in Sr^{2+} and Y^{3+} density profiles, images are constructed from the simulated coherent fractions and positions. The simulations are carried out for given ion positions close to those shown in Figure 4.7 at the reflections actually measured, as summarized in Table 4.3. One additional reflection is also listed in the table (as underlined) is (210), which turned out to be a useful reflection in term of determining Zn^{2+} adsorption positions.

In the simulation, isotropic vibration amplitude of 0.1 Å is assumed for all ions, which is used to calculate the DW factor and in turn lowers the coherent fractions accordingly. Shown in Figure 4.8 are the images constructed from the simulations with only 5 measured reflections (top ones in each subfigure) or with the additional (210) reflection (bottom ones in each subfigure). Sr^{2+} and Y^{3+} images are plotted out in (A) and (B). It is no doubt that the truncation of Fourier components contributes to the weak intensities in the middle of the box, again pointed to with pink arrows. And adding the

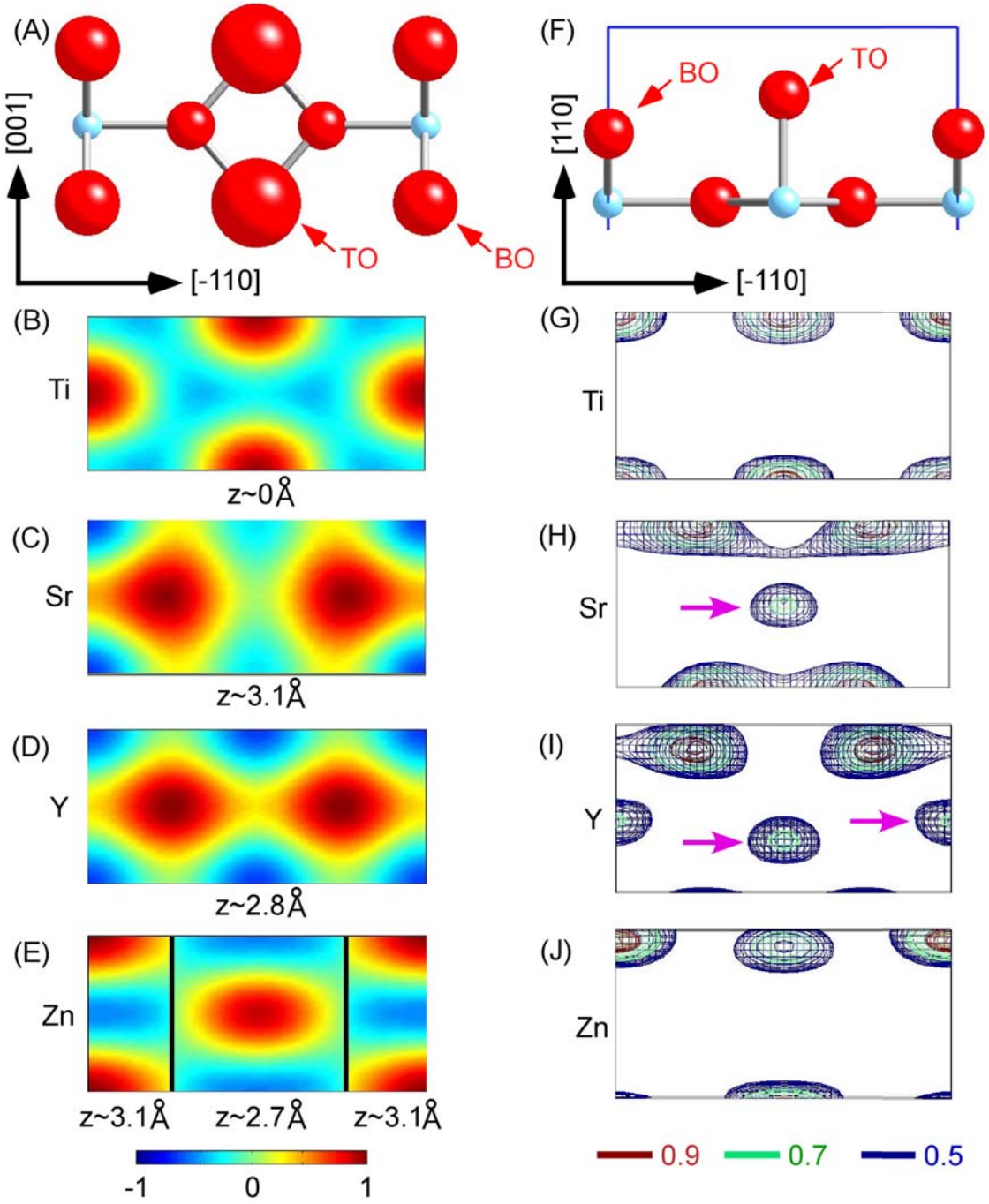

Figure 4.7. Ball and stick models of the rutile (110) surface structure are shown in (A) top view and (F) side view; same top and side view of the element distribution images and contour maps are shown for Ti atom (B, G); Sr^{2+} (C, H); Y^{3+} (D, I); and Zn^{2+} (E, J).

Table 4.3. The simulated coherent positions, *P*, and coherent fractions, *f*, for Zn^{2+}, Y^{3+} and Sr^{2+} ions at the given positions. As references, the surface BTi is at the origin, i.e., its coordination is (0.00, 0.00, 0.00); TTi at (0.50, 0.50, 0.00); TO at (0.50, 0.50, 0.31); and BO at (0.00, 0.50, 0.19). In the simulations, the vibration amplitudes of all ions are set as 0.1 Å. All the positions are in fractional non-primitive tetragonal unit cell coordinates.

		(110)	(111)	(200)	(210)	(101)	(211)
Sr^{2+}	position	**(0.21, 0.00, 0.47)**					
	P	0.94	0.94	0.44	0.41	0.47	0.41
	f	0.98	0.96	0.84	0.24	0.24	0.23
Y^{3+}	position	**(0.23, 0.00, 0.43)**					
	P	0.86	0.86	0.36	0.29	0.43	0.29
	f	0.98	0.96	0.93	0.12	0.12	0.11
Zn^{2+}	position1	**(0.00, 0.50, 0.48)**					
	P	0.96	0.46	0.96	0.44	0.98	0.94
	f	0.98	0.96	0.96	0.95	0.97	0.93
	position2	**(0.50, 0.00, 0.46)**					
	P	0.92	0.92	0.92	0.88	0.60	0.88
	f	0.98	0.96	0.96	0.95	0.97	0.93

reflection (210) does not help much on eliminating the false density. Compared with the density profiles from the simulation, it seems that the measured ones show higher density at those false peaks area for both Sr^{2+} and Y^{3+}. It is possible that part of the intensity is true, for instance, from the outer-sphere adsorbed ions at the indicated position but one or more unit cell height higher. Further quantitative analysis may give more insight into this possibility.

The situation is a bit different for the Zn^{2+} case. The two different Zn^{2+} positions are simulated separately. Shown in (C) and (D) are the images of Zn^{2+} density profiles for on top of the BO atom, labeled with TZn(Zn_1), and bridging the TO atoms, BZn(Zn_2), respectively. The false intensities are seen for both configurations when only 5 reflections are used. The lateral position of the false intensity of TZn is almost the same as actual BZn position and verse visa. This is because that the two sites are in phase in the standing wave field from reflections (110), (200), (101), and (211). The only measurement where the two sites are not in phase is (111). The two Zn^{2+} positions are $d_{111}/2$ (instead of d_{111}) apart along the (111) plane normal direction, which means they are actually out of phase in the standing wave field. This one reflection gives us sensitivity between the two positions, but apparently not enough.

These simulations show that relative intensity of the false peaks is typically small, and more importantly, that the false positions should be at the exactly same height as the actual Zn^{2+} position, which clearly is not the case in our measured Zn^{2+} profile. Both of these observations imply that the two Zn^{2+} positions yield by the XSW imaging are real rather than derived from truncation errors.

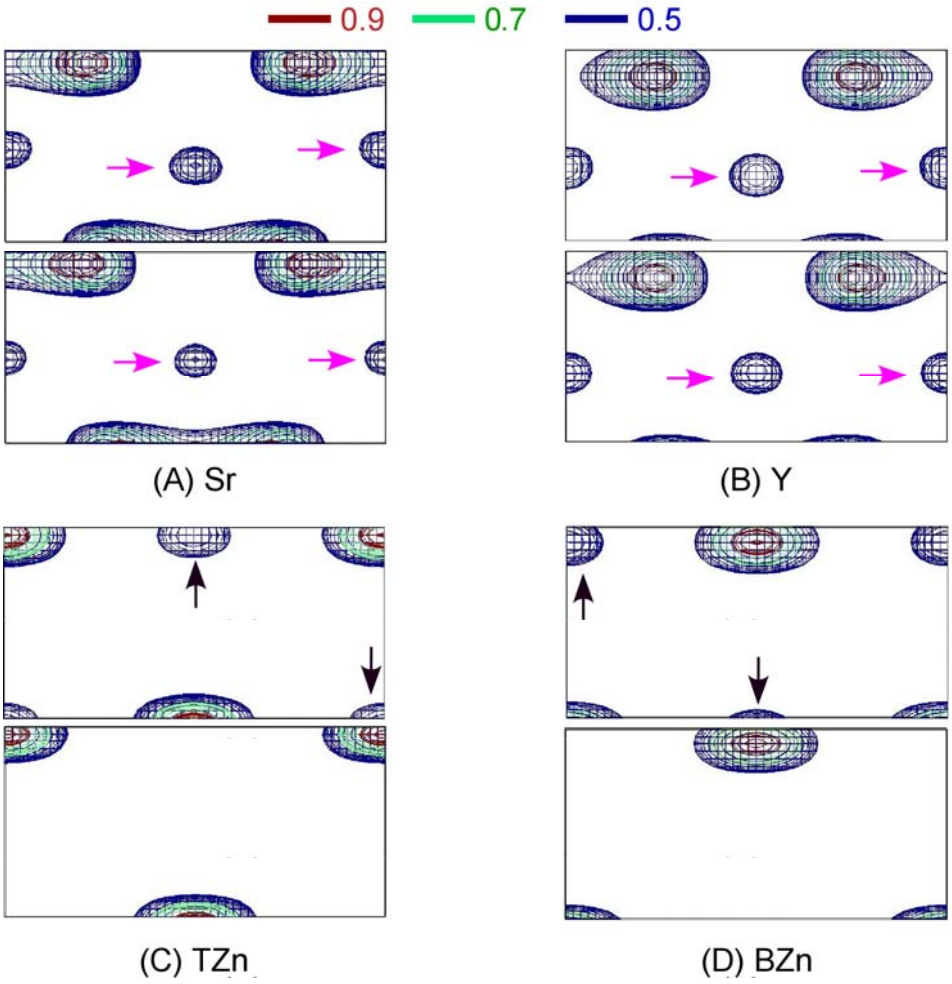

Figure 4.8. The density contour maps constructed from the simulated coherent fractions and coherent positions for ions (A) Sr^{2+}; (B) Y^{3+}; (C) and (D) two distinctive Zn^{2+} positions. In each subset of figure, the top ones are constructed with 5 reflections actually measured with XSW and the bottom ones include one more reflection, (210).

When the additional reflection (210) is included, the false intensities of Zn^{2+} simulated are significantly reduced. This is because that similar to (111), the (210) reflection distinguishes between the two Zn^{2+} adsorption sites. It would therefore be better if the (210) reflection (and other oxygen only reflections) is measured. The criterion was followed in the later measurements at different solution conditions.

The derived Ti distribution is dominated by the experimental resolution, indicated by the largely isotropic distribution in Figure 4.7 (B), as expected since the experimental resolution is substantially larger than the Ti atom vibrational amplitude (< 0.1 Å). In contrast, the adsorbate distributions exhibit some additional broadening (e.g., along [001] for Sr^{2+} and [-110] for Zn^{2+}) suggesting that the actual distributions may include either static or dynamic displacements from the nominal adsorption sites described above.

4.3.4 The XSW triangulation

Although the XSW imaging can directly give an element distribution profile, the resolution (~ 1 Å) is not good enough to precisely locate the adsorbate. Since the approximate positions of the ions have already been revealed, the more traditional XSW analysis—triangulation fittings— can be easily carried out with the methodology described in Chapter 2.

To directly address the weak intensity peaks that were observed in the XSW images of Sr^{2+} and Y^{3+} adsorption and to determine if they are due to ion adsorption or termination error, the fitting starts with and without an ion located at the weak intensity point, namely the two-position model and one-position model, respectively. The quality

of the fittings is indicated with the reduced χ_r^2, which is defined as:

$$\chi_r^2 = \frac{\chi^2}{(n-m)} = \frac{\sum_{i=1}^{n} \frac{(y_i - y_i^0)^2}{(\Delta y_i^0)^2}}{(n-m)} \tag{4.1}$$

Here y_i, y_i^0, and Δy_i^0 are the calculated, the measured value and the uncertainty of the measurement at point number i, respectively. n is the total number of data points. And m is the number of fitting parameters. The χ^2 is the sum of the deviation. The desired χ_r^2 value should be close to 1.

In the fitting for the ion positions, isotropic vibration amplitude is assumed again. The calculated Debye-Waller factors, D_H, are shown in Table 4.4 for all of the rutile reflections assuming the isotropic vibration amplitude, σ, as 0, 0.1, and 0.2 Å, respectively. The effects on the XSW triangulations are explored by fitting the data with $\sigma = 0$ Å and $\sigma = 0.2$ Å separately.

Table 4.4. The calculated Debye-Waller factor for each of the rutile reflections assuming the isotropic vibration amplitude as 0, 0.1, and 0.2 Å for the adsorbed ions.

TiO_2 reflection, H	(110)	(111)	(200)	(101)	(211)
d-spacing, d_H (Å)	3.25	2.19	2.30	2.49	1.69
Momentum transfer, $Q = 2\pi/d_H$ ($Å^{-1}$)	1.93	2.87	2.73	2.52	3.72
$D_H = \exp(-Q^2*\sigma^2/2)$; $\sigma = 0.0$ Å	1.00	1.00	1.00	1.00	1.00
$D_H = \exp(-Q^2*\sigma^2/2)$; $\sigma = 0.1$ Å	0.98	0.96	0.96	0.97	0.93
$D_H = \exp(-Q^2*\sigma^2/2)$; $\sigma = 0.2$ Å	0.93	0.85	0.86	0.88	0.76

The fitting parameters include the positions (x, y, z along the non-primitive tetragonal unit cell vector $\boldsymbol{a}$, $\boldsymbol{b}$, and $\boldsymbol{c}$ directions, respectively) and the corresponding occupation factors of the ions. Therefore normally for the one-position model, there are 4 fitting parameters. While for the two-position model, there are 8. The occupation factor is actually the fraction of the ions at the position out of the total coverage. The amount of ions at any position would be the product of the occupation factor and the total coverage.

Since the rutile (110) surface has two mirror planes, we can assume that the adsorbed ions inherit the same symmetry. If the ion positions deviate from the high symmetry point, they may be split into as many as 4 different positions that are surface symmetry equivalent. For instance, the fitted Sr^{2+} position (x0, y0, z0) would have three other symmetry equivalent positions as (x0, -y0, z0), (-x0, y0, z0) and (-x0, -y0, z0), with a quarter of the total occupation factor at each position.

Chances are that some of the parameters, such as the lateral position of the ion, are strongly correlated with each other, so that they can not be fitted together simultaneously. In such cases, the fitting is carried out with a series of fixed parameter (p) values and $\chi^2(p)$ is recorded for each fitting. At the minimum of $\chi^2(p)$, where $p = p_0$, $\chi^2_{min}(p) = \chi^2(p = p_0)$. p_0 is taken as the best-fit value and the one σ errorbar (std) of the parameter is set to be the half width of $\chi^2(p)$ curve at $\chi^2_{min}(p) + 1$. Generally the curve follows the parabolic shape $\chi^2(p) = a_1*p^2 + a_2*p + a_3$, where a_n (n = 1, 2, 3) are the coefficients. In such case, the standard deviation, $std^2 = 1/a_1$. An example is given in Figure 4.9. The $\chi^2(p)$ vs. p is plotted out (p is in the unit of Å). Here the $\chi^2_{min}(p) = 29.5$,

where p_0 = 0.44 (or 0.56). From the fitting, a_1 = 222, therefore $std \approx 0.07$, which agrees well with the half width of the curve at $\chi^2_{min}(p) + 1 = 30.5$, i.e., $std \approx 0.08$. Because the two p_0 positions are symmetric about 0.5, and $\chi^2(p = 0.5) - \chi^2_{min}(p) < 1$, p_0 is set to 0.5 instead of 0.44/0.56.

The data points include the coherent fraction and position at each rutile reflection. There are 5 independent reflections measured. Thus the independent data point number is 10. The symmetry equivalent reflections can also be included and the data point number can increase to 26 for Zn^{2+} and Sr^{2+}, and 18 for Y^{3+}. This will not put any additional restriction on the fitting, but changes the relative weight on each independent reflection. This actually is not desired since it puts more weight on the less well defined reflections (but with more symmetry equivalences) rather than on the better defined ones, namely (110) reflection. Therefore, no symmetry equivalents are included in the fitting.

The fitted results for Sr^{2+}, Y^{3+}, and Zn^{2+} are summarized in Table 4.5. Note that for Sr^{2+} measurements at (101) and (211) reflections, the coherent fractions, i.e., the amplitudes of the Fourier components, are essentially 0, therefore large error bars are set for the corresponding coherent positions artificially to account for the fact that the measured ones are not necessarily the actual phases of the Fourier components. The same is true for Y^{3+} (211) reflection. And for Y^{3+} (101) reflection, considering the similarity of adsorbed Y^{3+} and Sr^{2+} positions, values similar to Sr^{2+} case are generated for the fitting process, as $P_{101} = 0.50 \pm 0.50$ and $f_{101} = 0.05 \pm 0.05$. This is also equivalent to set a component with zero amplitude and an unspecified phase.

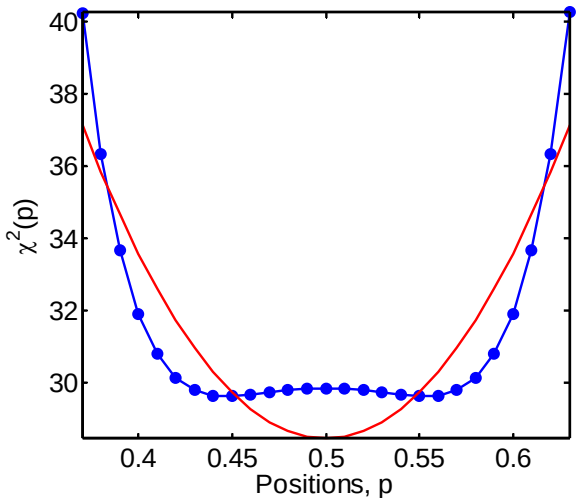

Figure 4.9. The illustration of achieving the best fit number and the one σ errorbar with a series of $\chi^2(p)$ fittings for one parameter. The blue line with dots is the $\chi^2(p)$ from the fit at each value of the parameter, on x axis. And the red solid line is the fit of the blue curve to a parabolic shape. The curve here shows that the best fit value should be 0.5 (Å) and the one σ errorbar should be around ± 0.08 (Å).

Table 4.5. The Sr^{2+}, Y^{3+} and Zn^{2+} adsorbed ion positions obtained with XSW triangulations.

Sr^{2+}	(hkl)	(110)		(111)		(200)		(101)		(211)											
		P	*f*	*P*	*f*	*P*	*f*	*P*	*f*	*P*	*f*		Fitting parameters								
	XSW	0.93	0.53	0.93	0.39	0.53	0.36	0.45	0.06	0.66	0.08			position 1				position 2			
	Error	0.02	0.02	0.03	0.03	0.04	0.06	0.50	0.06	0.50	0.08	χ^2		***x1***	***y1***	***z1***	***occ1***	***x2***	***y2***	***z2***	***occ2***
σ= 0.2 Å	One-position											**0.68**	Value	**0.21**	**0.10**	**0.48**	***0.56***	-	-	-	-
	Fitted	0.95	0.52	0.95	0.39	0.45	0.43	0.48	0.10	0.43	0.08		Error	0.01	0.01	0.01	0.02	-	-	-	-
	Two-position											**0.08**	Value	**0.21**	**0.08**	**0.48**	***0.50***	**0.50**	**0.19**	**0.39**	***0.15***
	Fitted	0.92	0.53	0.95	0.39	0.52	0.36	0.55	0.06	0.51	0.09		Error	0.00	0.01	0.00	0.01	-	0.02	0.01	0.02
σ= 0.0 Å	One-position											**0.79**	Value	**0.21**	**0.12**	**0.48**	***0.52***	-	-	-	-
	Fitted	0.95	0.54	0.95	0.37	0.45	0.37	0.48	0.08	0.43	0.04		Error	0.01	0.01	0.01	0.02	-	-	-	-
	Two-position											**0.08**	Value	**0.21**	**0.10**	**0.48**	***0.45***	**0.50**	**0.20**	**0.40**	***0.14***
	Fitted	0.92	0.53	0.94	0.39	0.52	0.36	0.56	0.05	0.52	0.10		Error	0.00	-	0.00	0.01	-	0.01	0.01	0.01

Zn^{2+}	(hkl)	(110)		(111)		(200)		(101)		(211)											
		P	*f*	*P*	*f*	*P*	*f*	*P*	*f*	*P*	*f*		Fitting parameters								
	XSW	0.95	0.45	0.60	0.35	0.89	0.17	0.91	0.37	0.89	0.37			position 1				position 2			
	Error	0.02	0.03	0.03	0.02	0.04	0.04	0.02	0.02	0.02	0.03	χ^2		***x1***	***y1***	***z1***	***occ1***	***x2***	***y2***	***z2***	***occ2***
σ= 0.2 Å	One-position											**5.54**	Value	**0.08**	**0.50**	**0.47**	***0.47***	-	-	-	-
	Fitted	0.93	0.43	0.43	0.40	0.93	0.23	0.97	0.36	0.90	0.31		Error	0.02	-	0.01	0.03	-	-	-	-
	Two-position											**4.20**	Value	**0.11**	**0.50**	**0.48**	***0.45***	**0.50**	**0.00**	**0.41**	***0.10***
	Fitted	0.93	0.49	0.48	0.33	0.89	0.16	0.96	0.40	0.89	0.31		Error	0.02	***0.05***	0.01	0.03	***0.07***	***0.08***	0.02	0.04
σ= 0.0 Å	One-position											**5.24**	Value	**0.08**	**0.50**	**0.47**	***0.40***	-	-	-	-
	Fitted	0.93	0.40	0.43	0.40	0.93	0.23	0.97	0.35	0.90	0.35		Error	0.02	***0.07***	0.01	0.02	-	-	-	-
	Two-position											**2.99**	Value	**0.11**	**0.50**	**0.48**	***0.38***	**0.46**	**0.00**	**0.40**	***0.11***
	Fitted	0.93	0.46	0.51	0.33	0.89	0.15	0.96	0.39	0.89	0.33		Error	0.01	***0.07***	0.01	0.02	***0.10***	***0.10***	0.01	0.03

Y^{3+}	(hkl)	(110)		(111)		(200)		(101)		(211)											
		P	*f*	*P*	*f*	*P*	*f*	*P*	*f*	*P*	*f*		Fitting parameters								
	XSW	0.83	0.36	0.86	0.5	0.35	0.36	0.5	0.05	0.34	0.07			position 1				position 2			
	Error	0.02	0.03	0.02	0.03	0.03	0.08	0.5	0.05	0.4	0.07	χ^2		***x1***	***y1***	***z1***	***occ1***	***x2***	***y2***	***z2***	***occ2***
σ= 0.2 Å	One-position											**1.21**	Value	**0.23**	**0.00**	**0.43**	***0.51***	-	-	-	-
	Fitted	0.85	0.47	0.85	0.43	0.35	0.42	0.43	0.06	0.28	0.05		Error	0.01	***0.02***	0.01	0.02	-	-	-	-
	Two-position											**0.03**	Value	**0.23**	**0.00**	**0.43**	***0.54***	**0.18**	**0.50**	**0.21**	***0.17***
	Fitted	0.83	0.36	0.86	0.50	0.34	0.36	0.48	0.06	0.25	0.06		Error	0.00	***0.15***	0.00	0.00	***0.07***	***0.30***	0.01	0.01
σ= 0.0 Å	One-position											**0.79**	Value	**0.23**	**0.00**	**0.43**	***0.45***	-	-	-	-
	Fitted	0.85	0.45	0.85	0.45	0.35	0.43	0.43	0.06	0.28	0.06		Error	0.01	***0.03***	0.01	0.02	-	-	-	-
	Two-position											**0.03**	Value	**0.23**	**0.00**	**0.43**	***0.46***	**0.18**	**0.30**	**0.21**	***0.12***
	Fitted	0.83	0.36	0.86	0.50	0.34	0.38	0.48	0.05	0.26	0.07		Error	0.00	***0.12***	0.00	0.00	***0.10***	***0.30***	0.01	0.01

First there are no significant differences between the fitting results with $\sigma = 0$ and 0.2 Å except for a slightly reduced χ_r^2 and increased occupation factor at higher σ value. And the χ_r^2 is already lower than 1 when one-position model is applied. Although in the two-position model case, the χ_r^2 are significantly reduced, it is too far below 1, which suggests that the data are over-interpreted. Therefore the one-position model is actually preferred in term of Sr^{2+} and Y^{3+} adsorption geometry. And the secondary positions of ions, though works well both mathematically and structurally (as outer sphere adsorbate), are not required based on our current data. These results suggest that in the XSW imaging, the weaker densities in the middle part of the box are very likely all from the truncation of the Fourier terms.

For the Zn^{2+} data, the two-position model actually does a better job and is chosen over the one-position model as the proper adsorption structure.

4.3.5 More discussions about the triangulation results

The schematic structure of adsorbed ions at the rutile (110)-aqueous interface is illustrated in Figure 4.10 with the ball-and-stick model. For all three ions, the adsorbed positions are off the surface mirror planes. For Sr^{2+} and Y^{3+}, the offset is mainly along [-110] direction to maintain roughly the same bond length between the ions and the underlying BO and TO atoms. The different heights of BO and TO atoms from the surface, (1.29 and 1.96 Å, respectively, if no surface relaxation occurs) cause the adsorbed Sr^{2+} and Y^{3+} to shift laterally closer to the BO atoms. Such lateral displacements for the primary Zn^{2+} ion, by moving away from atop of BO position,

makes the Zn-O bond length more favorable as compared with literature values. The metal ion-oxygen bond lengths are shown in Table 4.6, where the bond lengths are calculated based on the assumption that the rutile (110) surface undergoes no relaxation and reconstruction. TO* and BO* in the table denoted for the TO and BO atoms in the adjacent non-primitive tetragonal unit cell. And the $\sigma = 0$ Å results are used for this calculation. All the numbers listed should be changed once the rutile surface relaxation is considered. And they are simply shown as a first order reality check.

Seen from the calculation is that the TZn atom is only bonded to BO atoms. And BZn atom is very close to TO atoms. In fact, the Zn-O distance is significantly shorter than the normal Zn-O bond length, such as the average value of 1.98 Å in ZnO. This could be due to a few factors: first, the underlying TO atoms is not at its bulk lattice position. Secondly, the BZn is a minor species, which is only ~ 25% of the total specifically adsorbed Zn^{2+}. The fitted parameters come out with large standard deviations suggests the positions derived are not precisely defined. Finally it is possible that the ion and/or surface oxygen positions are displaced both laterally and vertically from their assumed locations.

The calculated ion-oxygen bond lengths for both Y^{3+} and Sr^{2+} are similar to their typical values, e.g., ~ 2.6 Å for Sr^{2+}-O and ~ 2.4 Å for Y^{3+}-O. The distances from Sr^{2+} to the four neighboring oxygen atoms are all different because of the lateral displacement from the high symmetry position.

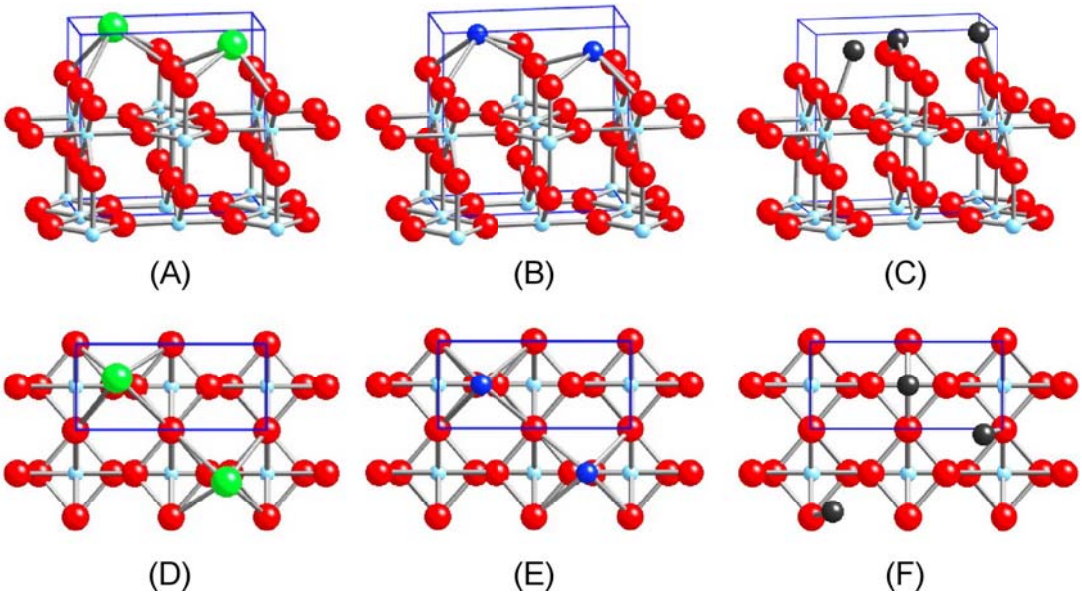

Figure 4.10. The schematic structures with ball and stick model of the adsorbed ions at the rutile (110)-aqueous interface. (A)-(C) are the perspective views of Sr^{2+} (in green); Y^{3+} (in blue); and Zn^{2+} (in black), respectively. (D)-(F) are the top views of the same ions. Outlined with blue is the non-primitive tetragonal unit cell. Two non-primitive tetragonal unit cells are shown in each subfigure. The symmetry equivalent positions are demonstrated in each plot.

Table 4.6. The metal ion-oxygen bond lengths at the rutile (110)-aqueous interface. Here no relaxation of the rutile (110) surface is assumed.

Lattice parameters	
a **=**	**6.4965 Å**
b **=**	**2.9587 Å**
c **=**	**6.4965 Å**

	BO	TO	BO*	TO*
X	0.00	0.50	0.00	0.50
Y	0.50	0.50	-0.50	-0.50
Z	0.20	0.31	0.20	0.31

	X	Y	Z	Bond length (in Å)			
TZn^{2+}	0.11	0.50	0.48	**1.98**	**2.78**	-	-
BZn^{2+}	0.46	0.00	0.40	**3.59**	**1.62**	-	-
Sr^{2+}	0.21	0.12	0.48	**2.56**	**2.47**	**2.94**	**2.86**
Y^{3+}	0.23	0.00	0.43	**2.60**	**2.43**	**2.60**	**2.43**

Now we can explain in more detail the measured coherent positions and fractions for the adsorbed ions. Again as described in Chapter 2, the measured coherent position and fraction are just the phase and amplitude of the Fourier component at the momentum transfer. In the case of one atom position, the coherent position should simply be the distance from the atom to the diffraction plane. And the coherent fraction should be primarily due to the ordered fraction. But it seems that this is not followed in the Sr^{2+} and Y^{3+} case—although only one position for each ion is obtained in the final structure, the coherent fractions for (101) and (211) reflections, being essentially 0, can not be explained by ordered fraction alone because from the (110) reflection, that number should be around 0.5 at least.

The key point is the surface symmetry equivalent positions are not necessarily the equivalent positions in term of bulk lattice reflections. According to the Equation (2.3), for a number of discrete projected atom positions, it is like:

$$\boldsymbol{G}(\boldsymbol{H}) = f_H \exp[i2\pi P_H] = \int_{UC} \rho(\boldsymbol{r}) \exp[i\boldsymbol{H} \bullet \boldsymbol{r}] d\boldsymbol{r} = \sum_j c_j \exp[i2\pi p_j] \tag{4.2}$$

Here j denoted the different projected positions, c_j is the fractional occupation and p_j is the fractional position in term of the d-spacing of H^{th} reflection for the j^{th} position. When there are two equally populated projected positions, $c_1 = c_2 = c_x$, the Equation (4.2) can be written as:

$$\boldsymbol{G}(\boldsymbol{H}) = f_H \exp[i2\pi P_H] = 2c_x \cos[\pi(z_2 - z_1)] \exp\left[i2\pi\left(\frac{z_1 + z_2}{2}\right)\right] \tag{4.3}$$

Therefore, $f_H = a_H = 2c_x \cos[\pi(z_2 - z_1)]$, and $P_H = \left(\frac{z_1 + z_2}{2}\right)$. Here the coherent fraction is primarily determined by the geometry factor, a_H, since it is already known that C ≈ 1 and $D_H \approx 1$. When the two positions differ by half of a d-spacing, i.e., z_2 - z_1=0.5, we find that the coherent fractions have zero value, $f_H = a_H = 0$. This geometry factor explains the low coherent fractions observed for some of the reflections.

To better demonstrate this, the rutile surface structure with the adsorbed Sr^{2+}, Y^{3+}, and Zn^{2+} ions are plotted for each reflection in Figure 4.11 (A), (B), and (C), respectively. The same crystal structure is viewed from the different directions to clearly show the diffraction planes (solid blue lines), which are set perpendicular to the plane of paper in all cases. Two Zn^{2+} positions are shown in different colors (shades) on the same plot. The center plane of each individual adsorbed ion position is marked with a dashed line and the distance from the center plane to the diffraction plane is labeled with purple line. For Sr^{2+} and Y^{3+} case, the symmetry equivalent positions, which should be equally occupied, are projected to be only a single ion height for reflections (110), and two almost same heights for (111) and (200) reflections. Thus the measured coherent fractions and coherent positions appear to be a single ion position alike in these three reflections. However, for reflections (101) and (211), the projected ion positions are different and close to half d-spacing apart. That results in a coherent fractions close to zero in those measurements.

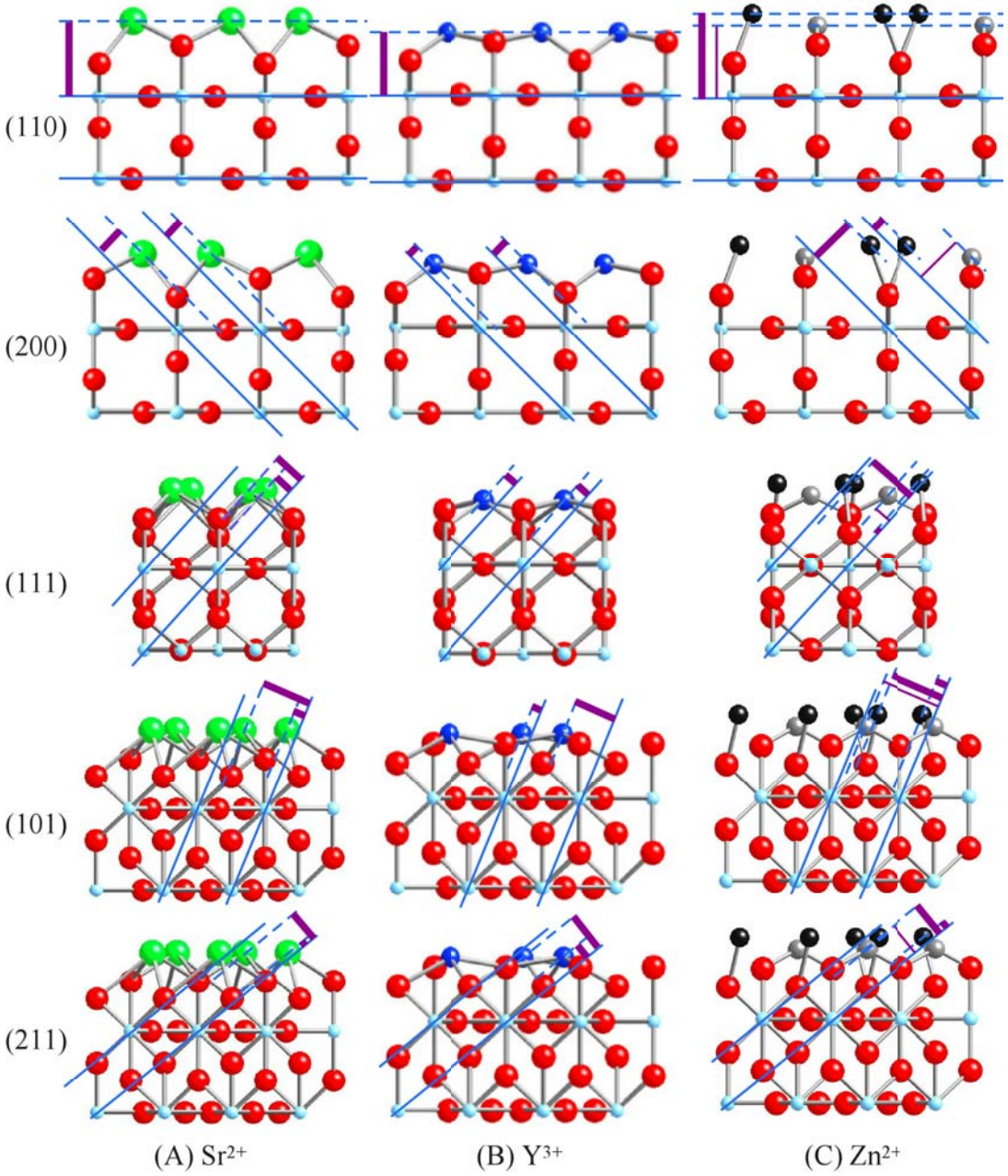

Figure 4.11. Projected view of rutile (110) surface and adsorbed ions (A) Sr^{2+}, in green, (B) Y^{3+}, in blue, and (C) Zn^{2+}, in black and grey for two different positions, TZn and BZn, respectively. The same rutile (110) unit is shown in each projection, viewed from different direction to reveal the diffraction planes (solid blue lines), perpendicular to the paper. The centers of the adsorbed atoms are labeled with dashed lines and their distances from the diffraction planes are indicated with the purple bars.

For the Zn^{2+} case, the projected views appear somewhat complicated because of the two different locations plus the symmetry equivalent positions. But actually the secondary position (BZn) is much lower coverage (~ 25%), indicated with thinner purple lines. Even if it is at a position that is a half d-spacing away from the primary adsorption site, its effects on the measured coherent fractions and positions are minimal. Furthermore, for the ions at the primary position, the separation of the projected positions (z_2 - z_1) is far from 0.5. Therefore for Zn^{2+}, all reflections have non-zero coherent fractions and suggestive coherent positions.

4.4 The significance of the ion location measurements

These data indicate that the Stern layer distributions are under crystallographic control by the substrate lattice, and reveal two potential difficulties of interpreting ion adsorption phenomena in the absence of such structural information: (1) the unexpected difference in adsorption site for two divalent metals, Sr^{2+} and Zn^{2+}, and (2) the similar adsorption sites for Sr^{2+} and Y^{3+}, even though Sr^{2+} and Y^{3+} are weakly and strongly bound, respectively (as indicated by their differing sensitivity to the concentration of indifferent background electrolytes), and have very different bare ionic radii. Such independent structural information is needed to interpret EDL phenomena using surface complexation models.

The difference in the ion adsorption positions can be interpreted in a simple way in terms of the ion size. First the Zn^{2+} ion size (R = 0.74 Å as VI-fold coordinated) is very close to that of Ti^{4+} (R = 0.75 Å) in the rutile crystal.[117.] So the adsorbed Zn^{2+} tends

to take a position similar to the bulk Ti atoms. On the rutile (110) surface, however, the lowest potential point should be the tetradentate site, i.e., in between the surface oxygen atoms. For the larger ions like Sr^{2+} and Y^{3+}, it is possible to be seated in such a position while their coordination shells are partially completed by the surface oxygen atoms. Therefore the tetradentate position on the rutile (110) surface offers a stable position for these larger ions. Zn^{2+} ion, on the other hand, is too small to locate at tetradentate position and bonded to the neighboring oxygen atoms at the same time. So the tetradentate position is not a desired position for smaller ions (pure geometrically speaking, $R \sim 0.88$ Å is the boundary for this). Similar adsorption geometry was observed when Co^{2+}, an ion with comparable size to Zn^{2+}, adsorbed onto the rutile (110) surface with EXAFS.[64.]

The Bragg-XSW approach used here is usually assumed to be applicable only to a few select materials that can be grown as perfect crystals (e.g., silicon, germanium). In contrast, the present XSW measurements were performed with imperfect synthetic rutile crystals that would normally be considered inappropriate for XSW analysis, but are made feasible with recent advances in high brilliance X-ray sources that can illuminate small (~ 100 μm in cross section) coherently scattering volumes with sufficient flux to retain sub-monolayer sensitivity. The present results demonstrate that XSW-based measurements, including the imaging approach described here, are now applicable to probe reactions at a far broader range of solid-liquid interface systems than previously thought to be possible.

This new model-independent image-based analysis of XSW data is especially important for understanding complex ion distributions. This is illustrated, in this case, by

its ability to directly resolve the two distinct Zn^{2+} adsorption sites in a manner that is no more difficult than determining the substrate atom locations or the simpler distributions for Sr^{2+} and Y^{3+}. In systems where there may be co-adsorption of two or more species (e.g., ternary sorption complexes), the elemental sensitivity of XSW allows the distributions of each element to be determined in the same manner as that described above as long as those elements are spectroscopically resolved (e.g., by their respective characteristic emissions).

4.5 Conclusion

XSW imaging offers a direct, model independent method to achieve the elemental distribution profile with sub-Angstrom resolution. Combining with the tradition XSW triangulation data fitting, more precise atom locations can be determined with relative coverage of each adsorption site.

With the XSW imaging and triangulation, Sr^{2+} and Y^{3+} ions are determined to be at tetradentate position at the rutile (110) surface. And Zn^{2+} ions are taking the extended bulk Ti atom positions at the surface with the primary one on top of the BO atoms and a minor species at the surface sites bridging the two TO atoms.

Bragg-XSW images of surface adsorbed species, described here, project 3D ion distributions into the primitive substrate crystallographic unit cell, and therefore emphasizes the Stern ion locations over the diffuse ion distribution (because the Debye length is substantially larger than unit cell dimensions). This also results in the well-

known modulo-d_H ambiguity in the derived adsorbate position.[79,80] The present results therefore do not distinguish if the adsorbate is, for instance, adsorbed directly to the surface (as an "inner-sphere" adsorbate), or above the surface plane (e.g., either as an "outer-sphere adsorbate" or in the diffuse layer). This inner- vs. outer-sphere ambiguity can be resolved with additional information (e.g., independent knowledge of ion-substrate interactions, X-ray reflectivity data, and molecular dynamics simulations). These additional constraints, especially the close agreement between XSW results and molecular dynamics simulations, demonstrate that each measured adsorbate species occurs as an inner-sphere adsorbate bonding directly to the rutile surface lattice.[87.] Bond lengths between adsorbed ions and surface oxygen atoms can be inferred by constraining the positions of surface oxygen atoms with X-ray reflectivity [87.] or through analysis of X-ray absorption fine structure data.[61,81]

For the SCM modeling, knowledge of the ion adsorption structure leads one step closer to reveal the exact reactions at the interface, such as the bond breaking and forming, proton adsorption and desorption, which will lead to a more detailed understanding of these interfacial processes. In such point of view, similar knowledge of the surface proton and oxygen structures would be of substantial help. While it is practically impossible to probe the locations of protons at an interface with X-rays under aqueous solution, neutron scattering may be able to provide some constraints in this area.

Simulations are another way to gain knowledge of the interfacial structure. Direct comparison between the measured adsorbed ion positions with the results from the MD simulation yield very good agreement. Therefore the MD simulation is proven to be able

to properly describe these interfacial processes. It is not only valuable in showing the proton adsorption behavior in the cases where ion adsorption measurements exist, but also for those situations where the measurement is not available or not feasible, such as lighter ions like Na^+, which cannot be measured with the XSW method. The combination of X-ray measurements and MD simulations can expand the knowledge about interfacial structure significantly.

Although XSW can not offer any surface oxygen or interfacial water molecule information, they should be able to probe with other X-ray methods, including EXAFS and CTR measurements.

Chapter 5 Probing rutile (110) surface structure with crystal truncation rod analysis

5.1 Purpose of the work

As we discussed in chapter 4, although XSW is a powerful tool in probing the adsorbed ion locations, the XSW method has limitations. XSW has the module-d ambiguity so that, by itself, the adsorbate location can not be determined uniquely (e.g., on the surface, or one d-spacing above the surface). Because the XSW technique relies on the X-ray fluorescence from the atom/ions, elements with low characteristic fluorescence energies are very difficult to measure *in-situ* because these signals would be greatly attenuated by the bulk solution present on top of the surface. Practically speaking, for less than half monolayer coverage (~ 5×10^{14} atom/cm^2), Zn is probably the lowest Z element that can be measured with XSW *in-situ*. A separate limitation derives from the need to limit the amount of non-coherent background signal from the fluorescing atom to be low, ideally lower than 10% of the total signal, since the X-ray fluorescence is not surface specific. If the background fluorescence signal is higher than the actual coherent signal, extra care must be taken when processing the data. Assuming that the coherent adsorbed ion has a coverage of half a monolayer, for the typical 2 μm thickness of solution, the concentration of the ion in the bulk solution should be normally lower than 10^{-3} mol/kg. This upper limit on the solution concentration is appropriate to study multi-

valent ions adsorption onto rutile (110) surface, which is normally measured at 10^{-4} or 10^{-5} mol/kg to stay well below the soluble limit of the ion carbonate or hydroxy might form in the solution where the pH is controlled to be above the ion adsorption edge. But for monovalent ions like Rb^+ no ordering of ions at the interface is observed for concentrations up to 10^{-3} mol/kg, as addressed in Chapter 3. Questions arise from these measurements: Is it that Rb^+ is not specifically adsorbed to the rutile (110) surface? Or, is the fraction of the total ions adsorbed is so low that the effect can not be seen by XSW method, especially in the presence of the larger fluorescence signal from solution? Because it utilizes the same fluorescence signal, EXAFS method shares the same problem. Also the XSW measures the ion location with respect to the bulk lattice, therefore the positions of the surface oxygen atoms and interfacial water molecules are not available, which are very important to understand the interfacial process, e.g., the precise ion oxygen distance would be a direct indication of what kind of bond forming at the interface; and the water molecule distribution would give a hint about the interfacial dielectric properties. So an independent method is needed which can be applied to probe the surface/interface structure without the above limitations. CTR is one candidate. By monitoring the weak intensities between the Bragg peaks, not only the adsorbate geometry, but also the interfacial structure can be solved.

Various studies show that the non-reconstructed TiO_2 (110) (1 × 1) surface is the most stable phase in the O_2 (> 10^{-4} Torr partial pressure) or wet environment.[31.] The CTR measurement of TiO_2 (110) surface in the vacuum shows that surface are terminated with the bridging oxygen rows and the 5-fold coordinated Ti atom rows alternatively with the

relaxation up to 0.25 Å for the first three layer of atoms.[35.] Those large relaxations and the possible reconstructions are come from the truncation of the bulk crystal, i.e., the minimization of the energy of the broken bonds. On the other hand, the study of rutile RuO_2 (110) surface in H_2O shows that the oxygen coordination shell around the Ru atom is completed by the adsorbed water molecule (or hydroxyl group).[70.] This indicates that the structure of the oxide surface could be quite different in vacuum and in contact with the aqueous solution. Although extensive efforts have been put to the rutile related study, there is still very little knowledge about the atomic scale surface structure for the rutile surface in contact with bulk aqueous solution. The details of such structure would set the foundation for the further studies concerning ion adsorption structure and interfacial chemistry.

5.2 Experimental details

5.2.1 Experiment setup

The CTR measurements were preformed primarily at beamline 1BM-C (XOR/ SRI-CAT) at Advanced Photon Source (APS), Argonne National Laboratory (ANL) {and at beamline 12BM-B, 11ID-D, and 12ID-D (BESSRC-CAT) at APS, ANL for the preliminary works}. At 1BM-C, a symmetrical Si (111) high heat load monochromator is used to select the X-ray energy of 14.9 keV for both TiO_2/H_2O and TiO_2/Rb^+ solution measurements (see Figure 5.1, beamline setup diagram.)[118] The incident beam was focused onto the center of the diffractometer both horizontally and vertically (with the

sagittal focusing monochromator and the vertical focusing mirror). The beam size is further reduced by a set of slit immediately in front of the diffractometer so that its size is $0.45(h) \times 0.3(v)$ mm^2 at the center of diffractometer (i.e., at the center of sample surface). The X-ray beam intensity after the incident slit is monitored (as I_0) with an ion chamber with pure dry N_2 gas flowing through. A CyberStar® scintillation detector was used to record the reflected X-ray beam intensity (as I_R) on the detector arm of the diffractometer at a distance of ~ 780 mm from the sample. The window setting of the detector amplifier is applied so that the primary elastic signal can be distinguished from low level electronic noise, harmonics in the incident X-ray beam (e.g., $\lambda/3$ from the Si(111) monochromator) and pulse pile-up due to large count rates. The signals that fall above the upper limit of the window are also recorded for the purpose of detector deadtime correction.

Cu-foil attenuators are inserted in front of the detector to measure the high reflectivity near the Bragg peaks. The attenuation factors of the different foils are calibrated during the measurements. The detector slits, immediately in front of the detector, define the Q resolution of the measurement and eliminate the diffuse background signals. Guard slits are put in between the detector slit and the sample to make sure that the only signal entering the detector are actually from the crystal-liquid interface other than scattering from sources such as the edge of the slits, the sample cell, etc.

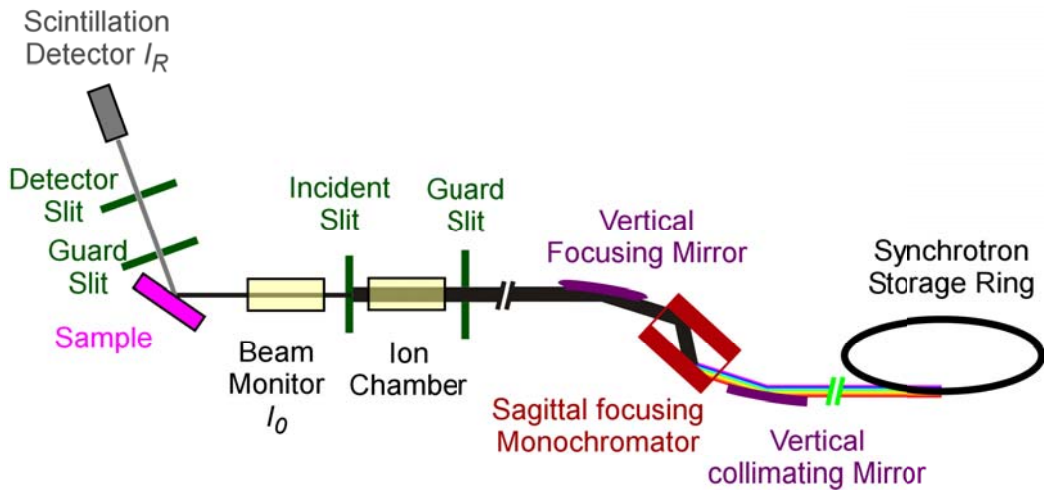

Figure 5.1. The schematic bending magnet beamline setup at 1BM (XOR), APS, ANL.

5.2.2 Geometry of the diffractometer

A six-circle diffractometer is used as a four-circle one. The axes of the 4-circle diffractometer, 2θ, θ, χ, and φ are used in stead of δ, η, ν, μ, χ, and φ. The orientation matrix is calculated and controlled by SPEC with FOURC geometry. Omega-equal-zero mode is used. The geometry relation we have as:

$$\theta = (2\theta)/2 = \sin^{-1}(Q*\lambda/4\pi) \tag{5.1}$$

$$Q^2 = Q_{\perp}^2 + Q_{//}^2; \tag{5.2}$$

$$\chi = ctg^{-1}(Q_{//}/Q_{\perp}); \text{ i.e. } \Psi = 90-\chi = tg^{-1}(Q_{//}/Q_{\perp}); \tag{5.3}$$

$$Q_{//}^2 = Q_X^2 + Q_Y^2; \tag{5.4}$$

$$\varphi = tg^{-1}(Q_Y/Q_X); \tag{5.5}$$

$$Q_X = (2\pi/a)*H; \qquad Q_Y = (2\pi/b)*K; \qquad Q_{\perp} = (2\pi/c)*L; \tag{5.6}$$

Here Q is the momentum transfer. $Q_{\perp}$ (also referred as Q_Z) and $Q_{//}$ are the sub-components of the momentum transfer along the surface normal direction ($[001]_S$ = [110] direction) and in the surface plane, respectively. The general relation has been described in Chapter 2 & 4. Q_Y and Q_X are the sub-components of $Q_{//}$ along X ($[100]_S$ = [-110]) and Y ($[010]_s$ = [001]) direction in the surface plane. a, b, and c are the lattice parameters of the non-primitive tetragonal unit cell. H, K, and L are the miller index of a point in the reciprocal space. Note here an orthogonal system is assumed, like in the case of rutile structure, to obtain the Equation (5.6) from a general expression Equation (2.17). For a crystal truncation rod, H and K should both be integers. E.g., for the specular rod, $H = K$

= 0.

The rutile bulk Bragg peaks, in primitive tetragonal notation, and the (110) surface truncation rods, in non-primitive tetragonal notations, are shown in reciprocal space in Figure 5.2. Only a quarter of the reciprocal space above the surface is shown. The other three can be achieved by the surface symmetries (two orthogonal mirror planes perpendicular to the surface along Q_x and Q_y direction, respectively.) Dashed lines indicate the weaker "oxygen only" rods, where Ti atoms have no contribution to the intensity. And the solid lines are the "strong rods" that have contributions from both lattice Ti and O atoms.

5.2.3 Details of CTR measurements

Care was taken to find a region on the crystal surface that was homogeneous (in terms of both structure and roughness) by measuring the reflectivity across the surface near a first mid-zone point, i.e., L = 1.1 on H = 0 & K = 0 rod (namely the 00_S rod), which is sensitive only to the surface structure. The final measured spot is at the center of the area, across which the mid-zone reflectivity is homogeneous. The area has the size about 2 or 3 times of beam footprint size (at L = 1.1 on 00_S rod) across, i.e., at least 1 millimeter in diameter. Under such conditions, even if there are relative motions of the X-ray beam over the sample surface during the measurements (e.g., caused by the minor misalignment, temperature change inside the hutch), the rods we measured can still be considered from the surface with the identical characterization so that one unique structure can be associated with all the data.

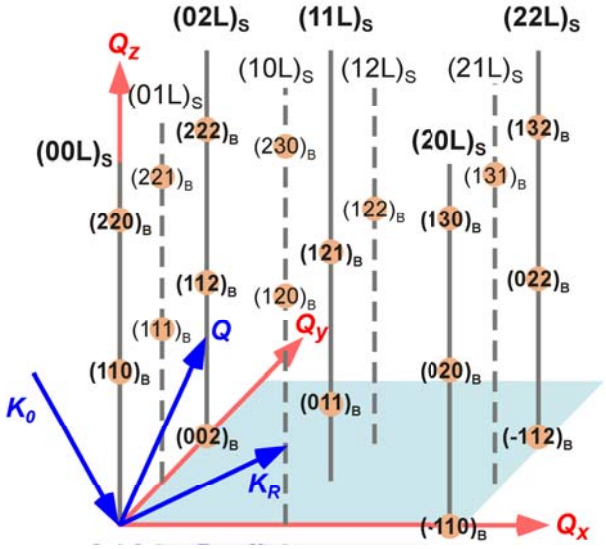

Figure 5.2. The bulk Bragg peaks (circles) and the surface truncation rods (solid and dashed lines) of rutile TiO_2 (110) surface in the reciprocal space. Dashed line indicates the weaker "oxygen only" rods, where Ti atoms have no contribution to the intensity. And the solid lines are the "strong rods" have contributions from both lattice Ti and O atoms.

The measurements were performed in-situ in a thin-film cell that was described previously in Chapter 3. Before each measurement, the solution between the Kapton film and the sample surface was minimized and the cell is sealed to maintain a minimal solution thickness during the whole CTR measurements. The minimal thickness of the solution is not as critical as in the XSW case. It does, however, help to reduce the angle-dependent attenuation at low Q, where the beam path through the solution is longer. The solution or water is occasionally flashed through the cell to prevent the cell from drying out.

The rutile TiO_2 (110) crystal is mounted initially in deionized ultra-filtered water (DIW, > 18 MΩ). And a full set of the CTR measurements, i.e., 00_S, 11_S, 20_S, 02_S rods, are carried out. A few fiducial points, i.e., L = 1.9 (blue squares, with Cu attenuator, therefore the intensity is multiplied by a factor of 0.032) and L = 1.1 (black diamonds), on 00_S rod, and L = 2.1 on 11_S rod (green triangles) are repeatedly checked. The fiducial points include the measurements of both bulk signal dominant (L = 1.9) and surface signal dominant (L = 1.1) points, which give us the sensitivity to any changes to either the crystal surface or the whole system. The integral intensities of the rocking scans are shown in Figure 5.3 (A). The intensities of L = 2.1 points on 11_S rod are scaled by a factor of 8 in the plot. The constant intensity at all fiducial points ensures that the surface was unchanged during the course of measurement.

Surface symmetry equivalent rods are checked for 11_S rod family, i.e., $(1, 1)_S$, $(1, -1)_S$, $(-1, 1)_S$, and $(-1, -1)_S$ rods. Both bulk dominant signal (L = 2.9 and L = 1.2) and surface dominant signal (L = 2.1 and L = 3.7) are checked for each rod. The integral

intensities are shown in Figure 5.4. The surface signal at L = 2.1 and L = 3.7 are multiplied by factors of 10 and 100, respectively. The intensities for each L position only fluctuate slightly, within 5% for the bulk signals and within 10% for the surface signals, which indicates that the systematic error for the off-specular rod measurements is small (< 10%) and the measured intensity modulation on the rod is dominated by the intrinsic surface structure, not the extrinsic factors, such as the setup or alignment error.

It has been known from the XSW measurement that when TiO_2 (110) surface is in contact with low concentration (< 10^{-3} mol/kg) of Rb^+ solution, which is the requisition of the XSW method, very few Rb^+ ions adsorbs directly onto the surface. To get more ions adsorbed to the surface, the 1 mol/kg RbCl solution, adjusted to pH = 12 with RbOH, is used for the CTR measurement of the TiO_2/Rb^+ interface structure. At this pH conditions, the TiO_2 (110) surface is further negatively charged than at lower pH. And with the high ionic strength, Debye length of diffuse double layer is going to be very short (a few Å). Therefore more Rb^+ ions will adsorb onto TiO_2 surface. The Rb^+ solution is injected into the cell to replace the DIW. For the experimental solution concentrations that were used, a single solution injection contains a substantial excess of ions with respect to the nominal available surface site density. For rutile in Rb^+ solution, 00_S, 20_S, 02_S, 11_S, and 40_S rods are measured with the exactly the same setup as the DIW measurements have. The fiducial points L = 1.1 (black diamonds) and L = 1.9 (blue squares) on 00_S rod are measured at the beginning, between different rods, and at the end of all the measurements to monitor the surface stability. Also measured as fiducial points

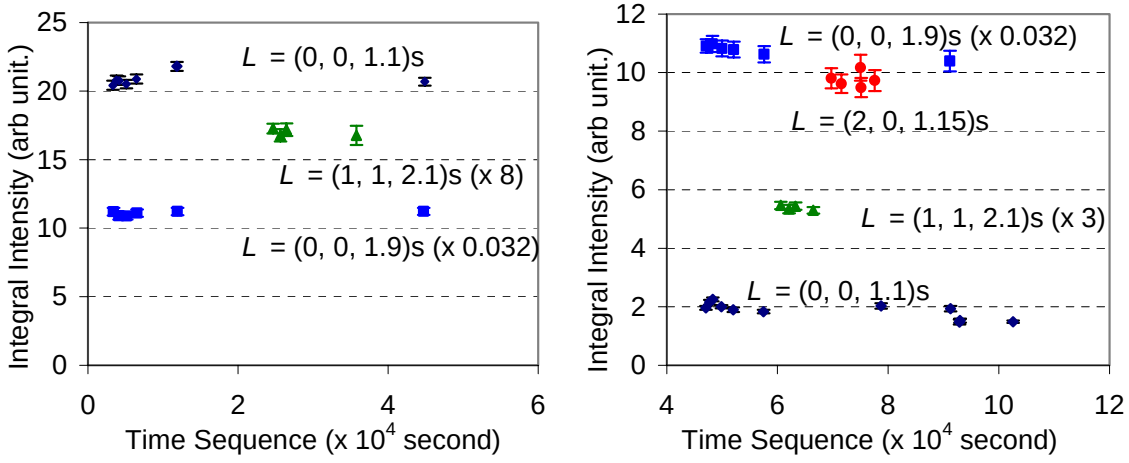

(A) (B)

Figure 5.3. The integral intensities on fiducial points for the measurements of rutile in (A) DIW and (B) Rb^+ solution. Primarily the L = 1.1 (black diamonds) and L = 1.9 (blue squares) on 00_S rod are used. Also monitored are points on the off-specular rod: L = 2.1 on 11_S rod (green triangles) in both DIW and Rb^+ solution, and L = 1.15 for 20_S rod in Rb^+ solution (red circles). The $(0, 0, 1.9)_S$ are multiplied by a factor of 0.032 due to the Cu attenuator used. The 11_S rod intensities are rescaled in the plot by a factor of 8 and 3 for DIW and Rb^+ case, respectively.

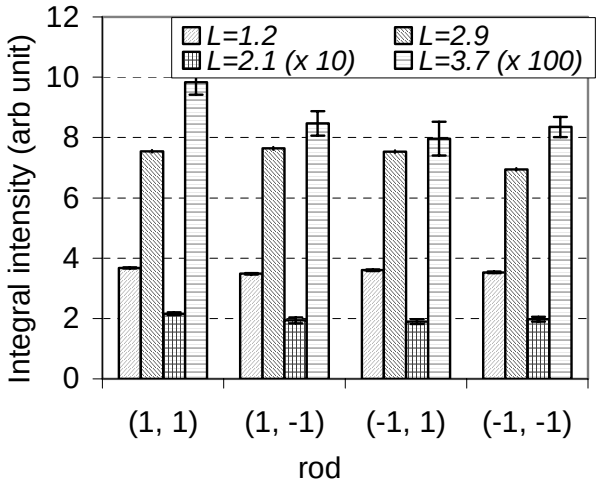

Figure 5.4. Measured integral intensity at L = 1.2, 2.1, 2.9 and 3.7 at the symmetry equivalent position on $(1, 1)_S$, $(1, -1)_S$, $(-1, 1)_S$ and $(-1, -1)_S$ rods. The surface signal at L = 2.1 and L = 3.7 are magnified by a factor of 10 and 100, respectively.

during the off-specular measurements are L = 2.1 on 11_S rod (green triangles) and L = 1.15 on 20_S rod (red circles). The integrated intensity is plotted out in Figure 5.3 (B). The intensities of points on 11_S rod are scaled by a factor of 3 on the plot. Again no significant change occurs during the whole measurement. The last few points at L = 1.1 on 00_S rod have 30% lower intensities than all the other measurements. That happened after flushing a fresh solution through the cell, which may have caused the sample to move slightly. And this lower intensity is stable during the final measurement, too. The change here is relatively small compared to the intensity drop upon the Rb^+ adsorption, which is almost a factor of 10 difference.

5.2.4 Data preparing details

The measured reflected X-ray signals are first corrected with the pileup correction. To do this it is assumed that all the counts in the detector upper level, i.e., above the upper limit of the signal window, are due to double pile-ups, which should be true in our case where the photon beam harmonics (e.g., λ/3) and multi-pileups are negligible. Thus, the total output count rate (*OCR*) from the detector should be

$$OCR = I_{window} + 2 * I_{upper} \tag{5.7}$$

Secondly applied is the deadtime correction of the scintillation detector with the equation:

$$OCR = ICR * exp(-ICR * \tau) \tag{5.8}$$

Where ICR, the input count rate, is the actual count rate of X-ray photons entering the detector; and τ is the time constant, which indicates the ability of a detector handling the

high count rate X-rays. τ depends on a few different conditions, such as the peaking time of the amplifier and the synchrotron storage ring fill pattern. But usually it is of the order of μs or tenths of μs. During our measurements, it is approximately $\tau = 2.74$ μs (Figure 5.5) with the Cyberstar peaking time set at 0.3 μs and the single bunch mode at APS. In the range we have data (*ICR* < 80 kcps), the calculation based on Equation (5.8) agrees with the data very well. As we can see, at the low count rate, e.g., < 10 kcps, there is hardly any difference between *OCR* and *ICR*. The higher *ICR* goes, the larger the deviation of *OCR* from *ICR*. We can either use Equation (5.8) to do the correction or insert beam attenuators to reduce the X-ray count rate. Either way some uncertainty is introduced as a price of gaining a larger dynamic range in measuring the reflected X-ray intensities.

In the cases that the filters are used, the attenuation factor needs to be normalized out after the deadtime correction, i.e., $ICR0 = ICR / ATTN$, where *ATTN* is the attenuation factor. *ATTN* can be either calculated based on the materials and the thickness of the attenuator and the X-ray energy. Or it can be measured with proper X-rays intensity.

Finally the corrected count rate at the detector *ICR0* is normalized to the incident beam intensity I_0 to get rid of any fluctuation in the incident beam (e.g., due to changes in the synchrotron storage ring (e.g., electron current) or the upstream optics) and the reflectivity is obtained as $R_M = ICR0 / I_0$. If absolute reflectivity is preferred, the incident X-ray photon flux can be estimated from the ion chamber count rate I_0 or the direct through beam intensity monitored with the calibrated attenuators. However, this estimation normally is not necessary since it is a constant factor in all the measurements.

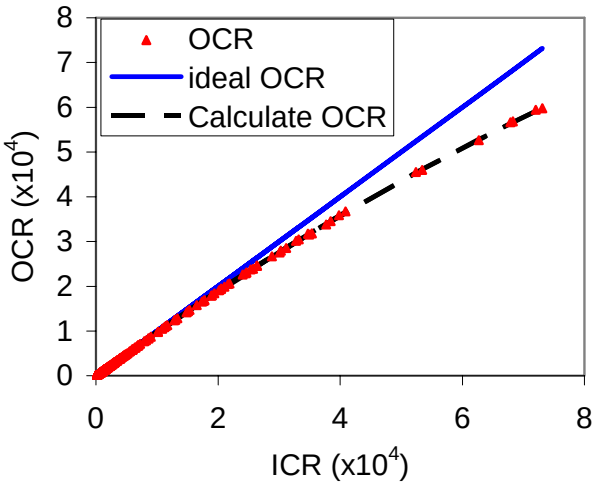

Figure 5.5. Deadtime correction of the Cyberstar detector with peaking time set at 0.3 μs and single bunch mode of APS fill pattern. Black dashed line is the calculation with the time constant $\tau = 2.74$ μs.

A prefactor can be applied in the afterward analysis to account for this. Another reason for not calculating this transform factor is that we use the integral intensity underneath the rocking curve instead of the peak intensity. The integral intensity is the convolution of the detector resolution (detector slit size related) and a segment of rod. In that sense the incident flux used as the normalization should be an integral too. This can be done with the measurement of the direct through beam at $\theta = 2\theta = 0$. The convolution of the detector slit with the incident beam is proportional to the incident beam intensity in the case that the detector slit size is fixed. If somehow, the detector slit size changes during the measurement, normalization to the detector resolution function ($|\boldsymbol{K}|(\Delta 2\theta)$) is needed, where $\Delta 2\theta$ is the FWHM of the detector scan at $2\theta = 0$ position and $|\boldsymbol{K}| = 2\pi/\lambda$ is the wave vector of X-ray beam. So in the case that the absolute reflectivity is not needed, it is simpler to use the beam monitor reading (I_0) and inserting a prefactor to account for the translation from the reading of the beam monitor to the integral incident intensity.

Once the measured reflectivity R_M is achieved, all the corrections listed in Chapter 2 need to be applied so that the normalized reflectivity R_N can be obtained and conveniently used in the structure fitting.

Except for a few points, the statistical errors for the measured reflectivity are very small (< 1%). However, to account for the (possible) systematic errors, the minimum error of 5% is applied on all data points.

5.2.5 Rutile-aqueous interface structure analyzing

The terminology of the surface atom positions are shown in Figure 5.6. TO is the

terminal oxygen; BO is the bridging oxygen; PO1 & PO2 are the two oxygen in the surface Ti-O plane; LBO is the lower bridging, i.e., the mirror image of the BO about the surface Ti-O plane; LTO is the lower terminal oxygen; LPO1 & LPO2 are the in plane oxygen in the second Ti-O plane (i.e., beneath the surface); TTi is the surface Ti bonded to the terminal oxygen; BTi is the surface Ti bonded to the bridging oxygen; LTi2 is the lower plane Ti which has the same geometry as BTi; LTi1 is the lower plane Ti which has the same geometry as TTi. The origin of the coordination system is at BTi position.

According to the theoretical calculations and the vacuum measurements, the TiO_2 (110) surface in DIW at room temperature and one atmosphere pressure (ambient condition) should have no significant reconstruction.[35,59] Therefore, a single non-primitive tetragonal unit cell is used as the basic structure unit. The bulk crystal is achieved by repeating the unit infinitely laterally and on one side of the crystal surface vertically. All the atom positions in the bulk are known and fixed. One more laterally infinite layer of the repeating unit is added to the surface to account for the surface layer of the crystal, which may undergo relaxations to some degree. Distinguished from the rutile surface in the vacuum, the terminal oxygen rows are thought to be present. All the atoms in this layer are able to relax from its bulk equilibrium position. And the initial relaxation are typically set < 0.1 Å. Water molecules are put onto such surface at different positions, e.g., the tetradentate position, bidentate position between two TO's, between two BO's, or between a TO and a BO, monodentate position above BO and their combinations are all explored.

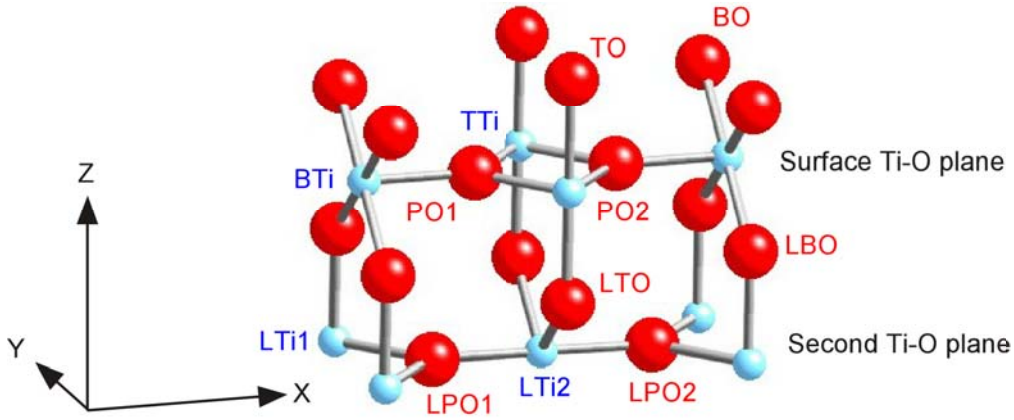

Figure 5.6. Schematic structure of the TiO_2 (110) non-primitive tetragonal unit cell. Shown here all the atoms are at their bulk crystal equilibrium positions. Atoms are labeled as they are called in the text. TO is the terminal oxygen; BO is the bridging oxygen; PO1 & PO2 are the two oxygen in the surface Ti-O plane; LBO is the lower bridging, i.e., the mirror image of the BO about the surface Ti-O plane; LTO is the lower terminal oxygen; LPO1 & LPO2 are the in plane oxygen in the second Ti-O plane; TTi is the surface Ti bonded to the terminal oxygen; BTi is the surface Ti bonded to the bridging oxygen; LTi2 is the lower plane Ti which has the same geometry as BTi; LTi1 is the lower plane Ti which has the same geometry as TTi. The origin is at BTi position.

The bulk water is modeled in two different ways, either as a structureless continuous profile, or as a layered fluid. For the layered water model, a series of Gaussian functions are distributed in layers extending from the interface into the bulk solution with an increasing Gaussian width as the distance from the interface increases. For the structureless water model, the water is treated as the medium without any internal structure and follows the error function profile. Unless it is found to be absolutely necessary to explain the data, the structureless water model is assumed to be preferable to the layered water model. The total thickness of the water layer is taken as the actual water thickness plus the plastic layer (Kapton window) thickness. This is based on the fact that the densities of the plastic and water are very close and the approximation simplifies the calculation. A total thickness of greater or equal to 10 μm—7.5 μm of kapton plus ≥ 2 μm water—is used typically.

For the atoms below the surface Ti-O plane in the TiO_2 crystal lattice, no lateral offset is allowed except for the surface in-plane oxygen atoms because of the restriction from the bulk symmetry. Only relaxations along the surface normal direction are allowed. For the surface in-plane oxygen atoms, the lateral relaxation, which primarily caused by the relaxation of the Ti atoms along the surface normal direction, can only occur along X-direction ([-110]). The BO, TO and the adsorbate at the interface, on the other hand, are given the freedom to move laterally. For BO atoms, however, because of the double bonds to the Ti atoms underneath, the offset along y-direction ([001]) is not allowed.

The symmetry of TiO_2 (110) surface is applied so that symmetry equivalent atoms are restricted to have the same symmetry equivalent relaxations. E.g., if one of the in-

plane oxygen atoms (say, PO1) moves 0.1 Å along X-direction ([-110]), the other in-plane oxygen atom (PO2) will have the offset of -0.1 Å from its equilibrium position. And for the adsorbate, it also means that the occupancies of an adsorbate at the symmetry equivalent positions are the same.

The vibration amplitudes of the atoms and adsorbates are included for calculating the Debye-Waller factor. Because of the anisotropy of the crystal structure, the vibration amplitudes are different along different directions. The projection of the 3d vibrational amplitude along the momentum transfer, $\boldsymbol{Q}$, direction is the quantity that affects the measured intensity. The vibration amplitudes along the three primary axes for each atom in rutile crystal are known.[112.] Therefore we can calculate the vibration amplitude along any direction. For the surface atoms, the adsorbate, and the bulk water molecules (isotropic vibration applied), the primary vibration amplitudes can be included as the fitting parameters.

Generally, the thermal vibration parameters are:

$$\begin{pmatrix} U_{11} & U_{12} & U_{13} \\ U_{12} & U_{22} & U_{23} \\ U_{13} & U_{23} & U_{33} \end{pmatrix} \tag{5.9}$$

where U_{11}, U_{22}, U_{33}, are along three axes $\boldsymbol{x}$, $\boldsymbol{y}$, and $\boldsymbol{z}$. Along a random direction $\boldsymbol{Q}$, the vibrational amplitude square is

$$U(\boldsymbol{Q}) = (X, Y, Z)\begin{pmatrix} U_{11} & U_{12} & U_{13} \\ U_{12} & U_{22} & U_{23} \\ U_{13} & U_{23} & U_{33} \end{pmatrix}\begin{pmatrix} X \\ Y \\ Z \end{pmatrix} \tag{5.10}$$

where the thermal Debye-Waller factor is $\exp(-|\boldsymbol{Q}|^2 U(\boldsymbol{Q})/2)$. Here X, Y, and Z are the

direction cosine of vector $\boldsymbol{Q}$ with respect to the three axes, i.e., $X = \cos^{-1}(|Q_x|/|\boldsymbol{Q}|)$, $Y = \cos^{-1}(|Q_y|/|\boldsymbol{Q}|)$, $Z = \cos^{-1}(|Q_z|/|\boldsymbol{Q}|)$, where Q_x, Q_y and Q_z are the component of $\boldsymbol{Q}$ along $\boldsymbol{x}$, $\boldsymbol{y}$, and $\boldsymbol{z}$ axis direction, respectively.

For rutile crystal, $U_{11} = U_{22}$, and $U_{23} = U_{13} = 0$. It turned out that the $U_{11} + U_{12}$ and $U_{11} - U_{12}$ directions are the principal axes of the thermal vibration ellipsoid, which are simply the rutile [110] and [-110] direction. Considering the non-primitive tetragonal unit cell has [110] as $[001]_S$, and [-110] as $[100]_S$, [001] as $[010]_S$. The principal axes are simply the axes of the rutile non-primitive tetragonal unit cell axes. If the direction cosine of the vector $\boldsymbol{Q}$ with respect to the non-primitive tetragonal unit cell axes are *X0*, *Y0*, and *Z0*, $U(\boldsymbol{Q})$ can be easily calculated as:

$$U(\boldsymbol{Q}) = (X0)^2(U_{11} + U_{12}) + (Y0)^2(U_{11} - U_{12}) + (Z0)^2U_{33}. \quad (5.11)$$

Because of the freedom of the adsorbate and the surface atoms, there would be more than 50 fitting parameters if all the structure parameters were allowed to be fitted independently. The fitting might be trapped at some local minimum so that the best parameter set, which corresponds to the actual structure, is missed. In practice, the fewer parameters, the better. The primary structure parameters, e.g., the positions and the occupation factors of the surface atoms in the first 3 layers and the adsorbate, which are normally significantly affect the structure factor, are always fitted. Other parameters, such as the relaxation of the atoms far away from the surface, the vibration amplitudes of the adsorbate, which has minimal effect on the structure factor, are normally fitted separately by varying only one or a few of them at a time while others fixed at the

optimized values.

For instance, normally the vibration amplitudes are smaller than the resolution we have, which means they are not uniquely defined by the data. So first the vibration amplitudes are fitted together with other primary parameters. Once a reasonable value obtained, the vibrational amplitudes are fixed in value and other primary parameters are fine-tuned. With this method, an optimal structure is obtained with fixed values of all the non-primary parameter and optimized values of the primary parameters. Finally the effect of varying the vibration amplitude is checked again to make sure the fitting quality (χ^2) is not changing at the vicinity of the current values.

The fitting results are checked for the physical and chemical feasibility, e.g., the packing density of the adsorbate and the bond length. For instance, given the surface area of a non-primitive tetragonal unit cell, a dense adsorbed water layer should have a coverage very close to 2 ML, i.e., two water molecules per rutile (110) surface unit cell (19.22 $Å^2$ in area), which is very similar to the 2-D pack density of liquid water—1 water molecule per ~ 10 $Å^2$. Any significant higher or lower number suggests deficiencies of the model and/or experimental data.

5.3 Results and discussions

5.3.1 The fitting result

The measured miscut of the TiO_2 (110) crystal surface is ~ 0.08°, which translates into the size of the terrace between adjacent steps is ~ 0.2 μm in average given that the

single step height on (110) surface is 3.25 Å. This number agrees well with what is shown on the AFM image in Chapter 3. Under such condition, the terrace sites are the dominant sites on the surface rather than the step edge sites, which validates the structure unit and the symmetry applied in the fitting/calculation on the surface, as discussed above. The lateral domain size, L, which can be estimated with the rocking curve width where the resolution is enough, is larger than 0.1 μm.

The fractional occupation factor, β ($0 < \beta < 1$), describes the surface roughness. In the model, the occupation factor of a full layer in the bulk is 1. At interface, the first partially occupied layer on the bulk crystal has an occupation factor β. For the next partial layer the occupation factor is β^2, and the next β^3, and so on. $\beta = 0$ corresponds to a perfect flat surface and $\beta = 1$ a very rough one. The β factor describes a randomly occupied layer without ordering or domains. β from the fitting is always smaller than 0.05 (± 0.03), which translates into $\sigma_{rms} = \frac{\beta^{1/2}}{(1-\beta)} d \leq 0.75$ Å. This means the roughness on the sample we measured is negligible. Therefore in the fine tuning of the structural fitting parameters, we set $\beta = 0$.

When lateral offsets of the TO and BO atoms are allowed, one BO position will split into two positions and one TO position could split into 4 different positions—with the equal occupancies at each possible position, i.e., ½ for each BO position and ¼ for each TO position. The occupancy of TO site is allowed to change since the oxygen (or oxygen group) at this site suppose to be coming from the external source other than the rutile crystal itself, i.e., the H_2O or OH^- from the bulk solution. Allowing this occupancy

to change is to check the long-time assumption that the rutile (110) surface immersed in the aqueous solution would gain the fully oxygen covered/terminated surface. The fitting yields the coverage of the TO atoms just at 1.03 ± 0.05 ML, as expected.

The measured CTR data are largely insensitive to the total water layer thickness, including both the water and kapton window (with fitted values of 15 ± 15 μm; the large error bar which means not well defined.). The thickness affects only the path length of X-rays, which is proportional to $1/\sin\alpha$, where α is the incident angle of X-ray on the surface. This effect is more significant at small $\boldsymbol{Q}$ with the correction term to the reflectivity $\exp\left(-\frac{T}{\sin(\alpha)t}\right)$, where T is the thickness and t is the attenuation length of water at the given energy. Changes of a few μm in the total thickness have almost no effect on the fitting results. Therefore, the total thickness is fixed at 15 μm.

The CTR data of rutile (110) surface in contact with DIW and 1 mol/kg RbCl solution at pH = 12 are shown in Figure 5.7. The data points show the integral intensities of the rocking scans taken at the given Q value. Lines show the best fits to the data.

Table 5.1 is the list of the primary fitting parameters for TiO_2 in (A), DIW and (B), 1 mol/kg Rb^+ solution.

The fitting results for both DIW and Rb^+ solution show that the surface atoms have minimal lateral relaxation but observable relaxations along surface normal direction, including the TTi and BTi atoms and BO and TO atoms. Other relaxations are all relatively small.

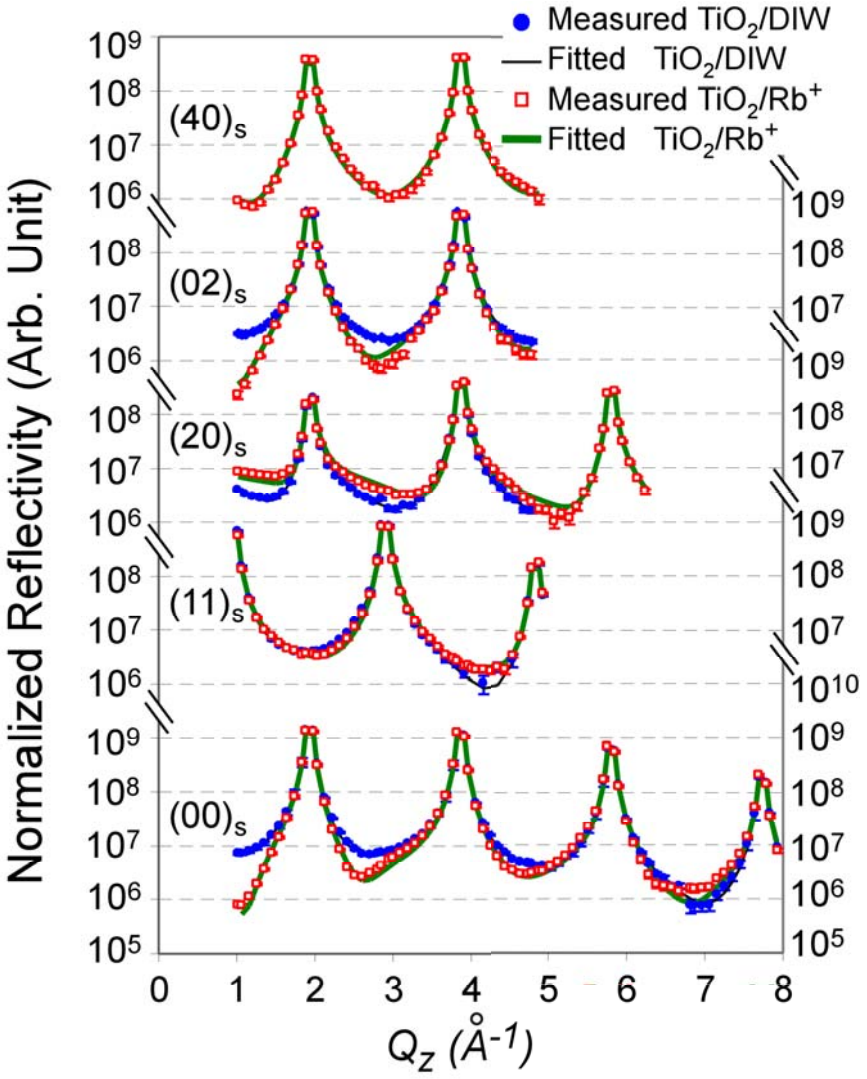

Figure 5.7. The CTR data of rutile (110) surface in contact with DIW (blue filled circles) and 1 mol/kg RbCl solution adjusted with RbOH to pH = 12 (red open squares). The lines are the best fits to the data.

For the TiO_2 (110) surface in DIW, the adsorbed water molecules are found in a few different positions, including the site tetradentate to two TO and two BO atoms, the site bridging one TO and one BO atom, and the site bridging between two TO atoms. The total coverage of the water molecules at these positions are around 2 ML, which agrees with the bulk water density. Above these adsorbed water molecules, there is no further structured water observed.

For the TiO_2 (110) surface in Rb^+ solution, the adsorbed species are assumed to be Rb^+ ions instead of water molecules. The fitted positions are pretty much similar to what water molecules would take at the TiO_2 (110) —DIW interface, including the tetradentate site, and two bidentate sites between TO and BO and between two TO's, respectively.

The total coverage at the interface, if all the sites are occupied by Rb^+ ions, is ~ 1 ML, which is well below the theoretical full packed density (~ 2 ML). This means that not all the sites are occupied by Rb^+ ions. Instead some of the adsorbed species must be water molecules. On the other hand, if all the sites are occupied by water molecules, the coverage required by the total electron density would be > 4 ML, which is also impossible. Directly comparing the lateral averaged electron density profile as a function of the distance from the interface, as shown in Figure 5.8, the higher interfacial electron density can be seen for the rutile-Rb^+ solution interface. To account for the increase of the electron density, the Rb^+ ions are required to be present at the interface. We can also fit the TiO_2/Rb^+ data with a mixture of Rb^+ ions and water molecule at different sites.

Table 5.1. The fitting parameters and the results of the fitting to CTR data of (A), rutile (110) surface in DIW and (B) rutile (110) surface in 1 mol/kg Rb^+ solution.

(A)

	Atom	*X0* (Å)	*X* (Å)	*Y0* (Å)	*Y* (Å)	*Z0* (Å)	*Z* (Å)	Occupancy (ML)
Surface Layer Atom Positions	**LBO**	0.00	0.00	1.48	1.48	-1.27	**-1.21(1)**	1.00
	BO	0.00	0.00	1.48	1.48	1.27	**1.17(4)**	1.00
	PO1	1.98	**2.00(5)**	0.00	0.00	0.00	**0.02(1)**	1.00
	LTO	3.25	3.25	1.48	1.48	-1.98	**-1.96(1)**	1.00
	TO	3.25	3.25	1.48	1.48	1.98	**2.13(3)**	**1.01(5)**
	PO2	4.52	**4.50(5)**	0.00	0.00	0.00	**0.02(1)**	1.00
	BTi	0.00	0.00	0.00	0.00	0.00	**0.07(1)**	1.00
	TTi	3.25	3.25	1.48	1.48	0.00	**-0.13(1)**	1.00
Adsorbed H_2O	**O2**		**1.13(12)**		1.48		**4.05(8)**	**0.46(10)**
	O2		**5.37(12)**		1.48		**4.05(8)**	**0.46(10)**
	O1		**2.21(5)**		0.00		**3.51(4)**	**0.34(5)**
	O1		**4.29(5)**		0.00		**3.51(4)**	**0.34(5)**
	O3		0.00		0.00		**3.66(7)**	**0.17(3)**
	O3		0.00		0.00		**3.66(7)**	**0.17(3)**
Bulk H_2O			-	-	-		***5.59(15)***	*1.90*

$\chi^2 = 2.088$; $\chi^2(r) = 2.309$; Scale factor = 23137(231). *

(B)

Surface Layer Atom Positions	**LBO**	0.00	0.00	1.48	1.48	-1.27	**-1.31(2)**	1.00
	BO	0.00	0.00	1.48	1.48	1.27	**1.28(2)**	1.00
	PO1	1.98	**1.98(3)**	0.00	0.00	0.00	**-0.03(2)**	1.00
	LTO	3.25	3.25	1.48	1.48	-1.98	**-2.05(1)**	1.00
	TO	3.25	3.25	1.48	1.48	1.98	**2.06(2)**	**1.00(4)**
	PO2	4.52	**4.51(3)**	0.00	0.00	0.00	**-0.03(2)**	1.00
	BTi	0.00	0.00	0.00	0.00	0.00	**-0.06(2)**	1.00
	TTi	3.25	3.25	1.48	1.48	0.00	**0.05(2)**	1.00
Adsorbed Rb^+	**Rb2**		**2.18(8)**		1.48		**3.97(6)**	**0.12(2)**
	Rb2		**4.31(8)**		1.48		**3.97(6)**	**0.12(2)**
	Rb1		**1.32(5)**		0.00		**3.45(3)**	**0.21(1)**
	Rb1		**5.18(5)**		0.00		**3.45(3)**	**0.21(1)**
	Rb3		0.00		1.48		**2.95(3)**	**0.12(1)**
	Rb3		0.00		1.48		**2.95(3)**	**0.12(1)**
Bulk H_2O			-	-	-		***5.42(15)***	*1.90*

$\chi^2 = 7.122$; $\chi^2(r) = 7.647$; Scale factor = 22049(330). *

* In both cases, the water layer thickness is set at 15 μm, and no surface roughness included, i.e., surface fractional occupation factor $\beta = 0$. $\chi^2(r)$ is the χ^2 divided by the data point number minus fitting parameter number.

Due to the difference of the form factor between Rb^+ and H_2O, the fitting quality is slightly different. But the final electron density profile is very much the same as the one obtained with only Rb^+ ions. The actual number density of Rb^+ ions and water molecules at the interface can be estimated based on the constrain of the sizes of Rb^+ ion and water molecule combined with the total electron density. The estimated Rb^+ ion coverage is ~ 0.4 ML.

Shown in Figure 5.9 are the ball-and-stick models for the interfacial structure of TiO_2/DIW and TiO_2/Rb^+ interface.

5.3.2 Degeneracy of the current data set

One significant draw back of these first measurements for both TiO_2/DIW and TiO_2/Rb^+ is that only a subsets of rods, where $H + K = 2n$, n is integer, are measured. Thus two atoms with the same heights that are laterally displaced by half the surface unit cell diagonal distance yield exactly the same structure factor for the measured rods, e.g., displacing an atom from (x, y, z) to ($x+a/2$, $y+b/2$, z), the structure factor does not change. Note the relations stated earlier in Equation (5.6), $Q_X a = 2\pi H$ and $Q_Y b = 2\pi K$, we have:

$$\begin{aligned} F_1' &= \sum_i f_i \exp\left[-i\mathbf{Q}\cdot\left(\mathbf{r}+\frac{\mathbf{a}}{2}+\frac{\mathbf{b}}{2}\right)\right] = \sum_i f_i \exp\left[-i\left(Q_x x + Q_y y + Q_z z\right) - i\left(\frac{Q_x a}{2}+\frac{Q_y b}{2}\right)\right] \\ &= \sum_i f_i \exp\left[-i\left(Q_x x + Q_y y + Q_z z\right)\right]\exp\left[-i(H+K)\pi\right] \\ &\underline{\underline{H+K=2n}} \sum_i f_i \exp\left[-i\left(Q_x x + Q_y y + Q_z z\right)\right]\exp\left[-i2n\pi\right] \\ &= \sum_i f_i \exp\left[-i\left(Q_x x + Q_y y + Q_z z\right)\right] \\ &= \sum_i f_i \exp\left[-i\mathbf{Q}\cdot\mathbf{r}\right] = F_1 \end{aligned} \tag{5.12}$$

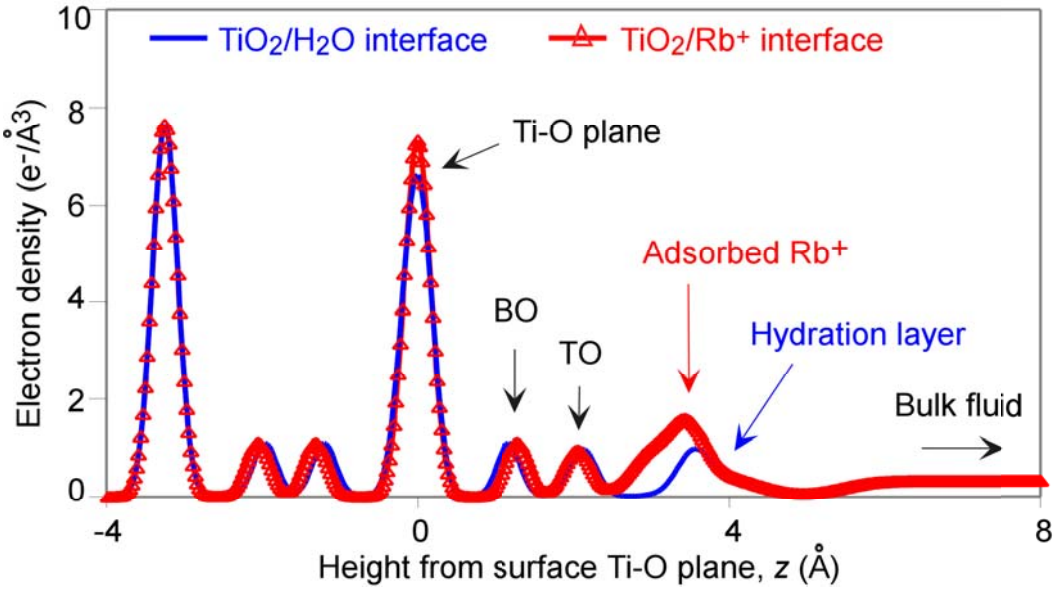

Figure 5.8. The lateral averaged 1-dimensional electron density profile at rutile-DIW and rutile-Rb^+ (1 mol/kg) interface.

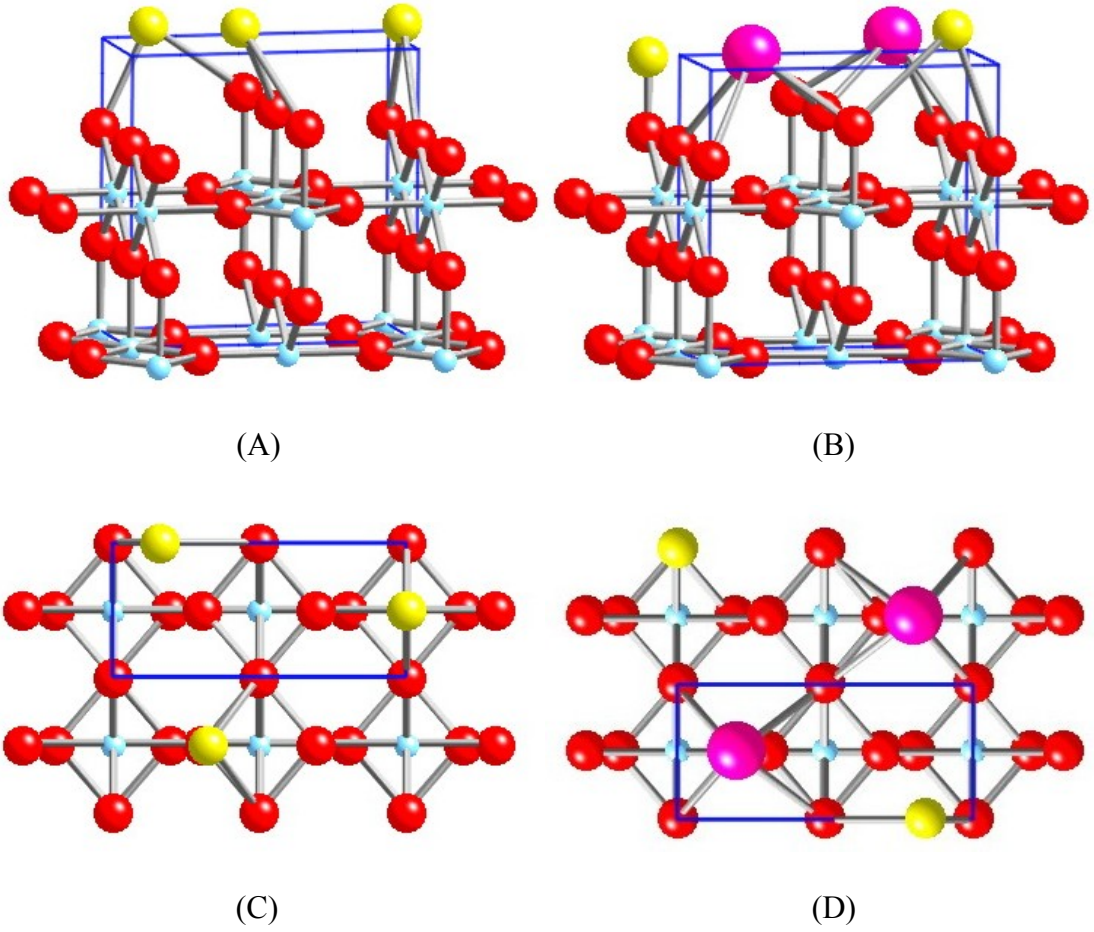

Figure 5.9. Ball-and-stick model for the adsorption structure at the rutile (110)-aqueous interface. (A) & (B), perspective views of the rutile-DIW and rutile-Rb^+ interface, respectively; (C) & (D), top views of rutile in DIW and Rb^+ solution, respectively. Shown in red are the bulk O atoms, in cyan the Ti atoms, in yellow the adsorbed water molecules, and in purple the adsorbed Rb^+ ions. Two adsorption positions in the Rb^+-rutile interface case are assigned as water molecules based on the comparison of the achieved electron density profile with the one from DIW-rutile interface.

This leads to a degeneracy of the fitted structure. It means that structures with the same atom displaced by (*a*/2, *b*/2) can not be distinguished from each other. For instance, for the two surface Ti atoms, BTi and TTi, one moves upwards and the other moves downwards. But we can not tell which one is up, which is down, because both configurations yield exactly the same structure factor for the rods measured. It also implies that any adsorbate position can also be displaced by (***a***/2, ***b***/2) away from the proposed position or even be distributed between these two positions. Measurements of additional rods with $H + K = 2n + 1$ are needed to eliminate the degeneracy. (The measurements have already been done. Data analyzing is in progress.)

5.3.3 Criteria to judge a good fit from a bad one

Normally we have the total number of fitting parameters between 15 and 20. For the non-linear χ^2 fitting we are working with, this usually leads to a very complex contour in χ^2 space, which could easily have the fitting ended up with some local minimum but not yield the real structure. Finding the real structure actually relies on the proper starting structure. This means the current analysis of CTR is model dependent. And to be sure with the fitting results, we not only have to compare the χ^2 obtained from the different fitting processes, also need to check the feasibility of the result structures. Considering the degeneracy issue discussed above, this is even more important at this stage since we may be able to eliminate some configurations of the atoms or adsorbates based on the measured inter-atom distances. Listed in Table 5.2 are some of the important inter-atom distances. The possible positions due to the degeneracy are labeled

with a prime.

As shown in Table 5.2 (A), the distance between the surface Ti atoms and the surface TO and BO atoms are listed first. The listed BTi and TTi' and TTi and BTi' are two pairs of degenerated positions. And the Ti-O distances are different by up to 0.2 Å. However, this is not large enough to rule out a possible configuration in spite of the expectation of the small relaxation/distortion of the TO and BO atoms and Ti-O bond length. In the bulk TiO_2 crystal, the Ti-O bond lengths are 1.94 and 1.98 Å, respectively. At the surface in the vacuum, Charlton et. al. report that the Ti-O bond length could be as small as 1.71 Å.[35.] Both sets of bond length numbers we have are larger than that, which means we have smaller bond contractions. But the TTi' to TO distance is suspiciously large, which maybe an evidence that this is not the right configuration. The definite answer needs the new data to be analyzed. For the adsorbed H_2O molecules, the O-O distances are all acceptable except H_2O_3'-TO distance, which is too small therefore can be eliminated. Therefore we can hardly tell which of the degenerated positions the adsorbates could be the correct one. And unlike the surface Ti atoms, the adsorbed water molecules theoretically could be at any lateral position. So it is also possible that both of the degenerate positions are occupied somehow.

Table 5.2. The inter-atomic distance at (A) rutile-DIW and (B) rutile-Rb^+ interface with degenerations.

(A)

	Coordinates (Å)			Inter-atomic Distance (Å)	
	X	*Y*	*Z*	BO	TO
BTi	0.00	0.00	-0.13	1.97	4.22
BTi’	0.00	0.00	0.07	1.84	4.12
TTi	3.25	1.48	0.07	3.43	2.06
TTi’	3.25	1.48	-0.13	3.50	2.26
H_2O_2	± 1.13	1.48	4.05	3.09	2.87
H_2O_2’	± 2.12	0.00	4.05	3.87	2.68
H_2O_1	± 2.21	0.00	3.51	3.54	2.27
H_2O_1’	± 1.04	1.48	3.51	2.56	2.60
H_2O_3	0.00	0.00	3.66	2.89	3.88
H_2O_3’	3.25	1.48	3.66	4.09	1.53

(B)

	Coordinates (Å)			Inter-atomic Distance (Å)	
	X	*Y*	*Z*	BO	TO
BTi	0.00	0.00	-0.06	1.99	4.15
BTi’	0.00	0.00	0.05	1.92	4.09
TTi	3.25	1.48	0.05	3.47	2.01
TTi’	3.25	1.48	-0.06	3.51	2.12
Rb_2	± 2.18	1.48	3.96	3.46	2.19
Rb_2’	± 1.07	0.00	3.96	3.25	3.26
Rb_1	± 1.32	0.00	3.45	2.93	2.80
Rb_1''	± 1.93	1.48	3.45	2.90	1.91
Rb_3	0.00	1.48	2.95	1.67	3.37
Rb_3’	3.25	0.00	2.95	3.94	1.72

Similar observations are found for the Rb^+ case. The relaxations of surface Ti atoms are less and there are slightly differences between the adsorbate positions. The electron densities contributed from H_2O_2 (at the TiO_2-DIW interface) and Rb_2 (at the 1 mol/kg RbCl-TiO_2 interface) are quite similar, which implies that the water molecules occupy the position solely even in the high concentration Rb^+ solution. The positions of H_2O_1 and Rb_1 are similar, too. But the electron density of Rb_1 is significantly higher than the H_2O_1, which suggests Rb^+ ions replace all or some of the water molecules at this position. The Rb_3 position is significantly different from that of water molecule H_2O_3, i.e., closer to the TiO_2 surface as well as shifted laterally, which may be induced by the adsorption of Rb^+ at the position 1. It is hard to tell whether it is all H_2O molecules, all Rb^+ ions, or maybe both present at this position. The limitation of the coverage does not help to determine the species and the coverages at Rb_3 because the species and the coverages at Rb_1 position are unknown either.

The Rb-O bond length restriction could be applied to eliminate some of the degeneracy. For the Rb_1' and Rb_2 configurations, there are Rb-O distances significantly smaller than expected. Thus these two degenerated positions can be ruled out. The Rb_3 position, however, can not be worked into the criteria since both degenerated positions have one Rb-O distance smaller than its normal value. One possibility is the lateral position is not at the position currently assigned. The lateral position is not fitted because the structure is inherent from that of TiO_2 (110)-DIW interface. The further analysis is needed to solve the structure, including the rods present here and the additional rods measured at a later time.

5.3.4 Significance and limitations of the CTR results

With CTR method, we also measured the interfacial structure of TiO_2 (110) surface in contact with the 10^{-4} mol/kg Sr^{2+} solution at pH = 10.7 (data and the analysis not shown in this thesis). Because the solution condition is exactly the same as those in the XSW measurements, the interfacial structure should be same. Only the 00_S rod is measured for Sr^{2+}, so that no lateral Sr^{2+} position is obtained from the CTR measurement. However, the Sr^{2+} position along the TiO_2 (110) surface normal direction is achieved and it agrees well with the XSW measurements. Such a measurement first removes the module-d ambiguity of the XSW measurements and directly reveals that the Sr^{2+} ions (as well as other multi-valent ions) are adsorbed at the TiO_2 (110)-aqueous interface as inner-sphere complexes, not below the surface or in the diffuse double layer. It also confirms that both the XSW and CTR measurements yield the actual interfacial structures, which are directly comparable.

The adsorbed Rb^+ ions primarily occupy the tetradentate sites, which is also the primary adsorption sites of Sr^{2+} and Y^{3+} ions based on the XSW measurements. Given the fact that without any ions in the aqueous solution, the water molecules occupy the same site, it is reasonable to believe that the tetradentate site is the site on the surface with the lowest potential thus the primary position to fill when an adsorbate comes onto the surface. The alkali metal ions, including Rb^+, used to be thought as the "indifferent background ions", which are only present in the diffuse part of the double layer. The measurements here directly prove that picture is incorrect. Just like the multi-valent ions, Rb^+ ions also adsorb specifically at the interface, only with a much weaker interaction

strength. Comparing with the Sr^{2+}, which yield ~ 0.4 ML with pH = 10.7 in $[Sr^{2+}] = 10^{-4}$ mol/kg solution. Rb^{+} ions show significant adsorption only in the pH = 12, $[Rb^{+}] = 1$ mol/kg solution. Therefore when present in the solution at the same time, the Rb^{+}, as well as other alkali metal ions, is normally out-competed by the multi-valent ions in the condensed double layer. From the ionic strength dependence measurements, it is demonstrated that even when the alkali metal to divalent ion ratio is as high as 10^{5}, there is no significant displacement of the divalent ion adsorbed at the rutile (110) surface. This suggests the binding constant for alkali ions is more than 5 orders of magnitude smaller than that of the multivalent ions.

As the discussions shown above, the CTR measures the electron density of the interfacial system. But it has no ability to reveal element specific information. In systems where more than one species occupies the same or similar position, the CTR method has difficulty revealing the occupation factor of each of the species.

Also as an X-ray method, for which the scattering power of an atom is proportional to the number of electrons it has, it works better for heavy elements, but not that good for light elements. And to be able to probe the ions in the presence of aqueous solution, larger atomic number is preferred because the contrast between the ion and the O from the water molecule is the key to see a significant CTR intensity change. For instance, according to the simulation, if instead of Rb^{+}, Na^{+} is used as the ion in the solution, the CTR change from the one in DIW would be negligible assuming the same interfacial structure. And it is practically impossible to probe hydrogen or protons in the oxide-aqueous system, which plays important role in the oxide-aqueous interfacial

processes. Neutron scattering and/or simulations could help on this point.

Comparing the structure of the TiO_2 (110) crystal surface in the aqueous solution with that in vacuum, we see smaller relaxations of the atoms from their bulk lattice positions. This can be explained in a simple way that the coordination shell of the surface atoms are all completed by the species from the solution. This absence of dandling bonds means that large structural relaxations are not needed to compensate for local changes in coordination. Finally, the crystal surface structure in DIW and in high concentration Rb^+ solution are very similar, which suggests the TiO_2 (110) surface structure are stable and reproducible in the aqueous solution. This provides us with a base structure for probing the adsorbed ions at the TiO_2 (110)-aqueous solution interface.

5.4 Conclusion

CTR measurements are carried out on rutile TiO_2 (110) surface in both DIW and 1 mol/kg RbCl solution. Specular and a subset of the non-specular rods are measured. Rutile surface relaxation is observed to be minimal, because the coordination shell of the surface atom is completed by the species (H_2O or OH^-) from the solution. In the aqueous solution, the terminal oxygen rows are fully recovered as compared with the surface in high vacuum. An additional water layer is observed on top of surface oxygen (TO and BO) in DIW. The water molecules in this layer are highly localized around available surface sites, namely, tetradentate and bidentate sites. No more water structure is found farther away from the interface.

For the rutile surface in Rb^+ solution, the Rb^+ ions primarily take the tetradentate sites—replacing some or all of the water molecules. This implies that the alkali metal ions are not just the indifferent background ions in the solution. Instead, at the rutile (110) surface, it behaves like other ions (e.g., Sr^{2+}, Y^{3+}, Zn^{2+}) but with a weaker adsorption strength. That explains the low coverage of Rb^+ at rutile (110) aqueous interface at lower concentration (< 10^{-3} mol/kg) because under those conditions the amount of ordered (i.e., adsorbed) ions is too small for the XSW measurements to observe a condensed layer in the presence of the background electrolyte concentration plus the ions in the diffuse layer. By going to high concentration such as 1 mol/kg, the Rb^+ coverage is increased so that it can be directly probed with CTR method. Although it is not directly measured by the CTR data, the coverage of the Rb^+ can be estimated as ~ 0.4 ML.

The measured surface BO, TO position together with the adsorbed H_2O molecule and Rb^+ ion positions are in good agreement with the MD simulations.[40,86] This further enhances the validity of the MD simulation about the rutile (110)-aqueous interface structure.

Because of the chosen subset of the rods we measured, we have a structural degeneracy in the results. Further analyzing the new data from other rods is needed to put more restriction and more confidence on the current results.

Chapter 6 Ongoing and future work

6.1 Further information desired for EDL

At the current stage, condensed layer ion locations at the rutile (110) aqueous interface have been successfully obtained for various ions, including the monovalent (Rb^{+}), divalent (Zn^{2+}, Sr^{2+}), and trivalent (Y^{3+}) ions. Also the surface structure in contact with the aqueous solution has been determined. The effect of the solution ionic strength on the divalent ion adsorption was investigated and no changes are observed over more than 3 order of magnitude changes in ionic strength. The partitioning of the ions in the condensed and diffuse double layer is modeled and compared to the measured coherent fractions and positions from the rutile (110) reflection for the divalent ions. No significant amount of divalent ions is found in the diffuse layer.

While a substantial amount of new information has been revealed for the EDL structure, there are more issues that need to be explored. First the coordination numbers of the adsorbate are of broad interest for their direct indication of the chemical and the bonding state of the ion. Our measurements are only carried out at a pH value where the ion uptakes reach the plateau in the powder titration measurements. The question about whether the adsorption sites, the partitioning and adsorption geometry vary with the pH has not been addressed. That is equivalent to the question whether the dominant adsorption process varies under different solution conditions, which is an important part of the whole adsorption picture. Another area where no structure information is available

is the EDL structure under the hydrothermal conditions, where the interface could behave differently. Very little is known about the diffuse layer ion distributions, which apparently controls the monovalent ion distribution at the rutile surface. There is no direct measurement of the diffuse layer ion distribution profile for this system, let alone its response to changes in the solution conditions. Such information would be useful to test the part of the SCM models primarily concerned with the diffuse double layer.

To address the above issues, more measurements are being carried out or on their way, including the in-situ EXAFS measurements of Zn^{2+} at rutile (110) aqueous interface, the TER-XSW and LSM-XSW measurements of diffuse double layer ions, such as Rb^{+}, Br^{-}, and Sr^{2+}, distributions, the Bragg XSW measurements of Zn^{2+} adsorbed at rutile (110) surface at lower pH, and the ions adsorption at the hydrothermal conditions.

6.2 Polarization dependent EXAFS measurements of Zn^{2+} on rutile (110) surface

It is well known that the Zn^{2+} ions is 6-fold coordinated in the aqueous solution in the form of $Zn(H_2O)_6^{2+}$. And it has been reported that it can undergo the coordination change to 4-fold coordinated upon adsorption to the α-Al_2O_3 single crystal (0001) and (10-12) surface.[67.] Interestingly, the coordination geometry also can be affected by in-situ versus ex-situ experiment conditions. The coordination change has only been observed for the in-situ measurement, but not the ex-situ ones. Considering the similar measurement for Co^{2+} adsorption onto the same α-Al_2O_3 surface as well as the rutile

TiO_2 (110) surface, where the ex-situ measurements all yields the solution alike 6-fold coordination and no in-situ measurement is available,[64,65] we would like to know whether this coordination change occurs for Zn^{2+} at rutile (110) surface at in-situ condition. Since it has a higher characteristic energy than Co, the Zn K_α fluorescence can penetrate the micrometer thick solution. Though quite difficult, the measurement can be done.

The measurements are carried out primarily at 11ID-D, BESSRC-CAT, APS, ANL, with the preliminary measurements done at 12BM-B, BESSRC-CAT, APS, ANL and X15A, NSLS, BNL.

Beamline setup at 12BMB and 11IDD is schematically shown in Figure 6.1. A collimated beam is incident on the sample surface at an incidence angle ~ 6°. The Zn K_α fluorescence signal is monitored with a multi-element Ge solid state detector (from Canberra) looking at the sample ~ 90° from the beam direction in the horizontal plane. The Ti signal from the bulk rutile crystal is attenuated by adding ~ 80 μm of Al foil in front of the detector. Furthermore, the elastic and Compton peak scattered from the sample are cut down with a ~ 7.5 μm thick Cu filter. A lead cone was place in front of the detector to only let the signal from the sample surface reach the detector. Finally, a small aperture was place in front of the sample to only allow the incident beam through and cut out any scattering signals (e.g., from air scatter, and/or incident beam slits). The spectrums from all elements of the solid-state detector are analyzed with separate single channel analyzers (SCAs) for each element to record the Zn K_α signal independently. The sample mounting and the preparation are the same as described in earlier chapters.

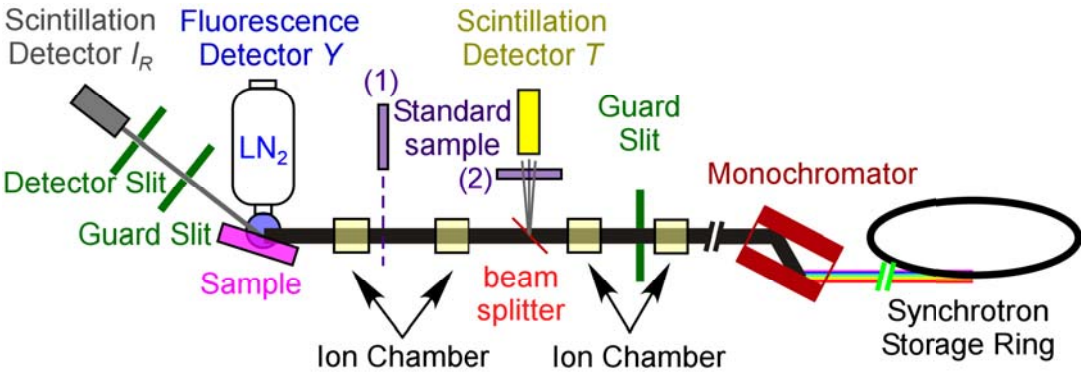

Figure 6.1. Experimental setup for EXAFS measurements at bending magnet beamline 12BMB and wiggler beamline 11IDD, APS, ANL.

The energy scan range was from 80 eV below to 570 eV above the Zn absorption K edge (~ 9660 eV). The scanning steps and counting time for a single scan is listed in Table 6.1, with the last row for the ZnO powder standard only. The EXAFS signal was collected for the incident X-ray polarization direction aligned with different crystal orientations, including the rutile in-plane direction [001] and [-110], and surface normal [110] directions. About 10 single scans were collected for each orientation to get enough counting statistics. The crystal orientation was determined by Bragg diffraction of the rutile crystal on the 6-circle diffractometer. Zincite (ZnO) powder was measured in transmission mode as the standard at two different positions, as label in Figure 6.1 with (1) and (2). In position (2), a thin Kapton film, which was placed 45° with respect to the incident X-ray beam, scatters X-rays thus acts as an X-ray source. The signal from this "secondary" source transmitted through the standard and was recorded with a "pin diode" detector. Such a measurement was done at the same time as the sample was measured primarily to monitor the stability of the experiment system. The standard was also measured separately at position (1) with the transmission measurement using the ion chambers before and after it.

The amplitudes of Fourier transform of k-weighted EXAFS data for three different orientations are shown in Figure 6.2 together with the standard—ZnO powder data. All the measured spectra are similar to the ZnO standard, which suggests that the Zn species on the rutile (110) surface are Zn^{2+} with probably 4-fold coordination. The detail analysis is underway.

Table 6.1. EXAFS scans energy steps and counting time of a single scan.

Segment	Start Energy (from edge, eV)	End Energy (from edge, eV)	# of points	Step size (eV)	Counting time (s)
1	-80	-30	50	1	2
2	-30	50	160	0.5	2
3	50	150	50	2	4
4	150	250	25	4	8
5	250	570	40	8	8
6	570	1050	40	12	16

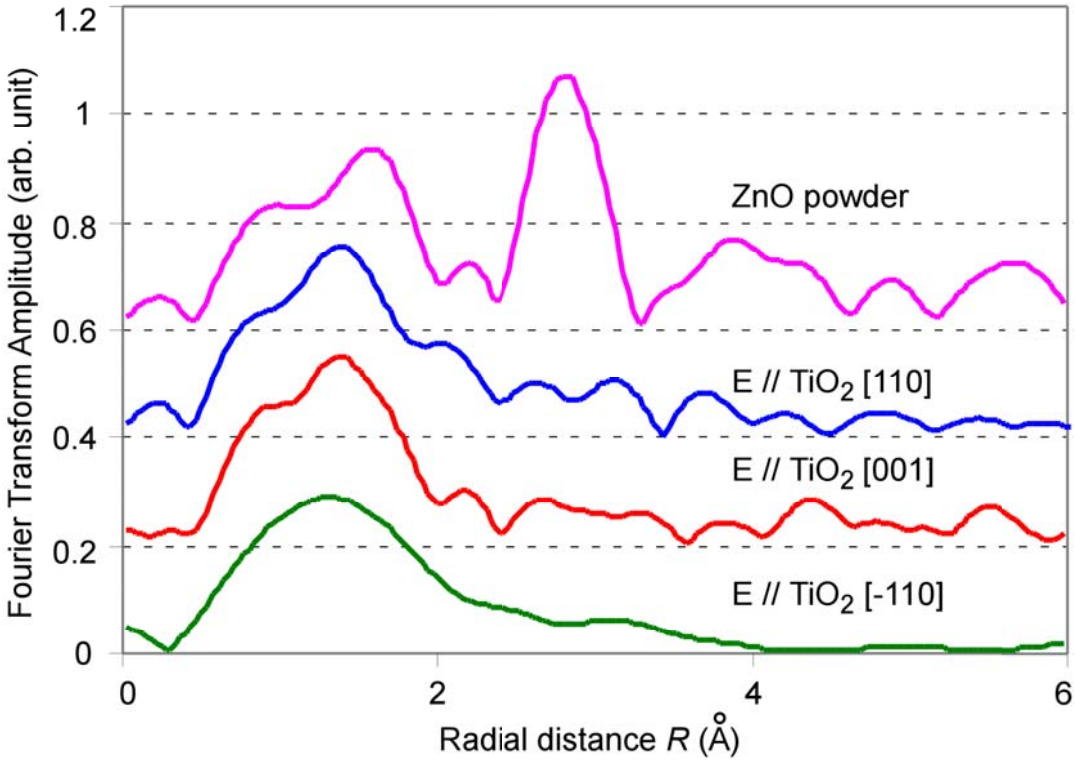

Figure 6.2. The amplitude of Fourier transform of the k-weighted EXAFS functions for Zn^{2+} at rutile (110) –aqueous interface at different crystal orientations, i.e., the polarization of the incident X-ray, ***E***, is parallel to [-110], [001] and [110] direction, respectively. Also shown is the ZnO powder data taken as a standard. The radial distance *R* has not been corrected for phase shift.

6.3 TER and LSM-XSW measurements of diffuse double layer

It has been known more than a decade ago that the long period standing waves can be used to probe the EDL ion distributions.[101.] Unlike the Bragg XSW, which yields one Fourier component at each reflection, the TER-XSW or LSM-XSW measures the Fourier transform of the element profile continuously. Therefore analysis of these data is done by modeling the ion distribution and comparing measured and calculated fluorescent yields as a function of incident angle. Theoretically, the diffuse EDL ions are following the simple exponential distribution profile at low surface potential as described in Chapter 1, which is a good starting model for the long period XSW data analysis.

6.3.1 TER-XSW measurements

TER-XSW measurements are carried out at 12IDD, BESSRC-CAT, APS, ANL. A longer rutile (110) sample ($25 \times 5 \times 1$ mm^3) is used in such measurements. The vertical beam size is 30 μm, which means the lowest angle without the beam spill off from the sample surface is ~ 0.07°. At the energy E = 17 keV, which is required for exciting Sr K fluorescence, the critical angle for TiO_2 is $\theta_c(TiO_2) \approx 0.14°$. Note although there is a layer of solution in between the air and the rutile crystal, the measured critical angle between the incident beam and the sample surface is the same as the one without any medium in between air and crystal assuming the medium thickness is homogeneous. The angular range between the critical angle and the spill off angle is important for the

reflectivity. At the same energy, the critical angle for the water layer is $\theta_c(H_2O) \approx 0.07°$, which is close to the spill off angle, thus it might not be seen on the reflectivity curve.

The solution condition for these measurements is $[SrCl_2] = 10^{-4}$ mol/kg and pH is adjust to 10.7 with NaOH, which is the same as used for the Bragg XSW measurements. From the Bragg XSW measurements, it can be estimated that the majority of the Sr^{2+} ions are in the condensed layer, i.e., they are at a very well defined position compared to the diffuse layer ion distribution as is expected for Rb^+. Therefore the result from the TER-XSW measurement of Sr^{2+} can be used as a reference for both analyzing the Rb^+ ion distribution and self-checking the method itself.

One typical measurement of Sr^{2+} at rutile (110) – aqueous interface with TER-XSW is shown in Figure 6.3 (A). The plot can be qualitatively explained with the division into different regions, as marked with the dashed lines in the figure. When the angle is lower than the (black) dashed line, most of the incident X-ray beam spills off the edges of the sample. Consequently the reflectivity is low and the fluorescence signals derive primarily from the solution and not from the top surface of the sample. In the second region, between the black dashed line and the magenta dotted line, the spill off of the X-ray over the surface still exist and the incidence angle is still smaller than the critical angle of water or kapton film (assumed the same electron density as water). The reflectivity increases and the fluorescence signal decreases as the spill off decreases. The next region, between magenta dotted line and green dot-dashed line, is the angular range between the critical angle of water and rutile. Here the reflectivity levels off and Sr^{2+}, which is above the rutile surface, can be seen but the Ti signal is very small because

below the critical angle the X-rays can only penetrate a few layer of crystal (e.g. ~ 24 Å at the experiment condition at $\theta = 0$) thus sees a small amount of Ti atoms. In the last region (above the green dot-dashed line), the reflectivity drops as predicted by Fresnel theory, and the Sr signal is primarily affected by the X-ray foot-print on the surface, decreases roughly following the functional form $1/\sin\theta$. Ti signal, on the other hand, rapidly increases as the penetration depth of the incident X-ray beam increases. That the Sr signal is peaked right at the rutile critical angle suggest that the Sr^{2+} ions are primarily located very close to the surface.

Shown in the Figure 6.3 (B) is the measurement for Rb^{+} at the condition [RbOH] = 10^{-4} mol/kg and the pH is adjusted with NaOH to 11. The general features of the curves are the same as the Sr^{2+} one. Only, for these data the Rb signal does not follow the functional form observed for Sr, which indicates a wider distribution profile at the interface.

In order to make any final conclusion about the ion profiles, a detailed and more precise ion distribution profile need to be modeled and fitted with the experimental data.

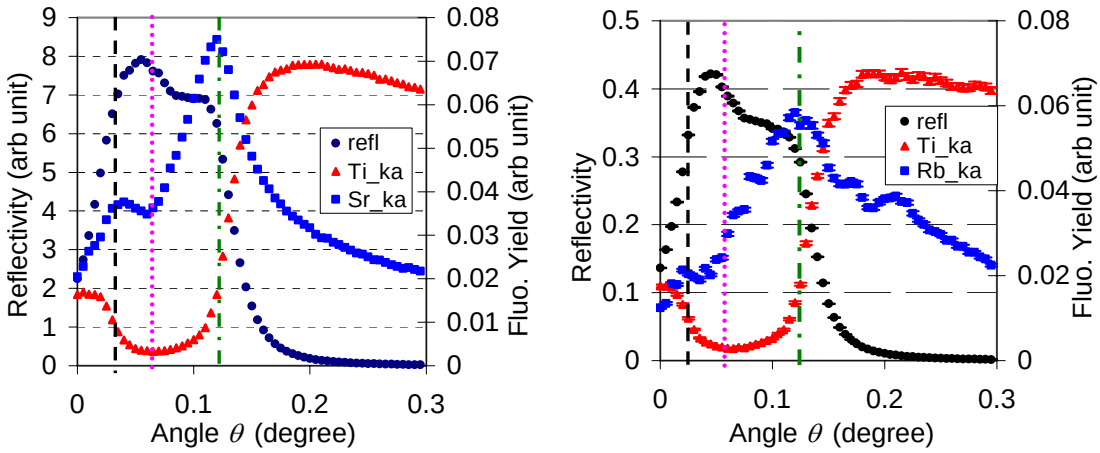

(A) (B)

Figure 6.3. TER-XSW measurements of the (A) Sr^{2+} and (B) Rb^{+} at rutile (110) surface. The reflectivity, the fluorescence signals from Ti in the bulk and Sr^{2+} or Rb^{+} ions are plotted together.

6.3.2 LSM-XSW measurements

With a multilayer substrate, the XSW measurements can be carried out at either total external region or the multilayer Bragg peaks. Normally multiple Bragg peaks are strong enough to be measured thus more than one component can be measured at a time.

The experiments are carried at 12IDD, BESSRC-CAT, APS, ANL and X15A, NSLS, BNL. The multilayer substrate was MBE grown with interlaced Si and Mo layers on the Si single crystal wafer (25 × 25 × 3 mm^3). The bi-layer thicknesses, i.e., the periods of the multilayer are ~ 200 Å and 40 Å, respectively. The top layer of the multilayer structure is Si and a very thin (~ 100 Å) layer of TiO_2 deposited on top of Si layer (presumably SiO_2). Checking along the surface normal direction, no Bragg reflection for either rutile or anatase can be seen, which suggests the TiO_2 thin film is amorphous. When contacted with the Sr^{2+} or Zn^{2+} solution, ion adsorption is observed with the significantly increased fluorescence signal. This means that the EDL structure forms next to such amorphous surface similar to that on the single crystal surface, although the detailed condensed layer structure might not be well defined because the roughness at such a surface.

The measurements are carried out at TER region as well as the multilayer Bragg peaks up to the 5^{th} order Bragg peak. Shown in the Figure 6.4 are one set of raw data for the TiO_2 surface on top of a 200 Å period (180 Å Si/20 Å Mo) multilayer sample in contact with the solution, where $[SrBr_2] = 10^{-4}$ mol/kg, $[NaCl] = 9.2 \times 10^{-3}$ mol/kg,

[RbOH] = 5×10^{-4} mol/kg at pH = 10.7. Signals from Sr^{2+}, Br^{-}, and Rb^{+} ions are all monitored at the same time. Rb_K_β line instead of the K_α line is used because that the Br_K_β and Rb_K_α line are not distinguishable. Due to the significant absorption by the solution and kapton film on top of the surface, the reflectivity is lower at first two Bragg peaks as well as in the TER region. The apparent modulation of the Sr^{2+} signal with respect to the reflectivity but not for Br^{-} and Rb^{+} signal, suggests the Sr^{2+} distribution is better defined than the other two. The overall slope of the fluorescence curve comes from the amount of the surface exposed to the X-ray beam, which should follow a simple trend of $1/\sin\theta$.

The higher order LSM Bragg peaks can be seen with bad shape, which can be explained by the gradient of the multilayer period. The gradient multilayer, which is initially proposed as a means to obtain XSW of different periods with a single sample, turns out only to add the complexity in determining the LSM structure. Without the precise and detail information about the structure of LSM, the analysis of the XSW data is very difficult if at all possible. An LSM sample with greater uniformity of layer spacing will be needed if further measurements are to be carried out. However, it is possible that the current data might be analyzed with appropriate approximations to obtain the qualitative features of the ion distributions for all the ions.

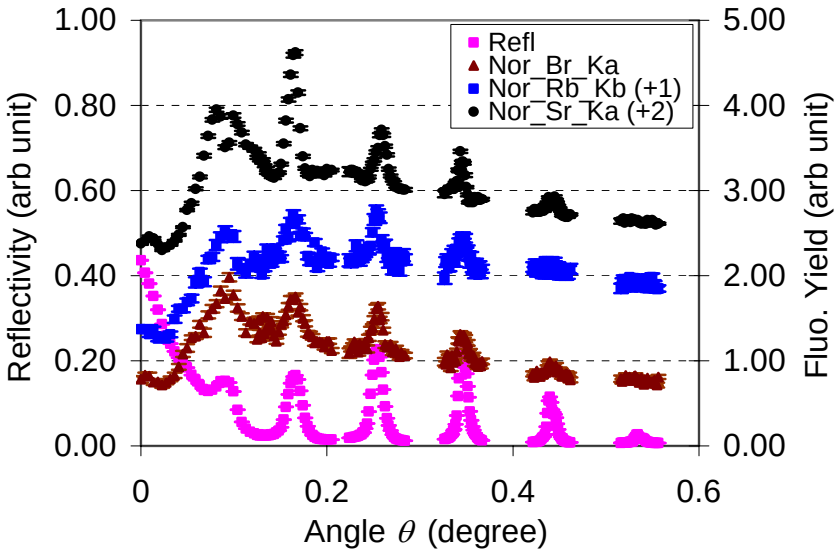

Figure 6.4. The XSW measurements of Rb^{+}, Br^{-}, and Sr^{2+} ions adsorbed onto amorphous TiO_2 thin film on top Si-Mo multilayer. For clarity, the fluorescence signals for Rb_K_β and Sr_K_α have been shifted upward by 1 and 2 units, respectively.

6.4 Bragg XSW measurements of Zn^{2+}/TiO_2 (110) at lower pH

To resolve the question whether there is any preference between the observed two Zn^{2+} positions at rutile (110) surface at different pH, a series of Bragg XSW measurements are carried out at the solution condition of pH = 6, $[Zn^{2+}] = 10^{-5}$ mol/kg, pH is adjusted and buffered with Tris and HTr. At this pH value, the rutile (110) surface charge is expected to be lower and the saturated Zn^{2+} coverage at the interface should be smaller according to the simulation with MUSIC model. The experiments are carried out at 12IDD, BESSRC-CAT, APS, ANL. The beamline setup, the sample mounting and preparations are all the same as described in Chapter 4. The Bragg XSW measurements are done at rutile single crystal reflection (110), (111), (200), (101), (211) and (210). The last one was missing from the previous measurements, which will clarify the issue concerning the finite Fourier term truncation error. The measured coherent fractions and coherent positions consistent with the previous measurements at pH = 8, though the total Zn^{2+} coverage, at < 0.1 ML, is only 10-20% of the previous number.

The image, Figure 6.5, from the XSW imaging shows the distribution profile similar to the one at higher pH. The final triangulation fitting is in progress to determine the precise positions and the occupancies at each position.

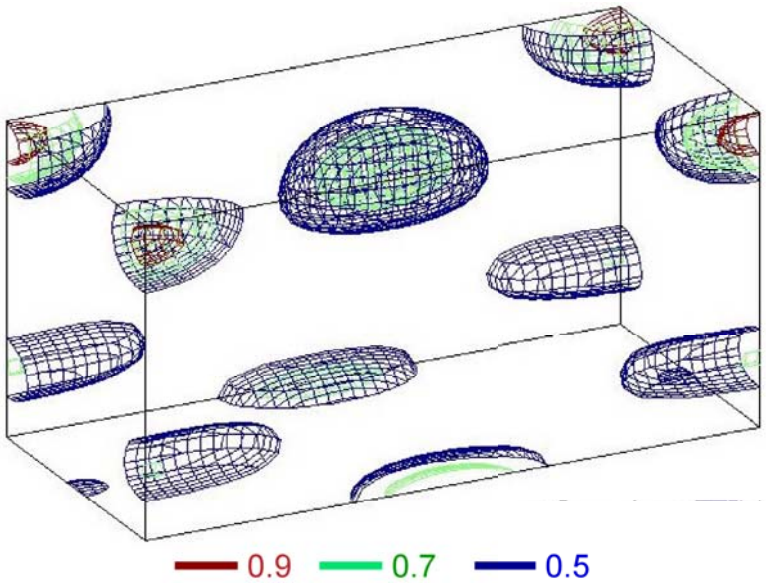

Figure 6.5. The XSW image of Zn^{2+} at rutile (110) surface at the solution condition of pH = 6, $[Zn^{2+}] = 10^{-5}$ mol/kg. The red, green and blue contours indicate the 0.9, 0.7 and 0.5 of the highest density of Zn^{2+} distributions, respectively.

6.5 The full CTR measurements of rutile (110) surface

More CTR measurements have been done on the rutile (110) surface both in contact with DIW or 1 mol/kg RbCl solution adjusted to pH = 12 with RbOH. The 0-1_S, 10_S, 1-2_S, and 2-1_S rods have been measured in addition to the 00_S rod. An additional 20_S rod is measured for Rb^+ solution to be compared with the old set of data.

A detailed analysis is on the way.

6.6 Further down the road

For further exploring the surface adsorption structure change at the elevated temperature, the X-ray measurements are proposed to be carried out at hydrothermal conditions. The sample, together with the cell and the solution can be heated above room temperature. However, at 1 atmosphere, the solution will boil at 100 °C. To reach even higher temperature, a special pressured vessel need to be built. With the special vessel holding the sample at higher pressure (up to 10 - 20 atm) and temperature (up to presumably 250 °C), X-rays can penetrate through the window area on the vessel without losing much intensity and the CTR or Bragg XSW measurement can be done.

A different surface of rutile crystal could be measured also. The (110) surface that was used throughout this study is the most studied surface of rutile crystals. Also present and being studied is the (001) surface. Looking at the rutile crystal along the (001) surface normal direction, long channels are visible between the lattice Ti and O

atoms, which could be a great candidate for hydrogen storage.

The surface of rutile (001) is more complicated than the (110) surface. Theoretically on the cleaved (001) surface all the Ti atoms are 4-fold coordinated, the high number of broken bond means higher surface energy therefore the (001) surface tends to facet or reconstruct.[24] Therefore the (001) surface is not as simple or direct to work with as the other surface.

A rutile single crystal with (001) surface, obtained from Princeton Scientific is cleaned and hydrothermally treated with the same method described for (110) surface. XSW measurements of Zn^{2+} adsorption on to the surface is measured with $[Zn^{2+}] = 10^{-5}$ mol/kg, pH = 8 solution. The (002) reflection is measured at 12IDD, APS, ANL. Although the coverage is ~ 1 ML, there is no evidence of ordering at the surface as shown in Figure 6.6. Further measurements of the surface structure in DIW with CTR measurement at 1BM, APS, ANL, reveals that the surface is very rough. It is hard to image the surface morphology without microscopic image (e.g., by AFM), but it is possible that high degree of roughness is due to the formation of small facets forming on the surface so that it is not an atomic scale flat surface at all. Further careful study is needed to settle the issue.

Once we gain enough knowledge about the rutile TiO_2 system, we can move onto another oxide. SnO_2 is the similar rutile structure but with a different dielectric constant (~ 10 for SnO_2 vs. 86 - 170 for TiO_2).[26,119] If the prediction about the EDL properties based on the bulk crystal dielectric constant is correct, we would observe significant difference of EDL structure at SnO_2 (110)-aqueous interface from TiO_2 while the

substrate structure are similar.[107.] All the measurements performed on TiO_2 surface can be applied on the SnO_2 surface and the investigation of a new system will help to expand the knowledge about the EDL into a new area.

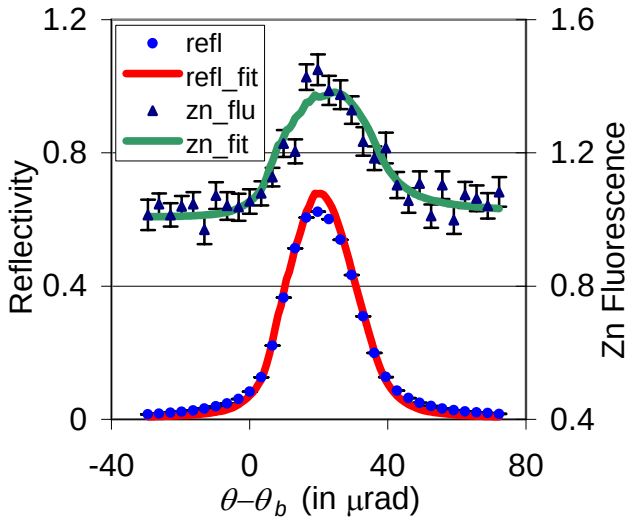

Figure 6.6. XSW measurement of Zn^{2+} at rutile (001) surface. The solution condition is pH = 8, $[Zn^{2+}] = 10^{-5}$ mol/kg. (002) reflection is measured. No significant modulation of the fluorescence curve with respect to the reflectivity suggests no ordering of Zn^{2+} ions at the interface.

Chapter 7 Summary

In situ X-ray standing wave and X-ray crystal truncation rod measurements were carried out at the rutile (110) aqueous interface for varies ions and solution conditions. The results provide direct measurement of condensed layer height from the interface, and show for the first time that condensed layer position is essentially independent of solution conditions even with large changes in ionic strength (by 3 orders of magnitude). The presence of other monovalent ions (Cl^-, Br^-, Tr^-, or Rb^+) has little effect on the condensed layer divalent cation positions. Negligible amount of divalent ions actually reside in the diffuse layer. The present Bragg XSW results provide direct proof that the GCS model is suitable for describing the divalent ions at TiO_2 (110) aqueous interface.

The surface charge can be directly associated with the measured coherent coverage of the adsorbed ions. For Sr^{2+} at pH = 10.7 and Zn^{2+} at pH = 8, the saturated coherent coverages are both around 0.4 ML. It is also learned from the data and the simulation that the significant amount of incoherent source of specific adsorbed ion (presumably some form of precipitation) does not have a measurable effect on the positions derived from the XSW measurements. This is a strong advantage of XSW method for probing such complex interfaces. Most of the measurements were actually done close to, but lower than, the surface saturation coverage, which is optimal for XSW measurements.

XSW imaging was shown to be a direct, model independent method to achieve

the elemental distribution profile with sub-Angstrom resolution. Combining with the tradition XSW triangulation data fitting, the precise atom positions and their occupation factors can be achieved. With the XSW imaging and triangulation, Sr^{2+} and Y^{3+} ions are determined to be at tetradentate position at the rutile (110) surface. And Zn^{2+} ions occupy the extended bulk Ti atom positions at the surface with the primary one on top of the BO atoms and a minor species at the surface sites bridging the two TO atoms.

CTR measurements were carried out on rutile TiO_2 (110) surface in both DIW and 1 mol/kg RbCl solution at pH = 12. Specular (00_S) and a subset of the non-specular (20_S, 02_S, 11_S, & 40_S) rods are measured. The rutile surface relaxation is observed to be minimal because the coordination shell of the surface Ti atom is completed by the species (H_2O or OH^-) from the solution, as determined from the CTR data. In the aqueous solution, the terminal oxygen rows are fully recovered compared with the surface in the vacuum where they are absent. An additional water layer formed on top of surface oxygen (TO and BO) in DIW was also observed. The water molecules in this layer are highly localized around available surface sites, namely, tetradentate and bidentate sites. No additional structure is found in the interfacial water further from the interface. For the rutile surface in the Rb^+ solution, the Rb^+ ions primarily take the tetradentate sites—replacing some or all of the water molecules. This implies that the alkali metal ions are not just an indifferent background ion in the solution. Instead, at the rutile (110) surface, it behaves like multivalent ions (e.g., Sr^{2+}, Y^{3+}, Zn^{2+}) but with a weaker adsorption constant. Although it is not directly measured with the CTR method, the coverage of the Rb^+ can be estimated as ~ 0.4 ML, even at such a high bulk solution concentration.

The detail structural information obtained from the X-ray measurements offers the first direct test for the understanding of these systems, e.g., as represented by the molecular dynamics simulations of the same system. It also provides the surface complexation models with the critical structural information as an input rather than using the nominal (i.e., assumed based on the bulk crystal structure) values that might not be appropriate for the particular situation. With the better defined surface adsorption structure, the models can be applied more precisely to well reproduce the features of the EDL.

On the other hand, the surface complexation model, the *ab initio* calculation, and the molecular dynamical simulation with the validation from X-ray data can offer other details X-ray can not probe. E.g., proton distribution at the oxide-aqueous interface is virtually invisible to X-ray methods, though it is an important aspect of the whole electrical double layer phenomenon. One long debated problem is whether the water molecules adsorb at the terminal oxygen sites associatively or dissociatively. X-ray method can not probe the difference between H_2O and OH^- group at the interface. However, the MD simulation results with different assumptions about the adsorbed water can be directly checked against the X-rays probed locations of the adsorbates (including both the ions and the water molecules). The comparison suggests that on the rutile (110) surface, the water is adsorbed dissociatively. There were also discussions about the surface enhanced ion hydroxylation, which is difficult to directly probe with X-rays if possible at all. With the knowledge of the exact adsorbed ion locations, the analysis of the powder titration data with SCM model suggests the adsorbed Zn^{2+} at rutile (110)

surface is hydroxylated.

For a complicated system as EDL, it is proven to be critical and very powerful in solving the century-old mystery to combine of the different methods, including the measurements of microscopic structures and macroscopic properties and the computational simulations. Without any question, the measurements of the atomic scale structure at the interface with high brilliance X-rays play a very important role.

With the further measurements on the system, more definitive information will be revealed and better understanding about EDL will be achieved.

REFERENCES

1. P. C. Hiemenz and R. Rajagopalan. *Principles of Colloid and Surface Chemistry,* 3rd edition**.** New York: Marcel Dekker, (1997).

2. G. E. Brown Jr.; V. E. Henrich; W.H. Casey; D. L. Clark; C. Eggleston; A. Felmy; D. W. Goodman; M. Grätzel; G. Maciel; M. I. McCarthy; K. Nealson; D. A. Sverjensky; M. F. Toney; and J. M. Zachara. "Metal oxide surfaces and their interactions with aqueous solutions and microbial organisms," *Chemical Reviews* 99 (1999): 77-174.

3. J. Lyklema. *Fundamentals of Interface and Colloid Science*, Vol. II. New York: Academic Press (1995).

4. H. L. F. von Helmholtz. "Über einige Gesetze der Vertheilung elektrischer Ströme in körperlichen Leitern mit Anwendung auf die thierisch-elektrischen Versuche," *Annalen der Physik und Chemie – Leipzig* 89 (1853): 211-233, 354-377. [Title translation: Some laws about the distribution of electrical currents in volume conductors, with application to animal electric experiments.]

5. G. Gouy. "Sur la constitution de la charge electrique à la surface d'un electrolyte," *Journal de Physique* 9 (1910): 457-468.

6. D. L. Chapman. "A contribution to the theory of electrocapillarity," *Philosophical Magazine* 25, no. 6 (1913): 475-481.

7. O. H. Stern. "Zur Theore der elektrischen Doppelschicht," *Zeitschrift fur Elektrochemie* 30 (1924): 508-516.

8. M. J. Bedzyk; J. M. Bommarito; M. Caffery; and T. A. Penner. "Diffuse-double layer at a membrane-aqueous interface measured with X-ray standing waves," *Science* 248 (1990): 52-56.

9. J. Wang; M. Caffrey; M. J. Bedzyk; and T. L. Penner. "Direct Profiling and reversibility of ion distribution at a charged membrane/aqueous interface: An X-ray standing wave study," *Langmuir* 17 (2001): 3671-3681.

10. M. L. Machesky; D. J. Wesolowski; D. A. Palmer, and Ken Ichiro-Hayashi. "Potentiometric titrations of rutile suspensions to 250°C," *Journal of Colloid and Interface Science* 200 (1998): 298-309.

11. L. Pauling. "Atomic radii and interatomic distances in metals," *Journal of the American Chemical Society* 69, no. 3 (1947): 542-553.

12. I. D. Brown and D. Altermatt. "Bond-valence parameters obtained from a systematic analysis of the inorganic crystal structure database," *Acta Crystallographica* B41 (1985): 244-247.

13. I. D. Brown. *The Chemical Bond in Inorganic Chemistry-The Bond Valence Model,* Oxford, UK: Oxford University Press, (2002).

14. M. L. Machesky. *Chemical Modeling in Aqueous Systems II*, Edited by D. C. Melchior and R. L. Bassett, Washington, D.C.: American Chemical Society (1990): 282

15. N. J. Barrow. "A brief discussion on the effect of temperature on the reaction of inorganic ions with soil," *Journal of Soil Science* 43 (1992): 37-45

16. Yu. V. Alekhin; M. P. Sidorova; L. I. Ivanova; and L. Z. Lakshtanov. *Kolloidn. Zh. (English Translation)* 46 (1984): 1195.

17. T. Hiemstra; W.H. Van Riemsdijk; and G.H. Bolt. "Multisite proton adsorption modeling at the solid/solution interface of (hydr)oxides: a new approach. I. Model description and evaluation of intrinsic reaction constants," *Journal of Colloid and Interface Science* 133 (1989): 91-104.

18. T. Hiemstra and W. H. Van Riemsdijk. "A surface structural approach to ion adsorption: The charge distribution (CD) model," *Journal of Colloid and Interface Science* 179 (1996): 488-508.

19. G. A. Parks and P. L. DeBruyn. "The zero point of charge of oxides," *Journal of Physical Chemistry* 66 (1962): 967-973.

20. P. W. Schindler and W. Stumm. *Aquatic Surface Chemistry: Chemical Processes at the Particle-Water Interface*, Edited by W. Stumm, New York: Wiley-Interscience (1987): 83-110.

21. R. Charmas. "Four-layer model for simple ion adsorption at energetically heterogeneous metal oxide/electrolyte interfaces: Quantitative thermodynamic description including related calorimetric effects," *Journal Physical Chemistry B* 106 (2002): 9059-9069.

22. M. L. Machesky; D. J. Wesolowski; D. A. Palmer; and M. K. Ridley. "On the temperature dependence of intrinsic surface protonation equilibrium constants: an extension of the revised MUSIC model," *Journal of Colloid and Interface Science* 239 (2001): 314-327.

23. M. K. Ridley; M. L. Machesky; D. J. Wesolowski; and D. A. Palmer. "Modeling the surface complexation of calcium at the rutile-water interface to 250°C." *Geochimica et Cosmochimica Acta* 68, no. 2 (2004): 239-251.

24. V. E. Henrich and P. A. Cox. "The Surface Science of Metal Oxides," Cambridge: Cambridge University Press (1996)

25. M. A. Henderson. "The interaction of water with solid surfaces: fundamental aspects revisited," *Surface Science Reports* 46 (2002): 1-306.

26. U. Diebold. "The surface science of titanium dioxide," *Surface Science Report* 48 (2003): 53-229.

27. G. E. Brown Jr. and G. A. Parks. "Sorption of trace elements on mineral surfaces: modern perspectives from spectroscopic studies, and comments on sorption in the marine environment," *International Geology Review* 43 (2001): 963-1073.

28. S. C. Abrahams and J. L. Bernstein. "Rutile: Normal probability plot analysis and accurate measurement of crystal structure," *The Journal of Chemical Physics* 55, no. 7 (1971): 3206-3211.

29. M. Ramamoorthy; D. Vanderbilt and R. D. King–Smith. "First-principles calculations of the energetics of stoichiometric TiO_2 surfaces," *Physical Review B* 49, no. 23 (1994):16721-16727.

30. B. Hird; R. A. Armstrong; and J. A. Seel. "Structure of TiO_2 rutile (110) (1×1) from ion scattering measurements," *Surface Review and Letters* 5, no. 1 (1998): 309-313.

31. R. E. Tanner; M. R. Castell; and G. A. D. Briggs. "High resolution scanning tunneling microscopy of the rutile TiO_2 (110) surface," *Surface Science* 412/413 (1998): 672-681.

32. D. Vogtenhuber; R. Podloucky; and A. Neckel. "Electronic structure and relaxed geometry of the TiO_2 rutile (110) surface," *Physical Review B* 49, no. 3 (1994): 2099-2103.

33. S. P. Bates; G. Kresse; and M. J. Gillan. "A systematic study of the surface energetics and structure of TiO_2 (110) by first-principles calculations," *Surface Science* 385 (1997): 386-394.

34. P. K. Schelling; N. Yu; and J. W. Halley. "Self-consistent tight-binding atomic-relaxation model of titanium dioxide," *Physical Review B* 58, no. 3, (1998): 1279-1293.

35. G. Charlton; P. B. Howes; C. L. Nicklin; P. Steadman; J. S. G. Taylor; C. A. Muryn; S. P. Harte; J. Mercer; R. McGrath; D. Norman; T. S. Turner; and G. Thornton. "Relaxation of TiO_2(110)-(1x1) using surface X-ray diffraction." *Physics Review Letters* 78, no. 3 (1997): 495-498.

36. E. Asari; T. Suzuki; H. Kawanowa; J. Ahn; W. Hayami; T. Aizawa; and R. Souda. "TiO_2 (110)-p(1×1) surface structure analyzed by impact-collision ion scattering spectroscopy," *Physical Review B* 61, no. 8 (2000): 5679-5682.

37. P. J. D. Lindan; N. M. Harrison; and M. J. Gillan. "Mixed dissociative and molecular adsorption of water on the rutile (110) surface," *Physical Review Letters* 80, no. 4 (1998): 762-765.

38. W. Langel. "Car-Parrinello simulation of H_2O dissociation on rutile," *Surface Science* 496 (2002): 141-150.

39. E. L. Bullock; L. Patthey; and S. G. Steinemann. "Clean and hydroxylated rutile TiO_2 (110) surfaces studied by X-ray photoelectron spectroscopy," *Surface Science* 352-354 (1996):504-510.

40. M. Předota; A. V. Bandura; P. T. Cummings; J. D. Kubicki; D. J Wesolowski; A. A. Chialvo; and M. L. Machesky. "Electric double layer at the rutile (110) surface. I. Structure of surfaces and interfacial water from molecular dynamics using *ab initio* potentials," submitted to *Journal of Physical Chemistry B* (2003).

41. G. Sposito. "On points of zero charge," *Environmental Science and Technology* 32, no. 19 (1998): 2815-2819.

42. D. A. Kulik. "Thermodynamic proeperties of surface species at the mineral-water interface under hydrothermal conditions: A Gibbs energy minimization signel-ite 2pKA triple-layer model of turile in NaCl electrolyte to 250°C," *Geochimica et Cosmochimica Acta* 64, no. 18 (2000): 3161-3179.

43. J. Fitts, Private communication.

44. C. J. Hirschmugl. "Application of storage ring infrared spectromicorscopy and reflection-absorption spectroscopy to geochemistry and environmental science" Chapter 6 in *Applications of Synchrotron Radiation in Low-Temperature Geochemistry and Environmental Science*, Edited by P. Fenter, M. Rivers, N. C. Sturchio and S. Sutton (Reviews in Mineralogy and Geochemistry, Vol. 49), New York: Geochemical Society (2002): 317-340.

45. P. Jones and J. A. Hockey. "Infrared studies of rutile surfaces. 1," *Transactions of the Faraday Society* 67, no. 9 (1971): 2669-2678.

46. P. Jones and J. A. Hockey. "Infrared studies of rutile surfaces. 2. Hydroxylation, hydration, and structure of rutile surfaces," *Transactions of the Faraday Society* 67, no. 9 (1971): 2679-2685.

47. P. Jones and J. A. Hockey. "Infrared studies of rutile surfaces. 3. Adsorption of water and dehydroxylation of rutile." *Journal of the Chemical Society, Faraday Transactions 1: Physical Chemistry in Condensed Phases* 68, Pt. 5 (1972): 907-913.

48. G. D. Parfitt; J. Ramsbotham; and C. H. Rochester. "Infrared study of ammonia adsorption on rutile surfaces." *Transactions of the Faraday Society* 67, Pt. 3 (1971): 841-847.

49. G. D. Parfitt; J. Ramsbotham; and C. H. Rochester. "Infrared study of pyridine adsorption on rutile surfaces." *Transactions of the Faraday Society* 67, Pt. 5 (1971): 1500-1506.

50. P. Jackson and G. D. Parfitt. "Infrared study of the surface properties of rutile. Water and surface hydroxyl species." *Transactions of the Faraday Society* 67, Pt. 8 (1971): 2469-2483.

51. G. D. Parfitt; J. Ramsbotham; and C. H Rochester. "Infrared study of hydrogen chloride adsorption on rutile surfaces." *Transactions of the Faraday Society* 67, Pt. 10 (1971): 3100-3109.

52. G. D. Parfitt; J. Ramsbotham; and C. H Rochester. "Infrared study of the Reactions of silicon, Titanium and tin Tetrachlorides with rutile," *Journal of Chemical Society, Faraday Transactions* 68, Pt. 1 (1972): 17-27.

53. G. D. Parfitt; J. Ramsbotham; and C. H Rochester. "An electrophoretic investigation of the effect of chloride and of silanol groups on the properties of the surface of rutile," *Journal of Colloid and Interface Science* 41 (1972): 437-445

54. D. M. Griffiths and C. H. Rochester. "Infrared study of the adsorption of water on to the surface of rutile." *Journal of the Chemical Society, Faraday Transactions 1: Physical Chemistry in Condensed Phases* 73, Pt. 10 (1977): 1510-1529.

55. M. B. Hugenschmidt; L. Gamble; and C. T. Campbell. "The interaction of H_2O with a TiO_2 (110) surface," *Surface Science* 302, (1994): 329-340.

56. L. Wang; D. R. Baer; M. H. Engelhard; and A. N. Shultz. "The adsorption of liquid and vapor water on TiO_2 (110) surfaces: the role of defects," *Surface Science* 344 (1995): 237-250.

57. I. M. Brookes; C. A. Muryn; and G. Thornton. "Imaging water dissociation on TiO_2 (110)," *Physical Review Letters* 87, no. 26 (2001): 266103(1-4).

58. M. Menetrey; A. Markovits; C. Minot. "Reactivity of a reduced metal oxide surface: Hydrogen, water and carbon monoxide adsorption on oxygen defective rutile TiO_2 (110)," *Surface Science* 524 (2003): 49-62.

59. C. Zhang and J. D. P. Linda. "Multilayer water adsorption on rutile TiO_2 (110): a first principles study," *Journal of Chemical Physics* 118, no. 10 (2003): 4620-4630.

60. C. Zhang and J. D. P. Linda. "Towards a first-principles picture of the oxide-water interface," *Journal of Chemical Physics* 119, no. 17 (2003): 9183-9190.

61. K. F. Hayes; A. L. Ro; G. E. Brown Jr.; K. O. Hodgson; J. O. Leckie; and G. A. Parks. "Insitu X-ray absorption study of surface complexes - Selenium oxyanions on α-FeOOH," *Science* 238 (1987): 783-786.

62. P. A. O'Day; A. J. Chisholm-Brause; S. N. Towle, G. A. Parks; and G. E. Brown Jr. "X-ray absorption spectroscopy of Co(II) sorption complexes on quartz (α-SiO_2) and rutile (TiO_2)." *Geochimica et Cosmochimica Acta* 60, no. 14 (1996): 2515-2532.

63. J. R. Bargar; S. N. Towle; G. E. Brown Jr.; and G. A. Parks. "XAFS and bond-valence determination of the structures and compositions of surface functional groups and Pb(II) and Co(II) sorption products on single-crystal α-Al_2O_3." *Journal of Colloid and Interface Science* 185 (1997): 473-492.

64. S. N. Towle; G. E. Brown Jr.; and G. A. Parks. "Sorption of Co(II) on metal oxide surfaces, I. Identification of specific binding sites of Co(II) on (110) and (001) surfaces of TiO_2 (rutile) by grazing-incidence XAFS spectroscopy." *Journal of Colloid and Interface Science* 217 (1999): 299-311.

65. S. N. Towle; J. R. Bargar; G. E. Brown Jr.; and G. A. Parks. "Sorption of Co(II) on metal oxide surfaces, II. Identification of Co(II)(aq) adsorption sites on the (0001) and (1-102) surfaces of α-Al_2O_3 by grazing-incidence XAFS spectroscopy." *Journal of Colloid and Interface Science* 217 (1999): 312-321.

66. T. P. Trainor; G. E. Brown Jr.; and G. A. Parks. "Adsorption and precipitation of aqueous Zn(II) on alumina powders." *Journal of Colloid and Interface Science* 231 (2000): 359-372.

67. T. P. Trainor; J. P. Fitts; A. S. Templeton; D. Grolimund; and G. E. Brown Jr. "Grazing-incidence XAFS study of aqueous Zn(II) sorption on α-Al_2O_3 single crystals." *Journal of Colloid and Interface Science* 244 (2001): 239-241.

68. I. K. Robinson. "Crystal truncation rods and surface roughness," *Physical Review B* 33, no.6 (1986): 3830-3836.

69. P. J. Eng; T. P. Trainor; G. E. Brown, Jr.; G. A. Waychunas; M. Newville; S. R. Sutton; and M. L. Rivers. "Structure of the hydrated -Al_2O_3 (0001) surface," *Science* 288 (2000): 1029-1033.

70. Y. S. Chu; T. E. Lister; W. G. Cullen; H. You; and Z. Nagy. "Commensurate water monolayer at the RuO_2 (110)/water interface," *Physical Review Letters* 86, no. 15 (2001): 3364-3367.

71. P. Fenter; M. T. McBride; G. Srajer; N. C. Sturchio; and D. Bosbach. "Structure of barite (001)- and (210)-water interfaces," *Journal of Physical Chemistry B* 105 (2001): 8112-8119.

72. M. L. Schlegel; K. L. Nagy; P. Fenter; N. C. Sturchio. "Structures of quartz (100)- and (101)-water interfaces determined by X-ray reflectivity and atomic force microscopy of natural growth surfaces," *Geochimica et Cosmochimica Acta* 66, no. 17 (2002): 3037-3054.

73. L. Cheng; P. Fenter; K. L. Nagy; M. L. Schlegel; and N. C. Sturchio. "Molecular-scale density oscillations in water adjacent to a mica surface," *Physical Review Letters* 87, no. 15 (2001): 156103(1-4).

74. P. Fenter; C. Park; L. Cheng; Z. Zhang; M. P. S. Krekeler; and N. C. Sturchio. "Orthoclase dissolution kinetics probed by in situ X-ray reflectivity: Effects of temperature, pH, and crystal orientation," *Geochimica et Cosmochimica Acta* 67, no. 2 (2003): 197-211.

75. M. F. Reedijk; J. Arsic; F. F. A. Hollander; S. A. de Vries; and E. Vlieg. "Liquid order at the interface of KDP crystals with water: Evidence for icelike layers," *Physical Review Letters* 90, no. 6 (2003): 066103(1-4).

76. G. D. Williams; A. K. Soper; N. T. Skipper; and M. V. Smalley. "High-resolution structural study of an electrical double layer by neutron diffraction," *Journal of Physical Chemistry B* 102 (1998): 8945-8949.

77. B. W. Batterman. "Detection of foreign atom sites by their X-ray fluorescence scattering," *Physical Review Letters* 22, no. 14 (1969): 703-705.

78. J. A. Golovchenko; J. R. Patel; and D. R. Kaplan; P. L. Cowan; M. J. Bedzyk. "Solution to the surface registration problem using X-ray standing waves," *Physical Review Letters* 49, no. 8 (1982): 560-563.

79. J. Zegenhagen. "Surface structure determination with X-ray standing waves," *Surface Science Reports* 18 (1993): 199-271.

80. M. J. Bedzyk and L. Cheng. "X-ray Standing Wave Studies of Minerals and Mineral Surfaces: Principles and Applications." Chapter 4 in *Applications of Synchrotron Radiation in Low-Temperature Geochemistry and Environmental Science*, Edited by P. Fenter, M. Rivers, N. C. Sturchio and S. Sutton (Reviews in Mineralogy and Geochemistry, Vol. 49), New York: Geochemical Society (2002): 221-266.

81. P. Fenter; L. Cheng; S. Rihs; M. L. Machesky; M. J. Bedzyk; and N. C. Sturchio. "Electrical double-layer structure at the rutile-water interface as observed in situ with small-period X-ray standing waves," *Journal of Colloid Interface Science* 225 (2000): 154-165.

82. M. V. Fedkin; X. Y. Zhou; J. D. Kubicki; A. V. Bandura; S. N. Lvov; M. L. Machesky; and D. J. Wesolowski. "High temperature microelectrophoresis studies of the rutile/aqueous solution interface," *Langmuir* 19 (2003): 3797-3804.

83. T. Miyatani; M. Horii; A. Rosa; and M. Fujihira. "Mapping of electrical double-layer force between tip and sample surfaces in water with pulsed-force-mode atomic force microscopy," *Apply Physics Letter* 71, no. 18 (1997): 2632-2634.

84. U. Raviv and J. Klein. "Fluidity of bound hydration layers," *Science* 297 (2002): 1540-1543.

85. A. V. Bandura and J. D. Kubicki. "Derivation of force field parameters for TiO_2-H_2O systems from *ab initio* calculations," *Journal of Physical Chemistry B* 107 (2003): 11072-11081.

86. M. Předota; P. T. Cummings; Z. Zhang; P. Fenter; and D. J Wesolowski. "Electric double layer at the rutile (110) surface. II. Adsorption of ions from molecular dynamics and X-ray experiments," submitted to *Journal of Physical Chemistry B* (2003).

87. Z. Zhang; P. A. Fenter; L. Cheng; N. C. Sturchio; M. J. Bedzyk; M. Předota; A. Bandura; J. Kubicki; S. N. Lvov; P. T. Cummings; A. A. Chialvo; M. K. Ridley; P. Bénézeth; L. Anovitz; D. A. Palmer; M. L. Machesky; and D. J. Wesolowski. "Ion adsorption at Rutile water interface: Linking molecular and macroscopic properties." *Langmuir* in press (2004).

88. J. D. Jackson. *Classical Electrodynamics*, 2nd edition. New York: John Wiley & Sons (1975): 291.

89. B. D. Cullity. *Elements of X-Ray Diffraction*, 2nd Edition, Reading, Massachusetts: Addison-Wesley (1976).

90. B. E. Warren. *X-ray Diffraction*, New York: Dover (1990).

91. L. H. Schwartz and J. B. Cohen. *Diffraction from Materials*, 2nd Edition, Berlin; New York: Springer-Verlag (1987).

92. R. W. James. *The optical principles of the diffraction of X-rays*, Woodbridge, Connecticut: Ox Bow Press, (1982).

93. R. Feidenhans'L. "Surface structure determination by X-ray diffraction," *Surface Science Report* 10 (1989): 105-188.

94. I. K. Robinson. "Surface crystallography," Chapter 7 in *Handbook on Synchrotron Radiation*, Vol. 3, edited by G. Brown and D. E. Moncton, North Holland: Elsevier Science Publishers B.V. (1991).

95. J. Als-Nielsen. "X-ray reflectivity studies of liquid surfaces," in *Handbook on Synchrotron Radiation*, Vol. 3, edited by G. Brown and D. E. Moncton, North Holland: Elsevier Science Publishers B.V. (1991).

96. APS graphics gallery.

97. N. C. Sturchio; R. P. Chiarello; L. Cheng; P. F. Lyman; M. J. Bedzyk; Y. Qian; H. You; D. Yee; P. Geissbuhler; L. B. Sorensen; Y. Liang; and D. R. Baer. "Lead adsorption at the calcite-water interface: Synchrotron X-ray standing wave and X-ray reflectivity studies," *Geochimica et Cosmochimica Acta* 61, no. 2 (1997): 251-263.

98. L. Cheng; P. A. Fenter; M. J. Bedzyk; and N. C. Sturchio. "Fourier-Expansion solutions of atom distributions in crystals using X-ray standing waves," *Physical Review Letters* 90, no. 25 (2003): 255503(1-4).

99. J. S. Okasinski; C.-Y. Kim; D. A. Walko; and M. J. Bedzyk. "X-ray standing wave imaging of the 1/3 monolayer Sn/Ge(111) surface," *Physical Review B* 69, no. 4 (2004): 041401(1-4).

100. Z. Zhang; P. A. Fenter; L. Cheng; N. C. Sturchio; M. J. Bedzyk; M. L. Machesky; and D. J. Wesolowski. "Model-independent X-ray imaging of adsorbed cations at the crystal–water interface," *Surface Science Letters,* 554, (2004): L95-L100.

101. M. J. Bedzyk; J. M. Bommarito; and J. S. Schildcraut. "X-ray standing wave at a reflecting mirror surface," *Physical Review Letters* 62, no. 12 (1989): 1376-1379.

102. M. J. Bedzyk; D. H. Bilderback; G. M. Bommarito; M. Caffrey; J. S. Schildkraut. "X-ray standing waves - A molecular yardstick for biological-membranes," *Science* 241 (1988): 1788-1791.

103. L. G. Parratt. “Surface studies of solids by total reflection of X-rays,” *Physical Review* 95 (1954): 359-369.

104. P. A. Fenter. "X-ray Reflectivity as a probe of mineral-fluid interfaces: A user Guide." Chapter 3 in *Applications of Synchrotron Radiation in Low-Temperature Geochemistry and Environmental Science*, Edited by P. Fenter, M. Rivers, N. C. Sturchio and S. Sutton (Reviews in Mineralogy and Geochemistry, Vol. 49.) New York: Geochemical Society (2002): 221-266.

105. E. A. Stern. “Theory of EXAFS.” Chapter 1 in *X-ray Absorption—principles, applications, techniques of EXAFS, SEXAFS and XANES*, Edited by D. C. Koningsberger; and R. Prins. (Chemical Analysis, Vol. 92.) New York: Wiley-Interscience (1988): 3-52.

106. M. L. Machesky. Private communication.

107. D. Sverjensky. “Interpretation and prediction of triple-layer model capacitances and the structure of the oxide-electrolyte-water interface,” *Geochimica et Cosmochimica Acta* 65, no. 21 (2001): 3643-3655.

108. M. K. Ridley; M. L. Machesky; D. J. Wesolowski; and D. A. Palmer. “Calcium adsorption at the rutile-water interface: a potentiometric study in NaCl media to 250°,” *Geochimica et Cosmochimica Acta* 63, no. 19/20 (1999): 3087-3096.

109. S. Takakusagi; K. Fukui; F. Nariyuki; and Y. Iwasawa. “STM study on structures of two kinds of wide strands formed on TiO_2 (110),” *Surface Science* 523 (2003): L41-L46.

110. K. F. McCarty and N. C. Bartelt. “Spatially resolved dynamics of the TiO_2 (110) surface reconstruction,” *Surface Science* 540 (2003): 157-171.

111. R. P. J. J. Rietra; T. Hiemstra; and W. H. Van Riemsdijk. “Interaction between calcium and phosphate adsorption on Goethite,” *Environmental Science and Technology* 35 (2001):3369-3374.

112. C. J. Howard; T. M. Sabine; and F. Dickson. “Structure and thermal parameters for rutile and anatase,” *Acta Crystallography* B47 (1991): 462-468.

113. S. Omori; Y. Nihei; E. Rotenberg; J. D. Denlinger; S. Marchesini; S. D. Kevan; B. P. Tonner; M. A. Van Hove; and C. S. Fadley. “Differential photoelectron holography: A new approach for three-dimensional atomic imaging,” *Physical Review Letters* 88, no. 5 (2002): 055504(1-4).

114. T. Gog; P. M. Len; G. Materlik; D. Bahr; C. S. Fadley; and C. Sanchez-Hanke. "Multiple-energy X-Ray holography: Atomic images of hematite (Fe_2O_3)," *Physical Review Letters* 76, no. 17 (1996): 3132-3135.

115. M. Tegze and G. Faigel. "X-ray holography with atomic resolution," *Nature* 380, no. 6569 (1996): 49-51.

116. R. J. Hamers. "Scanned probe microscopies in chemistry," *Journal of Physical Chemistry* 100 (1996): 13103-13120.

117. Y. Marcus. *Ion Properties,* New York: Marcel Dekker (1997).

118. J. C. Lang; G. Srajer; J. Wang; and P. L. Lee. "Performance of the Advanced Photon Source 1-BM beamline optics." *Review of scientific instruments* 70, no. 12 (1999): 4457-4462.

119. A. E. Taverner, C. Rayden, S. Warren, A. Gulino, P. A. Cox, and R. G. Egdell; "Comparison of the energies of vanadium donor levels in doped SnO_2 and TiO_2," *Physical Review B* 51, no. 11 (1995): 6833–6837.

120. D. A. Walko; O. Sakata; P. F. Lyman; T.-L. Lee; B. P. Tinkham; J. S. Okasinski; Z. Zhang; and M. J. Bedzyk. "Surface and interface studies at APS endstation 5ID-C," *American Institute of Physics Conference Proceedings*, *Synchrotron Radiation Instrumentation* in press (2003).

121. J. S. Okasinski. Atomic-Scale Structure Investigations of the Low-Temperature Phase Transitions for the 1/3 ML Sn/Ge(111) and 1/3 ML Pb/Ge(111) Surfaces, Department of Materials Science and Engineering, Northwestern University, Evanston, Illinois (2004)

122. X-ray Instrumentation Associates. *User's Manual Digital X-ray Processor*, Newark, CA. (2000).

Appendix A X-ray fluorescence detector system

A.1 Brief introductions

The energy dispersive X-ray fluorescence system is part of the equipment control and data acquisition systems, which is described in detail in references [120] and [121]. It consists of a fluorescence detector, a NIM bin, a CAMAC crate, and a host computer, as schematically shown in Figure A.1. In terms of the data flow, the system includes the data obtaining, processing, and transferring to host computer.

A.1.1 X-ray detection

The X-ray detection detects single X-ray photon event and transforms each event into a voltage step whose jump height is proportional to the X-ray photo energy.

The detectors we have now include, Si(Li) detectors (PGT), single element Ge detectors (Canberra), multi-element Ultra Low Energy Ge (UltraLEGe) detectors (Canberra), and Silicon Drift Diode Detector (SDD, Rontec Xflash 1000). Except for the SDD, which is Peltier cooled, other detectors are required to be run at low temperature with high voltage. Therefore, a liquid nitrogen Dewar and a high voltage supply are needed. Shown in Figure A.1, unit 1 is the liquid nitrogen monitor, which on the occasion the liquid nitrogen runs low sends inhibit signal to the high voltage power supply, unit 2, to shut down the high voltage. Normally the high voltage needed to run the detector is somewhere between -500 and -1000 V. (For Canberra detectors, they can

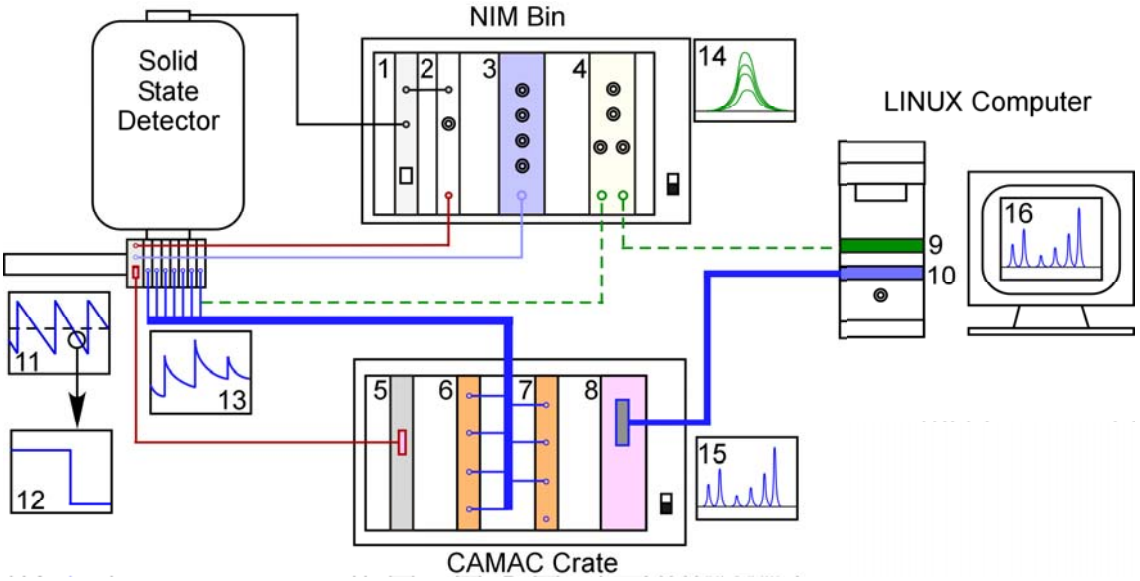

Figure A.1. The energy dispersive X-ray fluorescence detector system. Numbered in the figure are: 1, liquid nitrogen monitor (Canberra); 2, High voltage supply unit (Canberra); 3, Random pulse generator (BNC, DB-2 Random pulse generator); 4, Amplifier (Tennelec, TC-244 amplifier); 5, Detector preamplifier power supply (XIA); 6 & 7, XIA DXP2X units (four channels on each unit, XIA); 8, Jorway 73A interface card; 9, PCAIII card (Canberra/Oxford/Tennelec/Necleus); 10, SCSI-PCI interface card (Adeptec); 11 & 12, output spectrum from the optical reset preamplifier; 13, output spectrum from a resistive feedback preamplifier; 14, output spectrum from the TC-244 amplifier; 15, spectrum output from XIA DXP2X unit; and 16, the spectrum seen on the host computer running SPEC® and LabView®.

run without problem at as low as -300 V. However, the HV should be set at the manufactures recommended setting.) For all the detectors, the preamplifiers are built with the detector, for which the DC power (± 12 V & ± 5 V) is supplied by a separate preamplifier power supply, such as unit 5 shown in the Figure A.1.

Two kinds of preamplifiers are primarily used—the optical reset and the RC feed back. Both preamplifiers record a single X-ray event as a jump of the voltage level, whose height is proportional to the incident X-ray photon energy. For the optical reset preamplifier, when the accumulated voltage goes over the limit level, it will be reset back to the base level. The X-ray pulse could go either positive or negative direction, depending on the detector polarity, and the reset goes the other direction accordingly. Most of our Canberra detectors are negative polarity, i.e., X-ray pulse goes negative and reset goes positive. All the PGT ones and the oldest Canberra single element detector are positive polarity. The correct polarity information needs to be given to the next level amplifier for correctly amplifying the signal. The resetting ramp and the single X-ray event from an optical reset preamplifier are schematically shown in the inlet panel 11 & 12 of Figure A.1, respectively. For the RC feed back preamplifier, the voltage level returns back to it is base level after each X-ray event by way of discharging the capacitor, as shown in panel 13 of Figure A.1. The gain of the preamplifier is normally in the order of mV/keV. For instance, for the 7-element UltraLEGe Canberra detector, the gain is ~ 1.5 mV/keV, i.e., a Cu_Kα fluorescence photon at ~ 8 keV will yield a voltage jump of ~ 12 mV.

Shown in Figure A.2 are the examples of the output spectrum at the preamplifier

taken with a digital oscilloscope. Figure A.2 (A)-(C) are the optical reset ramp, single X-ray event and reset signal, respectively, from one element of the 7-element Canberra UltraLEGe detector. And Figure A.2 (D) is the single X-ray events from the Silicon Drift Diode Detector. For the 7-element detector, the base voltage level is ~ +5 V, the negative jump of the X-ray event and the leakage current lead the ramp downwards till it goes below the lower level, -5 V, where a reset occurs to return the voltage level back to the base level, as shown in Figure A.2 (A). The reset signal itself, Figure A.2 (C), takes normally less than 10 μs to finish, during which no X-ray event can be counted. So the optical reset is one source of deadtime (period of time that X-ray is not counted) for the optical reset preamplifier detectors. The reset rate depends on both the incident X-ray countrate and the leakage current. Normally it is very low (< 1 Hz) without X-ray signal. The high reset rate with X-ray signal absent usually indicates a high leakage current problem of the detector. The higher the X-ray countrate, the higher the reset rate therefore the longer the deadtime.

A single X-ray event is captured in Figure A.2 (B) as a voltage level drop. The fall time of the jump is typically between 50 and 100 ns. A faster fall time enables the detector to have a higher countrate. Note the small base line oscillations before and after the voltage drop. Those are caused by electronic noise in the system, including ground loop and noise from the micro-stepping motor drivers. This noise level limits the lowest X-ray photon energy the detector can actually precisely detect because the noise could be amplified and considered as X-ray signal by the amplifier. This is particularly a problem when the micro-stepping motor drivers are on. High frequency (~ 40 - 50 kHz) spikes

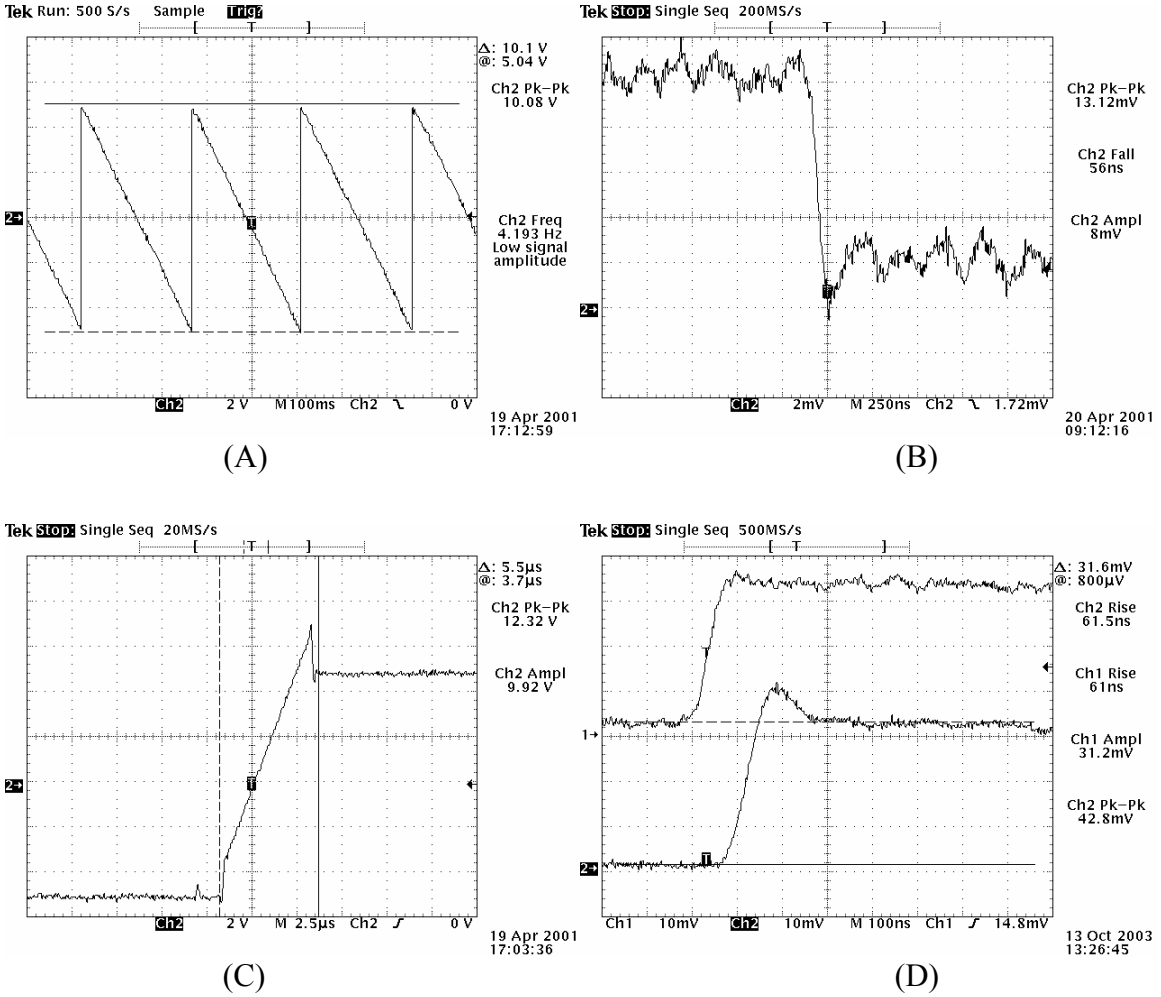

Figure A.2. The preamp output voltage vs. time spectrum captured on a digital oscilloscope for (A) reset ramp; (B) single X-ray event; and (C) reset signal for the 7-element Canberra® UltraLEGe detector; and (D) the X-ray events from the Rontec® Xflash 1000 Silicon Drift Diode Detector. The upper one is the signal from the output on the detector and the lower one is from the output on the power supply and signal processing unit. The voltage and time per major division is listed at the bottom edge of each plot.

with amplitude as high as 10 mV show up on the spectrum, which add to very high countrate at lower energy side as well as degrade the resolution. It is not clear at this time what path the noise takes to get into the detector preamplifier system. It does not help much even after carefully insulating the detector from any conducting part which could contact with the motor. The problem is with the driver unit not the motor because even the motor is disconnected from the driver, the noise still exists. On the other hand, turning off the micro stepping driver removes the noise completely. Most probably it is passed to the detector though the power line. More investigation is needed to precisely locate the source and remove it, since it is very convenient to use micro stepping to scan in angle θ through the very narrow range of the rocking curve.

A.1.2 Data processing

The data processing transforms the energy proportional voltage pulses into the digitized energy distributed spectrum. This can be done with an analog spectroscopic amplifier, such as a Tennelec TC-244 amplifier, unit 4 in Figure A.1, for which case the data flow is shown with the green lines in the figure. The output signals from the preamplifier are linearly amplified and shaped to Gaussian or triangular pulses, normally in the range of 0 – 10 V, as schematically shown in panel 14 of Figure A.1. The pulses, in time sequence, are fed into the Multi-Channel Analyzer (MCA) device, which has an analog to digital convert (ADC) for pulse-height analysis. In our case, the MCA is a PCAIII card in the host computer ISA slot. The energy distributed spectrum is generated and can be stored temporarily in the on-board memory. The shaping time (typically 4 μs)

and the ADC conversion time (~ 10 μs for a typical spectrum using 512 channels) contribute to the overall deadtime of the system.

The other way of amplification is to digitize the preamplifier output directly and analyze the voltage jump height digitally, for which the data flow is indicated with the blue lines in Figure A.1. The hardware we use for this is the XIA DXP2X, unit 6 & 7 in Figure A.1. The digitized energy distributed spectrum (i.e., MCA spectrum) generated can be stored in the on-board memory waiting for being transferred to the host computer.

The resolution and the countrate are determined by the parameters set for the amplifier and they are inversely related. To get better resolution, longer shaping time, which is normally in the order of μs, is needed to 'analyze' a single X-ray event. For example, the XIA DXP2X needs to sample the voltage level before and after the jump to calculate the exact height. The longer the sampling time (shaping time) is, the more precise the peak height is, i.e., the better the resolution. On the other hand, the total X-ray countrate it can handle decreases.

The pile-up rejection can also be setup during the amplification to reject irresolvable X-ray photons, which is defined as two or more X-ray photons coming into the detector at a time interval less than what the amplifier can resolve, roughly the same as the shaping time. The rejected photon signals are not counted towards the final output count rate (*OCR*) and are lost. This is another source of the deadtime, which is actually from the amplifier. The pile-up rate is proportional to the square of the input X-ray countrate when the incident X-ray photons arrive randomly in time sequence. The *OCR* is always smaller than the real X-ray input countrate (*ICR*) because of the pile-ups and

the short periods during which either the detector or the electronics is not really counting, such as reset time. To correct for this, typically a random reference pulse generator, such as a BNC DB-2 random pulse generator, unit 3 in Figure A.1, is used, which can randomly generate an electronic pulse with the identical shape as the X-ray induced pulse and fed into the detector preamplifier input. Knowing the actual input pulse rate of the reference pulser and its output rate in the MCA spectrum, assuming the incident X-rays are also random, the percent deadtime (*D%*) of the detector system can be calculated.

One can also determine the percent deadtime without use of a reference pulser in the spectrum. When the system is running at the identical condition except for a varying *ICR*, the system time constant, τ, can be used to express the relation between *OCR* and *ICR*.

$$OCR = ICR * exp[-ICR * \tau] \quad \text{(A.1)}$$

Once τ is determined, *ICR* can be obtained from measured *OCR* values. For the analog system, τ should be roughly 4 or 5 times of shaping time set for the amplifier (5.6 is the exact number for an analog system according to XIA manual). And its value can be obtained by fitting a set of *OCR*'s and *ICR*'s from the pulser with Equation (A.1). Generally speaking, the peaking time, which is also a frequently used term for the amplifier specification, is twice as long as the shaping time.

For XIA DXP2X unit, the percent deadtime can be estimated without using an electronic random pulse generator, which could introduce one more source of noise. When each time the DXP2X unit is instructed to count, six parameters are recorded together with the energy spectrum. They are: *LIVETIME*, *FASTPEAKS*, *EVENTSINRUN*,

OVERFLOWS, *UNDERFLOWS*, and *REALTIME*.

LIVETIME is the time span, in unit of 400ns, that the DXP2X unit is really counting X-rays, i.e., the real time subtract the detector reset time and electronics 'maintenance' time. The later includes the interrupt time the DXP2X unit performs periodically (every 500 μs) during the normal run to make sure the system works ok and updates the statistic parameters. *FASTPEAKS* is the total number of discrete preamp X-ray pulses detected in the DXP2X fast channel. *EVENTSINRUN* is the total number of counts recorded in the spectral data. *UNDERFLOWS* and *OVERFLOWS* are, respectively, the number of good (not piled up) events which lie below or above the designated energy range in the spectrum. *REALTIME* is the time period between the counting-start and counting-stop command, in the unit of 400 ns, not including the gate-off time.

The XIA DXP2X uses two kinds of digital 'filters', the fast filter, and the slow filter. Both work in a similar way to sample the digitized data, but have different sampling times, which is equivalent to the peaking time of an analog amplifier. For the fast filter, sampling time could be 50 - 500 ns. And the slow filter sampling time can be set similar to the shaping time of an analog amplifier, such as from 0.1 to 16 μs. The fast filter is to detect the arrival of the X-ray event and the slow filter is to measure the X-ray photon energy precisely. The value *FASTPEAKS* is actually the output countrate from the fast filter. Therefore the measured input countrate ICR_m is:

$$ICR_m = FASTPEAKS / LIVETIME \tag{A.2}$$

The relation between the true incident X-ray count rate, ICR_t, and ICR_m is:

$$ICR_m = ICR_t * exp[- ICR_t * \tau_{df}] \tag{A.3}$$

Where τ_{df} is the fast filter time constant, which is close to twice the fast filter peaking time. It would be a few tenths of microseconds.

The value of total output counts, *GOODPEAKS*, is the sum of all the X-ray events, whether inside or outside of the energy window on the spectrum, as:

$$GOODPEAKS = EVENTSINRUN + UNDERFLOWS + OVERFLOWS \quad (A.4)$$

And the measured Output Count Rate (*OCR*):

$$OCR = GOODPEAKS / LIVETIME \quad (A.5)$$

The relation between *OCR* and ICR_t should also follow the general Equation (A.1):

$$OCR = ICR_t * exp[- ICR_t * \tau_{ds}] \quad (A.6)$$

Where τ_{ds} is the slow filter time constant. And the overall percent deadtime is:

$$D\% = (ICR_t - OCR) / ICR_t \quad (A.7)$$

For estimation, when ICR_t is not very large, e.g., ~ 20 kcps, $\exp[- ICRt * \tau_{df}] \approx 1$, i.e., $ICR_t = ICR_m$. Assuming $OVERFLOWS = UNDERFLOWS = 0$, $GOODPEAKS = EVENTSINRUN$. Percent deadtime is:

$$D\% = (FASTPEAKS - EVENTSINRUN)/FASTPEAKS \quad (A.8)$$

The real input count rate, ICR_t, can thus be estimated with percent deadtime, *D%*. Also it is possible to obtain the time constants for the fast filter and slow filter by measuring the counts at different incident beam flux.

Because the count time of fluorescence detector (i.e. *LIVETIME*) may not be the same as the clock (i.e. *CLK*) used for all the other synchronized counters in SPEC (e.g. Ion Chambers, scintillation detector, etc), when calibrating to the incident beam, different counting time should be used for different detectors, i.e. there is a factor of

LIVETIME/CLK difference. This factor is normally very close to one. But to be precise, the correction could be included. For instance, when calculating the normalized fluorescence yield, *NORM_FY*, the total fluorescence yield, *FY*, and the beam intensity monitor, I_0, should be normalized to counting times *LIVETIME* and *CLK*, respectively.

$$NORM\_FY = [FY / (1 - D\%) / LIVETIME] / (I_0 / CLK)$$
$$\approx (FY / I_0) * (FASTPEAKS / EVENTSINRUN) * (CLK / LIVETIME) \quad \text{(A.9)}$$

A.1.3 Data transfer

The data transfer sends the digitized spectrum to the host computer. This is trivial for the PCAIII card since it resides in the computer. And for the XIA DXP2X units, the data are transferred via the high speed SCSI interface between the CAMAC crate and the host computer, unit 8 & 10 in Figure A.1, respectively. The transferring speed is fast (up to 20 MB/s). The energy spectrum can be displayed or saved into file on the host computer, on which runs the SPEC® and LabView®.

The combination of the multi-element detector, the faster digitized data processing and the faster computer allows the fluorescence detector system to be able to handle much higher countrate than it used to be.

A.2 Setting up the XIA DXP2X system

A.2.1 Before starting:

(1). Make sure the detector has been completely cooled down before applying the High voltage. This is true for all the Si or Ge solid state detector (SSD). The required minimum cooling time is labeled on the detector. It is usually between 4 and 12 hours for LN2 cooled detectors. The Silicon drift diode detector (SDD), which is Peltier cooled and does not need liquid nitrogen, takes only a few minutes to be cooled down. However, it may need one half to one hour to reach its best performance.

(2). Make sure that the computer is STARTED with the CAMAC crate power on and the cable between the computer and the CAMAC crate controller (Jorway 73A card) connected. If this is not the case, restarting the computer with all the cards, cables and connections in their positions should solve the problem. Upon starting up, the computer power-on self-test (POST) will find the 'Jorway 73A'—our CAMAC crate controller (before loading LINUX). Also LINUX will load the driver and initialize it. Check the 'SCSI ID' number on the front panel of the 'Jorway 73A' before start/restart the computer. Currently number 6 is used. Number 0 through 6 are all valid—but be careful changing this if there are other SCSI devices in the system. Also make sure if a number other than 6 is used the same number should be used for all the settings in both the MESA2X® and the SPEC® configuration files. It is highly recommended to use number 6 only for SCSI ID unless it is absolute necessary to do otherwise. The two DXP2X units are in CAMAC crate slot #7 and #8 at 5IDC and the single unit is in slot #7 at 12IDD. If

any one of those needs to be moved to another slot, it is necessary to update the configuration files for MESA2X, as well as in the 'config' and configuration files of SPEC. See the *configuration files* part below for details about changing the SPEC configuration files.

(3). There are two jumpers inside of XIA DXP2X unit that may need to be changed when changing detectors. One is the scale factor for the preamplifier gain. It can be 1 or ¼. If the preamplifier gain is too high for DXP2X to handle, set the jumper to ¼ position. Normally it is set at 1 position. The first time the new PGT detector arrived, its gain was about 10 times larger than other detectors. The jumper had to be changed to ¼ position to get the system working. After the preamplifier gain was reduced, the jumper was changed back to 1 position. The other jumper indicates whether the preamplifier is optical reset or RC feed back. Currently, for both 12IDD and 5IDC, the last channel of the DXP2X unit(s) is set for RC feed back to be able to work with the Rontec SDD detector. The channel is labeled as 'Rontec'. Do not connect any solid state detector to this channel and do not use any other channel for the SDD detector.

The jumpers are independent for each single channel on each DXP2X unit.

A.2.2 Running MESA2X

(1). Start LabView®: there is a shortcut on the computer desktop; double click to start it. Or if running remotely, it can be started by typing 'labview' in the shell prompt. An executable file named 'labview' was set in the directory $HOME/bin/, as:

```
/usr/local/lv51/labview >/dev/null &
```

where $HOME is the home directory of the current user.

(2). Always first load the ‘camac-ini’ from the file ‘cam73alx.llb’ locating in the directory: ‘/usr/local/xia/mesa2x-3.0.0/’. The file can be found from the open-file history list. After loading, change the ‘CAMAC Crate’ value to ‘6’, or the corresponding ‘SCSI ID’ number set on the front panel of ‘Jorway 73A’ card. Run it a few times until two green buttons show up on the program panel. Close this program.

(3). Now it is time to load MESA2X. Before doing that, make sure there is a file named ‘Mesa.ini’ in the same directory as the loaded program. For our case, it should be in the directory: ‘/usr/local/xia/mesa2x-3.0.0/’.

NOTE: for different detector setups, different ‘Mesa.ini’ files are needed. Normally there are backup directories, in ‘/usr/local/xia/mesa2x-3.0.0/configs/’, for all the configuration files of each detector. The correct ‘Mesa.ini’ file should be saved in the corresponding directory, some with the suffix indicating explicitly which detector it is for. Copying the backup file to overwrite the one in its running directory should be ok. Backup the file before overwriting it is always a good habit.

(4). Load ‘mesa2x_v30.vi’ (the first one in the list) from the file ‘mesa2x-v3.0.0.llb’. Be patient, it will take a while. Different from the earlier version, the program will not run automatically after being loaded. Click the ‘run’ button (the button on the top-left corner of the window with an arrow on it) to run it anytime.

(5). Once MESA2X starts to run, the firmware files and the parameters will be downloaded into DXP2X module(s). This will take quite a while depending on how many detector elements are in use. After downloading is finished, the ‘System Setup and

Initialization' menu shows up. Occasionally the initialization process stalls. If after a few minutes an error message pops up saying--"Timeout waiting for BUSY to go to 0. View Parameters?" Just answer 'No'. The program will try again, and it will always work properly the second time. Presumably, this error is caused by a communication error between the host computer and the CAMAC crate, and it can be avoided by loading and running the 'camac.ini'.

Usually only 'DXP Configuration' (the third one on the list) needs to be run to load a proper configuration file for the desired peaking time and/or the energy range. Simply click the 'Restore Config From File' button and choose the proper configuration file from the directory '/usr/local/xia/mesa2x-3.0.0/config'. The filename of each file indicates the detector type, the peaking time and the energy range, such as '7chan_8us_20ev.dxp' is for the 7-element detector with 8 microseconds peaking time and 20 eV per MCA channel corresponding to 0 - 20 keV energy range with a total of 1024 MCA channels. Also an extra copy of each configuration file is saved—they should be in the backup directories, '/usr/local/xia/mesa2x-3.0.0/config/xxxsave'. Here xxx indicates the detector, e.g., '3ele' means the 3-element detector; and 'rontec' means Rontec detector. The backup files are owned by 'root' so that unintentional changes can be prevented. If a configuration file in the original directory is suspected of being corrupt, just load the one with the same name from the backup directory and try again. Replace the bad one if necessary.

(6). Close the window after the file loaded AND the numbers on the program panels updated. Currently the configuration files cover the peaking time (about twice the

shaping time) of 1, 2, 4, 6, 8, 12 microseconds and the total energy range of (from 0 to) 8, 12, 15, 20 keV for each detector.

NOTE: DO NOT touch the button ‘Adjust Selected’.

(7). Quit the setup section and load the ‘Multi-Channel Analyzer’ function. Check if the spectrum can be seen as expected. This part runs extremely slow when more than one element is involved. Prepare for a delay of about 10 seconds or more for the 7-element detector before a real spectrum get updated on the screen. For the single element detector, it is much quicker. Switching between elements is arduous. It is recommended to do this after stopping the data collection and waiting until all three ‘time’s (elapsed time, real time and live time) shown on the panel come to the similar value. Using a faster computer does not solve this problem. Changing the ‘Update Time” in “Acquisition Options” to 5 seconds from 1 can speed up the process. This is only intrinsic to MESA2X. Reading spectra out from the DXP2X unit is fast (~ 2 MB/s) and SPEC experiences no significant delay when plotting a spectrum.

(8). If nothing shows up on the MCA spectrum or it does not make sense, quit this function and ‘Exit’ from MESA2X. Run it from step (2) again and check.

(9). NOTE: at this point, MESA2X software will crash on the ‘Gaussian fit’ routine unpredictably. It is probably due to some uninitialized pointer in the source code. So avoid using any of the following four functions: (a). ‘View baseline’; (b). ‘Gaussian iteration fit’ in the ‘Match Gain’ function; (c). ‘ROI’ sub-function in the ‘MCA’ function; (d). ‘Parameter Scans’ function.

(10). See the ‘MESA2X v3.0’ manual for more details.[122]

A.2.3 Working with SPEC

(1). IMPORTANT: SPEC will initialize the DXP2X module(s) every time SPEC starts or quits from running 'config', i.e., 'reconfig' is called. Since SPEC is not able to load the configuration files properly (not now, maybe not ever), these initializations are NOT wanted. However, we can not disable the SPEC initialization. So always run MESA2X from the beginning after either of these two types of SPEC operations is carried out or whenever needed.

(2). SPEC needs four specific configuration files to drive the DXP/DXP2X unit when started. Any problem with any of these files will prevent SPEC from initializing thus using the DXP2X. They are 'xiasystem.cfg', 'dxp.module', 'dxp.cfg' or 'dxp2x.cfg' and 'preamp.cfg'. All of these files are in the directory '/usr/local/lib/spec.d/dxp2x/config/'. Of course all of the XIA DXP/DXP2X firmware files and configuration files for DXP or DXP2X module are still need. Generally speaking, users do not need to touch or even know the existence of these files. The basic idea here is that SPEC always initializes all 7 channels (for SSD detectors). MESA will properly setup the channels that are being used, e.g., only 3 out of 7 channels for using the 3-element detector. And the data taking software (macros) should be set to only read data from the channels correctly setup.

The only exception is when switching between an SSD and an SDD, where a different kind of firmware is needed to be downloaded into a special channel, where the

jumper setting selects RC feedback instead of optical reset. In that case, a full set of files needs to be loaded from the backup directory into the working directory. The backup files are in '/usr/local/lib/spec.d/dxp2x/config/***cfg/', where '***' indicates the detector type, e.g., 'RT' stands for Rontec detector and '7ele' stands for 7-element detector.

(3). Make sure MESA2X is inactive (not taking data or having any kind of communication with DXP2X module) whenever SPEC is going to be used to talk to DXP2X, and vice versa.

(4). The 'dxp.mac' macro can view the spectrum. Always run 'setdxp' first. This macro is not that useful since we can always view the spectrum with MESA2X. One advantage of the macro is that the spectrum update are much faster than MESA2X.

(5). The 'xswdxp.mac' macro is used for standing wave measurements. Always run 'setxswdxp' first and then 'setdxpsca'. Usage is similar to 'xsw.mac' with PCAIII cards. Both macros are in the user macros directory. Resize the XTERM window to full screen long (≥ 40 rows) to allow the macro to display the information properly.

(6). The 'xswdxp.mac' macro now supports XAFS measurement by calling the 'moveE' macro in SPEC instead of controlling one real motor. To do this, set 'device' (the first one) to 'E' in the 'setxswdxp' macro. Also 8 SCA channels were added to the saved data. A user can define up to 8 SCA regions (with their starting and end value in MCA channels) based on the spectrum. A user can also choose to assign any of the SCA channels to a counter/scaler so that it can be recorded and plotted out after each scan (just like plotting the rocking curve after one XSW scan). By default, the starting and the end

MCA channels for the 8 SCA regions are set to 0, i.e., the SCA is disabled. It does not need to be set unless desired. However, it is recommended to set a few SCA's for the purpose of deadtime correction. See Appendix B.2 for details.

Currently, in the XSW data file, the first MCA channels are used to record the counters/scalers from SPEC. The number of channels used is determined by the number of enabled counters in SPEC, i.e., given by the constant 'COUNTERS' in SPEC. The next 6 channels are parameters from the DXP2X memory for deadtime correction purpose. The next 8 channels are SCA counts. These numbers are defined inside the macro as CONSTANT, change the constants if the data file format needs to be changed. Be aware here, that setup SCA's in 'setdxpsca' has the start and end spectrum channel numbers as 0 - 1023. But in the XSW data file, the spectrum channel numbers are from 1 - 1024. Do not forget the 1 channel shift when processing the data with SUGO or other software. For instance, if reflectivity is recorded in counter 'REFL', whose counter number is 1 (time base is always 0), in the data file the MCA channel number for it is 2.

A.2.4 Configuration files

(1). For MESA2X

(a). Firmware parameters need to be downloaded into DXP2X: 'd2xr0106b.hex' for SSD and 'd2xf0007a.hex' for SDD—this file can be updated from time to time by XIA. SPEC is supposed to have no problem with this. But keep an eye on that since the external library used by SPEC for DXP2X is independent from MESA2X software.

Modifications may be necessary for this library. At anytime, make sure MESA and SPEC use the same *.hex file. Otherwise the SPEC macros will not work properly. ‘f01x2p0g.fip’, ‘f01x2p2g.fip’, ‘f01x2p4g.fip’, and ‘f01x2p6g.fip’ are files for the SSD for different peaking times. And ‘f01x2p0j.fip’, ‘f01x2p2j.fip’, ‘f01x2p4j.fip’, and ‘f01x2p6j.fip’ are files for the SDD for different peaking times.

(b). User-defined files are ‘Mesa.ini’, ‘*.scf’, ‘*.ddf’, and ‘*.dxp’. See the ‘User’s Manual of MESA2X v3.0--Appendix B’ for a detail explanation of these files. A brief introduction goes here--

‘Mesa.ini’ contains the information for the filename and location of the firmware files, as well as other user-defined configuration files. Generally speaking, except for the first time running MESA2X on one specific setup, the user does not need to edit this file. For the case in which the system is being modified, such as, when an XIA module is moved to a different CAMAC slot, SCSI ID changes, or when a different detector is used, the user should change this file to notify the software where to look for the proper configuration file. The user should also modify the ‘*.scf’, ‘*.ddf’, and ‘*.dxp’ accordingly for the new setup. The MESA2X software will update this file automatically at some point (e.g., upon quitting the program).

The ‘*.scf’ file is for system configuration. The ‘crate’ and ‘slot’ number here are essential. If the information here is incorrect, the software will never find the hardware. ‘crate’ is the ‘SCSI ID’ number (6). And ‘slot’ is the slot number of the DXP2X unit in the CAMAC crate (7 or 8).

The ‘*.ddf’ file holds information about the detector—polarity, detector geometry,

preamplifier gain, etc.

The '*.dxp' file contains the calibrated parameters for the XIA electronics pertaining to the amplifier. The filename normally contains the peaking time and energy (in eV) per MCA channel.

All the files have backup copies in the backup directory '/usr/local/xia/mesa2x-3.0.0/config/***save'.

(2). For SPEC

(a). The firmware parameter files are the same as those used for MESA2X.

(b). User-defined files are 'xiasystem.cfg', 'dxp.module', 'dxp.cfg', 'dxp2x.cfg', and 'preamp.cfg'. The first two are critical for SPEC recognition of the hardware settings.

The 'xiasystem.cfg' file with the full path is pointed to by a system environmental variable—XIA_CONFIG. Change the definition of this variable if the file name or position changes. In the file '/home/username/.bash_profile', change the line to what it needs to be, such as:

'export XIA_CONFIG = /usr/local/lib/spec.d/dxp2x/config/xiasystem.cfg'

Example of the file:

Preamp /usr/local/lib/spec.d/config/preamp.cfg
Modules /usr/local/lib/spec.d/config/dxp.module
dxp4c NULL
dxp4c2x NULL

The filenames and file locations of 'preamp.cfg' and 'dxp.modul' are defined in

the first two lines. The other two lines are not really used for now.

The ‘dxp.module’ file defines where the module is located in CAMAC crate and what firmware parameters are needed for each module.

Example of the file:

board_type dxp4c2x
iolibrary camacdll.dll
interface CAMAC
module 0107 0 1 2 3
default_fippi /usr/local/lib/spec.d/config/f01x2p4g.fip
default_dsp /usr/local/lib/spec.d/config/d2xr0104b.hex
default_param /usr/local/lib/spec.d/config/dxp2x.cfg
*
board_type dxp4c2x
iolibrary camacdll.dll
interface CAMAC
module 0108 4 5 6 -1
default_fippi /usr/local/lib/spec.d/config/f01x2p4g.fip
default_dsp /usr/local/lib/spec.d/config/d2xr0104b.hex
default_param /usr/local/lib/spec.d/config/dxp.cfg

Explanation of the file:

‘*board_type*’ could be ‘dxp4c’ or ‘dxp4c2x’ for the old style DXP and DXP2X, respectively.

‘*iolibrary*’ is not really used on LINUX, leave it as it is.

‘*interface*’ is ‘CAMAC’, do not change.

‘*module*’ defines the slot # and channel #. The first two digits are not used. The next two digits are the slot # of the module. The following four numbers are the channel numbers for each of the four DXP channels, respectively. Use ‘-1’ for the channel that is

not being used. For instance, '*module 0107 4 5 6 –1*' means that the module is in CAMAC slot #7; its first three channels (marked as 0, 1, and 2 on board) are used as system channel 4, 5, and 6; and its last channel is not being used.

'*default_**' are the default files for the firmware parameters.

Repeat the list for additional DXP/DXP2X module.

The 'dxp.cfg' and 'dxp2x.cfg' files define the parameters for the different module.

Example of the file:

```
POLARITY        0       ! 0 = negative, 1 = positive
RUNTASKS        122
SLOWLEN         25      ! 1  usec peaking time example
SLOWGAP         3
PEAKINT         29
FASTLEN         4
FASTGAP         0
THRESHOLD       20
MINWIDTH        4
MAXWIDTH        20
PEAKSAM         28
DECIMATION      4
```

The 'preamp.cfg' file defines the polarity and the reset range of the preamplifier.

Example of the file:

```
ENERGY      5.9
0,      1.0,    0,      -5.,    5.,     10
1,      1.0,    0,      -5.,    5.,     10
2,      1.0,    0,      -5.,    5.,     10
3,      1.0,    0,      -5.,    5.,     10
*
4,      1.0,    0,      -5.,    5.,     10
5,      1.0,    0,      -5.,    5.,     10
6,      1.0,    0,      -5.,    5.,     10
```

7, 1.0, 0, -5., 5., 10

Explanation of the file:

'ENERGY 5.9' is the calibration energy, in keV.

'0' the 1st number, is the system channel #, (start from 0).

'1.0' the 2nd number, is the preamplifier gain factor.

'0' the 3rd number, is the polarity (0-negative, 1-positive).

'–5.' the 4th number, is the minimum voltage of the preamplifier output (in V).

'5.' the 5th number, is the maximum voltage of the preamplifier output (in V).

'10' the 6th number, is the typical step size of the preamplifier signal due to an incident X-ray (in mV), here for 5.9 keV X-rays.

Note in all these files, a line start with a star '*' is a comment line.

A.2.5 Brief explanation of a few MESA2X parameters

There are more than 100 parameters listed in the 'View Parameters' panel in MESA2X. Some of these are read-back values during counting, such as *FASTPEAKS* and *LIVETIME*. Some are user defined data taking related, which will not affect the function of the spectrum taking. And some are critical for the DXP2X to correctly amplify and analyze the preamplifier output. The default parameter values, according to XIA manual, should be a good starting point when calibrating a new detector. And the built-in calibration function with MESA2X should be able to optimize them automatically. However, this may not always be true. Sometimes the default value (or whatever starting value) can not get the DXP2X unit to work at all. In that case, the

calibration function will not help at all. Therefore, some knowledge about the parameters, at least the most important ones, is very useful.

First, all the time related parameters are based on some time unit and therefore are all integers. But not all the parameters use the same time base. And even the same parameter can be using a different time base in different circumstances, which is indicated by a parameter '*DECIMATION'*. *DECIMATION* should not be hand selected; rather, it is determined by the peaking time settings. It is '0' for the shortest peaking time, 0.125 - 0.625 μs; '2' for 0.5 - 2.5 μs; '4' for 2.0 - 10 μs; and '6' for 8 – 40 μs. Once a peaking time is chosen, a DECIMATION number is set and the corresponding firmware file (*.fip) is downloaded into the DXP2X memory.

Before any processing, the analog output from the preamplifier is digitized at a rate of 40 MHz, i.e., at 25 ns intervals. This is the basic (and smallest) time unit for the parameters.

The fast filter related parameters are all using the basic time unit, i.e., 25ns, including *FASTLEN*, *FASTGAP*, *MINIWIDTH* and *MAXWIDTH*. A fast-filtered signal for a single X-ray photon is the shape of a symmetric triangle.

FASTLEN is the fast filter length, i.e., the fast filter peaking time. The typical value is 4, i.e., 100 ns. *FASTGAP* is the fast filter gap, typically is 0. *MINIWIDTH*, combined with *THRESHOLD*, is used to reject the noise. To be counted as an X-ray event rather than noise, a fast-filtered signal, i.e., the triangle, has to have a time width longer than *25*MINIWIDTH* ns at the *THRESHOLD* value. A typical value of *MINIWIDTH* = 4 is used for *FASTLEN* = 4 according to the manual. If it is too small, the

sharp electronic noise (spikes) will not be rejected effectively. If it is too large, the real X-ray signals might be at risk of being rejected. *MAXWIDTH* is set to reject the pile-ups in the fast filter. When the fast-filtered signal does not go below the *THRESHOLD* level between two or more incident X-ray photons, the length of the fast-filtered signal that is above the *THRESHOLD* value will be significantly larger than a signal X-ray should be. And a typical value of:

$$MAXWIDTH = 2 * FASTLEN + FASTGAP + N \quad \text{(A.10)}$$

Where *N* is in the range of 4 - 8. If its value is too small, it will reject the real signals. And if it is too large, it can not reject the pile-ups properly. For a *FASTLEN* = 4, the *MAXWIDTH* around 15 should be all right. This method can not reject the double or multiple pile-ups where two or more X-rays arrive in the detector at the same time.

NOTE in MESA2X, the default values are *MINWIDTH* = 2 and *MAXWIDTH* = 20, which are not the best values.

The slow filter related parameters are using the time unit based on the *DECIMATION*, including *SLOWLEN*, *SLOWGAP*, *PEAKSAM*, and *PEAKINT*. For *DECIMATION* settings of 0, 2, 4, and 6, the time unit is ($25 * 2^{DECIMATION}$) ns, i.e., 25, 100, 400, and 1600 ns, respectively. The slow-filtered signal for a single X-ray photon is the shape of an isosceles trapezoid.

SLOWLEN and *SLOWGAP* are the slow filter length and gap value. Typically *SLOWGAP* = 6 for *DECIMATION* = 0 and *SLOWGAP* = 3 for all other cases.

PEAKSAM is the time from the fast-filtered signal reaches peak value to the point where the slow-filtered signal is taken as the X-ray photon energy reading. The energy

reading, i.e., the sampling, should be performed on the flat top of the trapezoid. Therefore *PEAKSAM* is roughly the time delay of the slow filter peak relative to the fast filter peak. For the optical reset preamplifier it should be close to

$$PEAKSAM = SLOWLEN + SLOWGAP/2 \quad \text{(A.11)}$$

Larger or smaller *PEAKSAM* values will lead to the sampling at a position off the flat top of the trapezoid and therefore will result in a bad resolution. And for the RC feed back preamplifier, the *PEAKSAM* value is generally a few time units smaller than that calculated with Equation (A.11). For the Rontec Xflash 1000 SDD detector, whose discharging time constant is around 100 μs, a *PEAKSAM* value with 3 time units smaller than the default value offered by MESA2X works best, e.g., the default value for *PEAKSAM* is 15, 12 would be the best number to use.

PEAKINT is used to reject pile-ups in the slow-filter signal when the X-ray photons are well resolved in the fast filter. The value could be set as:

$$PEAKINT = SLOWLEN + SLOWGAP + N \quad \text{(A.12)}$$

Where $N = 2$ or 3. A too large *PEAKINT* value will reject the non-pile-up X-ray signals. And a too small value will not reject the pile-up properly. Practically it is found that when *PEAKINT* is equal to or smaller than *PEAKSAM*, no X-ray signal passes though at all.

THRESHOLD is related to the energy level set for the threshold, the gain, and the *FASTLEN* value. Changing the energy threshold level in the 'DXP configuration' window should update the *THRESHOLD* value properly. It is the combination of this and the *MINWIDTH* that can properly reject the noise.

Finally, these parameters should be set correctly by MESA2X program. Knowing what they are and what value they should be would help to diagnose the problem if the software does not work as expected.

Appendix B SPEC macros associate with XSW data collection

The XSW measurement requires both the reflectivity and the fluorescence data to be recorded simultaneously. A simplified way to accomplish this is to set up the single channel analyzers (SCA's) to record the total count rate for the characteristic fluorescence signal of interest. Normally the fluorescence signal from the surface adsorbate is very weak. Therefore the real net count rate under the peak could be comparable to or even smaller than the background count rate in the fluorescence spectrum. To precisely measure the fluorescence yield of the element, a full fluorescence spectrum rather than one or a few SCA's is preferred. The full spectrum can be incorporated into the SPEC scans in two different ways. One is using the specially defined XSW macro. The other is recording the spectrum while doing the normal SPEC scans, e.g., ascan, dscan, or hklscan.

B.1 XSW macro

The XSW macro, originally written by Tien-Lin Lee, can collect the fluorescence spectra from a single detector element through the PCAIII or PCAII card. The macro also has a built-in drift control mechanism, which monitors and corrects the drifting of the rocking curve center at the end of each and every single scan. The data from the scan are either accepted or rejected based on the preset maximum drift value and the scan

center is adjusted accordingly. The accepted data from single scans are accumulated and saved into a special XSW data file upon finishing the preset number of single scans, i.e., one saveset. Multiple savesets can be recorded into one XSW data file. This way the temporal changes in the sample can be followed. Also the risk of losing useful data is minimized. The XSW data file is basically in the format of a two dimensional array with a column assigned to each step in the SPEC scan and the rows as the MCA channels. And the lowest MCA channels are overwritten with SPEC counters as described in A.2.3.

The XSWDXP macro, while inheriting all the XSW features, develops the ability to record and save the spectra from multiple detector elements. Although now the macro is written to read from the XIA DXP2X unit, it can be easily modified to work with the PCAIII card.

Since the XSWDXP macro is a custom built macro, it is under constant change. But mostly the changes are minor and the user interface is preferred to stay the same. The macro file, named xswdxp.mac, actually consists of dozens of SPEC macros, which are able to work together or independently. Based on the functionality, the macros can be grouped into three sub-sets, i.e., SETXSWDXP, SETDXPSCA, and XSWDXP.

B.1.1 SETXSWDXP macro set

SETXSWDXP is the set of SPEC macros that initialize the hardware and set up the software environment for collecting spectra. The flow chart of SETXSWDXP is shown in Figure B.1 and the hierarchy tree is shown in Figure B.2 (B), where the blocks in blue are the end macros, which are only called by other macros. And the blocks in red

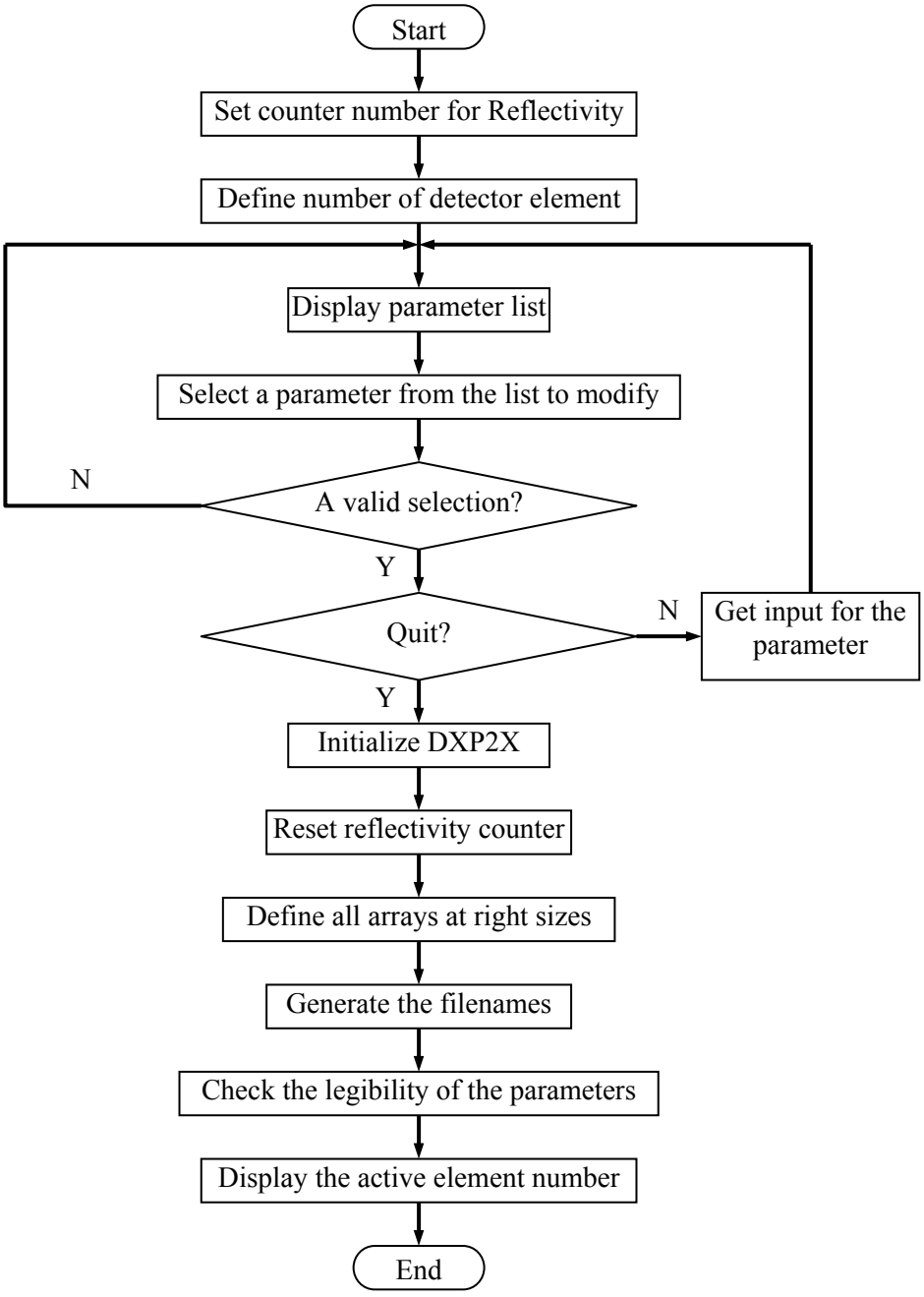

Figure B.1. Flow chart of the SETXSWDXP function.

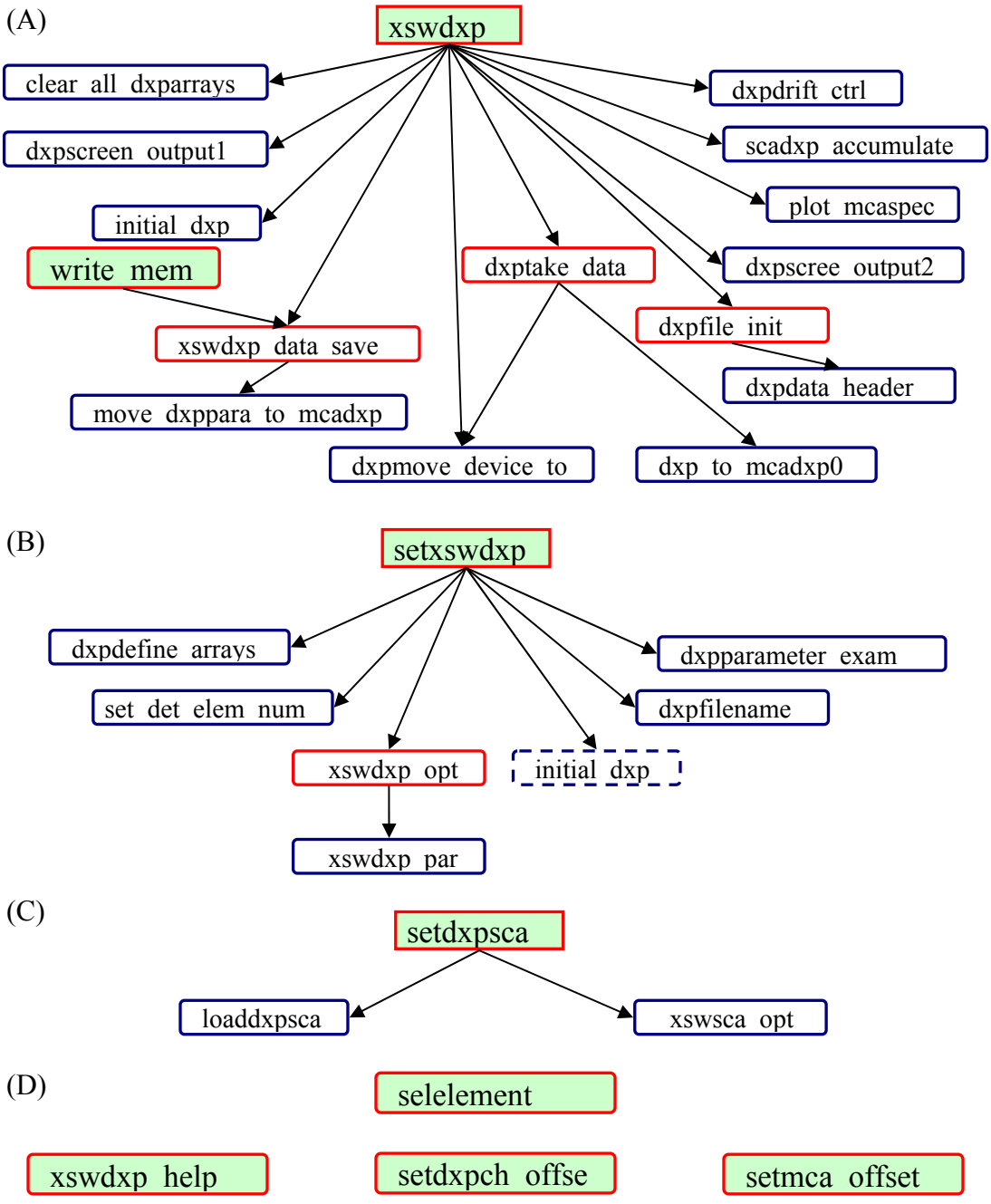

Figure B.2. The hierarchy tree of the macros in the file xswdxp.mac, including (A), XSWDXP function group; (B), SETXSWDXP function group; (C), SETDXPSCA function group; and (D), other functions.

are higher-level macros, which call upon other macros. And the blocks shaded with green are the interfacial macros, which are the only ones a user needs to be aware of.

The structure and the codes of the macros are simple and straightforward. There are a couple of points that need to be addressed. The drift control relies solely on the readings of the reflectivity counter. And it is the user's responsibility to make sure that the correct counter number is assigned as the reflectivity. This is given by the constant REFL, which can be redefined in the macro SETXSWDXP. Also the reflectivity curve should be well defined, i.e., a single peak is expected and the signal to noise ratio should be far greater than 1.

The number of detector elements used needs to be setup properly for communicating with the hardware and for initializing the size of the data array correctly. Because the XIA DXP2X unit is configured with the MESA2X program instead of SPEC, there is no way to check whether a DXP2X channel is used or not within SPEC. Accessing a non-configured channel might lead to an unpredictable error. Therefore it again requires the user to give a proper input. It is given by the constant num_ele, which can be redefined in macro SETXSWDXP or with macro set_det_ele_num. Currently the macro can only deal with the DXP2X channels in continuous mode, e.g., if three detector elements are used, they should be connected to the DXP2X channel 0, 1, and 2 or channel 1, 2, and 3. It is not acceptable to connect the three detector elements to the DXP2X channel 0, 1, and 3 or channel 0, 2, and 3. And the DXP2X channels in use are defined by num_ele together with two other constants, mca_offset and dxpch_offset. The former is the device number of the first multi-channel analyzer (MCA) device in use and the

later is the channel number of the first DXP2X channel in use on the MCA device. The details about the proper values for the two constants can be found in the next section as 'MCA device number' and 'MCA channel number'. The two constants can be reset with macros setmca_offset and setdxpch_offset.

The parameter list is easy to follow. The 'device' can be any single motor defined in SPEC. Other than that, the special devices can be used are listed in xswdxp_help macro. Other special devices can be added by changing the code of macros dxpmove_device_to and dxpparameter_exam. If a single motor is selected, the 'center' is automatically assigned as the current motor position. The DXP2X 'channel usage' determines whether the data is recorded for a channel or not. It is expecting a string with a series of 'y' or 'n', with 'y' as recording data, 'n' as ignoring data. The default is 'n'. The first letter corresponds to the first used channel and so on. For instance, for a 7-element detector, a string 'yynnyy' means data from channel 0, 1, 4, and 5 are recorded and those from channel 2, 3, and 6 are ignored. Note here even if the data from a channel is set to be 'ignored', the corresponding detector element is still working normally and the spectrum is read and analyzed by the DXP2X unit. The only thing that is 'ignored' is the data transfer from the DXP2X channel to the host computer.

The 'lower' and 'upper' energy channel limit can be used to record a partial instead of a full spectrum. The 'active DXP2X channel' defines which detector element is currently active, i.e., for which the SCA is recorded and the spectrum is plotted out.

After the parameters are set, the data arrays are initialized accordingly. A single two-dimensional array is used for storing all the data from all detector elements during

one scan. Each column represents an MCA spectrum from one detector element at one scanning step. And the total number of columns is one plus the product of the number of scanning steps and the number of detector elements. The additional column, always the first one, lists the MCA channel numbers.

In the case of a multi-element detector, there are always differences in behavior between the elements. Therefore the data from each element should be saved separately. The filenames for the datafiles are generated with the user-input name string and the formatted suffixes, including the version number user input and the detector element number. For example, a filename would be like 'user_given_name.002.ch2', where '002' indicates the version number is 2 and 'ch3' indicates the spectrum is from the detector element number 3.

The parameter legibility check helps to prevent improper operations. It is critical to setup a correct scanning device and record the spectra with at least one of the detector elements. Also to protect the existing datafile from being overwritten, the filenames are first checked to make sure that no identically named files are present. The macros will never overwrite an existing file. If a file with the same name is found, the version number will increase by 1 automatically before returning to the user. In SPEC, if the filename is invalid, no file will be opened and the data will be only dumped on screen. So another filename check is performed by actually opening the file. A new filename is required if the file cannot be opened successfully. If the filename is valid, the opened empty file then is closed and deleted. Note SPEC can handle up to 8 simultaneously opened files. If somehow the number of open files reaches 8, some of the opened files

have to be closed before the macro can run successfully. Use the SPEC command on() to check which files are open and the command close("file_name") to close an opened file. Make sure the file is not in use before closing it. If an error is found in the parameter check and a default value can be set for the problematic parameter, a warning message is generated. If no default value can be used, an error message is generated. At the end of the parameter check, if error messages are present, the user is asked to rerun the SETXSWDXP to correct them; if only warning messages are present, the user can either run SETXSWDXP again to give the proper input or go ahead with the default values.

B.1.2 SETDXPSCA macro set

SETDXPSCA is the set of macros that set up the software SCA, including the MCA channel range and the SPEC counter where the SCA value is stored. The flow chart of the SETDXPSCA is shown in Figure B.3 and the hierarchy tree is shown in Figure B.2 (C).

The number of software SCA's is defined with the constant MAXDXPSCA. The setting for each SCA includes three values—the start and end MCA channel number and the number of the SPEC counter to which the SCA is assigned. The last used values are saved in the file '$HOME/dxpsca.input' and loaded upon restarting SETDXPSCA, where $HOME is the home directory of the current user.

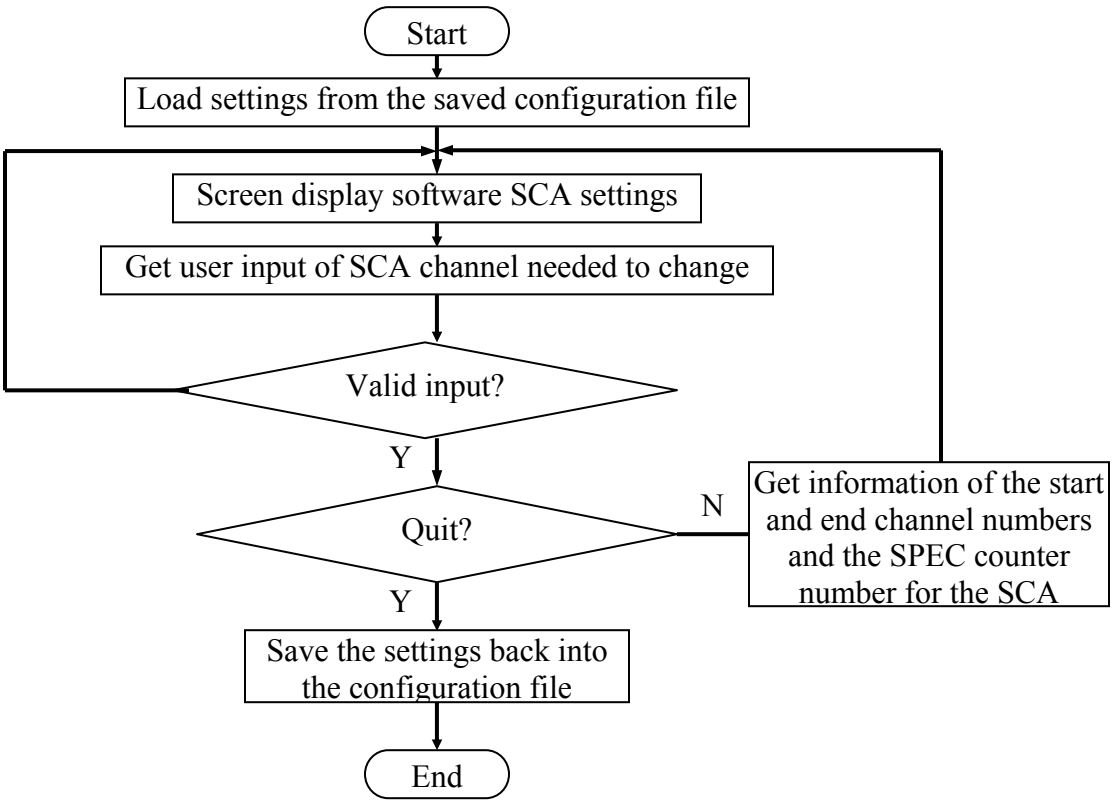

Figure B.3. Flow chart of SETDXPSCA function.

By default both the start and end MCA channel numbers are zero; and the counter number is –1, which means do not assign an SCA to any SPEC counter. It is after the SPEC counter is updated (getcounts) that the software SCA is assigned to the corresponding counter, which is quite inconvenient because it disregards the usage of the counter. Therefore be very careful when assigning the counter number to an SCA. It is recommended that the user always assign an unused counter to an SCA.

B.1.3 XSWDXP macro set

XSWDXP is the set of macros that run the multiple scans and collect both the reflectivity and the fluorescence data simultaneously. The flow chart of the XSWDXP function is shown in Figure B.4 and two sub-functions, Initialization and Data-taking, are detailized in Figure B.5 (A) and (B). The hierarchy tree is shown in Figure B.2 (A).

The XSWDXP macro does not require any input from the user once the setups have been done properly. The single SPEC scan with the designated device(s) will be repeated up to the preset number of times. At each scanning step, all the SPEC counters and the fluorescence detector will count for the predefined time period. The MCA spectra and the counter readings are loaded into their own data arrays. Also recorded are the SCA's and the special counting parameters for deadtime correction from the XIA DXP2X, as described in Appendix A. At the end of each single scan, the drift of the reflectivity curve center is checked (if the drift control option is on) and the data are accumulated. And at the end of each saveset, the accumulated data are saved into the separated files corresponding to the different detector elements. The lowest MCA

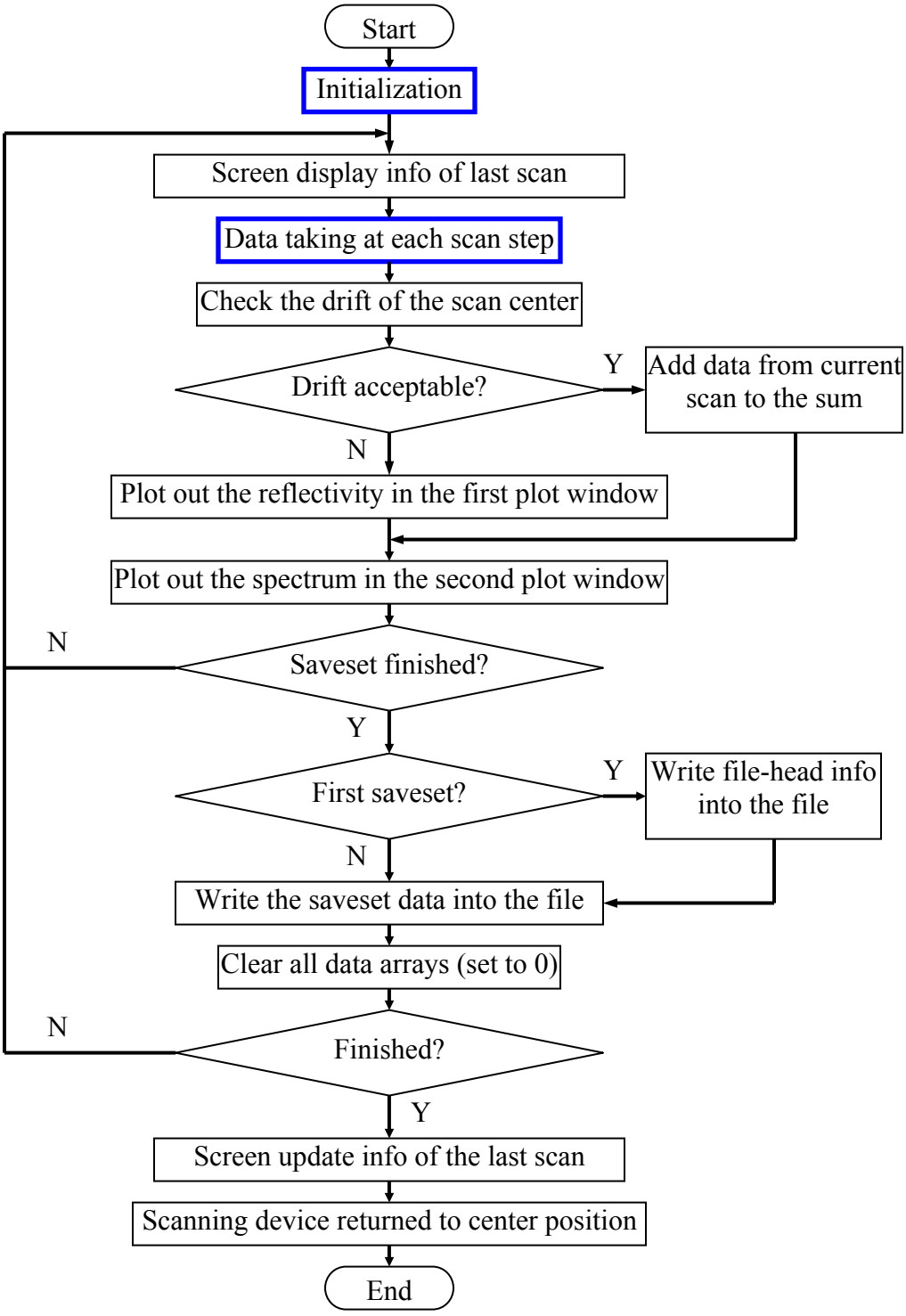

Figure B.4. Flow chart of the XSWDXP function.

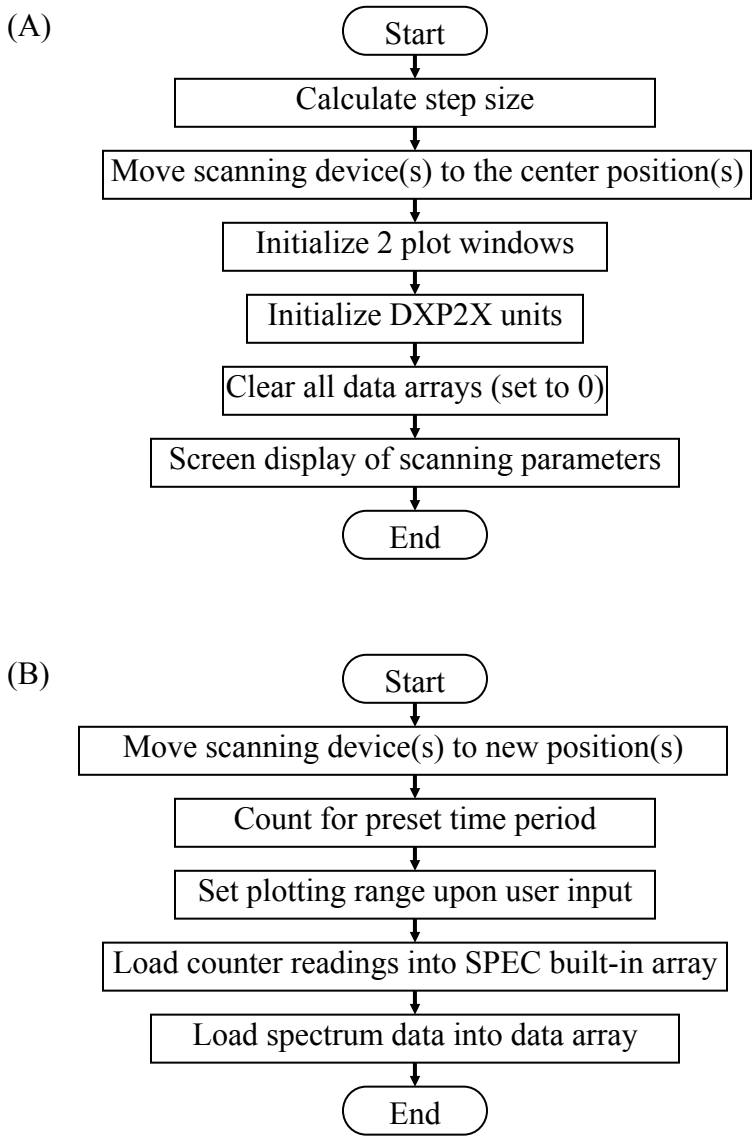

Figure B.5. Flow chart of the functions of (A) Initialization and (B) Data-taking at each scan step.

channels of the spectra are replaced with the SPEC counters, the DXP2X deadtime correction parameters, and the software SCA's, in that sequence. In the future, this part of the data-saving format should be changed to prevent the loss of the low energy spectrum. Also the deadtime correction parameters and the SCA's can be integrated into the SPEC counters as describe in the next section to simplify the data format. Before the data of first saveset are written, the general information about the XSW scan is written as the file-header into the file, including the motor name and positions at the scan center, the counter names and sequence, the software SCA settings, and information about the scan parameters and data format.

The on screen plot of the reflectivity and the spectra are updated after each scan, as well as the information about the reflectivity curve, such as the full width at half maximum (FWHM), center position of the full width at the half maximum (CFWHM), and the drift of the center. To get the screen plot displayed properly, a macro named 'plotini' needs to be run by the user before running the XSWDXP macro.

B.2 The MCA macro

The fluorescence spectrum can also be recorded during any SPEC counting operations by loading the MCA.MAC macro, which is a simplified version of ESRF macro *mca.mac*. Briefly, it can turn on and off the MCA data flow with software controls.

The basic idea in MCA.MAC is simple and straightforward. The centerpiece is a

counter named ‘mcatot’. To get the macro functional, a pseudo-counter needs to be setup in SPEC ‘config’. Just add a counter or rename an unused one to ‘mcatot’ and change the device for the counter to ‘NONE’. Other such pseudo-counters can be setup for software SCA’s or for other purposes if desired. When the MCA is turned on, the counter ‘mcatot’ will be enabled and the SPEC counting process will include an additional step to read the MCA spectrum out. And if the plot and/or filesave option is on, the spectrum will be plotted out and/or saved into the file, which could be either the current SPEC data file (in SPEC, the filename is saved in a string variable DATAFILE) or a separate file chosen by the user. When the MCA option is turned off, no MCA spectrum will be read out from the hardware. Therefore no plot or save-into-file functions will be carried out. Note that even if the MCA is turned off by software, the MCA device is still functioning, i.e., the MCA spectrum is still taken, but not read out. So if the slow process is the data-taking procedure instead of the data-transferring one from the MCA device to the host computer, turning off the MCA will not significantly help.

At this point, the MCA.MAC macro can only handle a single spectrum from one source. This means even with a multi-element detector, only the signal from one of the elements can be recorded at a given time. Recording multiple spectra should be easy to achieve.

The MCA macro includes a set of macros saved in the file also named mca.mac. Shown in the Figure B.6 is the hierarchy tree of the MCA macro.

The setup is the only part that the user needs to care about. The ‘user_Fheader’, ‘user_scan_loop’, and ‘user_getcounts’ macros are the SPEC ‘hook’ macros which will

be redefined upon turning on or off the MCA. When the MCA is turned on, they are directed to call the corresponding macros. And when the MCA is off, they exploit no action. Please use 'cdef' to include any other modifications to these macros if needed.

A special note here: at 5IDC, the macros that run the CCD detector also redefine some of the 'hook' macros mentioned above. However, they are not defined in the SPEC using conditional definition, 'cdef'. Instead they simply overwrite whatever the macros currently contain. The consequence is if the CCD macros are loaded, the MCA functions will not work. The user needs to reload the MCA macros with the SPEC command 'do/qdo' if the MCA function is desired. Although the 'hook' macros in the MCA macros are defined with 'cdef', therefore the codes CCD macros require should not be changed upon loading the MCA macros, the fully compatibility test has not been carried out yet. Currently, it is better to use only one device (CCD or MCA) at a time. And load the macro for the device before running it.

There are a couple of macros that can be used independently to control the MCA. But generally the 'mca_setup' should be enough for most occasions. There are nine options given when running 'mca_setup' macro. They are:

(1). **MCA device number**—this is the number assigned by SPEC to the MCA device (starting from 0). Generally, if a PCAIII card is present in the system, it would always be device 0. Any other MCA device, e.g., a XIA-DXP2X module, would have a device number starting from 1 and up. When the multiple MCA devices exist in the system, it could be tricky to find out the right MCA device number. Follow the general description below to do this. First in SPEC, check how many MCA devices are loaded

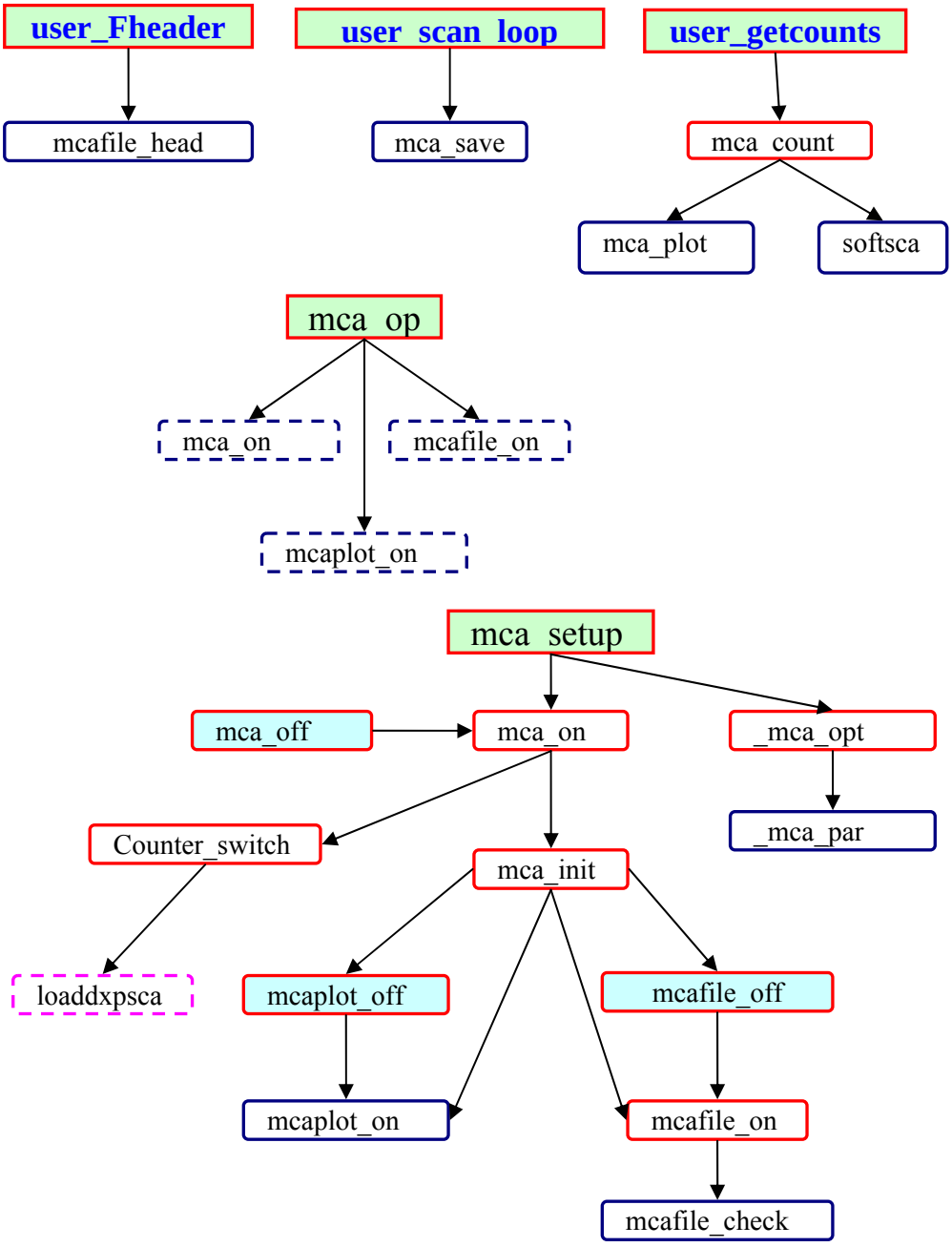

Figure B.6. The hierarchy tree of the functions in mca.mac macro.

with the command ‘mca_sel(“?”)’. If the desired MCA device is the only one, the device number will be 0. If more than one appears and it is not obvious which one is the desired device, pay attention to the description of each device. Those descriptions could be found accordingly on the config→CAMAC configuration screen. The CAMAC slot number will be given on that screen. The one with the desired detector (element) connected to it is the right one. For instance, for a 13-element detector (#1 - #13), the element #6 is the one wanted. The four XIA-DXP2X units are in CAMAC slot 3 - 6 and the signal from element #6 goes into the second channel of the unit in slot 4. In the CAMAC configuration list, slot 4 is assigned as DXP1. And from ‘mca_sel(“?”)’, DXP1 is device 1. Therefore the MCA device number is 1. NOTE that this description here is only good for the PCAIII card and the XIA DXP2X unit.

2). **MCA channel number**—this is the number of the channel on the DXP2X unit (always starting from 0). As in the example discussed above, the element #6 is in the second channel of the unit. So the channel number is 1. For devices like PCAIII card, this number will always be 0 since there is only one channel on a PCAIII card.

3). **Bin of active channel**—this is the number indicating how many MCA channels are in each spectrum.

For a PCAIII card, usually both the ‘gain’ and the ‘group_size’ are set to this number. If desired, an integer factor can be used such that gain = I * group_size to achieve another level of digital amplification. NOTE the ‘gain’ value cannot exceed the memory size physically present on the PCAIII card. E.g., if ‘gain’ = 4096 and ‘group_size’ = 512, I = 8 is the digital amplification factor achieved by this setting.

For an XIA-DXP2X channel, the setup is done through MESA2X; therefore usually the total bin number is 1024 (could be as high as 8192). Normally this bin number should be the same as that set in MESA2X. But if desired, this one can be smaller (e.g., 512 or any positive number).

4). **MCA on or off**—here 1 means on and 0 means off. This is the flag to turn on the MCA. Again to get this working, a pseudo-counter named mca_tot is required.

5). **MCAplot on or off**—turn on spectrum plot or not. If the MCA is turned off, no spectrum is plotted disregarding the setting of this parameter. The spectrum is supposed to be plotted in a second plot window. The second window should be initialized when the MCAplot on option is selected. But occasionally this does not work as expected. One known bug is when SPEC started with the MCAplot option turned on (due to the saved SPEC status upon quitting), the plot will appear in the text window before rerun 'mca_setup'. If this happens, it can be solved by simply running 'mca_setup' once or turning off the plot option.

6). **MCAfile on or off**—turn on spectrum data-recording or not. If MCA is turned off, no spectrum is saved disregarding the setting of this parameter.

So the MCA on/off is a master switch. MCAplot and MCAfile are only effective when the MCA is turned on.

7). **MCA filename**—the filename for the MCA spectrum data. If left empty, SPEC data file (DATAFILE) will be used. Input '-' to switch back to SPEC data file from another file. If a different file is chosen, the motor information is recorded for each scan. The software SCA information (see below for details) will be recorded in the scan

head in both cases. The data format is the same as the ESRF data format, e.g., in a normal SPEC file, the data following the symbol '@' indicate their difference from the normal scan data; and the spectrum data are always saved after the normal SPEC scan data. Because the line could contain hundreds or even thousands of integers, it is broken into multiple lines with 32 number on each line and a '/' is added to the end of each unfinished line.

Currently, 'ct' command does not record the spectrum any more.

8) & 9). **MCA plot range-lower/upper limit**—the plot range of the spectrum (in MCA channel number, in the range of 0 - 1023 normally). These are the same settings as those in 'setxswdxp'. If set improperly, they will be reset to full range.

There are also other simple function macros like 'mca_on' and 'mca_off', 'mcaplot_on' and 'mcaplot_off', 'mcafile_on' and 'mcafile_off'. Their names are self-explaining.

'mca_plot' [MCA_channel_lowerlimit MCA_channel_upperlimit] will replot the last read spectrum. If the two optional parameters are given, the new range will be defined with the parameters. Otherwise the last set range is used.

'mca_save' saves the spectrum into the assigned file with normal SPEC format (32 per line). If a string given as the optional parameter, the spectrum will be saved into that file as one column. E.g., 'mca_save zfile' will save the spectrum into file 'zfile.mcaspectrum' instead of the file assigned. This is to offer an easy way to transfer the spectrum into a plotting software such like 'Excel'.

One more macro that is useful is the ‘setdxpsca’. The macro is part of ‘xswdxp.mac’. By running the macro software SCAs can be setup. Just input the MCA channel starting and end number and the counter number (the counter name will be shown in the parentheses next to the counter number). The MCA macro will automatically work on the spectrum and assign the correct value. The counter number can be obtained with command ‘counters’. A series of special reserved values can be used for the MCA channel starting number (first column). When those values are given, the MCA channel end numbers have no effect and special operations are taken to read the deadtime correction related parameters out of XIA DXP2X unit. They are listed in Table B.1.

The meanings of the parameters have been discussed in Appendix A. Assign them to the pseudo-counters to help the deadtime correction.

CAUTION: Again, do not assign the software SCA to any real counters that are in use. Only use the pseudo-counters for this purpose. The macro does not have any fool-proof check and the software SCA always overwrites any hardware readings.

‘mcaop’ is a special macro, which when used preceding a normal SPEC scan command, turns on the MCA and runs the scan; then returns the MCA settings, including the MCA setting, the plot and save settings, back to its original status.

The MCA macro is easier to setup and run than the XSW one. However, currently it can only handle one detector element. A combination of MCA and XSW macro might be the next step for the multi-element detector system data collection.

Table B.1. Special setup for the digital Single Channel Analyzer (SCA).

Value	-1	-2	-3	-4	-5	-6
Read-in	*Livetime*	*Realtime*	*FastPeaks*	*EventsInRun*	*Overflow*	*Underflow*